Defect engineering of phase transition materials to create optical metasurfaces

Dissertation

zur Erlangung des akademischen Grades
doctor rerum naturalium
(Dr. rer. nat.)

vorgelegt dem Rat der Physikalisch-Astronomischen Fakultät
der Friedrich-Schiller-Universität Jena

von Diplom-Physiker Jura Rensberg
geboren am 09.02.1986 in Rostock

Gewidmet: Anton, Mara, Felix und Lara
- Habt Mut den Dingen auf den Grund zu gehen -

1. Gutachter: Prof. Dr. Carsten Ronning, Friedrich-Schiller-Universität Jena

2. Gutachter: Prof. Dr. Heidemarie Schmidt, Friedrich-Schiller-Universität Jena

3. Gutachter: Prof. Dr. Christina Trautmann, Technische Universität Darmstadt

Tag der Abgabe:	1.11.2017
Tag der Disputation:	1.02.2018

Gezielte Defekterzeugung in Phasenübergangsmaterialien – Eine Methode zur Herstellung optischer Metaoberflächen

Das Wisschenschaftsfeld der Photonik umfasst die Erforschung aller Technologien, die zur Erzeugung, zum Transport, zur Detektion und zur Manipulation des Lichtes genutzt werden können. Ähnlich wie in der Elektronik ist der technologische Fortschritt in diesem Feld im Wesentlichen von einer stetigen Miniaturisierung der optischen Bauelemente geprägt. Mit Hilfe von optischen Metaoberflächen gelingt schon jetzt auf sehr kleinem Raum eine gezielte Manipulation der Amplitude, Phase und Polarisation des Lichts, das entweder durch die Metaoberfläche transmittiert oder von dieser reflektiert wird. Dabei besteht eine Metaoberfläche aus einer Lage von künstlich hergestellten Strukturelementen, deren Größe deutlich geringer als die Wellenlänge des Lichts ist. Die effektiven optischen Eigenschaften dieser Oberflächen werden von der Größe, Form und Interaktion der einzelnen Strukturelemente bestimmt. Dennoch ist die Wirkung der Metaoberflächen auf die Ausbreitung des Lichts meist statisch und neue Konzepte für eine aktive Kontrolle der optischen Eigenschaften werden benötigt.

Eines der am häufigsten untersuchten optisch aktiven Materialien ist Vanadiumdioxid (VO_2), das einen reversiblen Phasenübergang zwischen einer isolierenden und metallischen Phase bei einer Übergangstemperatur von ungefähr 67 °C aufweist. Aufgrund der enormen Änderung der optischen Eigenschaften während des Phasenübergangs werden VO_2-Schichten zunehmend in bestehende plasmonische Metaoberflächen integriert. Kürzlich konnte experimentell gezeigt werden, dass eine extrem dünne VO_2-Schicht mit einer Dicke von weniger als ein Zehntel der Wellenlänge des Lichts in der Nähe des Phasenübergangs auf einem geeigneten Substrat ähnliche Eigenschaften aufweist wie eine Metaoberfläche (Metaschicht). Die vorliegende Arbeit zeigt, dass es bei extrem dünnen VO_2-Schichten auf metallähnlichen Substraten aufgrund der nichttrivialen Phasenverschiebung an der Grenzfläche zu destruktiver Interferenz kommt, die zu einer kompletten Unterdrückung der Lichtreflektion und fast vollständigen Absorption des einfallenden Lichts führt. Es wird gezeigt, dass dieser Effekt nur auf Substraten zu beobachten ist, deren Brechungsindex kleiner oder rund 1 ist.

Ziel dieser Arbeit ist es, aus den VO_2-Metaschichten optische aktive Metaoberflächen zu machen. Dabei sollen in einer extrem dünnen isolierenden VO_2-Schicht Strukturelemente aus metallischem VO_2 erzeugt werden. Die zentrale technische Herausforderung ist hierbei die dauerhafte lokale Senkung der Phasenübergangstempertur von VO_2 auf Werte nahe der Raumtemperatur. Hierfür wird bislang hauptsächlich die Dotierung mit Fremdatomen während des Wachstumsprozesses erforscht. Eine Alternative zur Dotierung mittels chemischer Substitution während das Wachstums ist die Ionenimplantation, bei der sich das Dotierprofil durch die Wahl der Implantationsparamter einstellen lässt. Diese Methode wird häufig kritisiert, da sich die Erzeugung von Strahlungsdefekten nicht vermeiden lässt. Die vorliegende Arbeit zeigt nun, dass schon die gezielte Erzeugung von Defekten durch Ionenbestrahlung die Übergangstemperatur von VO_2 bis hinunter zur Raumtemperatur senkt. Hierfür wurden die temperaturabhängigen strukturellen, elektrischen und optischen Eigenschaften von VO_2 als Funktion der Bestrahlungsparameter untersucht. Die Änderung der Übergangstemperatur wird durch die Deplatzierung von Sauerstoff- und Vanadiumgitteratomen hervorgerufen, die zu Gitterverspannungen und einer Änderung der Vanadiumvalenz führen und hängt insbesondere von der Volumendichte der erzeugten Defekte ab.

Die Ionenbestrahlung lässt sich mit gängigen Lithographieverfahren kombinieren. Bei der Bestrahlung von VO_2 durch strukturierte Masken werden gezielt nur die Bereiche der Schicht geschädigt, die nicht verdeckt sind. Dabei entstehen Bereiche, deren Übergangstemperatur deutlich geringer ist als die der unbestrahlten Regionen. In einem Temperaturbereich, in dem geschädigtes VO_2 bereits metallisch ist, während unbestrahltes VO_2 noch isolierend ist, führt die künstliche Phasenkoexistenz zu effektiven optischen Eigenschaften. Insbesondere bei anisotropen Stukturen konnten sehr hohe und veränderliche Werte der Doppelbrechung ($\Delta n = 0.8$) und des Dichroismus ($\Delta \kappa = -4.9$) erzeugt werden. Auf einem Sapphirsubstrat werden aus den künstlich strukturierten VO_2-Metaschichten aufgrund des starken Interferenzeffekts atomar flache optische Metaoberflächen. Exemplarisch wurden in dieser Arbeit schaltbare Absorber und veränderliche Polarisatoren hergestellt und deren temperaturabhängige optische Eigenschaften untersucht.

Contents

1 Introduction

Advanced technology gradually develops from the age of electronics to that of optoelectronics and photonics.[1] Precision optical components are ubiquitous in our daily life enabling high speed communication through fiber-optic cables, data recording, information processing, displays used in TVs and smartphones, medical treatment, and industrial manufacturing. The rapidly growing field of photonics is concerned with the generation, transport, detection, and manipulation of light. The amplitude, phase, and polarization of light waves can be controlled by conventional optical components, like lenses and waveplates. These components rely on gradually accumulated changes of the wave front, due to light propagation through homogeneous dispersive media of given refractive indices over distances much larger than the wavelength.[2] Consequently, conventional optical elements do not meet the increasingly demanding requirements of integration and miniaturization in modern photonic systems.

Metamaterials are artificially engineered media that are structured on a sub-wavelength scale. The effective optical properties of metamaterials arise from their internal structure, e.g. size, orientation, shape, and pattern of the constituents, and cannot simply be inferred from the materials they are composed of. Light propagation in metamaterials can be explicitly designed by spatial and spectral variation of the effective permittivity and effective permeability.[3–5] Not constrained by the optical response of naturally occurring materials, metamaterials enable negative refraction,[6,7] fabrication of super-lenses,[8–10] which are capable of imaging objects that are much smaller than the wavelength of light, cloaking devices,[11] efficient light confinement,[12] and perfect light absorption.[13] However, the required nano-fabrication of the three-dimensional structures is challenging and drastically limits the applications of metamaterials.

Metasurfaces - two-dimensional metamaterials - induce abrupt and controllable changes of the amplitude, phase, and polarization of light within a propagation length much smaller than the wavelength of light, and can be readily fabricated using existing lithography techniques (figure 1.1a). They usually consist of sub-wavelength patterned arrays of optical antennas with spatially varying geometry, size, shape or orientation. The local optical response is determined by resonant interaction of light with the antenna array, which often - but not exclusively - involves metallic nanostructures or apertures opened in metallic films.[2,5,14,15] The effective optical properties can deviate significantly from classical reflection and refraction laws.[2,5,14,16] As an example, Yu *et al.*[16] demonstrated that a constant gradient of phase discontinuity along the interface caused by optical resonators with spatially varying geometry leads to anomalous reflection and refraction of light. Among others, these findings were utilized to fabricate ultra-thin flat lenses, which allow distortion-free imaging at visible[17,18] and near-infrared wavelengths.[19]

To date, mainly plasmonic metasurfaces, which utilize strong interaction between light and localized surface plasmons of metallic antennas were demonstrated for applications like beam steering,[2,5,16] polarization control,[20,21] enhanced absorption,[22–26] enhanced thermal emission,[27] and anti-reflection coatings.[22,25,28] Although the traditionally used metals, like gold and silver, support strong collective oscillations of free electrons (plasmons),[29] they

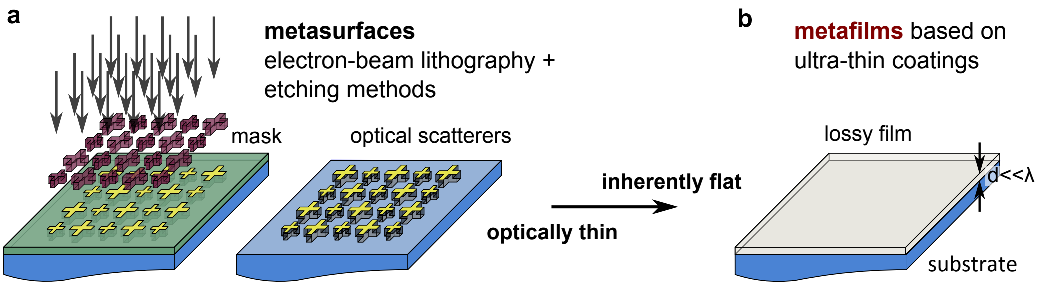

Figure 1.1.: **(a)** Typically, metasurfaces consist of sub-wavelength patterned arrays of optical scatterers and can be readily fabricated using existing lithography and etching methods. By strong interaction of light with the surface plasmons of metallic scatterers, an abrupt but controllable change of the wavefront is achieved. **(b)** Metafilms, created by using optically ultra-thin films made of lossy materials, have similar optical properties like metasurfaces. Here, the abrupt change of the wavefront originates from the phase jump difference between waves reflected and transmitted from the surface and the interface of the film.

suffer from high losses at near-infrared and especially visible wavelengths caused in part by interband transitions, which limit high device efficiency to reflection mode.[5,14,29,30] Besides attempts to use gain media as host materials,[31] which might provide a means to compensate the inherent losses of plasmonic metasurfaces, all-dielectric metasurfaces have recently been demonstrated.[14,32,33] These metasurfaces do not suffer from intrinsic losses and achieve high efficiency and full phase control in transmission mode. Further, alternative plasmonic material platforms that use low-loss materials with adjustable plasma frequencies are being developed. The most promising material classes are transparent conductive oxides (TCOs) and transition metal nitrides.[5,34] With carrier concentrations up to $10^{21}\mathrm{cm}^{-3}$ [35], highly doped TCOs enable low-loss semiconductor based plasmonic metasurfaces for the near-infrared spectral range,[36] while metal-nitrides at least match the optical performance of gold at visible wavelengths.[34,37] A controversial type of metasurfaces - termed metafilms[2] - was proposed by Kats *et al.*[38,39] (figure 1.1b). The authors demonstrated that optical coatings based on nanometer-thin lossy films substantially modify the light spectrum when applied to a metallic substrate. For these metafilms, abrupt changes of the wave front originate from the difference of the nontrivial interfacial phase shifts - each can be substantially different from 0 or π - on reflection or transmission of light at the surface and interface of the lossy film.[2,39] However, all metafilms demonstrated by Kats et al.[38,39] are not artificially patterned, and thus - per definition - no metasurfaces.

The emerging frontier of active tunability, reconfiguration and switching of the optical properties of metasurfaces and metafilms is particularly exciting, with promising applications including modulation, routing, dynamic beam shaping, and adaptive optics.[40–52] Dynamic control can be achieved by hybridizing existing metasurface designs with functional matter, e.g. microelectromechanical systems,[41] liquid crystals,[53,54] graphene,[55] strongly electron-correlated phase transition,[46,48,49,56,57] or chalcogenide phase change materials.[43,58–61] Both of the latter feature various structural and electronic transitions and have particular promise because of their large change of optical properties given an applied stimulus such as voltage,[62] temperature,[44,48,63,64] stress,[65,66] and light.[67–69]

Strongly correlated transition-metal oxides exhibiting insulator-metal transitions (IMT) are currently considered as basic functional materials of oxide electronics.[70] One of the most promising phase transition materials is VO_2, which exhibits a reversible IMT as the temperature exceeds a critical temperature of $T_C \sim 67\,^{\circ}\mathrm{C}$.[71,72] At the onset of the IMT, nanoscale islands of the metallic phase start to nucleate surrounded by insulating VO_2, which then grow and connect in a percolation process.[63] The gradually occuring IMT corresponds to a dramatic change in the complex refractive index.[38,44,48,63] Further, because of the inherent phase coexistence on a subwavelength scale, VO_2 in its transition region has been recently described as a natural disordered optical metamaterial with large optical absorption, especially at mid-infrared (mid-IR) wavelengths.[73] It was demonstrated by Kats *et al.*[38] that an ulra-thin VO_2 film with thickness much smaller than the wavelength of incident light deposited on a sapphire substrate can be tuned into a near-perfect absorption state (almost completely suppressed reflection) by varying the temperature in close proximity to the IMT. The easy fabrication of large-scale thin films makes VO_2 one of the most promising candidates for active, widely tunable optical materials in the emerging field of meta-devices. However, several key challenges remain for the successful integration of VO_2 metasurfaces into photonic and optoelectronic devices, which have been addressed in this thesis as follows:

i. Near-perfect absorption and almost completely suppressed reflection of light using ultra-thin VO_2 films was demonstrated so far only on metal and polar dielectric substrates.[38,74,75] Unfortunately, the wavelength at which light reflection can be suppressed is primarily determined by the nature of the particular substrate and is pinned to values close to the plasma or phonon resonances.[76] Despite the experimental demonstrations of suppressed reflection and enhanced light absorption in ultrathin absorbing films,[38,39,44,77–79] the parameter space of possible film and substrate combinations has not been fully explored.
   This thesis introduces and experimentally verifies a general strategy that facilitates the design of near-perfect absorbers and anti-reflection coatings based on ultra-thin films. It is identified that completely suppressed reflection of light using ultra-thin absorbing coatings with thickness much smaller than the wavelength of light can only be achieved on low-index substrates with real part of the complex refractive index $n \lesssim 1$. Such low refractive indices are most commonly found in the vicinity of phononic and plasmonic resonances, where a crossover of the real permittivity from positive to negative results in an epsilon-near-zero (ENZ) condition. This thesis theoretically and experimentally demonstrates, that the wavelength of suppressed reflection can be arbitrarily selected within the near- and mid-infrared wavelength range by adjusting the plasma frequency of tunable ENZ substrates, such as aluminum-doped zinc oxide (AZO).

ii. It has been noted that the intrinsic transition temperature of VO_2 films limits the utility of this material for device fabrication, which requires a T_C close to room temperature.[38,44] The common route for appreciable reduction of T_C is impurity doping during growth by chemical substitution methods.[80–96] In particular, doping VO_2 films with tungsten is very attractive since it reduces T_C by approximately $-20\,^{\circ}\mathrm{C/at.\%}$. Ion implantation is often used as an alternative approach to introduce impurity atoms into the crystal lattice of solids. On the one hand, ion implantation is a non-equilibrium process and thus, allows for high doping concentrations. On the other hand, the doping profile can be precisely adjusted by choosing appropriate implantation conditions. Ion implantation is accompanied by the inevitable formation of irradiation damage, which is considered disadvantageous for ion beam doping and subsequent post-implantation annealing procedures are required.
   This thesis now demonstrates that the formation of lattice damage by ion irradiation

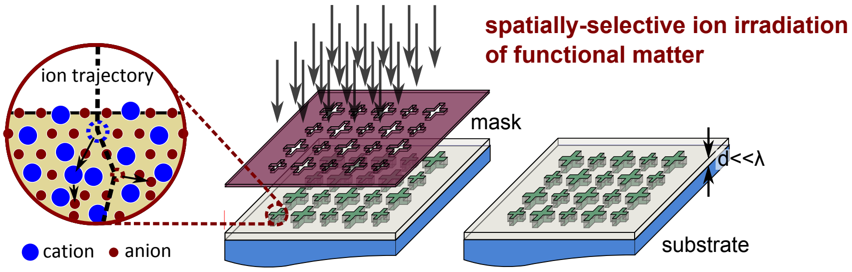

Figure 1.2.: A new method to fabricate metasurfaces is presented in this thesis: Spatially-selective ion irradiation using lithographically defined masks can dramatically change the optical properties of functional matter on a sub-wavelength scale. In materials like VO_2, the shape, temperature, and persistence of artificial phase co-existence of metallic and insulating regions can be controlled by locally introducing irradiation defects.

itself can dramatically reduce the phase transition temperature of VO_2 films, because the electronic structure of strongly correlated materials is very sensitive to small amounts of lattice defects. The intentional creation of structural defects and lattice damage ("defect engineering") by ion irradiation separated from any chemical doping is investigated as means to modify and engineer the thermally driven IMT of VO_2. The effect of ion irradiation on the electrical, optical, and structural properties of VO_2 across the IMT is studied as a function of ion fluence, ion energy, ion species, and post irradiation annealing treatments. Gaining insight into the underlying physics of modifying the IMT of VO_2 by defect engineering could potentially help to extend this approach to other phase change and phase transition materials, such as germanium antimony telluride and samarium nickelate.

iii. The ultimate goal is to fabricate inherently flat VO_2 metasurfaces, in which structural elements are composed of metallic VO_2 regions embedded in an insulating VO_2 matrix. To achieve this goal, lateral control over the phase transition temperature is required. Phase coexistence arranged in a stripe pattern has been observed in thin VO_2 films grown on titanium dioxide substrates and occurs naturally due to epitaxial strain.[97,98] Epitaxial strain also leads to regular pattern formation in spinodal decomposed VO_2-TiO_2 films. However, strain engineering requires particular substrates and provides little control over the pattern of phase coexistence. Unlike existing means to modify the IMT of VO_2 by doping during growth, ion irradiation can be combined with lithographic patterning to achieve artificial phase coexistence of metallic and insulating VO_2 regions laterally by locally adjusting the phase transition temperature (compare figure 1.2). This will turn VO_2 metafilms into actual metasurfaces, which are not only optically flat like plasmonic antenna, but remain truly inherently flat during device fabrication. By using area-selective ion irradiation, this thesis demonstrates several optical metasurfaces, including tunable absorbers and tunable polarizers and investigates their effective optical properties.

Spatially selective nanoscale defect engineering of phase change and phase transition materials might enable new inherently flat active tunable photonic structures. Because of their surface morphology, these structures potentially serve as a platform to design optoelectronic and photonic devices build up from stacked elements with tunable functionality.

2 | Fundamentals

This chapter summarizes fundamental properties of vanadium dioxide (VO_2), describes the concept of thin film optics, and provides an introduction to ion beam modification of materials with emphasis on the modification of VO_2.

2.1. Vanadium dioxide VO_2

The insulator-metal transition (IMT[I]) in many transition-metal oxides originates from strong Coulomb interactions between d-band electrons (electron correlation).[70,99–104] Vanadium is one of the transition metals with a partially filled d-band that exists in several oxidization states. It forms the stable Magnéli (V_nO_{2n-1}) and Wadsley ($V_{2n}O_{5n-1}$) homologous series of vanadium-oxygen compounds with closely related crystal structure, respectively.[105,106] The vanadium ions in the pure oxide phases VO, V_2O_3, and VO_2 have $V^{2+}(3d^3)$, $V^{3+}(3d^2)$, $V^{4+}(3d^1)$ electronic structure, respectively, whereas, V_2O_5 is formed by V^{5+} ions with no 3d electrons.

In single crystal form, several oxides of vanadium undergo a sharp IMT as the temperature is increased to a certain critical value (figure 2.1a), with a change of electrical resistivity by several orders of magnitude.[70,101,107–111] Although vanadium trioxide (V_2O_3) shows the largest resistivity change, the IMT in vanadium dioxide (VO_2) is of most practical use, because it is closest to room temperature. When heated above a critical temperature of $T_C \sim 67\,°\mathrm{C}$[112], bulk VO_2 undergoes an abrupt first order transition from an insulating to a metallic phase with up to 5 orders of magnitude change in resistivity within less than 0.1 °C with a hysteresis of $\sim 1\,°\mathrm{C}$.[113] The electronic phase transition is accompanied by a structural transition associated with lattice distortion, which leads to cracking of VO_2 crystals limiting the applicability of bulk materials.[114–116] The multiple valence states of vanadium result in a complex vanadium-oxygen phase diagram in which VO_2 is stable only within a very narrow region of phase space.[106] As a consequence nonstoichiometric VO_{2-x} is often a mixture of several stable phases. However, recent developments in stabilizing vanadium in a particular oxidization state using various thin-film deposition techniques, enabled the growth of high-quality epitaxial VO_2 films on various substrates.[100,117–120] Clamping to the substrate prevents VO_2 thin films from cracking and thousands of transition cycles have been demonstrated.[121]

The IMT in thin VO_2 films occurs gradually (figure 2.1b, and 2.1c) and the size, shape, and position of the hysteresis loop critically depends on the morphology, local stoichiometry,[97,122] distribution of elastic strain,[123–126] and concentration of structural defects.[127] The gradual change can be observed for example in the near-infrared spectral region, where the presence of free carriers in the metallic phase leads to enhanced absorption of light and reduced

---

[I] For simplicity, in this thesis (and many of the recent publications) the term IMT refers to the change in physical properties as the temperature is increased. Physically, electron correlation leads to electron localization and thus a transition from metallic to semiconducting or insulating behaviour, which is termed MIT in literature.

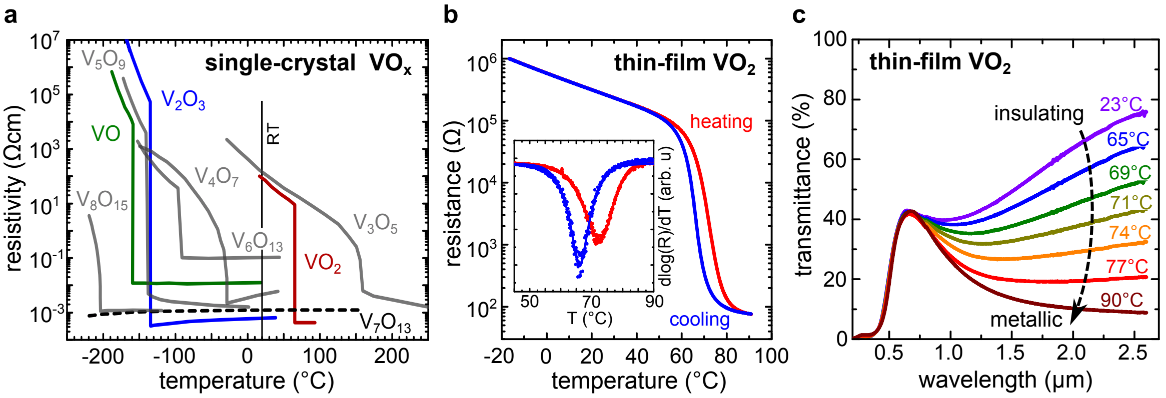

Figure 2.1.: **(a)** Temperature dependent resistivity of single-crystals of selected VO_x phases.[70,101,107–111]. Almost all of the vanadium oxides feature a sharp IMT at cryogenic temperatures. However, no IMT is observed for V_7O_{13} (dashed line) **(b)** Temperature dependent resistance of a $\sim 100\,\mathrm{nm}$ VO_2 thin-film grown on c-Al_2O_3. The phase transition is broadened with respect to single crystals and takes place over a temperature range of $\sim 25\,°C$ (compare inset: logarithmic derivative of the resistance). **(c)** Optical transmittance of a thin VO_2 film as a function of wavelength and temperature. The transmittance changes gradually from transparent to opaque in the near infrared upon heating through the IMT.

transmittance. The typical resistivity change of 3-4 orders of magnitude with a hysteresis width of $10 - 15\,°C$ is indicative of the high quality of the VO_2 films used in this thesis.

2.1.1. Crystallographic and electronic structure

In the metallic phase, VO_2 crystallizes in a rutile structure (R) characterized by vanadium atoms forming a tetragonal body-centered unit cell (space group $P4_2/mnm$) as schematically shown in figure 2.2. The lattice parameters are $a_R = b_R = 4.555\,Å$, and $c_R = 2.851\,Å$.[105,128,129] The vanadium atoms, centered each within an oxygen octahedron (VO_6 octahedron), form equidistant chains (V-V distance: 2.85 Å) along c_R. Adjacent VO_6 octahedra along c_R share a common edge, whereas the VO_6 octahedra at the body-centre and the corner of the rutile unit cell are rotated against each other by 90° with respect to c_R and share a common vertex. Since each of the VO_6 octahedra is slightly orthorombically distorted, oxygen atoms in the equatorial plane and in the apical direction (highlighted green and red in figure 2.2, respectively) show somewhat different V-O bond lengths:[130,131] $\sim 1.94\,Å$, and $\sim 1.92\,Å$, respectively. Next to the filled oxygen octahedra the VO_2 structure comprises the same amount of empty octahedra,[105] which are presumably preferential vanadium interstitial sites.

Across the phase transition (from high to low temperature) the vanadium atoms move from the octahedral sites by a combination of anti-ferroelectric displacement along the $[110]_R$ and $[1\bar{1}0]_R$ lattice directions, and dimerization along c_R, which results in a lowered crystal symmetry and a doubling of the unit cell (figure 2.1a). In the insulating phase, VO_2 has a simple monoclinic (M1) structure (space group $P2_1/c$) with lattice parameter and monoclinic angle:[132] $a_{M1} = 5.752\,Å$, $b_{M1} = 4.526\,Å$, $c_{M1} = 5.383\,Å$, and $\beta = 122.6°$, respectively. The density of monoclinic VO_2 used for calculations in this thesis is $\rho_{VO_2} = 4.57\,\mathrm{gcm}^{-3}$. The monoclinic lattice of VO_2 is related to the rutile lattice by the following relations: $\vec{a}_{M1} \sim -2\vec{c}_R$, $\vec{b}_{M1} \sim -\vec{a}_R$, and $\vec{c}_{M1} \sim \vec{b}_R + \vec{c}_R$.[133] All vanadium ions are dimerized and tilted in a zigzag-like fashion with respect to c_R forming chains with an alternating V^{4+}-V^{4+} distance of 2.619 and 3.164 Å.[134] The oxygen atoms stay roughly in the same position, which leads to three different V-O_1 bond lengths in the range from 1.76 to 1.87 Å and three V-O_2 bond lengths in the range from 2.01 to 2.05 Å.[135] Across the phase transition from high to low temperature

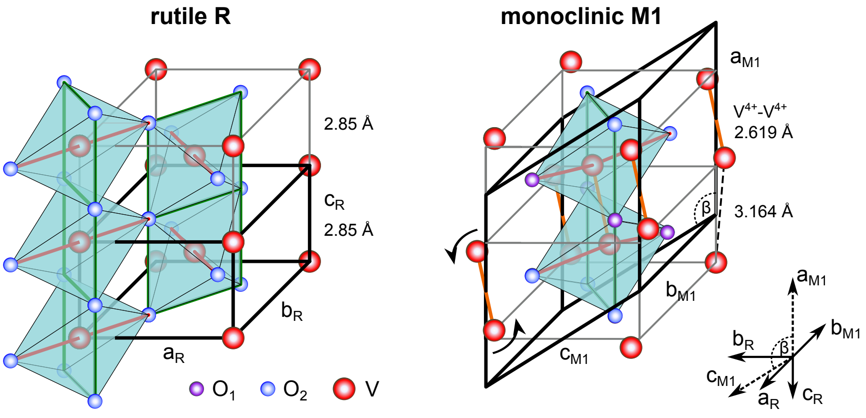

Figure 2.2.: Schematic drawing of the rutile (R) and monoclinic (M1) structure of VO_2. For clarity M1 is tilted about the a_{M1} (c_R) axis by 90° with respect to R. The equatorial plane and the apical V-O bonds are highlighted in green and red, respectively.

the lattice expands by $\sim 1\%$ along c_R, whereas it shrinks by $\sim 0.6\,\%$ and $\sim 0.2\,\%$ along a_R and b_R, respectively, which leads to a slight unit cell volume decrease of $\sim 0.04\,\%$.[132]
Besides the stable M1 and R phase, two metastable states, a monoclinic M2 phase and a triclinic T phase, can be induced by doping or strain.[125,136–138] In the M2 structure, half of the V chains dimerize but do not twist, and the other half of the vanadium chains twist but remain equidistant along the resulting zigzag chain. The lattice is expanded by 1.7% along the vanadium chains with respect to c_R. The T phase is a continuous intermediate phase between M1 and M2.

The electronic band structure of VO_2 near the Fermi level, first proposed by Goodenough,[80] results from the oxygen octahedral environment of the V^{4+} ions and the associated hybridization of the V 3d with O 2p orbitals, which are involved in chemical bonding.[80,100,131,139–144] The octahedral crystal field of the six O^{2-} ions splits the degeneracy of the five V 3d states into an upper two-fold degenerated e_g level and a lower three-fold degenerated t_{2g} level (figure 2.3a). The upper e_g consist of the two orbitals, which point directly toward the O^{2-} ions and thus form σ-type bonds (e_g^σ orbitals). The other three orbitals point in between the O^{2-} ions. The slight orthorombic distortion of the crystal field further splits the t_{2g} level into a doublet consisting of two orbitals, which form π-type bonds (e_g^π orbitals) and an a_{1g} level with slightly lower energy formed by the orbital, which is oriented towards adjacent V^{4+} ions along c_R ($d_{||}$ orbital). The V 3d orbitals hybridize with the O 2p orbitals and form lower-energetic completely filled bonding states (σ, π) with predominantly O 2p character, and higher-energetic anti-bonding states ($e_g^\sigma \rightarrow \sigma^*$, $e_g^\pi \rightarrow \pi^*$) with predominantly V 3d character (fig 2.3b).
In the metallic phase, the conduction band is formed by partially filled $d_{||}$ and π^* states, because the e_g^π orbitals have much smaller p-d overlap compared to the e_g^σ orbitals. Across the phase transition (from high to low temperature) the dimerization of V^{4+}-V^{4+}, and thus the direct cation bonding along c_R splits the $d_{||}$ band into completely filled bonding ($d_{||}$) and empty anti-bonding states ($d_{||}^*$). Further, the anti-ferroelectric displacement of V^{4+} ions increases the p-d overlap of the e_g^π orbitals and causes a shift of the π^* states up above the Fermi level. The combination of both mechanisms opens up a bandgap between the lower $d_{||}$ and π^* band of approximately $\alpha_0 \sim 0.65\,\text{eV}$.[80]
Following the assignment of Qazilbash *et al.*[145], electronic transitions, which are important for

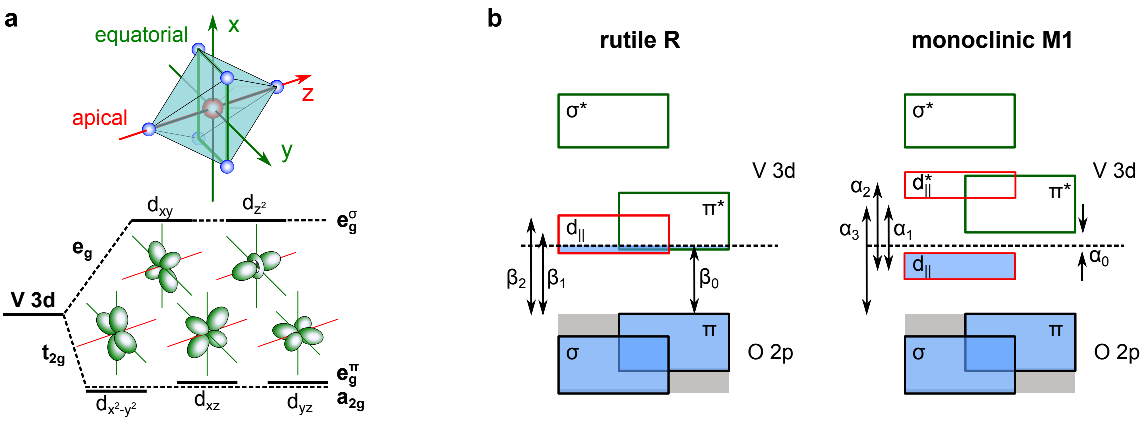

Figure 2.3.: (a) The octahedral environment of the V^{4+} ion and the orthorombical distortion splits the energetic degeneracy of the V 3d states in the rutile structure of VO_2. The d_{xy} and d_{z^2} orbitals point towards the O^{2-} and have larger p-d overlap compared to the d_{xz} and d_{zy} orbitals, which point in between the O^{2-}. The $d_{x^2-y^2}$ orbital points in between the O^{2-} and is involved in direct cation bonding along c_R and thus has smallest p-d overlap. Note that the orientation of the coordinate system differs compared to the conventional definition of axes pointing towards opposite anions, to account for direct cation bonding along x (c_R). **(b)** Schematic electronic band structure of VO_2 in the metallic rutile (R) and insulating monoclinic (M1) phase, as proposed by Goodenough.[80]

the interpretation of optical spectra, are marked. These include the transition from valence band to conduction band edge (β_0), and the transitions from valence band to $d_{||}$ (β_1) and to π^* band (β_2) in the metallic R phase, respectively, as well as the transitions from filled $d_{||}$ to π^* (α_0, α_1) and to $d_{||}^*$ band (α_2), and from valence band to π^* band (α_3) in the insulating M1 phase, respectively.

Owing to the fact that the structural and electronic transitions occur almost simultaneously within the time scale of picoseconds,[146–148] there is a long lasting debate on whether the IMT of VO_2 is a Peierls or a Mott transition.[63,80,99,133,146,149–152] A detailed discussion is given for instance in reference [153]. In the Peierls model, the structural transition, especially the dimerization of V^{4+}-V^{4+}, drives the IMT. It is responsible for the $d_{||}$ band splitting, and leads to the anti-ferromagnetic displacement that pushes the π^* band energetically up. For example Cavalleri *et al.*[146] found that the structural motion limits the time scale of the IMT and is much slower than the electronic excitation that was used in their time-resolved THz spectroscopy experiments. On the contrary, in the Mott picture, the phase transition is driven by electron-electron correlation. Strong correlations in the $d_{||}$ orbital are screened by electrons in the e_g^π orbitals in the metallic phase, whereas in the insulating phase the e_g^π orbitals are empty, and unscreened electron-electron correlation in the $d_{||}$ orbitals open the band gap. This picture is supported by near-field optical spectroscopy,[63,154] cluster dynamical mean-field theory,[155] X-ray absorption spectroscopy at the V $L_{2,3}$ edge,[149,156] and comparison with other insulating VO_2 phases.[151,157] However, the change in orbital occupancy across the phase transition results in charge ordering and makes the V^{4+} ions along c_R susceptible to a structural transition. As a consequence the electronic structure of VO_2 is very sensitive to slight changes of the structural properties, especially, to the introduction of structural defects and strain. But at the same time the structural properties react strongly to changes of the electronic structure, in particular to the introduction of charge carriers by impurity doping.

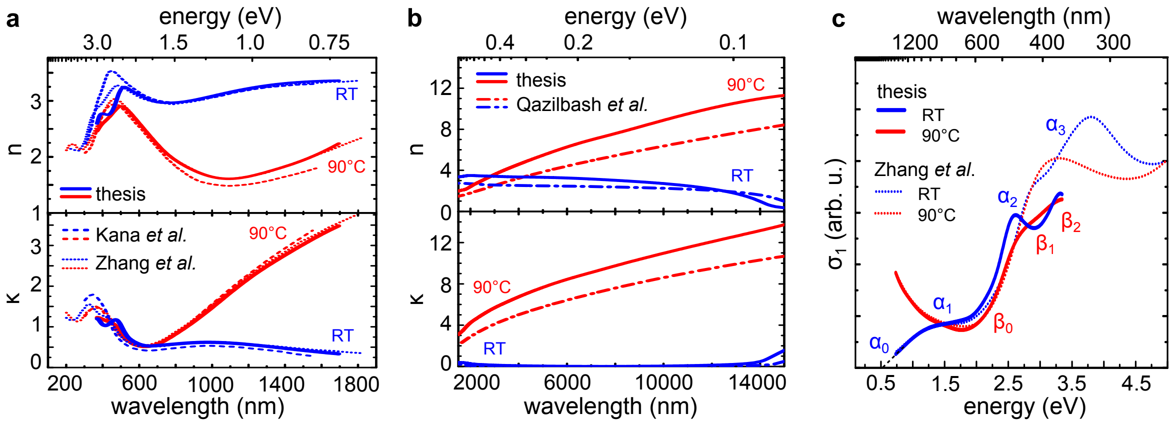

Figure 2.4.: (a, b) Real n and imaginary part κ of the refractive index of VO_2 thin films in the UV-VIS-NIR (a), and in the mid-IR spectral range (b), determined by spectroscopic ellipsometry at room temperature (RT, blue) and 90 °C (red), respectively. Literature values taken from Kana et al.[158], Zhang et al.[159], and Qazilbash et al.[63] are given for comparison. **(c)** Real part of the optical conductivity σ_1 calculated from refractive index data given in (a). Features, that correspond to optical transitions are labeled according to figure 2.3b.

2.1.2. Optical properties of VO_2

The changes of structural and electrical properties across the IMT are accompanied by changes of the optical properties of VO_2. In general, optical properties can be described in terms of the complex refractive index $\tilde{n} = n + i\kappa$ or the complex permittivity $\tilde{\epsilon} = \epsilon_1 + i\epsilon_2$, which are connected by the relation $\tilde{\epsilon} = \tilde{n}^2$. The real ($n$) and imaginary part ($\kappa$, extinction coefficient) of the complex refractive index of both phases of VO_2 (M1 at RT and R at 90 °C) are shown in figure 2.4a,b. In the spectral range from ultraviolet (UV) to near-infrared (NIR) literature data[158,159] and data obtained in this thesis are in good agreement (figure 2.4a). The striking feature across the phase transition of VO_2 is a significant increase of κ and a reduction of n in the NIR associated with the vanishing band gap. In contrast, almost no optical data are available in literature in the mid-infrared spectral range (mid-IR),[63] and the discrepancy of data obtained by Qazilbash et al.[63] and data obtained in this thesis might be caused by a different quality of VO_2 films used for spectroscopic ellipsometry, respectively (figure 2.4b). However, consistently VO_2 is transparent in the M1 phase ($\kappa \sim 0$ at RT) and optically metallic in the R phase ($\kappa > n$ at 90 °C) almost over the whole mid-IR.
Figure 2.4c shows the real part of the optical conductivity σ_1 as a function of photon energy $\hbar\omega$. In general, optical conductivity is defined as: $\sigma(\omega) = i\omega\epsilon_0[1 - \tilde{\epsilon}(\omega)]$. Thus, σ_1 is related to energy absorption ($\propto \omega\epsilon_2$) that arise from electronic transitions enabling the study of the electronic band structure. According to the assignment in figure 2.3b, transitions from the valence $d_{||}$ and O 2p band into the conduction band can be clearly distinguished in the M1 phase, and the band gap energy $\alpha_0 \sim 0.5$ eV of intrinsic VO_2 can be determined. The strong pronounced α_2 transition in the σ_1 data obtained in this thesis is attributed to the limited spectral range of the measurement. Nevertheless, this transition can be also seen in the data of Zhang *et al.*[159] as a shoulder on the low energy side of the strong σ_1 peak. Further, a comparable pronounciation of the α_2 transition was found by Qazilbash *et al.*[145]. In the metallic phase the band gap is vanished and all transitions from the valence to the conduction band (β_0 to β_2) form one broad peak in the σ_1 spectrum.

2.1.3. Strain in VO_2

Much effort has been devoted to control the critical phase transition temperature T_C of vanadium dioxide across a wide range by electron-doping or strain.[100,119,123–125,144,160–167]. It was demonstrated by Ladd *et al.*[160] that hydrostatic pressure p affects T_C only slightly: $\mathrm{d}T_C/\mathrm{d}p \sim 0.6\,^{\circ}\mathrm{C/GPa}$. In contrast, a relatively large reduction of T_C was found for uniaxial stress s applied along c_R: $\mathrm{d}T_C/\mathrm{d}s \sim -12\,^{\circ}\mathrm{C/GPa}$.[160] In the elastic regime s is linearly related to strain η by Hooke's law: $s = E\eta$, where E is the modulus of elasticity (Young's Modulus) and $\eta = \Delta l/l$ is the change in length per unit length of the axis under consideration.

Compressive ($\eta < 0$) and tensile strain ($\eta > 0$) can be easily applied to epitaxial VO_2 films by engineering the lattice mismatch between substrate and film as long as the thickness of the film is small. Various strain states can be obtained by growing epitaxial thin films on different crystalline substrates and substrate planes (figure 2.5a).[119,123,124,161,162,167,168] As an example, 10 nm VO_2 thin films epitaxially grown on TiO_2 (001) by Jeong *et al.*[119] are compressively strained along c_R by -1.2% and T_C is lowered by $\sim -45\,^{\circ}\mathrm{C}$ compared to bulk VO_2. When the film thickness exceeds a certain threshold value for the introduction of interfacial misfit dislocations, these dislocations noticeably reduce the long-ranging internal strain in the film.[126] Nakano *et al.*[169] have shown, that a 70 nm VO_2 film grown on a TiO_2 (001) substrate is completely relaxed and T_C is comparable to the VO_2 bulk value. Another approach, presented by Aetukuri *et al.*[100], is growing thin VO_2 films on TiO_2 using a RuO_2 buffer layer. The strain state of the VO_2 film can be continuously controlled by the RuO_2 layer thickness leading to a large variation of T_C over 60 °C. By means of polarization-dependent X-ray absorption spectroscopy measurements and synchrotron reciprocal space mapping combined with transport measurements, Aetukuri *et al.*[100] and Fan *et al.*[124] pointed out, that the phase transition temperature is closely related to the orbital occupancy, and decreases with decreasing c_R/a_R ratio (figure 2.5b).

In the rutile R phase, the V^{4+}-V^{4+} bond length is directly related to c_R, and the apical V-O bond length is only related to $\sim 0.42\,a_\mathrm{R}$, whereas the equatorial V-O bond length is related to both lattice parameters $\sim [(c_\mathrm{r}{}^2 + 0.32\,a_\mathrm{R}{}^2)^{1/2}]$.[124] A decrease of c_R decreases the V^{4+}-V^{4+} bond length and thus increases the direct overlap of $d_{||}$ orbitals along c_R, which results primarily in a stronger $d_{||}$ level splitting in the monoclinic M1 phase (figure 2.5c). An increase of a_R mainly increases the apical V-O bond length, which decreases the p-d overlap of the e_g^π orbitals. The decreased overlap results in an energy level decrease of the π^* band with respect to the Fermi level in both phases (figure 2.5c). As a consequence, in the rutile R phase, the increased overlap of π^* and $d_{||}$ increases the orbital occupancy of e_g^π orbitals, whereas it decreases the $d_{||}$ orbital occupancy. This charge transfer shifts up the $d_{||}$ band in energy and stabilizes the rutile R phase. In the monoclinic phase, the energy decrease of the π^* band decreases the band gap and screening of the $d_{||}$ band electrons (collaps of the band gap) is more likely to occur at lower temperatures.

Strain can be redistributed and relaxed in epitaxial thin films by the presence of misfit dislocations, grain boundaries, and other structural defects, which typically results in a microscopic domain structure.[123,125,126,164] On a macroscopic scale the coexistence of epitaxial domains in various strain states results in a distribution of critical temperatures broadening the overall phase transition of VO_2.[63,123] Further, the presence of compositional variations, such as oxygen vacancies, and the dependence on grain size makes it almost impossible to extract a complete strain-temperature phase diagram for VO_2 thin films. However, such a

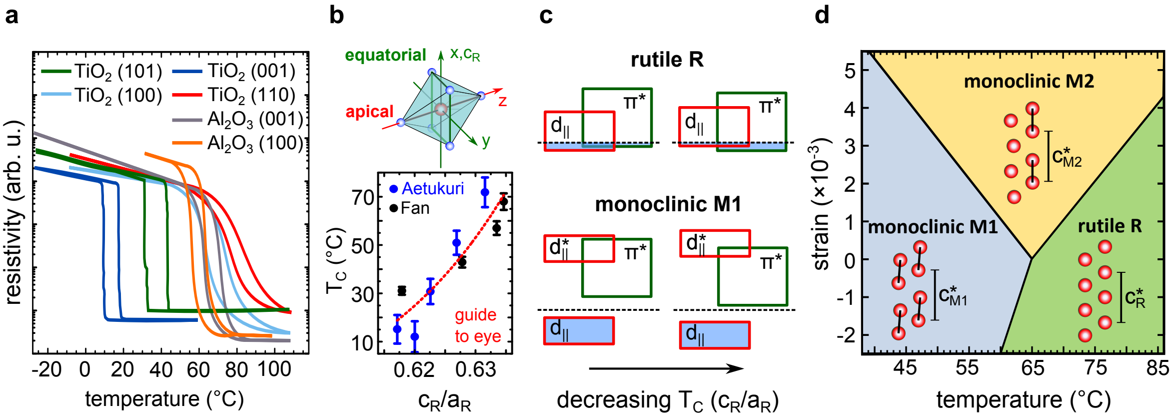

Figure 2.5.: **(a)** Temperature-dependent resistivity of ~ 10 nm thin VO_2 epitaxial films grown on various orientations of TiO_2 and Al_2O_3 single-crystal substrates (after Jeong *et al.*[119]). **(b)** In the rutile R phase, the V^{4+}-V^{4+} bond length is just related to c_R, and the apical V-O bond length is only related to a_R, whereas the equatiorial V-O bond length is related to both c_R and a_R (compare figure 2.2). The critical temperature T_C of VO_2 is highly sensitive to the c_R/a_R ratio, and directly related to epitaxial strain. Values are taken from Aetukuri *et al.*[100] and Fan *et al.*[124]. **(c)** Schematic of the band structure changes in the valence electron states in the rutile R and monoclinic M1 phase as T_C (c_R/a_R) is decreased. **(d)** Strain-temperature phase diagram deduced from optical measurements of phase coexistence in VO_2 nanowires strained along c_R (after Park *et al.*[125]). Each inset depicts the arrangement of vanadium ions in the respective phase, indicating the different vanadium chain periods and the V^{4+}-V^{4+} dimerization.

phase diagram was experimentally obtained and theoretically verified by Cao *et al.*[163,164], Park *et al.*[125] and Gu *et al.*[165] using free-standing, single-crystalline VO_2 nanomaterials, which have only few structural defects and can be continuously strained along the growth direction (figure 2.5d).

In agreement with the previous section, uniaxial compressive strain along c_R reduces T_C of the transition from M1 to R. In contrast, tensile strain along c_R stabilizes the M2 phase and two distinct transitions, M1 to M2 and M2 to R, occur. The rate at which T_C is modified by strain along c_R for the respective structural phase transition from phase i to j is given by the Clausius-Clapeyron equation:[125,163–165]

$$(\mathrm{d}T_C/\mathrm{d}\eta)_{i,j} = E V_m \alpha_{i,j} T_C^0/\Delta H_{i,j}, \tag{2.1}$$

where E is Young's modulus, V_m is the molar volume of VO_2, T_C^0 is the critical temperature of unstrained VO_2, $\Delta H_{i,j}$ is the latent heat per mole formula unit for the respective structural phase transition, and $\alpha_{i,j} = c_i^*/c_j^* - 1$ is the corresponding c-axis expansion (compare figure 2.5d). As an example Park *et al.*[125] obtained a decrease of T_C by $\sim -20\,°C/\%$ for compressive strain applied along c_R, which seems to be significantly smaller compared to $\sim -45\,°C/1.2\,\%$ obtained for thin VO_2 films by Jeong *et al.*[119]. But this comparison neglects that epitaxial strain in thin films is biaxial, and thus c_R and a_R are always strained simultaneously. However, the decrease of T_C due to uniaxial strain along c_R in thin films can be estimated hypothetically from data[100,124] given in 2.5b. Assuming, that a_R is constant: $\eta \sim [(c_R/a_R)_{20\,°C}/(c_R/a_R)_{70\,°C} - 1] \sim -2.8\,\%$ for a temperature difference of 50 °C. Hence, if a thin film could be strained uniaxially, the decrease of T_C would be approximately $-18\,°C/\%$, which is then in perfect agreement with strained VO_2 nanostructures.

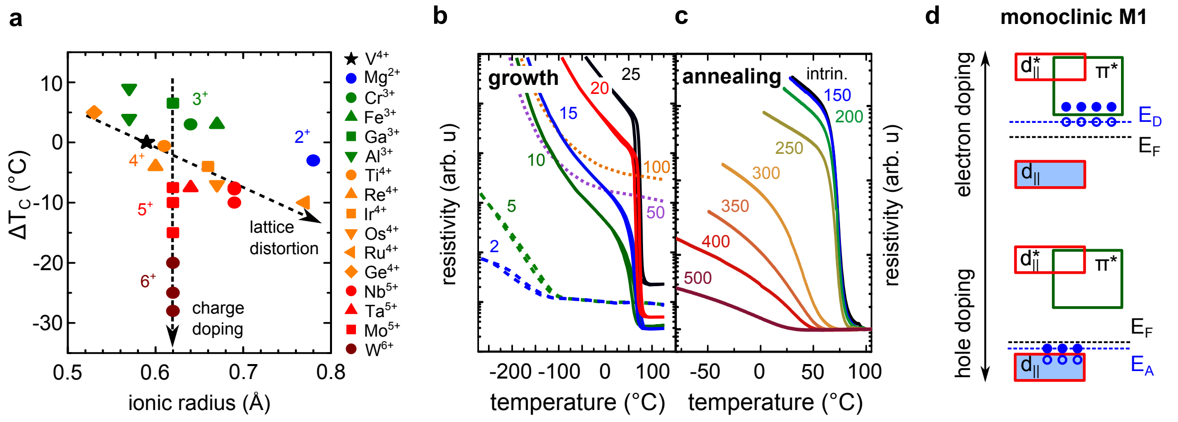

Figure 2.6.: **(a)** Change of the critical temperature of doped VO_2 with respect to undoped VO_2 (ΔT_C) as a function of the ionic radius of the respective metal ion dopant. ΔT_C depends on the size (lattice distortion) and the valence state (charge doping) of the dopand with respect to V^{4+}. Data are taken from references: [80–88]. Note, that different values are reported for some dopands. **(b)** Resistivity of VO_2 thin films deposited at various oxygen partial pressures $p(O_2)$ as a function of temperature taken from Lee et al.[172]. Dashed, solid, and doted lines represent the dominant vanadium oxide phase, i.e V_2O_3, VO_2, V_2O_5, respectively. Values of $p(O_2)$ are indicated in mTorr. **(c)** Resistivity of VO_2 thin films annealed for 30 min at different annealing temperatures in ultra-high vacuum (10^{-8} mbar) as a function of temperature. Annealing temperatures are indicated in °C. For clarity, only the heating cycles are shown. **(d)** Schematic band structure of electron and hole doped VO_2 in the monoclinic M1 phase near the Fermi level (synopsis of [131, 173–175]). The change in valence of the V^{4+} ions due to electron and hole localization leads to the formation of donor (E_D) and acceptor levels (E_A) in the fundamental band gap between $d_{||}$ and π^* band, respectively.

2.1.4. Impurity doping of VO_2

An effective route to control the critical temperature T_C of the IMT of VO_2 is impurity doping.[80–96] Substitutional doping of VO_2 with higher valent metal ions such as W^{6+}, Mo^{6+} and Nb^{5+} has been demonstrated to reduce T_C,[80–85,87,88,94] whereas doping with lower valent metal ions, like Al^{3+}, Cr^{3+}, Fe^{3+} and Ga^{3+} has been shown to increase T_C.[80,87] A plot of available literature data on the change of T_C (ΔT_C) by 1 at.% metal ion incorporation into the lattice of VO_2 as a function of the ionic radius of the dopand reveals that ΔT_C depends on both, the relative size and the relative valence of the dopands with respect to that of the V^{4+} ions (figure 2.6a). However, the mechanism responsible for the change of T_C in doped VO_2 is still a matter of debate, in particular, the unclear contributions of lattice distortion and charge doping effects.[89,91,94]

Charge transfer in tungsten (W^{6+}) doped VO_2 breaks V^{4+}-V^{4+} bonds and leads to the formation of W^{6+}-V^{3+}, and V^{3+}-V^{4+} pairs, which destabilize the M1 phase and lower the energy barrier for the phase transition, thus reduce T_C.[91] However, X-ray absorption fine structure spectroscopy (XAFS) conducted at room temperature reveals a local rutile structure around W^{6+} dopands.[84,170] This local structure induces a perturbation of the monoclinic structure lowering T_C by internal strain. To rule out the contribution of charge doping, Wu et al.[94] investigated VO_2 doped with Ti^{4+}. Incorporation of Ti^{4+} basically does not alter the band structure of VO_2 due to a lack of charge transfer between Ti^{4+} and V^{4+} ions. Although Ti^{4+} has an ionic radius comparable to W^{6+} and the appearance of a local rutile structure around Ti^{4+} dopands was observed, the neglectable reduction of T_C points out that charge carrier doping might be more effective than the induced lattice distortion.[94] A detailed review of existing literature on elemental doping of VO_2 can be found elsewhere.[171]

2.1.5. Defects in VO_2

A deficiency in oxygen or vanadium is known to influence the physical properties of intrinsic VO_2, especially the phase transition temperature.[122,140,159,175–177] It has been reported that VO_{2-x} films grown (figure 2.6b) or annealed (figure 2.6c) in an oxygen deficient ambient can have dramatically lower T_C compared to stoichiometric VO_2.[97,119,122,159,177–179] Under extreme conditions, the rutile phase can even be stabilized down to cryogenic temperatures, which is often refered to as metalization of VO_2.[159,176]

The most abundant intrinsic defects in oxygen poor VO_{2-x} are oxygen vacancies ($V_O^{\bullet\bullet}$ in Kröger-Vink notation) introduced to keep charge neutrality: $O_O{}^x \leftrightarrow V_O^{\bullet\bullet} + 2e' + 1/2O_2$, where $O_O{}^x$ denotes oxygen on a lattice site.[174,175,177] The two electrons e' are trapped at V^{4+} sites and lower the valence of the vanadium ions (similar to high-valence impurity doping). The lower valance states of $V^{(4-\delta)+}$ introduce donor levels (E_D) below the π^* band in the monoclinic M1 phase (figure 2.6d).[173–175] Electrons localized at the donor levels are ionized at room temperature and transferred to the empty π^* band. The π^* band shifts down in energy as a consequence of orbital occupancy, and the electron-electron correlation is screened. Thus, the energy barrier for the phase transition is lowered and T_C is reduced.

In contrast, the most likely intrinsic defects in oxygen rich VO_{2+x} are oxygen interstitials at octahedral sites ($O_I{}''$) and vanadium vacancies ($V_V^{4'}$).[175] The corresponding defect reactions are: $O_2 \leftrightarrow V^{4'} + 4h^\bullet + 2O_O{}^x$ and $O_2 \leftrightarrow 2O_I^{2'} + 4h^\bullet$. In both cases, holes $h^\bullet$ are localized at V^{4+} sites and increase the valance of the vanadium ions (similar to low-valance impurity doping). V^{5+} in the VO_2 host lattice introduces acceptor levels (E_A) above the filled $d_{||}$ band in the monoclinic M1 phase (figure 2.6d).[173–175] Holes on E_A are recombined by $d_{||}$ band electrons and suppress charge transfer to the π^* orbitals. Consequently, the energy barrier of the phase transition is lifted and T_C is increased.

The presence of vacancy and interstitial defects lead to band tailing, and a reduction of the fundamental band gap.[173,174] Further, the introduction of structural defects is associated with lattice distortions, which significantly influence the electronic band structure.

2.2. Thin-film optics

Thin films with a thickness on the order of the wavelength of light can have remarkable optical properties due to the interference of coherent light waves that are partially reflected and transmitted at the film interfaces. Single and multilayer thin-films are used as coatings that alter the optical properties of a given substrate, for example decreasing or increasing light reflection and transmission.[180] The following section will provide a concise understanding of the optical properties of layered thin-films. The very basic optical theories of multilayer thin-films will be covered, with emphasis on antireflection coatings. A comprehensive description of optical phenomena of layered thin-films can be found in references [181–184].

2.2.1. Reflection and transmission at a single interface

In principle, the determination of the intensity of light reflected by or transmitted through a single interface is straightforward.[183] The Fresnel coefficients relate the amplitudes, phases, and polarization of the transmitted and reflected electric field amplitudes of light waves traveling across an interface between two media i, j with different (possibly complex-valued)

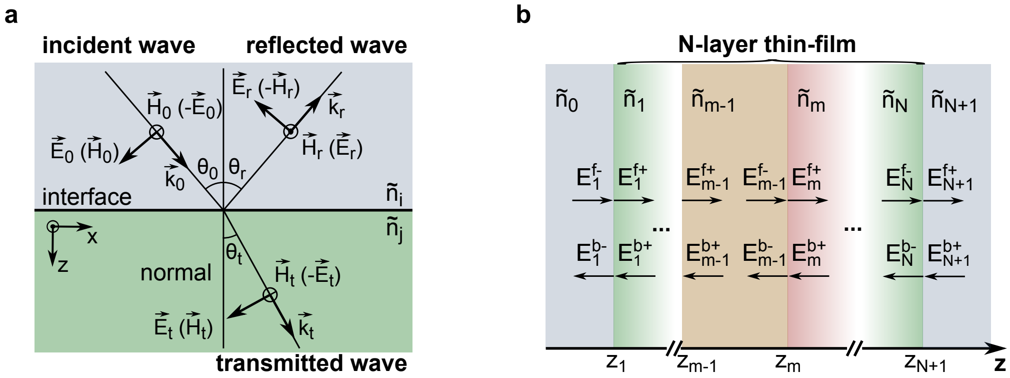

Figure 2.7.: **(a)** Definition of field vectors of the incident (0), reflected (r), and transmitted waves (t) for the p-(s-) polarized electric field component. **(b)** Notation of electric field amplitudes within an arbitrary multilayer stack. The complex amplitudes of the forward (f) and backward (b) propagating waves at the left- (-) and right-hand (+) side of an interface between adjacent layers m-1 and m. For simplicity, the incident angle is not considered.

refractive indices: $\tilde{n}_{i,j} = n_{i,j} + \mathrm{i}\kappa_{i,j}$ to the coresponding parameters of the incident light wave.[181–184] Figure 2.7a depicts a plane optical wave, which is propagating toward the interface of i and j, with electric field amplitude E_0, wave vector $\vec{k}_0$ and incident angle θ_0 with respect to the interface normal. The wave will be partially reflected (E_r) at an angle of $\theta_r = \theta_0$ and partially transmitted (E_t) at an angle which is determined by Snell's law:

$$n_i \sin\theta_0 = n_j \sin\theta_t. \tag{2.2}$$

Because the electromagnetic wave is transverse, the $\vec{E}$-field incident onto the interface can be decomposed into a p-polarized $\vec{E}_0^p$ (field vector inside the plane of incidence formed by $\vec{k}_0$ and the interface normal) and a s-polarized (orthogonal to the plane of incidence) component $\vec{E}_0^s$. Due to symmetry, the reflected and transmitted waves will have the same polarization (compare figure 2.7a). Based on Snell's law, Maxwell equations and the boundary conditions for the $\vec{E}$ and $\vec{H}$ fields at the interface between i and j, the amplitude reflection $r_{p,s} = E_r^{p,s}/E_0^{p,s}$ and amplitude transmission $t_{p,s} = E_t^{p,s}/E_0^{p,s}$ coefficient can be written in form of the well-known Fresnel equations for the p-component of the electric field:[181–184]

$$\begin{aligned} r_{i,j}^p &= \frac{\tilde{n}_i \cos\theta_j - \tilde{n}_j \cos\theta_i}{\tilde{n}_i \cos\theta_j + \tilde{n}_j \cos\theta_i} \qquad &\text{(reflection)} \\ t_{i,j}^p &= \frac{2\tilde{n}_i \cos\theta_i}{\tilde{n}_i \cos\theta_j + \tilde{n}_j \cos\theta_i} \qquad &\text{(transmission)} \end{aligned} \tag{2.3}$$

and for the s-component of the electric field:

$$\begin{aligned} r_{i,j}^s &= \frac{\tilde{n}_i \cos\theta_i - \tilde{n}_j \cos\theta_j}{\tilde{n}_i \cos\theta_i + \tilde{n}_j \cos\theta_j} \qquad &\text{(reflection)} \\ t_{i,j}^s &= \frac{2\tilde{n}_i \cos\theta_i}{\tilde{n}_i \cos\theta_i + \tilde{n}_j \cos\theta_j} \qquad &\text{(transmission).} \end{aligned} \tag{2.4}$$

The intensity reflection coefficient R (reflectance) and intensity transmission coefficient T (transmittance), rather than the amplitude coefficients, are of interest for most practical purposes:

$$R = \frac{|E_r|^2}{|E_0|^2} = |r|^2 \qquad \text{and} \qquad T = \frac{n_j \cos\theta_t |E_t|^2}{n_i \cos\theta_0 |E_0|^2} = \frac{n_j \cos\theta_t}{n_i \cos\theta_0}|t|^2. \tag{2.5}$$

Constructive and destructive interference is caused by superposition of coherent light waves that are partially reflected at the surface and interfaces of a single or multylayer thin-film. Although summing up the amplitude coefficients of the partially reflected waves and considering their respective phase shifts at interfaces yield the transmittance and reflectance for a single thin-film easily, this method becomes cumbersome for a film composed of N thin layers.[181]

2.2.2. Transfer matrix method

The transfer matrix method was used in this thesis in order to calculate the reflectance and transmittance of single and multilayer thin-films (see also Supplementary A.6). This method takes into account the Fresnel coefficients, and represents the optical response of coherent multilayer thin-films in 2×2 matrix form.[181–183,185,186]

Figure 2.7b shows a thin-film composed of N isotropic, homogeneous layers with thickness d_m, complex refractive index $\tilde{n}_m = n_m + \mathrm{i}\kappa_m$, and $N+1$ interfaces. The tangential electric field amplitude at any position within a layer can be expressed as a superposition of a forward (E^f) and backward (E^b) propagating plane wave: $E = E^f + E^b$. The field amplitudes on the left- (superscript $-$) and right-hand side (superscript $+$) of the m-th interface are related by a product of the refraction ($\mathbf{D}_{m-1}^{-1}$) and transmission ($\mathbf{D}_{m-1}$) *dynamical matrices*, and can equally be expressed for s- and p-polarized light in terms of the corresponding Fresnel coefficients (equations 2.3, and 2.4):[186]

$$\begin{pmatrix} E_{m-1}^{f-} \\ E_{m-1}^{b-} \end{pmatrix} = \mathbf{D}_{m-1}^{-1}\mathbf{D}_{m-1}\begin{pmatrix} E_m^{f+} \\ E_m^{b+} \end{pmatrix} = \frac{1}{t_{m-1,m}}\begin{bmatrix} 1 & r_{m-1,m} \\ r_{m-1,m} & 1 \end{bmatrix}\begin{pmatrix} E_m^{f+} \\ E_m^{b+} \end{pmatrix}. \tag{2.6}$$

The field amplitudes for wave propagation within the $(m-1)$-th layer are related by the *propagation matrix* $\mathbf{P}_{m-1}$:[186]

$$\begin{pmatrix} E_{m-1}^{f+} \\ E_{m-1}^{b+} \end{pmatrix} = \mathbf{P}_{m-1}\begin{pmatrix} E_{m-1}^{f-} \\ E_{m-1}^{b-} \end{pmatrix} = \begin{bmatrix} \exp(\mathrm{i}\tilde{\Phi}_{m-1}) & 0 \\ 0 & \exp(-\mathrm{i}\tilde{\Phi}_{m-1}) \end{bmatrix}\begin{pmatrix} E_{m-1}^{f-} \\ E_{m-1}^{b-} \end{pmatrix}, \tag{2.7}$$

where $\tilde{\Phi}_{m-1} = 2\pi\lambda_0^{-1}\tilde{n}_{m-1}d_{m-1}\cos\theta_{m-1}$ is the complex phase shift imposed by the $(m-1)$-th layer, λ_0 is the free-space wavelength, and θ_{m-1} is the propagation angle with respect to the interface normal, found by applying Snell's law (equation 2.2).

The complete system *transfer matrix* $\mathbf{T}$, which relates the field amplitudes on opposite sides of the entire film, is found by repeated application of the corresponding dynamical and propagation matrices:[186]

$$\begin{pmatrix} E_0^{f-} \\ E_0^{b-} \end{pmatrix} = \mathbf{D}_0^{-1}\left(\prod_{m=1}^{N}\mathbf{D}_m\mathbf{P}_m\mathbf{D}_m^{-1}\right)\mathbf{D}_{N+1}\begin{pmatrix} E_{N+1}^{f+} \\ E_{N+1}^{b+} \end{pmatrix} = \begin{bmatrix} T_{11} & T_{12} \\ T_{21} & T_{22} \end{bmatrix}\begin{pmatrix} E_{N+1}^{f+} \\ E_{N+1}^{b+} \end{pmatrix}. \tag{2.8}$$

As there is usually no incident wave from the right-hand side: $E_{N+1}^{b+} = 0$, equations 2.8 are used to derive the amplitude reflection and transmission coefficients of N-layered thin-films:

$$r = \frac{E_0^{b-}}{E_0^{f-}} = \frac{T_{21}}{T_{11}} \qquad \text{and} \qquad t = \frac{E_{N+1}^{f+}}{E_0^{f-}} = \frac{1}{T_{11}}. \tag{2.9}$$

The transfer matrix elements, expressed in terms of the Fresnel coefficients, and equations 2.5 allow to calculate the reflectance and transmittance of any homogeneous multilayer thin-film. Advantageously, all interference effects are already considered within this method.

2.2.3. Anti-reflection coatings

Figure 2.8a schematically shows the first partially reflected r_n and transmitted waves from a three-layer system. The system comprises air ($n_0 = 1$) and a thin film with thickness d and refractive index $\tilde{n}_f = n_f + \mathrm{i}\kappa_f$, which is deposited on a semi-infinite substrate with refractive index $\tilde{n}_s = n_s + \mathrm{i}\kappa_s$ (asymmetric Fabry-Perot cavity). Light incidences from air under an angle of θ_0. The reflectance R of such a system is given by $R = |r|^2$ with:

$$\begin{aligned} r &= \sum_{n=0}^{\infty} r_n = \frac{r_{0,f} + r_{f,s}e^{2\mathrm{i}\tilde{\Phi}}}{1 + r_{0,f}r_{f,s}e^{2\mathrm{i}\tilde{\Phi}}}, \\ \text{where:} \quad \tilde{\Phi} &= \Phi + \mathrm{i}\Phi' = 2\pi\frac{d}{\lambda_0}\tilde{n}_f\cos\theta_f = 2\pi\cos\theta_f\left(\delta + i\delta\frac{\kappa_f}{n_f}\right). \end{aligned} \tag{2.10}$$

Φ is the phase accumulated by light passing through the layer, Φ' is an attenuation coefficient, and $\delta = \frac{d}{\lambda_0}n_f$ is the reduced film thickness.

Figure 2.8b represents the amplitude reflectance r of a conventional anti-reflection (AR) coating ($\kappa_f = \kappa_s = 0$) in the complex plane as a function of δ. Both, the first reflection r_0 and the bottom interface reflections have a phase shift of π with respect to the incident wave and point to the left along the real axis in the complex plane (green and black arrow in 2.8b). Destructive interference is achieved if each partial wave, which emerges from the film, accumulates a phase shift of π with respect to r_0 due to wave propagation in the film. This occurs when δ is an odd integer multiple of 1/4 (compare figure 2.8d), that is d is an odd integer multiple of $\lambda_0/4n_f$ (quarter-wave AR coating[180]). The reflection is completely suppressed ($r = 0$) for all film/substrate combinations with $n_f = \sqrt{n_0 n_s}$, because the surface reflection $r_{0,f}$ equals the effective bottom reflection $r_{f,s}e^{2\mathrm{i}\Phi}$ (the nominator in equation 2.10 vanishes).

The bottom interface reflection phase shift becomes substantially different from π provided at least the substrate (figure 2.8c) or film (figure 2.8e) is optically lossy ($\kappa_{f,s} > 0$). As a result, in the former case, destructive interference occurs for δ much smaller than 1/4 (compare figure 2.8d), because less phase shift has to be accumulated by propagation through the film. In the latter case all partially reflected waves are increasingly attenuated due to light passing through the lossy film ($\Phi' > 0$). Nevertheless - given the right combinations of $\tilde{n}_f$ and n_s - destructive interference occurs, but for $\delta > 1/4$ (compare figures 2.8d,e). However, δ can be reduced, comparable to the situation in figure 2.8c, applying the same lossy film to a lossy substrate (compare figures 2.8d,f). This demonstrates the role of the substrate in order to minimize the necessary film thickness to achieve completely suppressed reflection and will be investigated in greater detail in chapter 3.

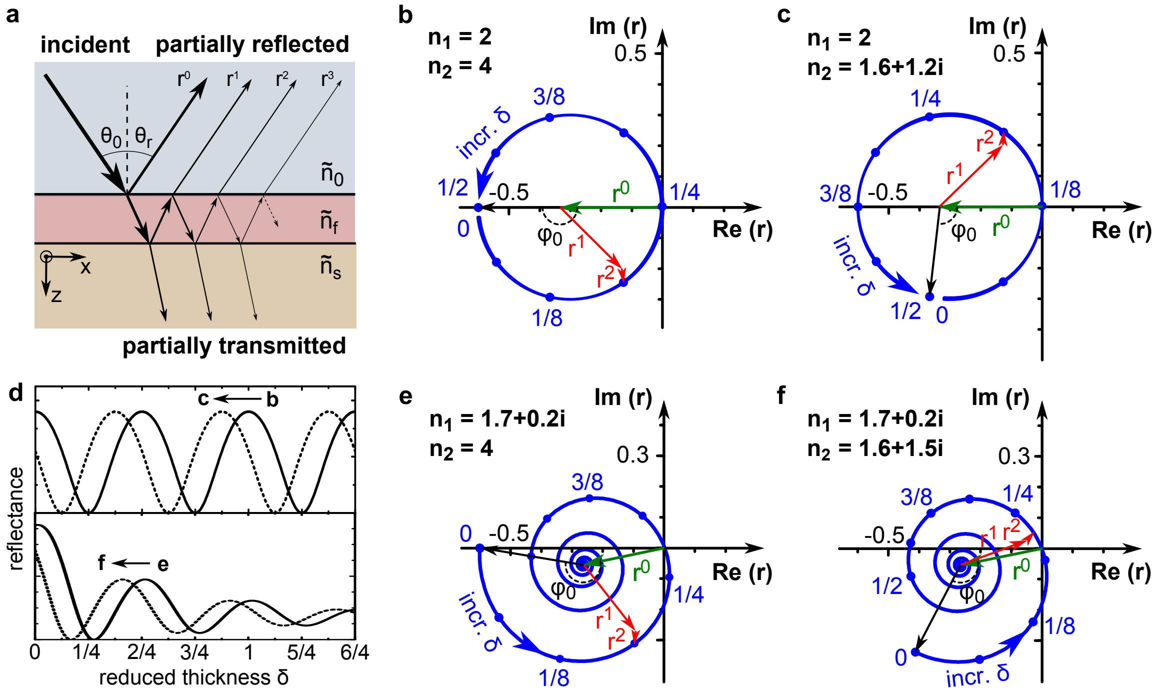

Figure 2.8.: **(a)** Partially reflected r_n and partially transmitted waves for light incidence onto a three-layer system. The system comprises air ($\tilde{n}_0 = 1$), a thin film (reduced thickness δ, $\tilde{n}_f = n_f + \mathrm{i}\kappa_f$) and a semi-infinite substrate ($\tilde{n}_s = n_s + \mathrm{i}\kappa_s$) **(b)** Amplitude reflectance r as a function of the reduced thickness δ represented in the complex plane. Destructive interference $r = 0$ for a conventional quarter-wave anti-reflection coating with $\tilde{n}_f = 2$ and $\tilde{n}_s = 4$ is achieved when a phase difference of $\phi_0 = \pi$ is accumulated due to light passing through the coating. This occurs for $\delta = 1/4$. **(c)** Destructive interference of light is achieved for much thinner films if the substrate is lossy, e.g. $\tilde{n}_s = 1.6 + 1.2\mathrm{i}$ (compare d). In this case, the phase shift at the coating/substrate interface deviates significantly from π and is accumulated already within $\delta = 1/8$. **(e,f)** Although r is increasingly attenuated with increasing δ, destructive interference is also observed for lossy thin films, e.g. $\tilde{n}_f = 1.7 + 0.2\mathrm{i}$. Similar to b,c δ can be significantly reduced when the films are deposited on lossy substrates (compare d).

2.2.4. Effective medium approximation

In the limit where the wavelength of light is much larger than the spatial dimension of the structures that constitute an optical material, it is possible to regard this material as being homogeneous and possessing effective optical properties $\tilde{\epsilon}_{\mathrm{eff}} = \tilde{n}^2_{\mathrm{eff}}$.[187] Restricted by the Wiener theory for bonds of $\tilde{\epsilon}_{\mathrm{eff}}$ of composites,[188] Lichtenecker assumed that $\tilde{\epsilon}_{\mathrm{eff}}$ of a composite of two phases A and B with dielectric functions $\tilde{\epsilon}_A$ and $\tilde{\epsilon}_B$ satisfies:[189]

$$\tilde{\epsilon}^k_{\mathrm{eff}} = (1-f)\tilde{\epsilon}^k_A + f\tilde{\epsilon}^k_B, \quad \text{with} \quad k \in [-1, 1], \tag{2.11}$$

where $(1-f)$ and f are the filling fractions of phase A and B, respectively, and k is a parameter where each k accounts for a specific composite topology. The extreme values of k describe highly anisotropic systems consisting of parallel layers with sub-wavelength thickness disposed along the electrical field ($k = 1$) or perpendicular to the electrical field ($k = -1$) (figure 2.9a). If the system consists of finely dispersed phases with no preferential orientation, then $k \to 0$ and equation 2.11 is written as:[190]

$$\ln \tilde{\epsilon}_{\mathrm{eff}} = (1-f) \ln \tilde{\epsilon}_A + f \ln \tilde{\epsilon}_B. \tag{2.12}$$

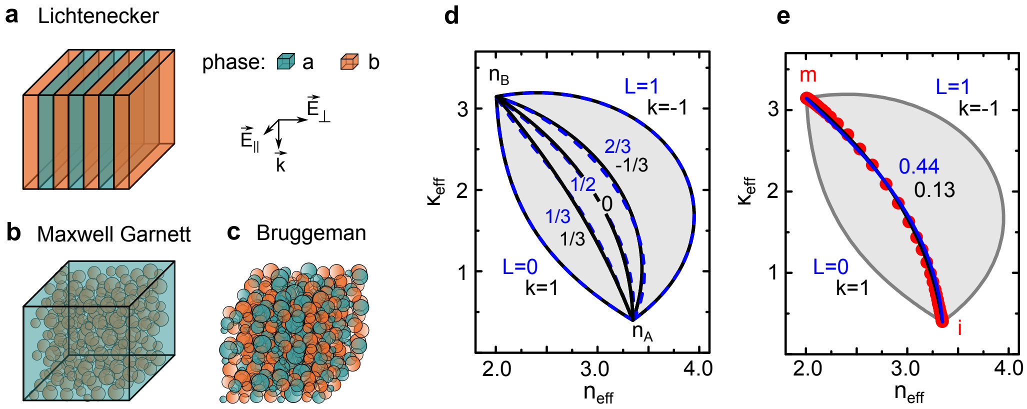

Figure 2.9.: (a-c) Representation of a composite of two phases considered by Lichtenecker (a), Maxwell Garnett (b), and Bruggeman (c). **(d)** Effective optical properties attainable for a composite of two phases A and B with refractive index n_A and n_B, respectively (grey area). The effective optical properties were calculated as a function of the filling fraction f using Lichtenecker's equation and generalized Bruggeman formalism for different values of k and $L = L_A = L_B$ as indicated, respectively. Although the expressions of both effective medium approximations are different, they yield comparable results. **(e)** The effective optical properties of VO_2 (experimentally obtained data for a wavelength of 1550 nm) in the transition region from purely insulating (i) to purely metallic (m) can be equally well fitted using both approximations.

Although the parameter k describes a transition from anisotropy in one direction to anisotropy in a perpendicular direction, intermediate values of k have no specific physical meaning and Lichteneckers equation can be also applied to isotropic composites.[190] For example Looyenga's effective medium approximation deduced for a homogeneous mixture of spherical particles is consistent with Lichtenecker's equation for $k = 1/3$.[191]

The best known effective medium theories for macroscopically homogeneous and isotropic composites are the Maxwell Garnett equation:[192]

$$\left(\frac{\epsilon_{\text{eff}} - \epsilon_A}{\epsilon_{\text{eff}} + 2\epsilon_A}\right) = f\left(\frac{\epsilon_B - \epsilon_A}{\epsilon_B + 2\epsilon_A}\right), \tag{2.13}$$

and Bruggeman's symmetrical effective medium approximation:[193]

$$(1 - f)\frac{\epsilon_A - \epsilon_{\text{eff}}}{\epsilon_A + 2\epsilon_{\text{eff}}} + f\frac{\epsilon_B - \epsilon_{\text{eff}}}{\epsilon_B + 2\epsilon_{\text{eff}}} = 0. \tag{2.14}$$

The former is represented by a distribution of spherical particles of phase B dispersed in a continuous matrix of phase A (figure 2.9b) and the latter implies that both phases are spherical inclusions dispersed in the effective medium itself (figure 2.9c). Equation 2.14 can be easily generalized to the case of multiphase composite system of m constituents each composed of anisotropic inclusions of ellipsoidal shape with filling fraction f_n and dielectric function ϵ_n. If the ellipsoids are equally oriented and the electric field is directed along one of the major ellipsoid axes ($j = x, y, z$), $\epsilon_{\text{eff},j}$ satisfies:[194,195]

$$\sum_{n=1}^{m} f_n \frac{\epsilon_n - \epsilon_{\text{eff},j}}{\epsilon_{\text{eff},j} + (\epsilon_n - \epsilon_{\text{eff},j})L_{n,j}} = 0, \tag{2.15}$$

where $L_{n,j} \in [0, 1]$ is the depolarization factor of the ellipsoid of phase n along axis j. $L_{n,j}$ depends on the shape of the respective ellipsoid with respect to the polarization of the incident electric field. A value of $L_x = L_y = L_z = 1/3$ corresponds to isotropic spherical inclusions in three dimensional materials. The limiting case of spheroids are disk-like inclusions (e.g. flat in z-direction) with $L_x = L_y = 0, L_z = 1$. Although the generalized Bruggeman formalism has been extensively used for the analysis of anisotropic thin films,[196–199] Lichtenecker's equation yields comparable results for two phase composites of specific topology (compare figure 2.9d). To demonstrate the applicability of both effective medium approximations to VO_2 thin films, figure 2.9e exemplary shows fitted experimentally obtained refractive index data of VO_2 at 1550 nm throughout its phase transition. Both models fit the experimental values equally well for $k = 0.13$ and $L = L_A = L_B = 0.44$, respectively. For simplicity, Lichtenecker's equation is used to model the optical properties of VO_2 thin films in this thesis. Note that the value of k depends on the wavelength.

2.3. Ion beam modification of materials

Energetic ion beams are widely used to modify the electrical, optical, and structural properties of solids by introducing impurity atoms into the crystal lattice (ion implantation). Ions that impinge onto a solid material loose their kinetic energy by elastic collisions with target nuclei (nuclear energy loss) and inelastic scattering with target electrons (electronic energy loss). In the energy range up to 500 keV, which is the typical energy range of ion implanters, nuclear energy loss is the dominant energy transfer mechanism. In this regime energy is transferred from the ions to the target atoms by ballistic collisions. Consequently, the ion will eventually come to rest at a certain depth within the target. The penetration depth depends on ion energy, ion mass, and target density. Lattice atoms are displaced if sufficient energy is transferred to overcome the displacement energy E_D. The displaced lattice atoms (recoils) can knock off further lattice atoms leading to a collision cascade. A collision cascade is schematically shown in figure 2.10a. Within this collision cascade the displacement of lattice atoms primarily leads to the formation of point defects such as vacancies and interstitials. The vacancy-interstital defect is referred to as Frenkel defect. In dense collision cascades or when several successive collision cascades overlap extended defects such as defect clusters, dislocation loops and stacking faults or amorphous regions may be formed. Furthermore, atoms may be ejected from the solids surface, if sufficient energy is transferred to near-surface atoms to overcome the surface binding energy. This process is called sputtering. For high energetic ions exceeding ~ 1 MeV per nucleon, electronic energy loss dominates. Intense local ionization of lattice atoms can lead to the formation of severe irradiation damage and in some materials the formation of ion tracks is observed.[200] At intermediate ion energies both electronic and nuclear energy loss are of similar magnitude, which can lead to additive defect accumulation effects or competitive defect recovery processes.[200]

The amount of damage created by ion irradiation depends on the atomic mass and energy of the ions as well as external irradiation conditions, such as temperature, and is characteristic for given materials.[201] Typically, the irradiation damage that accompanies ion implantation has to be removed by subsequent annealing processes in order to achieve the desired material modification. However, irradiation damage can also result in useful changes of the material properties. A detailed description of ion beam modification of solids can be found in references [200–203].

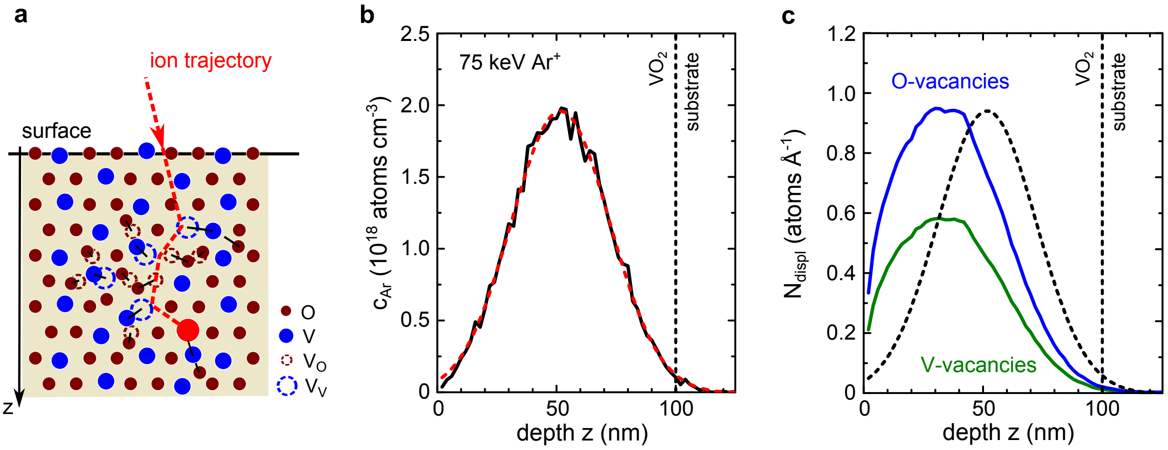

Figure 2.10.: (a) Schematic drawing of a collision cascade in a VO_2 sample initiated by the impact of an energetic ion. **(b)** Ar concentration (c_{Ar}) as a function of depth z for the implantation of 75 keV Ar^+ into VO_2, according to SRIM simulations. The red dashed curve is a gaussian fit to the simulation data. **(c)** Number of displaced oxygen and vanadium lattice atoms as a function of depth z for 75 keV Ar irradiation of VO_2. A fluence of $1 \times 10^{13}\,\mathrm{cm}^{-2}$ was used for the calculation. For comparison, the Ar distribution (not to scale) is given as black dashed curve.

2.3.1. The range of ions and the defect distribution

Each implanted ion penetrates through the target material on a different ion trajectory. However, ion implantation typically involves a large number of ions which enables to predict the penetration depth by statistical methods. The most used computer code for the simulation of the spatial distribution of ions and displacements in solid materials is SRIM (Stopping and Range of Ions in Matter[204]). SRIM averages a large number of collision cascades, each simulated as a series of binary collisions, respectively.

In the following, the irradiation of a 100 nm thin VO_2 film with 75 keV Ar ions serves as an example. The ion fluence used for calculations is $N_I = 10^{13}\,\mathrm{cm}^{-2}$, a value typically used in this thesis. Figure 2.10b shows the simulated depth distribution of implanted Ar ions. Since the stopping of energetic ions is a statistical process, the range distribution is approximately a gaussian function.[203] The depth of the maximum is called the projected ion range R_p and the standard deviation of the distribution is referred to as the projected range straggle. In this case a maximum Ar concentration of $c_{\mathrm{Ar}} = 2 \times 10^{18}\,\mathrm{cm}^{-3}$ is reached in a depth of approximately 50 nm. For comparison, the atomic density of VO_2 is $N_0 \sim 1.0 \times 10^{23}\,\mathrm{cm}^{-3}$. Thus, the relative maximum Ar concentration is only 0.002 at%. Note that the lateral distribution of implanted ions, in the direction perpendicular to the surface normal, limits the feature size for masked ion implantation. The lateral projected ion range here is approximately 15 nm at a depth of R_p. Note also that for high ion fluences above $10^{15}\,\mathrm{cm}^{-2}$ sputter effects, and redistribution of already implanted ions have to be taken into account, which are both neglected in SRIM.

Within the simulated collision cascade, each displaced lattice atom leaves a vacancy and creates an interstitial. Figure 2.10c shows the simulated average number of displacements per ion und unit length $N_{\mathrm{displ}} = N^O_{\mathrm{displ}} + N^V_{\mathrm{displ}}$ as a function of depth (the superscript indicates the displacement of oxygen and vanadium atoms, respectively). The distribution of oxygen and vanadium vacancies is shifted towards the sample surface with respect to the Ar distribution, because atoms can be displaced only when sufficient energy is transferred. Although the value of N_{displ} critically depends on the displacement energy of the lattice atoms (E_d), the shape of the distribution does not significantly change with changing E_d. For some materials, E_d

has been determined experimentally by monitoring changes in the electrical resistivity upon electron irradiation at low temperatures.[205] However, for most materials standard values of E_d on the order of 10 to 50 eV are used, regardless of the material composition.[205] Using a displacement energy of $E_D = 28$ and 25 eV for vanadium and oxygen lattice atoms, a maximum value of $N^O_{\text{displ}} = 0.95$ and $N^V_{\text{displ}} = 0.58\,\text{atoms}\text{Å}^{-1}$ is found at a depth of approximately 33 nm, respectively.

A commonly used measure of irradiation damage is the relative number of displacements per lattice atom $n_{\text{dpa}} = N_0 N_I / N_{\text{displ}}$, where N_0 is the atomic density of the target, N_I the considered ion fluence.[205] If every lattice atom has been displaced on average once from its lattice site, the value of n_{dpa} equals unity. In case of 75 keV Ar irradiation of VO_2 with a fluence of $N_I = 10^{13}\,\text{cm}^{-2}$ the value of n_{dpa} is as low as 0.02. That is, on average only 2% of all lattice atoms are displaced.

Note, that the number of lattice atoms which have experienced a displacement is calculated without reference to their final location.[202] Since the recombination of defects is neglected, the actual number of displaced atoms will be smaller than the simulated values. Especially for increasing irradiation temperatures, that facilitates defect migration and point defect recombination, simulated and experimentally determined defect concentrations may differ greatly.

2.3.2. Previous studies on ion beam irradiation/doping of VO_2

The incorporation of impurity atoms in VO_2 by means of ion implantation is not very well studied. On the one hand, high doping concentrations on the order of several atom percents can be easily achieved during VO_2 growth.[171] On the other hand, the ion fluence necessary to obtain a doping concentration of at least one atom percent typically exceeds the amorphization threshold of VO_2. Unfortunately, the narrow phase diagram prevents irradiation at elevated implantation temperatures, which might reduce the amount of lattice defects created during the irradiation process, and post implantation annealing remains challenging. The possibility to utilize the defects created by ion irradiation of VO2 has so far been almost completely neglected.

Tungsten doping of VO_2 films by means of 1 MeV ion implantation and subsequent thermal annealing was achieved by Jin *et al.*[206]. The ion fluences that were used range from 0.86 to $6.12 \times 10^{15}\,\text{cm}^{-2}$ and led to complete amorphization of the VO_2 films. However, after thermal annealing at 400 °C in air a reduction of the phase transition temperature of 24 °C/at.% was found, which is in agreement with results obtained for VO_2 films doped with tungsten during growth.[95] Similar results were obtained by Ufert.[207] Irradiation of VO_2 with Ar^+, P^+ and B^+ in the energy range from $50 - 250$ keV and at fluences ranging from 10^{15} to $5 \times 10^{16}\,\text{cm}^{-2}$ led to complete amorphization.

There are only very few studies that investigate the effects of lattice displacements and structural defects caused by ion irradiation on the phase transition of VO_2. Hofsäss *et al.*[208] irradiated approximately 100 nm thin VO_2 films with 1 GeV uranium ions at ion fluences ranging from 0.5×10^{10} to $1 \times 10^{10}\,\text{cm}^{-2}$. At this energy latent tracks with nanometer diameter are formed by rapidly melting and quenching small regions of VO_2 around the ion trajectories. A slight decrease of the phase transition temperature was observed and attributed to stress around the ion tracks. Heckman *et al.*[209] investigated the effect of $70 - 250$ keV O^+ irradiation on T_C of 600 nm thick VO_2 films in the fluence range from 10^{14} to $10^{16}\,\text{cm}^{-2}$. Although a decrease of T_C was found, no fluence dependence was reported. However, the authors attribute the observed reduction of T_C to the formation of lattice defects which produce local compressive strain in the surrounding lattice and thus, modify the transition temperature. Furthermore, Raman spectroscopy indicated that the irradiation effects remain stable in the samples that had been annealed up to 120 °C. In contrast, Lim *et al.*[210] observed an increase of T_C after irradiation of approximately 100 nm thin VO_2 films with 100 keV Er^+ in the fluence range from 2×10^{13} to $1 \times 10^{15}\,\mathrm{cm}^{-2}$.

Parallel to this thesis, Ramirez *et al.*[211] compared the effect of 110 keV O^+ irradiation on the IMT of VO_2 and vanadium sesquioxide (V_2O_3) by means of structural and electrical characterization for ion fluences ranging from 5×10^{12} to $2 \times 10^{15}\,\mathrm{cm}^{-2}$. At the same time Khan *et al.*[212] investigated the effect of SHI irradiation with 200 MeV Ag^{9+} on the IMT of VO_2. In both cases, the observed reduction of T_C with increasing ion fluence is in very good agreement with results obtained in this thesis.

3 | Suppressed reflection and perfect absorption of light

The enhancement of light absorption is of great importance for numerous applications including photovoltaics,[213–217] biosensing,[218] light detection,[219] thermal imaging,[27,220,221] and efficient light emission.[73,222,223] Unfortunately, highly absorbing materials with large extinction coefficients ($\kappa >> 1$) tend also to be highly reflecting, which limits the total amount of power absorbed within these materials. It is well known, that interface reflections can be suppressed efficiently by using single- and multi-layer dielectric anti-reflection (AR) coatings. However, these coatings are typically at least a quarter-wavelength of light in thickness, which limits the applicability at longer wavelength such as in the mid- and far-infrared.

Recently it was demonstrated that the quarter-wavelength limit of conventional unpatterned AR coatings can be circumvented using lossy coatings on reflecting substrates.[38,39,44,74–79,223–225] Due to the nontrivial phase shifts at the film interfaces, the thickness necessary to obtain destructive interference can be substantially lowered by varying the degree of loss (related to the extinction coefficient κ) in the film and substrate (compare section 2.2.3). Since no light is transmitted through an opaque substrate, efficient suppression of light reflection results in near-perfect absorption within the film and substrate. Several material combinations have been successfully demonstrated to be suitable to achieve near-perfect absorption.[74] These include semiconducting materials applied to metals like gold, silver and aluminum, which are usefull for applications in the visible.[39,74,77,79,224] Second, phase transition materials like vanadium dioxide, semiconductors and dielectrics on polar dielectric materials in their respective Reststrahlen band are promising for applications in the mid-infrared and infrared spectral region.[38,44,74,78]. And third, dielectrics on highly-doped semiconductors are suitable for applications in the mid-infrared.[77]

Ultra-thin absorbing AR coatings with thickness d much smaller than the wavelength of light λ_0 ($d \ll \lambda_0$) are useful in situations where high transmission through the film is unimportant or undesirable, but very low reflection or near-perfect absorption is required. However, despite numerous recent experimental demonstrations of ultra-thin absorbing AR coatings, the parameter space of possible substrate and film combinations has not been fully explored. This chapter deals with the investigation of required optical properties of films and substrates for the design of absorbing AR coatings based on ultra-thin films. The results can be understood as a roadmap to create single layer AR coatings and are valid for all wavelengths. Based on these calculations, tunable near-perfect AR coatings using ultra-thin VO_2 films are theoretically demonstrated on various substrates. Active control of the optical properties of thin films (or substrates) enable optical devices that can be tuned in and out of the destructive interference condition at will. The extension to multilayer systems is briefly outlined. Parts of the results presented in this chapter are published in references [44, 76].

3.1. Absorption in ultra-thin films

The simplest thin-film structure, that readily supports light absorption due to strong interference effects, is a free standing film with refractive index $\tilde{n}_f = n_f + \mathrm{i}\kappa_f$ and thickness d (compare inset in figure 3.1c). The reflectance R, and transmittance T of light depends on the optical properties of the film, e.g. the real n_f and imaginary part κ_f of the complex refractive index, and the polarization and incident angle of the light with respect to the surface normal, respectively (compare section 2.2 and figure 3.1a). Since no light is scattered from a uniform film and energy conservation must apply, the absorptance of light within the film A is given by: $A = 1 - R - T$ (figure 3.1b). Clearly, maximizing A in these films requires the presence of optical losses ($\kappa_f > 0$). But obviously, A cannot simply be maximized by increasing κ_f, because lossy films are also highly reflective. For each value of d a combination of n_f, κ_f exists such that A reaches a maximum. For *optically ultra-thin films*[I] with $\delta \ll 1$, where δ is the reduced film thickness ($\delta = d/\lambda = d \cdot n_f/\lambda_0$, with free-space wavelength λ_0), the maximum attainable value of A is 0.5 (compare figure 3.1c). For example, for $d = 6\,\mathrm{nm}$, $\lambda_0 = 1\,\mu\mathrm{m}$, and normal light incidence, the maximum absorption of $A = 0.5$ is reached when $n_f = \kappa_f \sim 5.2$ (that is $\delta = 0.03$ for the point of maximum absorption, (I) in figure 3.1c). Note, that for ultra-thin films, $A = 0.5$ remains the maximum attainable absorption value for any angle of incidence and for both polarizations of light.[74] However, this limit can be surpassed when light enters the film from a high-index medium at the critical angle for total internal reflection.[226] For angles larger than this angle, no light is transmitted and all incident light is either reflected or absorbed. As an example Driessen *et al.*[226] measured absorptance values above $A = 0.9$ for a 4.5 nm thin niobium nitride layer ($\tilde{n} = 3.5 + 4.5\mathrm{i}$ at $\lambda_0 = 775\,\mathrm{nm}$, $\delta = 0.02$) on sapphire illuminated from the substrate side at oblique incidence. Although near-unity absorptance can be reached, light incidence from a high-index medium requires a prism or equivalent techniques to couple the incident light into the layer. Furthermore the operation is limited to oblique incidence and a specific polarization of light.[74]

Note, that the maximum attainable absorptance increases with increasing film thickness and reaches $A \to 1$ for bulk (figure 3.1b,c). Additional absorption maxima with absorptance $A > 0.5$, which correspond to damped Fabry-Perot modes,[227] are observed for films with a thickness of at least $d \sim \lambda/2$ (figure 3.1b,c). However, the film thickness is no longer in the ultra-thin-film limit of $\delta \ll 1$ ($d \ll \lambda$).

3.2. Suppressed reflection using ultra-thin coatings

According to Beer-Lambert's law, light is exponentially attenuated when propagating trough an absorbing medium (figs. 3.2a,c I). By definition, no light is transmitted through a semi-infinite absorbing substrate ($T = 0$) since all light is gradually absorbed. Hence, all light that is not reflected is absorbed ($A = 1 - R$) and maximizing A requires simply minimizing R. However, the reflectance of any substrate with refractive index $\tilde{n}_s = n_s + \mathrm{i}\kappa_s$ is always > 0, despite the trivial case of $\tilde{n}_s = 1$ (figs. 3.2b I).

The reflection of light from the surface of an absorbing substrate can be completely suppressed when a suitable optically ultra-thin coating with refractive index $\tilde{n}_f = n_f + \mathrm{i}\kappa_f$ and thickness

---

[I] Usually, a film with thickness on the order of a quarter of the wavelength ($d = \lambda/4$, $\delta = 1/4$) is called optically thin. In this thesis, films with a thickness at least smaller than a tens of the wavelength ($d = \lambda/10$, $\delta = 1/10$) are regarded as optically ultra-thin films.

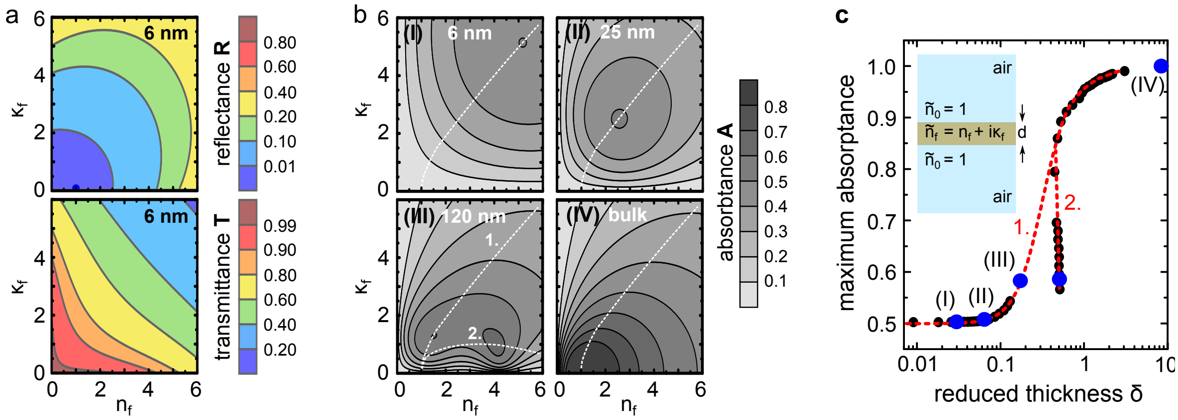

Figure 3.1.: A light absorbing cavity is readily formed by a free-standing lossy film with refractive index $\tilde{n}_f = n_f + i\kappa_f$ and thickness d (compare inset in c) **(a)** Reflectance R and transmittance T maps of a 6 nm thin film as a function of the real n_f and imaginary κ_f part of the refractive index of the film for a free-space wavelength λ_0 of 1 μm and normal light incidence. **(b)** Absorptance A maps of a thin film with a thickness of $d = 6$ nm (I), 25 nm (II), 120 nm (III), and a semi-infinite substrate (IV bulk), respectively. The point of maximum absorption follows a trajectory (dashed line 1.) as a function of film thickness. The additional absorption maximum observed in (III) corresponds to a higher order cavity mode, which follows a different index trajectory (dashed line 2.). **(c)** Maximum absorptance as a function of the reduced film thickness δ. For ultra-thin films ($\delta << 1$, that is $d << \lambda$) the maximum attainable absorptance is $A = 0.5$. Data points taken from (b) are highlighted. Higher order cavity modes (2.) only appear when d is at least $\lambda/2$ ($\delta \sim 0.5$).

$d \ll \lambda$ is applied (figs. 3.2a II,III and section 2.2.3).[38,39,44,74–79,223–225] Two types of single layer AR coatings can be distinguished: transparent AR coatings ($\kappa_f = 0$, fig 3.2a II) and absorbing AR coatings ($\kappa_f > 0$, fig 3.2a III). In both cases the system can be treated as an asymmetric Fabry-Perot cavity and according to equation 2.10 (section 2.2.3) a reflection map for normal light incidence can be calculated as a function of real (n_s) and imaginary (κ_s) parts of the substrate refractive index by keeping n_f, κ_f and δ constant.

Figure 3.2b II shows the reflection map for a transparent coating with $\tilde{n}_f = 2$ and $d = 62.5$ nm ($\delta = 1/8$) at $\lambda_0 = 1\,\mu$m. A point of zero reflection [$\tilde{n}_s(R = 0)$] occurs for one particular combination of n_s and κ_s - in this case at $\tilde{n}_s \sim 1.6 + 1.2$i (marked in figure 3.2b II with an x). For all other combinations of n_s and κ_s light is partially reflected. Since no light is absorbed within the coating and no light is reflected from the surface at the point of zero reflection, the incident light is completely absorbed within the substrate with a penetration depth of $\alpha^{-1} = \lambda_0/(4\pi\kappa_s)$, where α denotes the absorption coefficient (figure 3.2c II). The reflection map for a comparable absorbing coating with $\tilde{n}_f = 2 + 0.6$i ($d = 62.5$ nm, $\delta = 1/8$) at $\lambda_0 = 1\,\mu$m is shown in figure 3.2b III. A point of zero reflection occurs for $\tilde{n}_s \sim 0.315 + 1.5$i (also marked in figure 3.2b III with an x). In contrast to the transparent AR coating, light is predominantly absorbed within the coating ($A \sim 0.81$, figure 3.2c III). Since no light is reflected from the surface, all light that is not absorbed within the coating is absorbed within the substrate. For comparison: A free standing film with the same properties ($\tilde{n}_f = 2 + 0.6$i, $d = 62.5$ nm) but without the substrate absorbs only about half ($A \sim 0.38$). An uncoated substrate with the same refractive index ($\tilde{n}_s \sim 0.315 + 1.5$i) absorbs approximately 22% in the first 62.5 nm and $A \sim 0.32$ in total [figs. 3.2c I,III (1)].

Perfect absorption of light within the film and substrate can be achieved by using both transparent or absorbing AR coatings. Further, light absorption within an ultra-thin film can be enhanced by strong interference effects using a suitable substrate material. This was

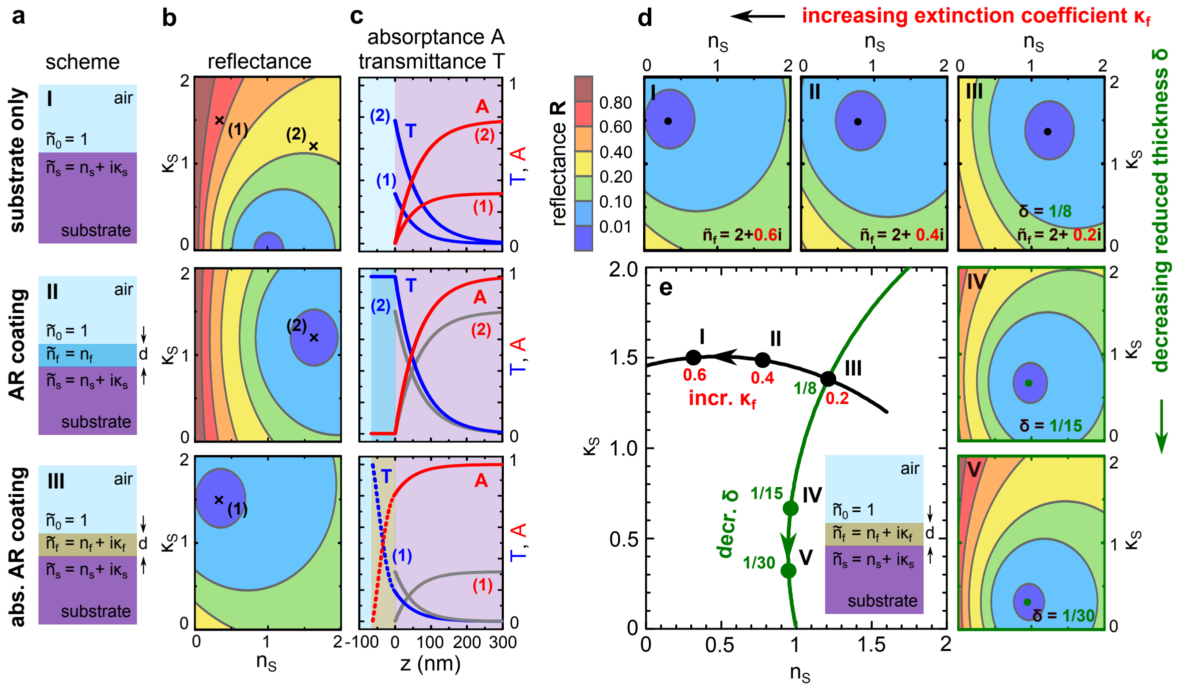

Figure 3.2.: **(a)** The inevitable reflection of light at an interface between air ($\tilde{n}_0 = 1$) and a substrate with refractive index $\tilde{n}_s = n_s + \mathrm{i}\kappa_s$ (I, substrate only) can be completely suppressed by applying either a transparent anti-reflection (AR) coating (II, $\tilde{n}_f = n_f$), or an absorbing AR coating (III, $\tilde{n}_f = n_f + \mathrm{i}\kappa_f$) to the surface. **(b)** Maps of the calculated reflectance as a function of n_s and κ_s without a coating (I), with a transparent AR coating (II, $\tilde{n}_f = 2$), and with an absorbing AR coating (III, $\tilde{n}_f = 2 + 0.6\mathrm{i}$), respectively. Values are calculated for $d = 62.5\,\mathrm{nm}$ ($\delta = 1/8$) and $\lambda_0 = 1\,\mu\mathrm{m}$. In the two latter cases, a point of zero reflection occurs for one particular combination of n_s, κ_s, which is marked [(1),(2),respectively]. Both combinations of n_s, κ_s are also marked in (b,I) **(c)** Transmittance T and absorptance A as a function of depth z with respect to the film/substrate interface for the two index combinations (1 and 2) mentioned in (b). **(d)**(I-III) and (III-V) Maps of the calculated reflectance R of a substrate coated with an absorbing AR coating ($\tilde{n}_f = 2 + \mathrm{i}\kappa_f$) as a function of n_s and κ_s for various κ_f and reduced thicknesses of the film δ, respectively. **(e)** For a given complex refractive index of the film, the point of zero reflection follows an index trajectory $\tilde{n}_s(\delta)$ (green line). A similar index trajectory $\tilde{n}_s(\kappa_f)$ (black line) results for a constant reduced thickness δ of the film. Parts of the figure are published in [76].

experimentally verified for example by Kats *et al.*[38] using a $d = 180\,\mathrm{nm}$ ($\delta = 1/20$) thin VO$_2$ film in its transitional state deposited on a sapphire substrate. At $\lambda = 11.8\,\mu\mathrm{m}$ light reflection is almost completely suppressed ($R \sim 0.003$, $\tilde{n}_s \sim 0.1 + 0.8\mathrm{i}$) and $\sim 90\%$ of the incident light is absorbed within the VO$_2$ coating ($\tilde{n}_f \sim 3.25 + 1.5\mathrm{i}$). A comparable free standing VO$_2$ film would only absorb 41%. Park *et al.*[79] even achieved $A = 0.98$ within a 12 nm thin germanium coating ($\delta \sim 1/10$, $\tilde{n}_f \sim 5.5 + 0.9\mathrm{i}$) on top of a silver substrate ($\tilde{n}_s \sim 0.06 + 4.2\mathrm{i}$) at $\lambda = 625\,\mathrm{nm}$. In this case, light absorption is enhanced by a factor of ~ 5 compared to the free standing germanium film ($A = 0.21$).

A roadmap for suppressed reflection

Efficient suppression of reflection is a key requirement for perfect absorption of light. However, the parameter space of possible film/substrate combinations that yield zero reflection for absorbing AR coatings has not been fully explored due to the multitude of constraints. A possible representation of this parameter space is introduced in figure 3.2e. As a starting point, figure 3.2d III shows the reflection map for a film with $\tilde{n}_f = 2 + 0.2\mathrm{i}$ and $\delta = 1/8$.

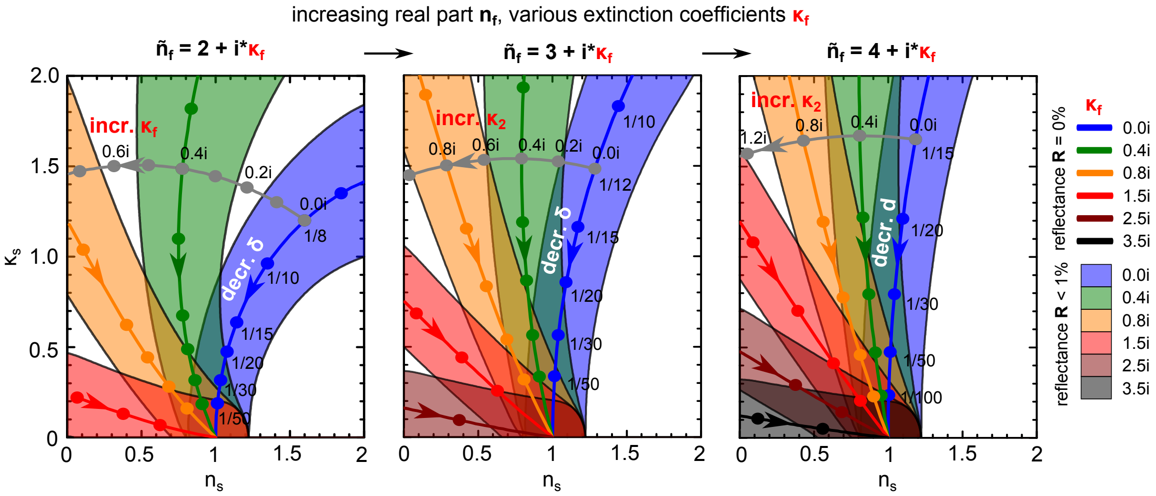

Figure 3.3.: General strategy to suppress reflection from the surface of a substrate with refractive index $\tilde{n}_s = n_s + \mathrm{i}\kappa_s$ using ultra-thin absorbing coatings with thickness d, and $\tilde{n}_f = n_f + \mathrm{i}\kappa_f$ (compare figure 3.2a II,III and 3.2e). Zero reflection index trajectories $\tilde{n}_s(\delta)$ are given for different n_f, and various extinction coefficients κ_f of the film, respectively. The corresponding colored semi-transparent areas indicate those refractive index regions for which the reflectivity is smaller than 1%. Zero reflection using ultra-thin absorbing films only occurs for films with $0 \leq \kappa_f < n_f$ and suitable δ. For ultra-thin films $\delta \ll 1$ ($d \ll \lambda$), zero reflection almost exclusively occurs on substrates with n_s smaller or in the vicinity of $n_s \sim 1$ and small optical losses. Parts of the figure are published in [76].

A point of zero reflection occurs for $\tilde{n}_s \sim 1.21 + 1.38\mathrm{i}$. By decreasing δ while keeping the refractive index of the film constant (figs. 3.2d III-V), the point of zero reflection moves in n_s-κ_s parameter space along a curved index trajectory $\tilde{n}_s(\delta)$ toward $\tilde{n}_s = 1$, as shown in figure 3.2e with a green line.[76] Similarly, an index trajectory $\tilde{n}_s(\kappa_f)$ for zero reflection is obtained for a constant reduced thickness of the film, for instance $\delta = 1/8$, by increasing the extinction coefficient κ_f while keeping n_f constant (figs. 3.2d I-III, and figure 3.2e - black line).[76]
Figure 3.3 summarizes some of the combinations of $\tilde{n}_f$, $\tilde{n}_s$, and δ that result in a complete suppression of light reflection for normal light incidence. According to figure 3.2e, each of the colored lines in figure 3.3 indicates the point of zero reflection $\tilde{n}_s(\delta)$ in n_s-κ_s parameter space as a function of δ for a specific film index $\tilde{n}_f$. Index trajectories are given for different $n_f = 2$, 3, and 4, and various κ_f, respectively. Correspondingly, the refractive index regions of the substrate for which the reflectance is smaller than 1% are semi-transparent colored for each of the index trajectories. Grey lines exemplify the dependence of the point of zero reflection $\tilde{n}_s(\kappa_f)$ on the extinction coefficient κ_f for a given real part of the refractive index of the film n_f and fixed δ, respectively. Thus, figure 3.3 serves as a roadmap to find appropriate refractive index combinations and a suitable film thickness to suppress light reflection for a given wavelength. Note, that the substrate index region shown is limited to values attainable with ultra-thin coatings. Further, the reflectance is not very sensitive to small changes of the refractive indices of either the film or the substrate. To demonstrate this, the colored semi-transparent areas in figure 3.3 indicate the index regions in which the reflectance is still smaller than 1 %. Note, the reflectance has only a weak dependence on the angle of incidence for small angles < 30 ° [74, 172, 224].
The roadmap can be used as follows: On the one hand, suitable coatings can be found for a given substrate at a wavelength of choice. For example, in order to increase the thermal emissivity of silicon dioxide (SiO_2) at room temperature, a suitable coating is sought to suppress light reflection in the atmospheric window between 8 and 13 μm.[228,229] At $\lambda = 9\,\mu$m

the refractive index of SiO_2 is $\tilde{n}_s = 0.59 + 1.77\mathrm{i}$.[230] Refractive index values and thicknesses for a possible coating can be easily estimated from the roadmap (figure 3.3). These are $\tilde{n}_f \sim 2 + 0.5\mathrm{i}$, $\tilde{n}_f \sim 3 + 0.55\mathrm{i}$, and $\tilde{n}_f \sim 4 + 0.6\mathrm{i}$ (and interpolated values in between these values) with thickness $d = 640\,\mathrm{nm}$, $d = 270\,\mathrm{nm}$, and $d = 140\,\mathrm{nm}$, respectively. On the other hand, for a given film, both a suitable refractive index of the substrate and the corresponding film thickness can be read off the roadmap. For example, silicon carbide (SiC) is a material used for ultraviolet photodiodes in the spectral range from 210 to 380 nm.[231] To enhance the amount of light absorbed within the SiC layer and simultaneously reduce the film thickness of the layer, this material can be used as an ultra-thin coating applied to a suitable substrate. At 230 nm the refractive index of SiC is $\tilde{n}_s = 3 + 1.9\mathrm{i}$.[232] For a 3 nm ($\delta \sim 1/25$) SiC coating, complete suppression of light reflection is achieved on a substrate with refractive index $\tilde{n}_s \sim 0.1 + 0.5\mathrm{i}$. When applied to such a substrate, more than 90% of the incident light would be absorbed within the SiC coating. Conversely, only 43% of light is absorbed within a comparable free standing SiC film.

Although the difficulty to find materials with roughly the envisaged refractive indices remains, some general findings can be derived from the roadmap. First, suppression of light reflection using ultra-thin AR coatings can only be achieved for coatings with $n_f \geq \kappa_f$, regardless of their thickness. In most cases, the magnitude of the first partial reflection ($r_{0,f}$ in equation 2.10 section 2.2.3) is already larger than 50% of the incident light and cannot be completely extinct by destructive interference. In all other cases, the required film thickness to obtain the necessary phase shift for destructive interference is large compared to the penetration depth of light and therefore, no interference effect occurs. Second, although for each combination of substrate indices n_s and κ_s an ultra-thin AR coating with suitable combinations of n_f and κ_f can be found theoretically, the maximum acceptable film thickness significantly limits the possible n_s-κ_s parameter space. To demonstrate this, figure 3.4a shows the possible n_s-κ_s parameter space, provided the reduced film thickness is $\delta \leq 1/10$ (optically ultra-thin coatings). For example, zero reflection using coatings with $\tilde{n}_f = 4 + \mathrm{i}\kappa_f$, where $0 \leq \kappa_f \leq n_f$, can only be achieved on substrates with refractive indices corresponding to the blue shaded area in figure 3.4a (compare also figs. 3.3 and 3.2d,e). Obviously, in this case the substrate indices must satisfy at least $n_s \leq 1.5$ and $\kappa_s \leq 2.7\mathrm{i}$. The red shaded area in figure 3.4a is the n_s-κ_s parameter space that yields zero reflection for any combination of n_f and κ_f provided $\delta \leq 1/10$. For a fixed reduced thickness of $\delta = 1/10$ and for increasing n_f the maximum value of n_s saturates at $n_s = 1.52$ (red curve in the inset of figure 3.4a). Hence, it is impossible to find suitable single layer AR coatings with $\delta < 1/10$ to completely suppress light reflections for a substrate with real part of the refractive index higher than this value. Note, that for increasingly thin layers ($\delta \to 0$) the maximum attainable value approaches $n_s \to 1$. Thus, completely suppressed reflection and perfect absorption of light using ultra-thin coatings almost exclusively occurs on substrates with real part of the refractive index approximately or smaller $n_s \lesssim 1$. Further, although there is no maximum value for κ_s, the imaginary part is limited by the choice of n_f and approximately $\kappa_s < n_f$. That is, the substrate has to be low-loss.

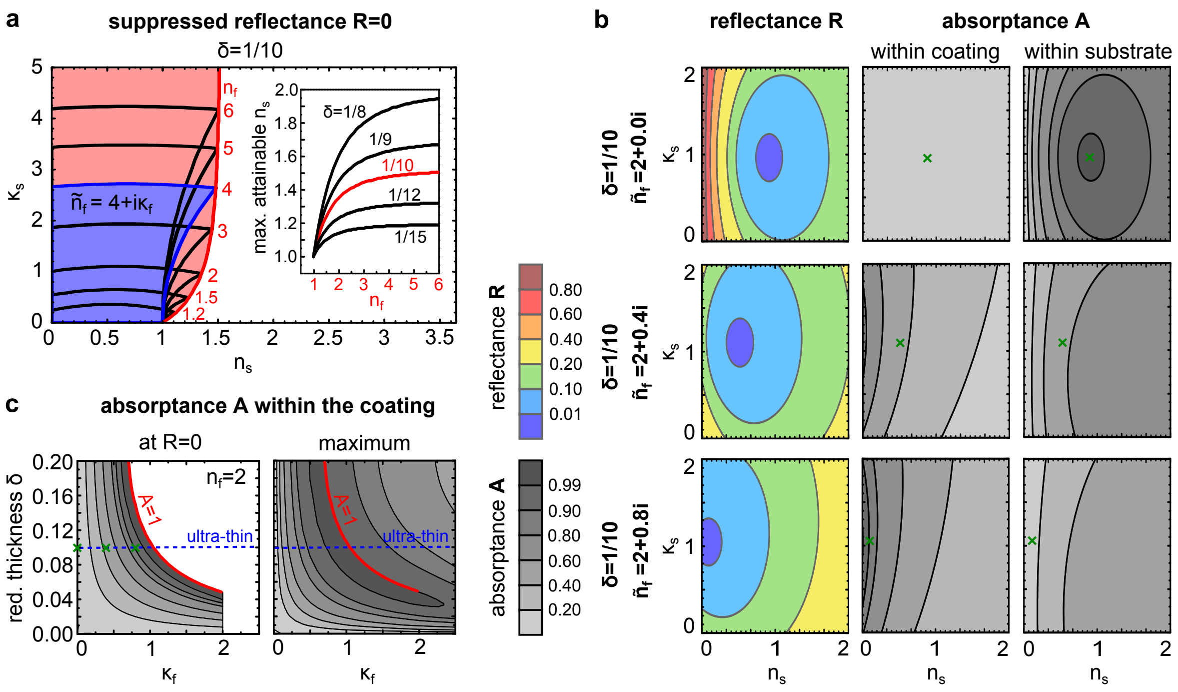

Figure 3.4.: Zero reflection and perfect absorption of a cavity comprising air, an ultra-thin coating with $\tilde{n}_f = n_f + \mathrm{i}\kappa_f$ and a substrate with $\tilde{n}_s = n_s + \mathrm{i}\kappa_s$. **(a)** Representation of the n_s-κ_s parameter space, that can possibly yield zero reflection given a reduced thickness of the coating of $\delta \leq 1/10$ (red shaded area, compare also figs. 3.3 and 3.2d). The blue shaded area corresponds to a specific value of $n_f = 4$. Black lines indicate the index region accessible for various values of n_f, as indicated. The red curve corresponds to the maximum attainable value of n_s as a function of n_f for a given $\delta = 1/10$. The inset compares $n_s(n_f)$ for various given values of δ, as indicated. **(b)** Maps of the calculated reflectance R, absorptance A within the film, and within the substrate for $\tilde{n}_f = 2 + 0.0\mathrm{i}$, $\tilde{n}_f = 2 + 0.4\mathrm{i}$, and $\tilde{n}_f = 2 + 0.8\mathrm{i}$ as a function of the real n_s and imaginary part κ_s of the refractive index of the substrate. The reduced thickness of the film is fixed to $\delta = 1/10$. **(c)** Exemplary grey-scale contour plot of the absorptance A within the coating at the point of zero reflection (R=0) and at the point of maximum absorptance as a function of κ_f and δ for a fixed value of $n_f = 2$. Perfect absorption $A = 1$ (red line) is achieved, when $R = 0$ occurs at $n_s = 0$. Points of zero reflection that correspond to (b) are marked (green x). Parts of the figure are published in [76].

3.3. Perfect absorption using ultra-thin coatings

In a cavity comprising an ultra-thin coating on a substrate, perfect total absorption is the complete absorption of light within both the film and the substrate. On an opaque substrate this is easily achieved, when the applied coating leads to complete suppression of light reflection ($R = 0$). However, perfect absorption within the film or within the substrate is different from perfect total absorption. This is illustrated by three different scenarios in figure 3.4b: First, no light is absorbed within a transparent coating ($\kappa_f = 0$). The point of zero reflection in n_s-κ_s parameter space equals the point of unity absorption within the opaque substrate. In this case, perfect total absorption and perfect absorption within the substrate is the same. Second, if the point of zero reflection is found at $n_s > 0$ for an absorbing coating ($\kappa_f > 0$), both the maximum of absorption within the film and the maximum of absorption within the substrate significantly differ from the point of zero reflection. Thus, it is neither possible to reach perfect absorption in the film nor in the substrate. Third, if the point of zero reflection is found at $n_s = 0$ for a lossy film ($\kappa_f > 0$), perfect absorption within the film is found exactly at the point of zero reflection and no light is able to enter the substrate.

Maximizing the absorptance A within a single-layer absorbing coating is not the same like minimizing the reflectance R. A comparison of the absorptance achieved within the coating at the point of zero reflection and the maximum attainable absorptance within the coating as a function of κ_f and δ is given in figure 3.4c, exemplarily for a fixed value of $n_f = 2$. Regardless of the choice of δ and κ_f, the maximum value of A is always obtained on a substrate with real part of the refractive index $n_s = 0$. Thus, a low-index substrate is needed to maximize absorptance. Note, the imaginary part of the refractive index of the substrate needed to achieve perfect absorption within the coating depends on the thickness of the coating. Theoretically, the minimum possible reduced thickness is always found for $n_s = \kappa_s = 0$. With increasing losses in the substrate (increasing κ_s), the necessary thickness to obtain perfect absorption within the coating increases (compare intersections with the ordinate figure 3.3). Although no substrate material exists with $n_s = \kappa_s = 0$, these findings demonstrate that near-perfect absorption within an ultra-thin film can only be achieved on substrates where both the real and imaginary parts of the refractive index are as small as possible (low-index, low-loss materials). However, certain materials like metals in the ultraviolet to visible (UV-VIS) spectral region and polar materials in the infrared (IR) have appropriate optical properties ($n_s < 0.1$ and small κ_s) to support strong absorption ($A > 0.9$) within suitable ultra-thin coatings (compare also appendix A.1).

3.4. Angle dependence of suppressed reflection

The general strategy of suppression of light reflection using ultra-thin coatings applied to suitable substrates can be easily extended to oblique incidence. According to figure 3.3, figure 3.5a depicts the point of zero reflection $\tilde{n}_s(\delta)$ as a function of δ for an incidence angle of 0, 30 and 45 ° for both, s- and p-polarized light, respectively. For clarity, $\tilde{n}_s(\delta)$ is only shown for a fixed value of $n_f = 2$ and two different values of κ_f, 0i and 0.8i, as blue and orange lines in figure 3.5a, respectively. The refractive index regions of the substrate for which the reflectance is smaller than 1% for normal light incidence are correspondingly semi-transparent colored. The point of zero reflection moves in n_s-κ_s parameter space when the incidence angle is varied. The direction of this change depends on the polarization of light. The index trajectory $\tilde{n}_s(\delta)$ is found at higher values of n_s compared to normal incidence for p-polarization, small δ, and an increasing angle of incidence. Conversely, for s-polarized light an opposite trend is found and $\tilde{n}_s(\delta)$ mostly shifts to lower values of n_s. However, independent of the reduced thickness and for incidence angles up to 45 ° $\tilde{n}_s(\delta)$ is mainly within the refractive index region that yields less than 1% light reflection for normal light incidence. Thus, ultra-thin AR coatings show only a weak dependence of the reflectance on the angle of incidence.

Figures 3.5b and 3.5c compare the angle dependent reflectance of ultra-thin transparent and absorbing AR coatings with that of conventional $\lambda/4$ AR coatings. Three different film/substrate combinations, each yielding completely suppressed reflection at normal incidence, were selected: An ordinary AR coating consisting of a $\delta = 1/4$ film with $\tilde{n}_f = 2 + 0\mathrm{i}$ and a substrate with $\tilde{n}_s = 4 + 0\mathrm{i}$, an ultra-thin ($\delta = 1/10$) transparent AR coating comprising a film with $\tilde{n}_f = 2 + 0\mathrm{i}$ and a suitable substrate with $\tilde{n}_s = 1.35 + 0\mathrm{i}$, and an ultra-thin ($\delta = 1/10$) absorbing AR coating consisting of a film with $\tilde{n}_f = 2 + 0.8\mathrm{i}$ and a substrate with $\tilde{n}_s = 0.11 + 1.04\mathrm{i}$. For completeness, figure (3.5b) shows the calculated reflectance of the semi-infinite substrates as a function of the incidence angle without any coating. The reflectance for s-polarized light monotonically increases with increasing angle of incidence.

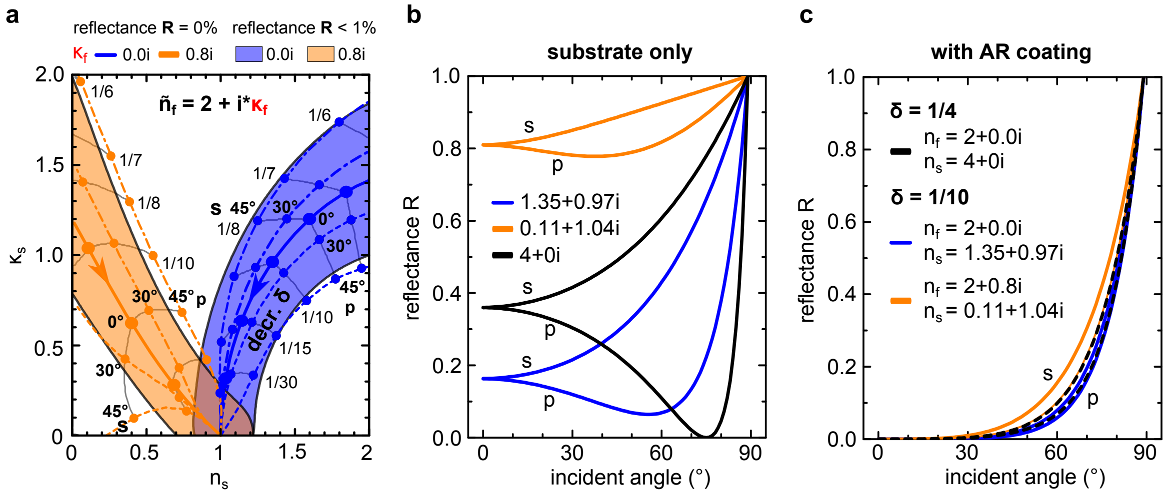

Figure 3.5.: Angle dependence of light reflection from the surface of a substrate ($\tilde{n}_s = n_s + \mathrm{i}\kappa_s$) coated with an ultra-thin film with reduced thickness δ, and $\tilde{n}_f = n_f + \mathrm{i}\kappa_f$ (compare figure 3.3). **(a)** Zero reflection index trajectories $\tilde{n}_s(\delta)$ as a function of δ are given for various angles of incidence and both s- and p-polarized light, respectively. The index trajectories are calculated for fixed $n_f = 2$ and two different values of κ_f. Semi-transparent regions indicate those refractive index regions for which the reflectivity is smaller than 1% for normal light incidence. **(b)** Angle dependence of the reflectance R for three different semi-infinite substrates with refractive indices $\tilde{n}_s$ as indicated. **(c)** Angle dependence of R for these substrates when coated with a suitable AR coating. Refractive indices and reduced film thicknesses used for calculation are given in the figure.

The reflectance for p-polarized light goes to zero at the Brewster angle for the transparent substrate ($\tilde{n}_s = 4 + 0\mathrm{i}$). In contrast, when the substrate is absorbing, the reflectance for p-polarized light goes through a non-zero minimum at the so-called pseudo-Brewster angle.[233] Note, that the phase shift of the amplitude reflection coefficient upon light reflection at the surface of a transparent substrate is constant π at all angles less than the Brewster angle, and zero above this angle. In case of an absorbing medium the phase shift is a monotonic function and decreases from π at normal incidence down to 0 at grazing incidence.[233] Figure 3.5c shows the angle dependent reflectance for the above mentioned AR coatings. Despite minor deviations, all reflectance curves show the same behavior with minor polarization dependence. However, the reflectance is near-zero ($R \sim 0$) for angles up to 45 ° and increases monotonically above this angle. For transparent coatings, the additional accumulated phase shift due to an increased optical path length at oblique incidence drives the cavity out of the destructive interference condition. Consequently the reflectance increases. Interestingly, a comparable change of the incident angle does not significantly alter the optical path length of light within an ultra-thin film and therefore the additional phase accumulation is neglectable. However, in contrast to transparent films/substrates, the angle dependence of reflectance using ultra-thin absorbing films/substrates originates from the angle dependent phase shift at interfaces. In conclusion, conventional $\lambda/4$ AR coatings and ultra-thin AR coatings show almost the same angle dependence of reflection.

3.5. VO$_2$: Dynamically tunable zero reflection

In 2012 Kats *et al.*[38] demonstrated that an ultra-thin film of VO$_2$ on a sapphire substrate can be tuned into a zero-reflection state by varying the temperature in proximity of the IMT. In this transitional state VO$_2$ behaves as a natural disordered metamaterial, because nanoscale

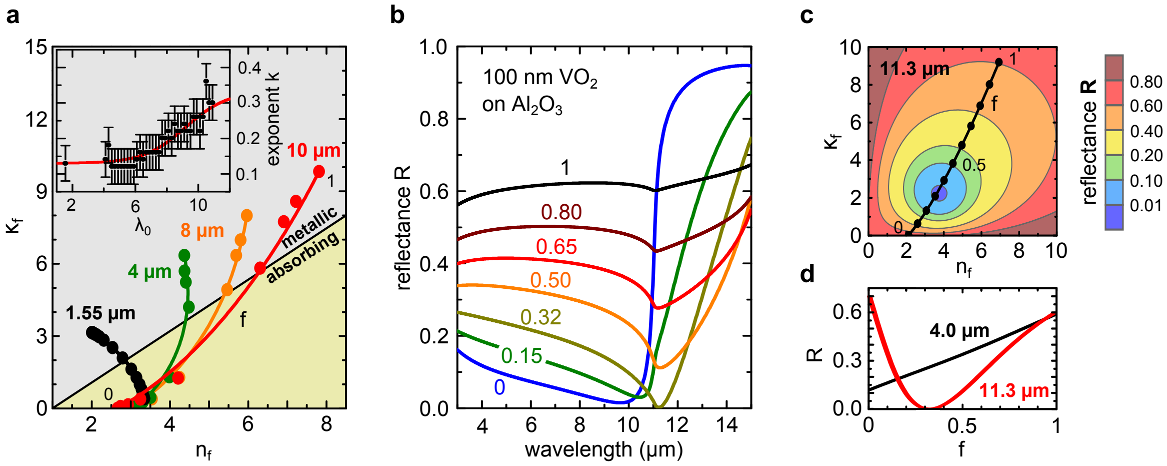

Figure 3.6.: **(a)** Refractive index of VO$_2$ experimentally obtained by spectroscopic ellipsometry at specific wavelengths and for various temperatures across the phase transition (dots). For each wavelength Lichtenecker's equation was fitted to the data (lines) and the exponent k was determined (inset). The red curve in the inset is a guide to the eye. **(b)** Calculated reflectance of 100 nm VO$_2$ on Al$_2$O$_3$ as a function of free-space wavelength λ_0. Reflectance data are calculated for insulating ($f = 0$), for metallic ($f = 1$) VO$_2$ and for different homogeneous mixtures of these two phases (metallic fraction f, as indicated). **(c)** Map of the calculated reflectance as a function of n_f and κ_f of a uniform film of 100 nm thickness on sapphire for $\lambda_0 = 11.3\,\mu$m. The calculated index trajectory of VO$_2$ as a function of f passes very close to the minimum reflection point in n_f-κ_f parameter-space (black line). **(d)** Reflectance as a function of f for $\lambda_0 = 4$ and $11.3\,\mu$m.

islands of metallic phase start to nucleate surrounded by insulating VO$_2$, which then grow and connect in a percolation process.[63] The IMT in VO$_2$ is particularly useful for tunable optical devices, because it occurs gradually over a range of temperatures and provides access to a wide range of complex refractive index values, especially at mid-infrared and infrared wavelengths.

Figure 3.6a shows refractive index data of VO$_2$ experimentally obtained by spectroscopic ellipsometry at various temperatures across the phase transition in n_f-κ_f space for several wavelengths: $\lambda_0 = 1.55$, 4, 8, and 10 μm. For each of these wavelengths the optical properties change dramatically from transparent dielectric ($\kappa_f \sim 0$) via highly absorbing ($\kappa_f < n_f$) to optically metallic behavior ($\kappa_f > n_f$). To obtain complete effective index trajectories as a function of the metallic fraction f, the refractive index data for each wavelength were modeled with Lichtenecker's equation (compare eqn. 2.11). Using k as a free parameter (see inset 3.6a), a good agreement of modeled and experimentally determined refractive index data was found for all wavelength. Hence, by carefully tuning the metallic fraction in VO$_2$ films by means of temperature control the effective refractive index can be adjusted at will.

Using Lichtenecker's equation with the just determined exponent k (see inset 3.6a) and the optical properties of insulating ($\tilde{n}_{\text{ins}}$) and metallic VO$_2$ ($\tilde{n}_{\text{met}}$), determined by spectroscopic ellipsometry by Qazilbash *et al.*[63], the effective optical properties $\tilde{n}_{\text{eff}}$ of VO$_2$ can be estimated as:

$$\tilde{n}_{\text{eff}} = \left[(1-f)\tilde{n}_{\text{ins}}^{2k} + f\tilde{n}_{\text{met}}^{2k}\right]^{1/(2k)}. \tag{3.1}$$

Figure 3.6b shows the calculated reflectance of a 100 nm VO$_2$ film applied to a sapphire (Al$_2$O$_3$) substrate using the effective optical properties for various values of the metallic fraction f. At low metallic fractions ($f \sim 0$) VO$_2$ is insulating and essentially transparent. The reflectance spectrum is dominated by the onset of a prominent Restrahlen band of the Al$_2$O$_3$ substrate, which leads to metal-like reflectivity above $\sim 11\,\mu$m. As f is increased, the reflectance changes monotonically in the mid-IR for wavelength up to $\sim 10\,\mu$m and non-monotonically in the Al$_2$O$_3$ Restrahlen band region. A point of minimal reflectance with $R \sim 0.001$ is reached for $f = 0.32$ at $\lambda_0 = 11.3\,\mu$m, which is a result of the strong interference effect of ultra-thin absorbing films on low-index low-loss substrates. For this wavelength the refractive index of sapphire is $\tilde{n}_s = 0.09 + 0.49$i. Figure 3.6c shows the reflectance map of a 100 nm thin film applied to sapphire as a function of real n_f and imaginary part κ_f of the complex refractive index of the film at $\lambda_0 = 11.3\,\mu$m. A point of zero reflection occurs given a film with refractive index $\tilde{n}_f = 3.77 + 2.25$i. At this wavelength the calculated index trajectory of VO$_2$ (black line in figure 3.6c) almost crosses the point of zero-reflection ($\tilde{n}_f = 3.63 + 2.25$i for $f = 0.32$). Because the refractive index of VO$_2$ is highly tunable, the system can be tuned in and out off a suppressed reflectance state by adjusting the metallic fraction, as shown in figure 3.6d. This suppressed reflectance state corresponds to a near-perfect absorption state with remarkable $\sim 93\%$ light absorption within the ultra-thin ($\delta \sim 0.03$) VO$_2$ film (99.9% total absorption). Note, a linear dependence of reflectance on the metallic fraction in the VO$_2$ film can be hardly found for mid-infrared wavelengths. This makes it difficult to extract the phase transition temperature, which is defined as the temperature at which 50% of the film is in the metallic state, from reflectance measurements. When the phase transition temperature is evaluated from reflectance data, a wavelength of $4\,\mu$m is used in this thesis (compare 3.6d).

3.5.1. Natural occurring phase coexistence

Across the IMT small domains of the metallic and insulating phase coexist in thin VO$_2$ films with individual domain sizes much smaller than the wavelength of mid-infrared light.[63] A schematic drawing of the phase coexistence is shown in figure 3.7a. Insulating domains are given in blue, whereas metallic regions are given in red. At a metallic fraction of $f = 0$ all individual domains are insulating and the entire film appears blue (insulating). As the metallic fraction increases, individual domains undergo a phase transition and appear red (metallic). Neglecting correlation effects, metallic and insulating domains are randomly distributed in the schematic drawing. At a metallic fraction of $f = 1$, the entire film is metallic and appears red. Because of the phase coexistence on a subwavelength scale, effective optical properties can be assigned. The phase coexistence itself can be empirically considered as a first-order equilibrium[234] and hence the metallic fraction f can be correlated with temperature T:

$$f(T) = \frac{1}{1 + \exp\left[W/k_b\left(1/T - 1/T_C\right)\right]}, \tag{3.2}$$

where W is an energy, which contains information about the total width (sharpness) of the IMT, k_b is the Boltzmann constant, and T_C is the critical temperature at which half of the VO$_2$ is in the metallic state. This model was used previously to describe the electrical properties of VO$_2$.[234]

Figure 3.7b shows the calculated metallic fraction as a function of temperature for different critical temperatures T_C = 70 (I), 60 (II), 40 (III), and 20 °C (IV). A constant value of $W = 2.3$ eV, which was obtained by fitting experimentally obtained temperature-dependent resistance data (not shown), is used for the calculations. Smaller (higher) values of W broaden (narrow) the width of the phase transition. By using equation 3.2 in Lichtenecker's equation (compare fig 3.6) the effective refractive index of VO$_2$ can be expressed in terms of

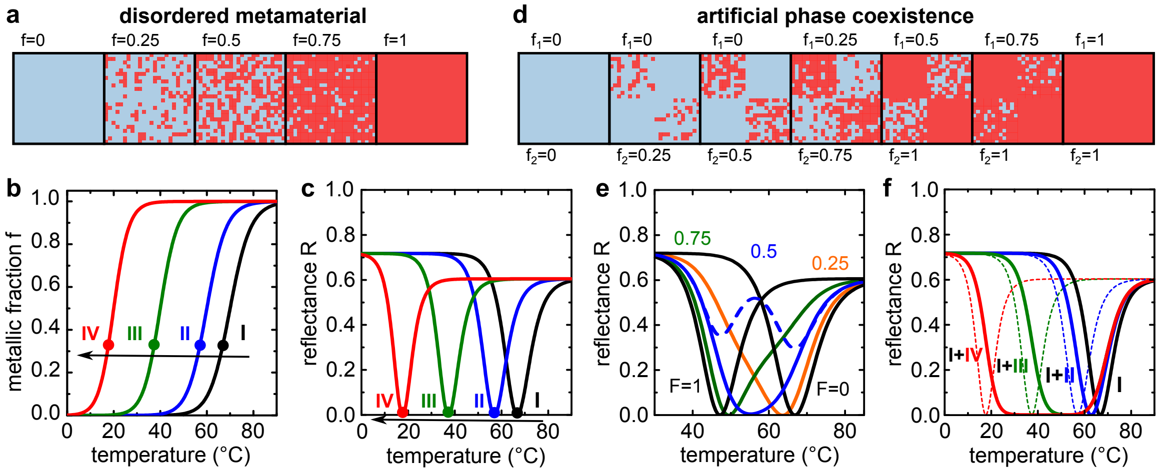

Figure 3.7.: **(a)** VO_2 is modeled as a disordered metamaterial. Blue: insulating, red: metallic phase with metallic fraction f. **(b)** f as a function of temperature for different phase transition temperatures: $T_C = 70\,°C$ (I), $60\,°C$ (II), $40\,°C$ (III), and $20\,°C$ (IV). **(c)** Calculated reflectance R for (I)-(IV) as a function of temperature at $\lambda_0 = 11.3\,\mu m$. **(d)** Artificial phase coexistence in defined areas. The metallic fractions f_1 and f_2 in both regions differ. **(e)** Calculated R for sub-wavelength checkerboard patterned VO_2 films with various duty cycles F as a function of temperature. T_C of region 1 and 2 is set to $T_C^1 = 70\,°C$ and $T_C^2 = 50\,°C$, respectively. The dashed line is the average of the reflectance of region 1 and 2 for $F = 0.5$ **(f)** Calculated R for checkberboard patterned VO_2 films with fixed $T_C^1 = 70\,°C$ and decreasing T_C^2 [assignment according to (b)] at the wavelength at which zero reflection occurs, respectively [dashed lines compare (c)].

temperature. Thus, the reflectance can be calculated as a function of temperature. Figure 3.7c shows the temperature-dependent reflectance of a 100 nm VO_2 film on Al_2O_3 at $\lambda_0 = 11.3\,\mu m$ using the metallic fractions given in figure 3.7b. Taking into account that the point of zero reflection occurs at $f = 0.32$ (dots in figure 3.7b), it is obvious that zero reflection occurs at a temperature T_{min} slightly lower ($\sim 3\,°C$) than the phase transition temperature T_C. However, by tuning the phase transition temperature of VO_2, the temperature at which zero reflection occurs can be precisely adjusted.

Artificial phase coexistence on a sub-wavelength scale greatly enhances the possibility to tune the reflectivity of VO_2 based devices. For this purpose it is necessary to create nanometer-sized regions within the film in which the phase transition takes place at temperatures lower or higher than in the intrinsic VO_2. As an example, figure 3.7d schematically depicts the phase coexistence in the unit cell of a checkerboard pattern, in which half of the squared regions have a different T_C and already undergo the phase transition (region 2, with T_C^2 and metallic fraction f_2) while the other half is still insulating (region 1, with T_C^1 and metallic fraction f_1). Effective optical properties can be individually assigned for the two different regions (1 and 2) using Lichtenecker's equation: $\tilde{n}_1(f_1)$ and $\tilde{n}_2(f_2)$. The effective optical properties of the entire checkerboard pattern are estimated by applying Lichtenecker's equation again:

$$\tilde{n}_{\text{eff}} = \exp\left\{(1-F)\ln\left[\tilde{n}_1^2(f_1)\right] + F\ln\left[\tilde{n}_2^2(f_2)\right]\right\}^{1/2}, \tag{3.3}$$

where F is the duty cycle of the checkerboard pattern, which is the area fraction of region 2 with respect to the entire film. Note, that an exponent of $k = 0$ is used, which takes into account the isotropic nature of the checkerboard pattern (compare section 2.2.4). Equation 3.3 can be significantly simplified using logarithmic and exponentiation identities for $F = 0.5$:

$$\tilde{n}_{\text{eff}} = \sqrt{\tilde{n}_1(f_1)\tilde{n}_2(f_2)}. \tag{3.4}$$

Figure 3.7e shows the calculated reflectance of a 100 nm thin checkerboard patterned VO_2 film on Al_2O_3 as a function of temperature at a wavelength of $\lambda = 11.3\,\mu$m for various duty cycles F. The phase transition temperature of region 1 and 2 was taken to be $T_C^1 = 70\,°C$ and $T_C^2 = 50\,°C$, respectively. The reflectance for $F = 0.5$ clearly shows that the sub-wavelength structured VO_2 possesses effective optical properties that cannot be trivially deduced by averaging the reflectance of the two different regions (dashed line in 3.7e). While the reflectance minimum of region 1 and 2 occurs independently at $T_{\text{min}}^1 \sim 67\,°C$ and $T_{\text{min}}^2 \sim 47\,°C$ and has a full width at half minimum (FWHM) of $\sim 12\,°C$, respectively, the patterned VO_2 appears to have a single effective reflectance minimum at $T_{\text{min}}^{\text{eff}} \sim 55\,°C$ with a FWHM $> 20\,°C$. The temperature of minimal reflectance $T_{\text{min}}^{\text{eff}}$ can be precisely tuned between T_{min}^1 and T_{min}^2 by adjusting F. Further, the temperature range of phase coexistence can be greatly increased by shifting the phase transition temperatures apart (figure 3.7f). The optical properties can then be tuned in and out of an artificially designed effective medium state over a desired range of temperatures by controlled phase coexistence in VO_2.[44] Optical functionality, especially large and controllable dichroism, is introduced by anisotropic patterning of VO_2.[44]

3.5.2. Wavelength of zero reflection

Besides controlling the temperature range of minimal reflectance, adjusting the wavelength is of great importance. Figures 3.8a-c show the calculated reflectance of intrinsic VO_2 on three different substrates: Al_2O_3, SiO_2 and gold (Au) for different VO_2 film thicknesses and at a metallic fraction f that results in a point of zero reflection, respectively. The wavelength λ_{min} at which light reflection can be efficiently suppressed by applying an ultra-thin VO_2 coating is mostly determined by the refractive index of the substrate (figs. 3.8d-f) and can be tuned by the thickness of the VO_2 film. For the polar dielectric materials Al_2O_3 and SiO_2 suppressed reflection can be achieved within their Reststrahlen band region. This region is located between the longitudinal optical (LO) and transverse optical (TO) phonon frequencies and characterized by low index values $n_s < 1$ (compare figures. 3.8d,e). Similarly, very low index values $n_s < 1$ are found for low-loss noble metals like Au near their plasma frequencies (figs. 3.8f).

The onset of the Reststrahlen band of the substrate is characterized by a minimum in reflectance, as indicated by the arrows in figures 3.8a,b. This minimum is caused by very low values of κ_s at the low wavelength side of the Reststrahlen band, in particular at a wavelength at which $n_s = 1$ (compare figures. 3.8d,e). High reflectance of polar materials within their Reststrahlen band is a result of optically metallic behaviour ($\kappa_s > n_s$). The thickness of a VO_2 coating necessary to suppress light reflection at a particular wavelength within this region depends on the specific value of κ_s. Ultra-thin ($\delta < 1/10$) VO_2 coatings on Al_2O_3 can suppress light reflection within the spectral region ranging from $\lambda_0 = 9.6$ to $12.9\,\mu$m (see inset in figure 3.8c). In this regions κ_s increases from ~ 0 to 1.5 with increasing wavelength. Suppression of reflection using ultra-thin VO_2 coatings applied to SiO_2 is possible for the spectral region from $\lambda_0 = 7.4$ to $9\,\mu$m (inset in figure 3.8c). The value of κ_s at $\lambda_0 = 9\,\mu$m is 1.8. Although single layer VO_2 coatings can completely suppress light reflection outside these regions, the necessary layer thickness is no longer in the ultra-thin limit.

Although most of the metals feature a large spectral region of $n_s < 1$, they often exhibit

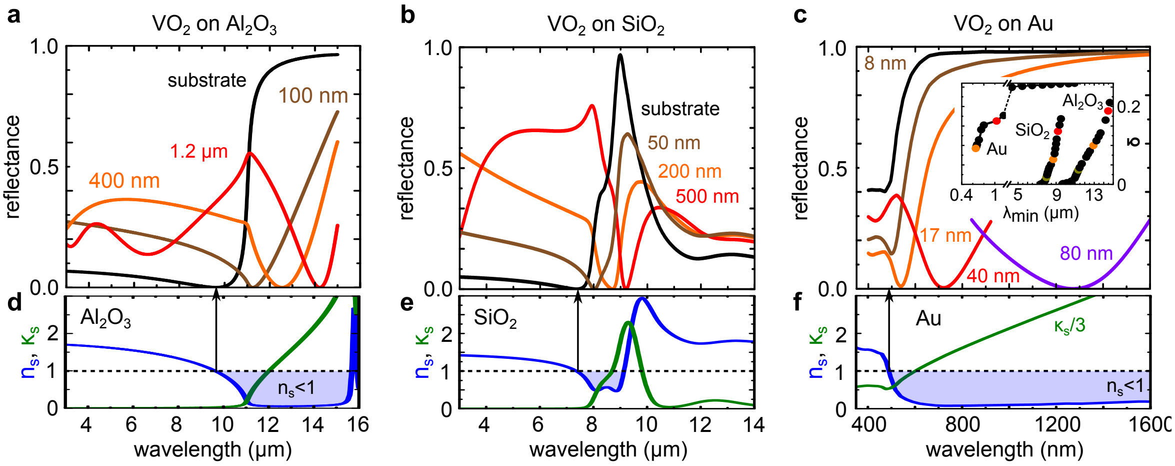

Figure 3.8.: (a-c) Calculated reflectance of VO_2 films with different thickness on Al_2O_3 (a), SiO_2 (b), and Au (c) for metallic fractions that yield zero reflection, respectively. The reflectance of the substrate is given for comparison, respectively (black curve). The inset in (c) correlates the reduced film thickness δ with the wavelength λ_{min} at which the reflectance minimum occurs. Note that zero reflection does not occur for VO_2 coatings thinner than $\delta < 0.09$ on Au. **(d-f)** Real n_s and imaginary κ_s part of the refractive index of Al_2O_3 [235], SiO_2 [230], and Au [236]. Points of minimal reflection in (a)-(c) are only found in the wavelength region where the real part of the refractive index of the substrate is $n_s \lesssim 1$. For a comparable representation, κ_s of Au is divided by 3. Arrows indicate the wavelengths of $n_s = 1$ and the corresponding minima of reflectance.

inherent losses at the onset of this spectral region attributed to interband transitions.[237] Babar and Weaver[236] report a value of $\tilde{n_s} = 1 + 1.6i$ for Au at a wavelength of $\lambda_0 = 471\,\text{nm}$, which leads to $R \sim 0.4$. The thinnest possible VO_2 coating that achieves zero reflection when applied to a gold substrate is already 17 nm thick ($\delta = 0.09$) and suppresses light reflection at 527 nm (inset in figure 3.8c). At this wavelength κ_s is already 2. The strongly increasing value of κ_s with increasing wavelength leads to a rapidly increasing VO_2 layer thickness, which is necessary to suppress light reflection, quickly exceeding the ultra-thin limit (see inset in figure 3.8c). Note that light reflection from a gold surface can be completely suppressed over the entire near- and mid-infrared spectral region by applying $\sim \lambda/4$ VO_2 coatings. For example a 500 nm VO_2 coating on gold suppresses light reflection at a wavelength of $11.3\,\mu\text{m}$. However, this is five times the layer thickness when compared to VO_2 on sapphire (compare figure 3.6b).

3.6. Summary

Ultra-thin absorbing coatings with a thickness much smaller than the wavelength of incident light ($d \ll \lambda_0$, $\delta < 1/10$) can completely suppress light reflection from certain reflective substrates caused by a destructive interference condition. The substrates must have a low index of refraction ($n_s \lesssim 1$) and low optical losses. The wavelength at which light reflection can be fully suppressed is primarily determined by the nature of these substrates, and is pinned to particular values near plasma or phonon resonances - the former typically in the ultraviolet or visible, the latter in the infrared.[76] On opaque substrates ($\kappa_s > 0$) suppressed reflection is equivalent to perfect total absorption within the film and substrate. Perfect absorption within the ultra-thin films cannot be achieved for naturally occurring substrates, because the refractive index necessary would be $n_s = 0$. However, absorption values well above 90% within the film are possible for ultra-thin coatings less than a tenth of wavelength in thickness when deposited on low-loss index-near-zero[238] materials.

An ideal coating material is vanadium dioxide, which can be tuned in and out of a highly absorbing/non-reflecting state by utilizing the phase coexistence of metallic and insulating domains across its IMT. In this transitional state, effective optical properties of VO_2 can be estimated using effective medium theory and a chemical equilibrium model. The effective refractive index of VO_2 can be adjusted by carefully tuning the metallic fraction in intrinsic VO_2 films by means of temperature control. Further, a specific metallic fraction can be maintained over a certain temperature range by introducing artificial phase co-existence in spatially defined regions. Thus a persistent effective medium state can be created. The widely tunable effective optical properties make VO_2 coatings applicable in a wide variety of optical and optoelectronic systems such as bolometers, modulators, and tunable thermal emitters.

3.7. Outlook: Multilayer systems

Optical coatings consisting of multiple thin layers offer a much higher degree of freedom in the design of optical devices. Besides the well known Bragg mirror, which almost perfectly reflects light of specific wavelengths when properly designed, perfect absorbers based on metal-insulator-metal (MIM) multilayer systems have been widely discussed throughout the literature.[239–241] A common MIM thin-film interference structure comprises an ultra-thin metallic layer, a dielectric spacer layer, and metal back reflector. Strong interference effects are enabled by separating phase accumulation necessary to obtain destructive interference and amplitude attenuation due to light absorption. The interference effect also leads to field confinement within the dielectric layer. However, every multilayer systems can be treated as a single homogeneous effective layer, provided that the individual layer thickness is much smaller than the wavelength of light (figure 3.9a). The effective optical properties are than determined by the refractive indices and thicknesses of each layer. For a two-layer coating the effective refractive index is:[187]

$$\tilde{n}_{\text{eff}} = \left[(1-D)\tilde{n}_1^2 + D\tilde{n}_2^2\right]^{1/2}, \tag{3.5}$$

where $\tilde{n}_1$ and $\tilde{n}_2$ are the refractive indices of layer 1 and 2 (figure 3.9a), and $D = d_2/(d_1 + d_2)$ is the thickness fraction of layer 2 with respect to the summed thickness $d_1 + d_2$. Note, equation 3.5 is consistent with Lichtenecker's equation for $k = 1$ (compare section 2.2.4). Absorbing AR coatings ($\kappa_f < n_f$, $\kappa_f > 0$) can be created by combining metals ($\kappa_2 > n_2$) and transparent dielectrics ($\kappa_1 = 0$).

VO_2 layers can be stacked in order to create a MIM structure. Figure 3.9b shows a map of the calculated reflectance R of a stack of metallic VO_2(R), and insulating VO_2(M1) deposited on Al_2O_3 as a function of the VO_2(R) fraction F and the combined VO_2 layer thickness $d_1 + d_2$ at $\lambda = 11\,\mu$m. A point of zero-reflection occurs when the metal layer thickness is one tenth of the total VO_2(R)/VO_2(M1) layer thickness ($F = 0.1$) and $d_1 + d_2 = 100\,$nm. For all other layer thickness combinations light is partially reflected. Such a device can be realized when the IMT of VO_2 in different layers occurs at a different temperature. Figure 3.9c shows the calculated temperature-dependent reflectance of two VO_2 layers with different phase transition temperature: $T_C^1 = 70\,°$C and $T_C^2 = 20\,°$C, which are deposited on an Al_2O_3 substrate. The total thickness $d_1 + d_2$ of the coating is 100 nm. Note, that the resulting reflectance does not depend on the stacking sequence. Comparable to a laterally patterned VO_2 film (compare

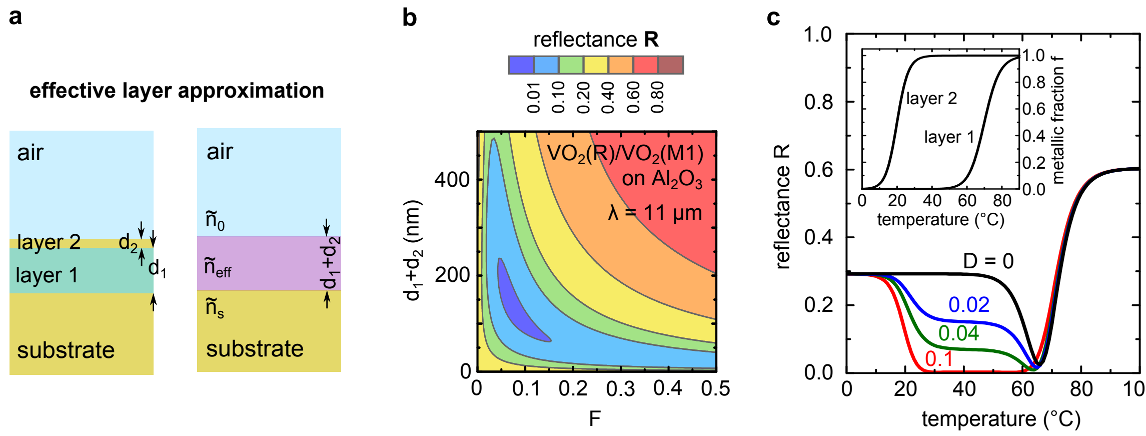

Figure 3.9.: (a) A coating consisting of two sub-wavelength thick layers (thickness d_1 and d_2) can be approximated by a single effective layer with effective refractive index $\tilde{n}_{\mathrm{eff}} = n_{\mathrm{eff}} + \kappa_{\mathrm{eff}}$ and thickness $d_1 + d_2$. **(b)** Map of the reflectance of a VO_2(R)/VO_2(M1) coating on Al_2O_3 as a function of the VO_2(R) fraction F and $d_1 + d_2$ calculated for $\lambda_0 = 11\,\mu$m. A point of zero reflection occurs for $D = 0.1$ and $d_1 + d_2 = 100\,$nm. **(c)** Calculated reflectance of a 100 nm thick two-layer VO_2/VO_2 coating on Al_2O_3 as a function of temperature and for different fractions F of the top VO_2 layer at $\lambda_0 = 11\,\mu$m. The phase transition of both VO_2 layers is assumed to take place in different temperature regions (inset). Therefore, the top VO_2 layer is already metallic when the bottom VO_2 layer is still insulating.

figure 3.7), the vertical incorporation of a sub-wavelength VO_2 pattern results in an effective phase transition in the temperature range between the IMTs of the individual VO_2 layers. By carefully adjusting the layer thicknesses the temperature range of zero reflection can be greatly enhanced ($D = 0.1$ in figure 3.9c).

A vertical distribution of phase transition temperatures has been achieved in doped VO_2 synthesized in solution and effective optical properties have been observed.[242] It is noteworthy, that any lateral and vertical distribution of phase transition temperatures lead to a broadend effective phase transition. Thus, it might be intricate to compare the phase transition of VO_2 measured optically with other integral techniques like X-ray diffraction.[65] However, the combination of lateral and vertical patterning of VO_2 opens up a pathway to create complex widely tunable optical materials.

4 | Experimental methods

This chapter briefly introduces the experimental methods used in this thesis and concisely summarizes all experimental details. When possible, the reader is referred to detailed descriptions of the experimental methods in the literature.

4.1. Growth of VO_2 layers

Most of the VO_2 thin films used in this work were grown by the group of Prof. Shriram Ramanathan (Purdue University) on c-plane sapphire substrates using radio frequency (rf) magnetron sputtering from a V_2O_5 target in an Ar/O gas mixture.[168,243] In the sputter process ionized Ar is accelerated towards the target and ejected (sputtered) atoms are deposited onto the substrate. During film growth the temperature, pressure, the ratio of Ar/O and the gas flow were maintained at 450 to 550 °C, $5-15\,\mathrm{mTorr}$, 90:10, and 40-75 sccm, respectively. The sample holder was rotated at a speed of $\sim 30\,\mathrm{min}^{-1}$ to improve sample homogeneity. The same VO_2 growth recipe, initially optimized for sapphire substrates, is used to grow VO_2 thin films on (001) quartz (SiO_2), (001) zinc oxide (ZnO), and (001) aluminum-doped zinc oxide (AZO).

4.2. Ion beam methods

All ion beam methods are based on the acceleration and focusing of charged particle beams that are directed towards a sample to probe or modify the physical properties. Details about ion irradiation and charactization methods using ion beams can be found in references [244–246].

Ion irradiation

Ion irradiation in the energy range from $\sim 10-300\,\mathrm{keV}$ was performed at the Institute of solid state physics at the Friedrich Schiller University Jena using the implanter ROMEO. For ex-situ experiments approximately 100 nm thin VO_2 films were irradiated with 75 keV argon ions (Ar^+) or 190 keV cesium ions (Cs^+) at room temperature in a fluence range starting from $N_I = 5 \times 10^{12}$ to $N_I = 1 \times 10^{15}\,\mathrm{cm}^{-2}$. The ion fluence was estimated by directly measuring the beam current on the sample holder. The flux was kept as low as possible to prevent heating effects. Since the number of displaced lattice atoms created by Cs^+ irradiation is roughly three times higher compared to Ar^+ irradiation of VO_2, a flux of $\Phi_I = 6 \times 10^{10}\,\mathrm{cm}^{-2}\mathrm{s}^{-1}$ and $\Phi_I = 2 \times 10^{10}\,\mathrm{cm}^{-2}\mathrm{s}^{-1}$ was used for Ar^+ and Cs^+ irradiation, respectively. This guarantees the formation of a comparable number of defects during a comparable irradiation time.

Area selective ion irradiation

Area selective ion irradiation of VO_2 was achieved by covering the samples with an irradiation mask much thicker than the penetration depth of the ions. Sample areas that are not protected by the mask are irradiated, while covered areas remain intrinsic VO_2. E-beam lithography (Raith 150TWO, Helmholtz Center Dresden Rossendorf, and Elionix ELS F-125, Harvard University) was employed to cover at least $100 \times 100\,\mu m^2$ areas of the VO_2 thin films with Poly(methyl methacrylate) (PMMA) masks. Two different masks were fabricated. The first mask consists of parallel ridges with a width of $0.5\,\mu$m and a period of $1\,\mu$m and was fabricated in the fixed-beam-moving-stage mode. This method guarantees continuous ridges without any offset. The checkerboard mask was composed of squares with a period of $0.5\,\mu$m. Various duty cycles F were realized by keeping the period constant and changing either the ridge width or the edge length of the squares. For $F = 0.5$ the width and length of each square was 250 nm. After ion irradiation the PMMA mask was lifted-off with dimethyl sulfoxide in an ultrasonic bath for at least 30 min.

Direct writing using the focused ion beam

Area selective ion irradiation was also achieved using a focused ion beam (FIB) system. A dual beam system from FEI (Helios NanoLab 600i), which incorporates both a FIB and an electron beam for scanning electron microscopy (SEM), was used to irradiate approximately 100 nm VO_2 films grown on Al_2O_3 with 30 keV Ga^+. To determine suitable patterning parameters, first, large areas ($400 \times 400\,\mu m^2$) were irradiated at normal incidence with different total charge densities ranging from 30 to $180\,fC\mu m^{-2}$, corresponding to ion fluences N_I ranging from approximately 2 to $12 \times 10^{13}\,cm^{-2}$. Note that the penetration depth of 30 keV Ga^+ in VO_2 is approximately 16 nm as calculated with SRIM.[204]

Preparation of aluminum-doped zinc oxide substrates

Aluminum-doped zinc oxide substrates were fabricated using ion implantation. Zinc oxide (ZNO) single crystals with (001) orientation were implanted at an elevated temperature of 500°C with Al^+ ions with energies ranging from 30 to 350 keV, and suitable ion fluences, to achieve homogeneous boxlike doping profiles. The doped region extends 400 nm from the surface into the substrate with constant aluminum concentrations c_{Al} ranging from 10^{19} to $10^{21}\,cm^{-3}$ and has a Gaussian doping tail ranging an additional 200 nm into the substrate (compare appendix A.2). The Al^+ implantation is followed by thermal annealing in air for one hour at 700 °C. No long-range diffusion of aluminum dopants is expected at this temperature. The high-temperature annealing step is necessary to reduce the amount of ion beam induced lattice defects and to activate the majority of the aluminum dopants (compare appendix A.2).

Rutherford Backscattering Spectrometry

Rutherford Backscattering spectrometry (RBS) is a non-destructive ion beam analysis technique widely used to study the composition of thin-film solids and to determine their crystallinity.[247] Typically high energetic ($\sim 2\,$MeV) helium ions (He^+) are directed towards a sample and the energy of backscattered ions, which contains information about the depth of the scattering event, is measured with a solid state detector. Ion channeling along a low indexed crystallographic axis steers ions by small angle collisions through rows or planes of atoms in crystalline materials. As a consequence the backscattering yield for an aligned sample is dramatically reduced with respect to a random orientation of the sample. This allows to determine the depth and distribution of lattice disorder (channeling method).[245,248]

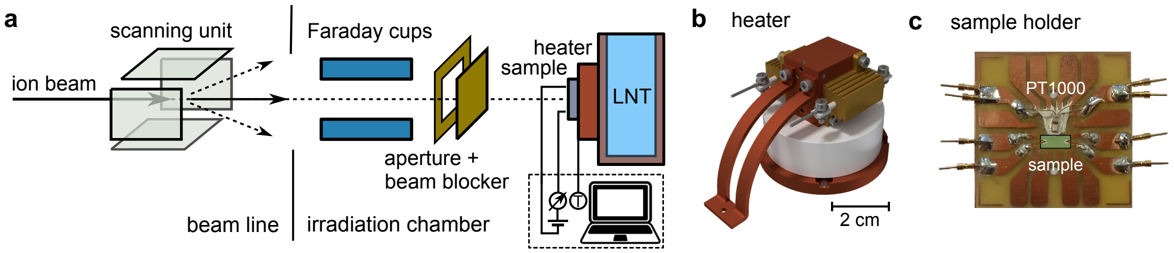

Figure 4.1.: **(a)** Schematic drawing of the experimental setup used for in-situ temperature-dependent electrical measurements during ion irradiation. **(b)** Cad 3D drawing of the self-build heater. **(c)** Photo of the sample holder.

RBS in channeling geometry (RBS/C) was performed using the 3 MeV tandetron accelerator JULIA at the Friedrich Schiller University Jena. Aligned and random spectra of ion irradiated VO_2 thin films on Al_2O_3 substrates were recorded for the backscattering of 1.8 MeV He^+ ions at 170 ° with a total accumulated charge of 10 μC.

4.3. In-situ electrical measurements during ion irradiation

Temperature-dependent electrical measurements were performed in-situ during and after ion irradiation in the irradiation chamber of the ion implanter ROMEO. A schematic overview of the experimental setup, which was developed within the frame of this thesis, is shown in figure 4.1. The ion beam, which is provided by the ion implanter, is typically focused and scanned over the implantation area to guarantee a homogeneous lateral ion distribution (figure 4.1a). Since no direct beam current measurement is possible on the target holder the beam current is permanently measured via Faraday cups placed within the outer regions of the scanned area. After passing a rectangular aperture of roughly $2.5 \times 2.5\,\mathrm{cm}^2$ a beam blocker is installed before the ion beam hits the target. The target holder consists of a liquid nitrogen cooled copper target, which serves as thermal mass, and a self-build computer controlled resistance heater. The heater itself consists of a copper block on which the sample holder is mounted, two low-impedance resistors (24 W), which can easily heat up the copper block to more than 200 °C, a Teflon spacer to partially decouple the heater from the thermal mass, a thermal bridge to allow some heat transport, and a copper connector (compare figure 4.1b). A thermocouple (type K) is placed within the copper block for temperature control. Thermal radiation limits the accessible lowest temperature of this system to roughly -120 °C. The average maximum cooling rate in the temperature interval from 100 to 0 °C is approximately -20°C/min. A maximum heating rate was not determined but exceeds 100 °C/min. The sample holder is a simple circuit board, which is screwed to the sample heater (compare figure 4.1c). Vacuum-proof thermal paste is used to improve heat transport. Both the sample and a thermal resistor PT1000 are glued to the sample holder with silver paste and are electrically contacted in four-wire geometry, respectively. The resistance of both the sample and the PT1000 are determined by four-terminal sensing (Keithley 2400 source meters). Electrical contacts were realized with a sputter deposition of titanium and gold or with silver paste. Ohmic behavior with linear current-voltage characteristic was observed for both contact methods. A software package based on LabView was developed within the frame of this thesis to automatically control the sample temperature and measure the temperature dependent resistance of the sample.

4.4. Structural characterization

X-ray diffraction

X-ray diffraction (XRD) is a powerful technique used to determine the atomic structure of crystalline materials. In the study of thin films it provides information about structural parameters such as lattice mismatch, phase, preferential orientation of grains, average grain size, strain and crystallinity. Details about the crystallographic structure of solids, XRD methods and XRD analysis can be found in references [249–251].

XRD experiments were performed at the Bergakademie Freiberg (group of Prof. Meyer) at room temperature or as a function of temperature using a Bruker D8 Discover diffractometer in Bragg-Brentano geometry. The diffractometer was equipped with a parabolic multilayer mirror, a two-reflection asymmetrically cut (220) Ge monochromator (Cu K_{α_1} radiation, $\lambda = 1.5406\,\text{Å}$), and an aperture with 0.1 mm width to collimate the beam, as primary optics. The secondary optics consisted of an aperture with variable width to collimate the reflected X-rays and a silicon strip detector, used as a point detector (LynxEye in 0D modus) to increase signal intensity. Temperature-dependent XRD measurements were performed on a tantalum strip-heater. The samples were glued onto the heater with silver paste and a resistance temperature detector was tightly placed on the sample surface outside the X-ray beam path. The temperature was slowly ramped with a heating rate of less than 1 °C. XRD patterns were continuously recorded with a short acquisition time that corresponds to a temperature interval of $\sim 1\,°\text{C}$. The short acquisition time significantly limits the 2θ range of the measurement and the 2θ resolution.

Raman spectroscopy

Raman spectroscopy is based on the inelastic scattering of light by molecules and the corresponding energy shift of the scattered light provides information about the vibrational phonon states of matter. A detailed description of the theory and application of Raman spectroscopy can be found in reference [252].

Raman spectroscopy measurements have been carried out with a confocal Raman microscope (inVia Qontor, Renishaw) using continuous Nd:Yag laser light ($\lambda = 532\,\text{nm}$). The laser light was focused on the sample with a long working distance 50× objective (numerical aperture of 0.5) to a spot size of approximately $2\,\mu\text{m}$ in diameter. A frequency callibration was performed by measuring the TO mode of a standard Si sample ($520\,\text{cm}^{-1}$). All Raman spectra were taken in backscattering configuration with unpolarized excitation and detection. To minimize heating of the VO_2 films by intense laser light[253] the intensity of the light was reduced to $< 10\,\mu\text{W}$, measured at the position of the sample. Temperature-dependent Raman measurements were performed in air using a Linkam TMS heating stage.

Electron microscopy

Scanning electron microscopy (SEM) is an imaging method to obtain nanometer-resolved information about the sample morphology. An energetic electron beam is focused down to a few nanometers and scanned across the sample surface. Primary and secondary electrons, which are emitted due to scattering with the impinging electrons are detected as a function of the electron beam position. Scanning transmission electron microscopy (STEM) and transmission electron microscopy (TEM) directly image the electrons, which are transmitted through a thin specimen of roughly 100 nm. An electron beam of several keV is scanned across the specimen in STEM mode, whereas a stationary parallel electron beam of several hundred keV is used in TEM. Details about the different electron microscopy methods are presented in references [254, 255].

In this thesis SEM, STEM as well as TEM was applied to investigate the morphology, thickness and grain structure of thin VO_2 films and cross-sectional VO_2 lamellae. The electron beam of the dual beam FEI Helios NanoLab 600i was used for SEM and STEM investigations. The gallium ion beam of the same system was employed to prepare TEM specimens via FIB milling. Cross section TEM was carried out by Philipp Schöppe using a JEOL Jem-3010 system at the Otto Schott Institute of Materials Research (FSU Jena).

4.5. Optical methods

Transmittance and reflectance

The temperature dependent optical transmittance and reflectance of VO_2 thin films was measured in collaboration with Dr. Ronny Nawrodt (FSU Jena). The measurements were performed at a wavelength of $4\,\mu$m using a halogen lamp attached to a Shamrock 500 monochromator. The transmitted light was detected with a PbSe detector. A self built heating stage was used to control the temperature during the measurements.

The reflectance in the mid-IR wavelength range of all VO_2 samples was investigated during two research stays in the group of Prof. Federico Capasso (Harvard University) via near-normal incidence measurements using a mid-infrared microscope Hyperion 2000 with a Cassegrain objective (NA = 0.4) attached to a Fourier transform infrared (FTIR) spectrometer (Bruker Vertex 70). Reflectance measurements of the patterned samples were performed with the microscope using an aperture of $50 \times 50\,\mu\text{m}^2$. Temperature dependent reflectance spectra were collected in the middle of the respective pattern while gradually increasing/decreasing the sample temperature in the range between 25 °C and 100 °C at 1 and 5 °C increments. A Linkam TMS heating stage was used to control the temperature during the measurements.

Variable angle spectroscopic ellipsometry

Variable angle spectroscopic ellipsometry (VASE) measures the change in polarization state of a light beam after reflection on the surface of a thin film sample as a function of wavelength and angle of incidence. The optical properties of the film under investigation are determined by comparing a suitable model of the layer system with the experimental values. A detailed discribtion of VASE can be found in reference [256].

In this thesis, the optical properties of intrinsic and irradiated VO_2 films on Al_2O_3 were obtained from ellipsometric data in the UV-VIS-NIR spectral region from 0.73 to 3.34 eV (J.A Woollam VASE) and in the mid-IR from 0.04 to 0.74 eV (J.A Woollam M2000) as a function of temperature. A self built heating stage was used to control the temperature during the measurements. The room temperature ellipsometric measurements were performed at different angles of incidence, whereas all temperature dependent ellipsometric measurements were performed at a fixed angle of incidence of 65 ° and 55 ° for the UV-VIS-NIR and mid-IR spectral region, respectively. The backside of the substrates were roughened to prevent coherent back-reflections. A Kramers-Kronig consistent numerical B-Spline layer model, as implemented in the Woollam CompleteEASE software, was used to determine the complex refractive index of the VO_2 films. The layer thickness and the roughness of the VO_2 films were determined via SEM cross-sections and taken into account in the model. Further, the complex refractive index of the bare sapphire substrate has been obtained via ellipsometric measurements and was incorporated into the model.

Further, the optical properties of undoped and aluminum-doped ZnO substrates were obtained from ellipsometric data using the same experimental set-up. All measurements were performed at room temperature at three different angles of incidence. The complex refractive index of undoped ZnO was determined using an anisotropic single Lorentzian oscillator dielectric function model. The complex refractive index of the AZO layers on ZnO substrates were determined using a model dielectric function comprising a single Lorentzian oscillator taking into account the phonon resonance and a Drude term that describes the free-carrier contribution caused by aluminum doping. The surface roughness was neglected.

All measurements and the data analysis were performed in the group of Dr. Schmidt-Grund (Leipzig University) by Steffen Richter.

Near-field infrared microscope

Scattering-type scanning near-field optical microscopy (s-SNOM) provides access to spectroscopic imaging of the surface of nano-structured materials at a spatial resolution of $< 20\,\mathrm{nm}$. A sharp metallic tip is used to locally probe the electric field in close proximity to the sample surface. Light is scattered from the tip according to its polarizability, which is modified by the presence of the sample according to its dielectric function. By scanning the metallic probe over the sample with an atomic force microscope (AFM) in tapping mode, the s-SNOM signal can be used to simultaneously obtain an image of the sample surface and near-field spectra at wavelengths of choice. A detailed review of the s-SNOM method and experimental results obtained by s-SNOM can be found in references [257, 258] and references therein.

A scattering-type scanning near-field optical microscope with a CO_2 laser operating at $\lambda_0 = 10.9\,\mu\mathrm{m}$ was used to investigate the local contrast between electronic phases of patterned VO_2 samples. A topographic and near field image is simultaneously recorded by lateral scanning of the sample while the tip is oscillating at the tapping frequency.[259] The amplitude modulated scattered light is collected with a CaF_2 lens and focused on a mercury cadmium telluride detector using phase-sensitive, lock-in detection.[259] The scattering amplitude signal demodulated at the third harmonic of the tapping frequency and AFM topography maps obtained in tapping mode were recorded simultaneously at various temperatures ranging from room temperature to 90 °C. The measurements were performed during a research stay within the group of Dimitri N. Basov (University of California San Diego) in collaboration with Alexander Swinton McLeod, Michael Goldflam and Prof. Mengkun Liu (Stony Brook University). Details about the used setup and measuring mode can be found in the PhD thesis of Alexander Swinton McLeod.[260]

5 Ion beam modification - Defect engineering

Energetic ion beams are widely used to modify the electronic and structural properties of solids by introducing impurity atoms into the crystal lattice. Commonly, the inevitable formation of irradiation damage during ion bombardment is described as disadvantageously for ion beam doping and subsequent post-implantation annealing procedures are required. Since the electronic structure of strongly correlated materials is very sensitive to small amounts of lattice defects, this chapter investigates the effect of intentional creation of structural defects and lattice damage ("defect engineering") by ion irradiation on the electrical, optical and structural properties of VO_2 - a prototypical electron-correlated material. Parts of the results presented in this chapter are published in references [44, 159].

5.1. Initial VO_2 film quality

The quality of VO_2 thin films is considered as one of the main challenges in order to achieve a high optical and electrical contrast between the insulating and metallic state.[118,261–263] The IMT characteristics of VO_2 thin films, such as the phase transition temperature, temperature width of the hysteresis and modulation of the optical and electrical properties across the phase transition, critically depends on the phase purity, crystallinity, grain boundaries, grain size distribution, residual strain related to epitaxial mismatch with the growth substrate and defects caused by non-stoichiometry. For the ion irradiation experiments, it is desirable to clearly distinguish all measurable effects on the IMT from defects already present in the as grown samples and to rule out significant sample-to-sample variations. The influence of the latter on the experimental results is minimized in this thesis by either performing in-situ experiments using one and the same sample whenever possible, or by cutting a sample in small pieces and hence, perform experiments with a comparable initial film quality.

5.1.1. Morphology of VO_2 films

In recent years plenty of studies demonstrated the growth of high quality VO_2 thin films on Al_2O_3.[117,118,168,177,224] Therefore, for this work VO_2 films were grown on c-plane Al_2O_3 substrates by the group of Prof. Shriram Ramanthan (Purdue University) using rf magnetron sputtering (compare section 4.1). The morphology of the as grown VO_2 films was investigated by means of SEM, TEM and AFM. Figure 5.1a shows a cross-sectional SEM image of a VO_2 lamella cut out from a thin film using a FIB. Note, that platinum was deposited on top of the VO_2 film prior to lamellar preparation. The interface between VO_2 and Al_2O_3 is flat and smooth. In accordance with the cross-sectional TEM image shown in figure 5.1b, all samples consist of highly oriented columnar grains forming a continuous thin film. In agreement with Kovács *et al.*[264] all grains extend through the entire film and the grain boundaries are parallel to the growth direction. As will be discussed later, epitaxial growth of VO_2 on

Al_2O_3 leads to three equivalent domain orientations[177] forming large angle grain boundaries, which suppresses grain boundary migration during growth. Therefore, the growth mode was identified as epitaxy-stabilized columnar growth.[177,264,265] The film thickness of this sample is approximately 60 nm. Figure 5.1c shows a representative plane-view SEM image of a VO_2 film surface. All samples are found to be rough and exhibit an average lateral grain size on the order of 20-50 nm. The surface roughness was determined by atomic force microscopy (not shown). The root-mean-squared roughness (R_{RMS}) is given by the standard deviation of the heights in the measured sample area and is approximately 5 - 8 nm for all samples shown in this thesis, which is in good agreemend with values obtained by Yang *et al.*[266]. However, much smoother VO_2 films were grown by Fan *et al.*[261] using pulsed laser deposition. They obtained R_{RMS} values of ~ 0.4 nm for approximately 100 nm VO_2 films grown on c-plane Al_2O_3. The difference might be attributed to the higher growth temperature of 600 °C, which enhances self surface diffusion.[267] However, the specific film microstructure may also be dependent on the deposition technique and specific growth conditions.[168] On top of the VO_2 films an approximately 3 nm thin amorphous layer is found, which can be seen in the TEM image in figure 5.1b. According to XPS measurements, this layer mainly consists of V_2O_5 (compare section A.4).

5.1.2. Structural properties of VO_2 films

The initial structural properties of the VO_2 films were examined using XRD. Figure 5.1d shows a coupled θ-2θ XRD pattern taken from an approximately 60 nm thin VO_2 film on c-Al_2O_3. Besides the (0 0 6) and (0 0 12) reflection from Al_2O_3, at room temperature only the $(0\,2\,0)_{\mathrm{M1}}$ and $(0\,4\,0)_{\mathrm{M1}}$ reflection from monoclinic VO_2 are observed at $2\theta \sim 39.9\,°$ and $\sim 86.3\,°$, respectively, indicating phase pure film growth with high preferential orientation. Note, that the small additional reflection at $\sim 65°$ originates from the poly-crystalline tantalum heater. Figure 5.1e compares the in-plane XRD patterns obtained at room temperature and 90 °C, a temperature well above the phase transition temperature. At high temperatures, the diffraction peak at $2\theta \sim 39.8°$ is attributed to the $(2\,0\,0)_{\mathrm{R}}$ reflection of the rutile VO_2 phase, indicating a complete structural phase transition. The slightly lower 2θ value of the $(2\,0\,0)_{\mathrm{R}}$ reflection is attributed to the lattice expansion during the IMT.[132] The FWHMs of the $(0\,2\,0)_{\mathrm{M1}}$ and $(2\,0\,0)_{\mathrm{R}}$ reflections are both 0.22°. One of the main contributions to the reflection broadening is the finite size of the crystalline domains in out-of-plane direction, which is equal to the film thickness. A lower boundary for the domain size L can be estimated using the Scherrer equation: $L = K\lambda/(\Delta(2\theta)\cos\theta)$, where K is a shape factor, which has a typical value of 0.9, $\lambda = 0.154$ nm is the X-ray wavelength, $\Delta(2\theta)$ is the FWHM of the reflection and θ the Bragg angle. An L value of approximately 50 nm was found and is in good agreement with the layer thickness found in SEM/TEM investigations considering the large roughness. However, extended defects and inhomogeneous strain further contribute to the reflection broadening.

Figure 5.1f shows the off-axes coupled θ-2θ XRD pattern obtained at a sample inclination of $\Psi = 44.3°$. Besides the $(1\,1\,\overline{2}\,6)$ reflection from Al_2O_3, broad reflections from $(1\,1\,\overline{1})_{\mathrm{M1}}$ and $(2\,2\,\overline{2})_{\mathrm{M1}}$ are observed at room temperature at approximately $2\theta = 27.7°$ and $57.2°$, respectively. Note, that it was not possible to locate the (1 1 0) and (0 1 1) lattice planes from off-axes scans due to a much lower intensity of these reflections compared to the $(1\,1\,\overline{1})$ reflection

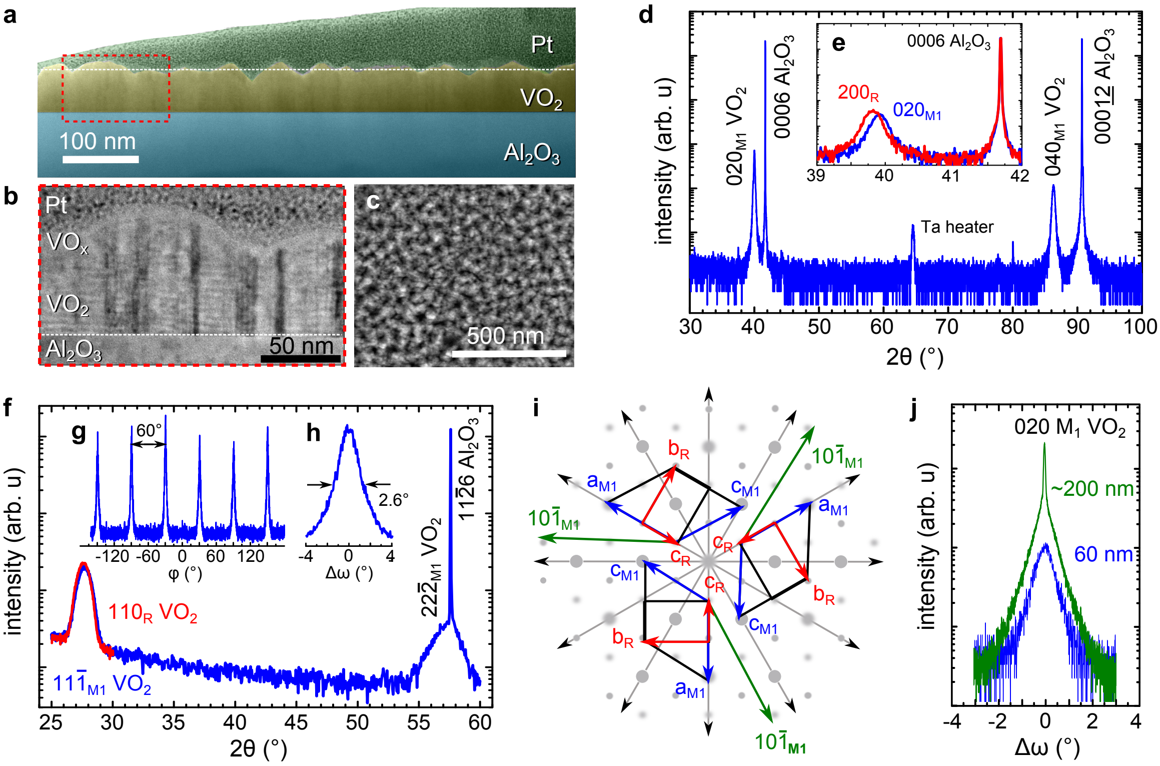

Figure 5.1.: Structural characterization of an approximately 60 nm thin VO_2 film grown on Al_2O_3. SEM cross-section **(a)**, TEM cross-section **(b)** and SEM plane-view image **(c)**. **(d)** In-plane $\theta - 2\theta$ XRD pattern obtained at room temperature. The measurement was conducted on a tantalum heater, causing an additional reflection at approximately 65°. **(e)** Comparison of the XRD pattern obtained at room temperature (blue) and 90 °C (red). **(f)** Off-axis $\theta - 2\theta$ XRD pattern obtained at room temperature (blue) and 90 °C (red) for a sample inclination angle of $\Psi = 44.3°$. ϕ-scan **(g)** and rocking curve **(h)** of the $(1\,1\,\bar{1})_{M1}$ reflection obtained at room temperature. **(i)** Epitaxial variants of the monoclinic and rutile VO_2 unit cell in the b_{M1}- and a_R-plane, respectively, which are caused by the three-fold symmetry of the c-plane of the Al_2O_3 substrate (grey). The corresponding $[1\,0\,\bar{1}]_{M1}$ direction, which matches the b_r-direction of a 120° rotated domain, is highlighted with a green arrow. For clarity, the two-fold symmetry of VO_2 along $[0\,1\,0]_{M1}$ ($[1\,0\,0]_R$) is not considered. **(j)** Rocking curve of the $(0\,2\,0)_{M1}$ reflection of a 60 (blue) and an approximately 200 nm (green) VO_2 film.

(compare ICSD[I] 34033). Hence, no direct determination of the in-plane lattice parameters was possible. Off-axis ϕ-scans were performed in order to elucidate the in-plane epitaxial relation between the VO_2 film and the Al_2O_3 substrate. The appearance of six peaks in the VO_2 $(1\,1\,\bar{1})_{M1}$ ϕ-scan, which is shown in figure 5.1g, can be attributed to the three-fold symmetry of the hexagonal c-plane Al_2O_3 substrate and the intrinsic two-fold symmetry along the VO_2 $[0\,1\,0]_{M1}$ out-of-plane direction. In agreement with references [118, 127, 177, 261, 268, 269] the epitaxial relationship between the monoclinic VO_2 film and the c-plane Al_2O_3 substrate can be concluded as pseudo-six-fold symmetry[177] with two-fold VO_2 $\{0\,2\,0\}_{M1}$ // Al_2O_3 $(0\,0\,0\,6)$ out-of-plane symmetry and three-fold VO_2 $[2\,0\,\bar{2}]_{M1}$ // Al_2O_3 $<1\,1\,\bar{2}\,0>$ in-plane orientation. The three equivalent domains of VO_2 on top of c-plane Al_2O_3 are illustrated in figure 5.1i. Both the monoclinic M1 and rutile phase with their corresponding in-plane lattice vectors given in blue and red are shown, respectively. For clarity, all domains are depicted with an offset from the Al_2O_3 c-plane center. Note, that the $[1\,0\,\bar{1}]_{M1}$ lattice direction of each domain

---

[I] The Inorganic Crystal Structure Database (ICSD) lists reference patterns for most of the inorganic crystal structures.

is parallel to the b_R axis of a 120° rotated VO_2 domain. This explains the occurrence of the $(1\,1\,0)_\mathrm{R}$ at 90 °C for the same sample orientation at which the $(1\,1\,\bar{1})_\mathrm{M1}$ reflection was found (see figure 5.1f). Note, that Zhou *et al.*[270], Yang *et al.*[265] and Moatti *et al.*[98] concordantly observed the coexistence of different domain orientations each having three growth plane equivalents using high-resolution TEM imaging.

Lattice mismatch between the substrate and rutile VO_2 lattice at the growth temperature introduces biaxial strain in the VO_2 thin films.[164,166,266,269,271,272] However, it has been demonstrated that VO_2 films grow in a strain-relaxed state, in which strain is released through the formation of geometrical dislocations.[98,269,272] Remaining strain in the film is due to a slight mismatch of the film and substrate thermal expansion coefficients upon cooling from the growth temperature. The deviation of the observed lattice parameter $b_\mathrm{M1} = 4.517\,\text{Å}$, deduced from the $(0\,2\,0)_\mathrm{M1}$ reflection, from its theoretical value $\mathrm{b}^*_\mathrm{M1} = 4.526\,\text{Å}$ [132] is used to quantify the out-of-plane strain:[269]

$$\eta_a = \frac{b_\mathrm{M1} - b^*_\mathrm{M1}}{b^*_\mathrm{M1}}. \tag{5.1}$$

Note, that the subscript of η indicates the lattice direction in the rutile system. In agreement with Théry *et al.*[269], a value of $\eta_a = -0.2\%$ indicates that VO_2 films grown on c-plane Al_2O_3 are slightly compressively strained in out-of-plane direction. Lattice distortions (mosaicity) resulting from geometric dislocations are confined to a rather thick VO_2 layer (distorted layer) at the Al_2O_3 interface. This is especially evident in figure 5.1j, which compares the rocking curves of the $(0\,2\,0)_\mathrm{M1}$ reflection of a 60 and of an approximately 200 nm thin VO_2 film given in blue and green, respectively. The rocking curve of the 60 nm film is broad with a FWHM of $\sim 0.8°$, whereas the rocking curve of the 200 nm film comprises a comparable broad peak with FWHM of $\sim 1.0°$ superimposed with a narrow peak with FWHM of $\sim 0.1°$. The shape of the latter rocking curve is typical for a thin film in which random lattice distortions are confined into a layer close to the film/substrate interface.[269,272,273] Since this distorted layer accomodates the lattice and thermal expansion mismatch, the near-surface layer is typically relaxed with much lower defect density.[269,273] The thickness of the distorted and relaxed layer can be roughly estimated from the ratio between the integrated areas of the two peaks. The distorted and relaxed layer thickness is ~ 120 and ~ 80 nm, respectively, which is in good agreement with values obtained by Chen *et al.*[273]. Random lattice distortions usually lead to heterogeneous in-plane strain. This might be a main reason for the broad $(1\,1\,\bar{1})_\mathrm{M1}$ and $(1\,1\,0)_\mathrm{R}$ reflections (compare figure 5.1f) and a very broad peak observed for the rocking curve of the $(1\,1\,\bar{1})_\mathrm{M1}$ reflection (compare figure 5.1h).

In summary, the VO_2 films used in this thesis are phase pure, highly oriented with six-fold domain symmetry and almost completely relaxed. Strain relaxation is achieved by the formation of dislocations, which locally distort the VO_2 films and thus leading to the observed mosaicity.

5.1.3. Electrical properties of VO_2 films

The initial electrical characterization of the VO_2 films was performed using 4-point resistance and Hall-effect measurements. Figure 5.2a shows the temperature-dependent resistivity (ρ) during a heating and a cooling cycle, respectively. Upon heating and cooling the resistivity shows a steep transition from insulating to metallic behavior and vice versa with a narrow hysteresis loop. The sample was cycled several times through the IMT without noticable differences in

$\rho(T)$. The resistivity of the insulating (semiconducting) phase of VO_2 can be well described by activated behavior characteristic for an intrinsic semiconductor: $\rho \propto exp\{E_a/(k_bT)\}$, where E_a is an activation energy, typically on the order of half the band gap energy for non-degenerated semiconductors, and k_b is the Boltzmann constant. The activation energy was determined by fitting experimental data in the temperature interval from −20 to +20 °C and is $\sim 0.19\,\mathrm{eV}$, which is in good agreement with previous reports.[112,274–276] However, the activation energy is smaller than half the the band gap energy of 0.6 eV. This might be an indication for the presence of defects creating shallow donor- and acceptor-like states within the band gap region. Zhong *et al.*[277] pointed out, that low activation energies are obtained because the contribution of small polaron hopping is neglected. At high temperatures in the metallic phase, the resistivity is well described by a linear T dependence: $\rho = \rho_0(1 + \alpha T)$, where α is a temperature coefficient and ρ_0 is a residual resistivity. To prevent any sample oxidation, resistivity measurements were only performed up to 90 °C. Therefore, the value of $\alpha = 6 \times 10^{-3}\,\mathrm{K}^{-1}$ was taken from literature[278] and ρ_0 was estimated from the resistivity values at the highest temperatures to be $\sim 1.3 \times 10^{-4}\,\Omega\mathrm{cm}^{-1}$, which is in good agreement with previous reports.[278] The obtained $\rho(T)$ model curves were extrapolated to high and low temperatures, respectively, as shown in figure 5.2a by dashed lines.

The following parameters are used to describe the IMT characteristics and are indicated in figure 5.2a: The critical temperature $T_C^{h,c}$ at which the phase transition occurs for the heating (h) and cooling cycle (c) is defined as the minimum of the logarithmic derivative of the resistivity $d(log\rho)/dT$, respectively, as shown in the inset of figure 5.2a. The critial temperature of the IMT T_C is the mean value of T_C^h and T_C^c. The hysteresis width W is the difference between T_C^h and T_C^c. Note, that in polycrystalline VO_2 films the phase transition temperature locally varies, caused by heterogenous strain and a non-uniform distribution of lattice defects. Thus, T_C describes the distribution of phase transition temperatures. The phase transition width ΔT, which is the temperature interval in which insulating and metallic phase coexist, is estimated from the appearance and disappearance of a resistivity hysteresis marked with arrows in figure 5.2a. The resistivity ratio $\rho_{\mathrm{M1}}/\rho_{\mathrm{R}}$ is defined as the ratio of the resistivities of the insulating M1 phase $\rho_{\mathrm{M1}}(T_C)$ and of the metallic R phase $\rho_{\mathrm{R}}(T_C)$ both extrapolated to T_C.

T_C^h and T_C^c were determined by gaussian fitting of $d(\log\rho)/dT$ to be 74.1 and 66.7 °C, respectively. This results in a T_C of 69.2 °C, which is slightly higher than the reported value for bulk VO_2. This might be attributed to residual strain in the VO_2 film, which was observed using XRD. The hysteresis width was found to be $W = 7.4\,°\mathrm{C}$, which is in good agreement with values reported for VO_2 on c-plane Al_2O_3.[276,278] A relatively large value of $\Delta T = 45\,°\mathrm{C}$ can be attributed to a local variation of the phase transition temperature as described above. The resistivity ratio across the IMT is on the order of 10^3 indicating a high film quality. The free carrier concentration N_c and carrier mobility μ_H was determined by Hall effect measurements (not shown). With an almost constant low carrier mobility of $\mu_H \sim 0.1\,\mathrm{cm^2V^{-1}s^{-1}}$ in both phases, which is in accordance with previously reported Hall effect measurements,[276,279] the increase in N_c from $\sim 3 \times 10^{19}$ to $\sim 3 \times 10^{22}\,\mathrm{cm^{-3}}$ almost entirely accounts for the decrease in electrical resistivity. Taking into account the vanadium concentration in VO_2: $N_V = 3.3 \times 10^{22}\,\mathrm{cm^{-3}}$, approximately one electron per vanadium atom contributes to the electrical transport in the metallic phase.

In summary, although the initial structural properties lead to a broadening of the phase transition of the VO_2 thin films, a resistivity change of three orders of magnitude in these samples is promising to observe the effects of ion irradiation on the IMT.

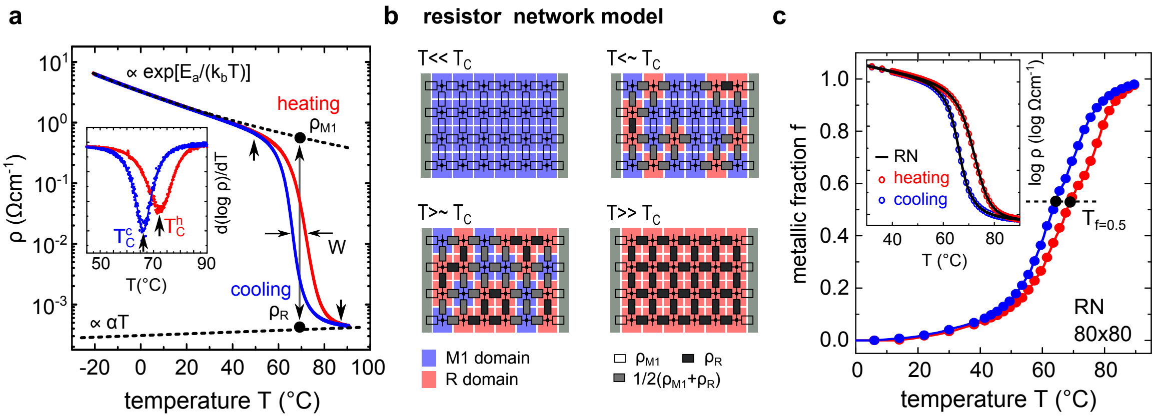

Figure 5.2.: Evaluation of electrical properties of a VO_2 thin film. **(a)** Temperature-dependent resistivity ρ for a heating and cooling cycle, respectively. Dashed lines are fits to the resistivity of the insulating and metallic phase, respectively. The inset shows the derivative of the logarithmic resistivity as a function of temperature. The critical temperature $T_C^{h,c}$ of the heating (h) and cooling (c) cycle, the hysteresis width W, and the resistivity ratio $\rho_{\mathrm{M1}}/\rho_{\mathrm{R}}$ are determined from electrical measurements. **(b)** Schematic drawing of the resistor network model of VO_2. Insulating (blue) and metallic domains (red), which coexist in the vicinity of the IMT, are modeled by different resistors in a $m \times n$ resistor network, according to their adjacent domains. **(c)** Metallic fraction as a function of temperature obtained from fitting the resistivity of an 80×80 resistor network model to the experimentally determined resistivity given in (a). The inset compares the experimentally determined and calculated resistivity of the heating and cooling cycle, respectively.

5.1.4. Resistor network model

It is well established that in thin VO_2 films the metallic R and insulating M1 phase coexist in the vicinity of the IMT.[63,278,280] In a microscopic picture of VO_2 each individual domain can be considered as a small region of single-crystalline VO_2 with a sharp IMT. Caused by heterogeneous strain and a non-uniform distribution of defects, the IMT of all domains does not proceed simultaneously. It is more likely, that the phase transition temperatures are distributed over a certain temperature interval. Thus, on a macroscopic scale, the IMT is not a single well-defined transition but smeared out over a temperature range. Unfortunately, no direct determination of the metallic phase fraction from resistance measurements is possible, because of the no-one-dimensional arrangement of metallic and insulating domains.[274] Following an approach of Dai *et al.*[281] a thin VO_2 film can be modeled as a binary composite consisting of randomly distributed metallic and insulating domains and the resistivity of the composite can be determined using a resistor network model. Such a resistor network model of VO_2 is schematically depicted in figure 5.2b. For temperatures much smaller (higher) than the critical temperature the entire film consists of insulating (metallic) domains, represented by blue (red) squares in a lattice arrangement of $m \times n$ domains. In the vicinity of the phase transition metallic and insulating domains are randomly distributed according to the phase fraction $f(T)$ of metallic domains at the respective temperature. Between each pair of adjacent domains a resistance is assigned whose value is determined by the neighboring domains. The value is $\rho_{\mathrm{M1}}(T)$, $\rho_{\mathrm{R}}(T)$, or $1/2[\rho_{\mathrm{M1}}(T) + \rho_{\mathrm{R}}(T)]$ for purely insulating, purely metallic, or mixed domains, respectively. The values of $\rho_{\mathrm{M1}}(T)$ and $\rho_{\mathrm{R}}(T)$ are obtained from fitting experimental resistivity curves at temperatures far away from the IMT, as discussed previously. The only free parameter in this model is the metallic fraction $f(T)$. A computer code based on the mesh-current method[281] was developed and used in this thesis to determine the resistivity of the resistor network (see also appendix A.7).

Figure 5.2c shows the metallic fraction $f(T)$, which was obtained by fitting the resistor model to the experimentally determined resistivity of the VO$_2$ film given in figure 5.2a. For each temperature a 80×80 resistor network with randomly distributed metallic domains was solved. The number of metallic domains (metallic fraction) was varied individually for each temperature to match the experimentally obtained resistivity values (compare inset in figure 5.2c). The metallic fraction increases continuously from zero to unity over a broad range of temperatures, indicating the temperature range of phase-coexistence. The observed hysteresis of f is caused by the hysteresis of individual VO$_2$ domains. Note, that a metallic fraction of $f = 0.5$ is obtained in the heating and cooling cycle at $T = 67.8$ and $63.5\,°\mathrm{C}$, respectively, which is significantly smaller than the value of $T_C^{h,c}$ determined previously from resistivity measurements. Consequently, $T_C^{h,c}$ is not equal to the temperature, at which half of the domains are in the metallic state. This is especially critical when the structural and electronic phase transition temperatures, determined with different methods, are compared. For most of the methods, such as resistivity, reflectance and transmittance measurements, no linear dependence of the observable quantity with f is expected, whereas structural methods like XRD directly probe f. The resistor network model of VO$_2$ is very useful to describe changes of the IMT properties caused by modification of individual domains, such as stress induced pattern formation, or patterning by ion irradiation.

5.1.5. Optical properties of VO$_2$ films

The optical properties of as grown VO$_2$ films were investigated using temperature-dependent spectroscopic ellipsometry, reflectance and transmittance measurements. As an example, figure 5.3a shows the mid-infrared reflectance of an approximately 100 nm thin VO$_2$ film grown on Al$_2$O$_3$ measured for various temperatures across the IMT. At low temperatures VO$_2$ is in the insulating state and basically transparent. Thus, the reflectance spectrum is dominated by the onset of the reststrahlen band of Al$_2$O$_3$ at approximately $11\,\mu$m (blue curve in figure 5.3a). At high temperatures VO$_2$ is in the metallic state and highly reflective (brown curve in figure 5.3a). As the temperature is increased in the vicinity of the IMT of the VO$_2$ film, the reflectance changes monotonically in the mid-infrared wavelength range up to approximately $10\,\mu$m, and non-monotonically in the wavelength range above. A point of minimal reflectance with $R = 0.005$ occurs at a wavelength of $\lambda_0 = 11.3\,\mu$m for $T_{\mathrm{min}} = 70\,°\mathrm{C}$, which is in perfect agreement with previous calculations (compare section 3.5). Taking into account that Al$_2$O$_3$ is opaque and highly reflective at this wavelength, the reflectivity of the VO$_2$ film can be tuned from a highly reflective state ($R = 0.55$) at room temperature into a near-perfect absorption state ($R \sim 0, T = 0$) in the vicinity of the IMT back into a highly reflective state ($R = 0.64$) at high temperatures above 90 °C (see figure 5.3c). The reflectance minimum is caused by strong interference effects of the ultra-thin VO$_2$ film in its transitional state on highly reflective Al$_2$O$_3$ (compare section 3.5).

For comparison, figure 5.3b shows the reflectance of the VO$_2$ film as a function of the temperature at fixed wavelengths of $\lambda_0 = 4$ and $10\,\mu$m. Similar to the evaluation of electrical data, the reflectance change can be used to obtain characteristic parameters of the IMT of VO$_2$. Here, the critical temperature $T_C^{h,c}$ at which the phase transition occurs for the heating (h) and cooling cycle (c) corresponds to the maximum of the reflectance derivative (compare inset in figure 5.3b). The amplitude of the IMT is defined as the reflectance difference in the insulating and metallic state: $\Delta R = R(100\,°\mathrm{C}) - R(25\,°\mathrm{C})$. At a wavelength of $4\,\mu$m the following

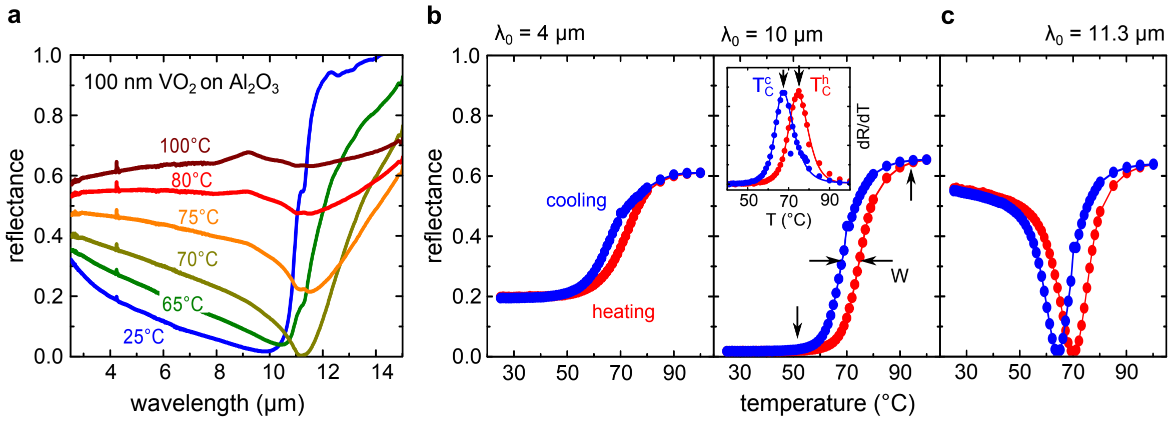

Figure 5.3.: (a) Reflectance of an approximately 100 nm thin VO_2 film grown on Al_2O_3 for various temperatures across the IMT. For clarity only spectra obtained in the heating cycle are shown. **(b,c)** Temperature-dependent reflectance of the VO_2 sample at a fixed wavelength of $\lambda_0 = 4$, 10 (a), and 11.3 μm (b). Values are obtained from the heating (red) and cooling (blue) cycle, respectively. The critical temperature of the IMT is obtained from the maximum of the corresponding reflectance derivative (inset).

values were obtained: $T_C^h = 72.5\,°C$, $T_C^c = 62.5\,°C$, $W = 10\,°C$, and $\Delta R = 0.41$. In contrast, evaluation of those parameters at 10 μm yields: $T_C^h = 74.6\,°C$, $T_C^c = 67.4\,°C$, $W = 7.2\,°C$, and $\Delta R = 0.63$. The considerable wavelength dependence of $T_C^{h,c}$ is caused by the phase coexistence of insulating and metallic domains and a non-linear relation between the effective reflectance and metallic fraction of VO_2. Nonetheless, the critical temperatures obtained from reflectance measurements are in good agreement with values previously determined from electrical measurements, especially when taking into account that different samples and different heating stages were used.

Note, that in agreement with previous calculations the critical temperature and the temperature of minimal reflectance slightly differ, because minimal reflectance occurs at a fixed metallic fraction across the IMT, rather than at a fixed temperature (compare section 3.5).[44]

5.2. Ion irradiation: In-situ electrical measurements

In-situ measurements of the resistance during ion bombardment and subsequent temperature-dependent resistance measurements were used to investigate the effects of ion irradiation on the IMT of VO_2 thin films. Figure 5.4a shows the resistance of a ~ 100 nm VO_2 thin film on c-Al_2O_3 that was continuously measured during irradiation with 75 keV Ar^+ ions at a constant temperature of $T = -30\,°C$ as a function of ion fluence N_I. Argon was chosen because it is a noble gas and is thus not chemically incorporated in the VO_2 lattice, enabling the study of the effects of irradiation induced lattice defects separate from any impurity doping.[44] The ion flux was kept as low as possible and constant at $\Phi_I^1 = 6 \times 10^{10}\,\mathrm{cm^{-2}s^{-1}}$ for low ion fluences up to $N_I = 2 \times 10^{14}\,\mathrm{cm^{-2}}$ and $\Phi_I^2 = 1.3 \times 10^{12}\,\mathrm{cm^{-2}s^{-1}}$ for higher N_I to prevent any heating effects caused by the ion beam. The resistance of VO_2 during irradiation shows a distinct minimum at $N_I \sim 7.5 \times 10^{13}\,\mathrm{cm^{-2}}$ ($n_{\mathrm{dpa}} \sim 0.1$) and two fluence regions can be clearly distinguished: I) For low ion fluences the resistance decreases, which is mainly attributed to the formation of isolated point defects. II) For high ion fluences the resistance increases, which is associated with point defect accumulation, defect cluster formation, and amorphization of the VO_2 lattice.

In this thesis only the effects of irradiation in the ion fluence region I are presented. Amorphous films of VO_2 do not feature an IMT.[44,207] However, ion irradiation in the ion fluence region II at elevated temperatures suppresses the amorphization and leads to a metalization of VO_2 caused by preferential out-diffusion of displaced oxygen atoms (see appendix A.5), which is in perfect agreement with high temperature and ultra-low oxygen partial pressure annealing.[159]

Ion beam induced damage formation

To investigate the formation of lattice defects in VO_2 caused by ion irradiation RBS in channeling geometry (RBS/C) was used. Several 100 nm thin VO_2 films on Al_2O_3 were irradiated with 75 keV Ar^+ in the fluence range from $N_I = 3 \times 10^{13}$ to $5 \times 10^{15}\,\mathrm{cm}^{-3}$ at room temperature. RBS/C measurements using 1.4 MeV He^+ ions were conducted shortly after irradiation without any prior temperature treatment of the samples. Figure 5.4b shows the aligned RBS spectra and a typical random spectrum of the implanted samples. The aligned spectra were obtained by carefully orienting the samples with the b_{M1} axis parallel to the He^+ ion beam. The backscattering yield related to vanadium atoms within the VO_2 film (vanadium signal) is clearly separated from the backscattering yield related to oxygen and aluminum atoms (oxygen and aluminum signal, respectively) within the VO_2 film and surface layer of the Al_2O_3 substrate, respectively. Flattened edges at the low energy side of the vanadium signal and at the high energy side of the aluminum signal measured in random direction are characteristic for rough films.[282] The oxygen signal of the VO_2 film is superimposed with the aluminum signal of the substrate, because of the smaller kinematic factor of oxygen, and not clearly separated from the oxygen signal of the substrate. Therefore, only the vanadium signal was further investigated.

The vanadium signal extends from 1.02 to 0.94 MeV corresponding to the VO_2 film thickness. The aligned RBS spectrum of the intrinsic VO_2 film shows a distinct vanadium surface peak at 1.02 MeV and a very low backscattering yield across the entire film, indicating a low number of structural defects. The backscattering yield in aligned direction increases with increasing N_I, caused by the displacement of vanadium atoms from their lattice sites into the channels formed by vanadium atom rows, which increases the probability of large angle scattering events. The number of displaced lattice atoms is approximately related to the minimum yield $X_{\min} = Y_{\text{aligned}}/Y_{\text{random}}$, which is the ratio between the backscattering yield Y in aligned and random direction.[245] $X_{\min}$ was evaluated in a $30\,nm$ depth interval centered at the damage peak that appears behind the surface peak for small ion fluences. Typically, single crystals or perfectly matched epitaxial thin films exhibit a $X_{\min}$ value of 0.02-0.03 [283]. The $X_{\min}$ value of the intrinsic VO_2 film was found to be 0.05 indicating a very low density of defects. Moreover, the slightly higher value of $X_{\min}$ could also be fully explained by the spread of domain orientations (mosaicity) and the amount of grain boundaries.

A comparison of $X_{\min}$ and R measured as a function of N_I is given in figure 5.4c. In region I $X_{\min}$ is almost constant with a slight increase indicating that only a small amount of point defects is formed, whereas in region II a strong increase of $X_{\min}$ is observed. This increase can be attributed to a large number of point defects and the formation of defect clusters, extended defects and amorphous regions. From point of RBS the VO_2 film is completely amorphized ($X_{\min} = 1$) for fluences above $N_I = 1 \times 10^{15}\,\mathrm{cm}^{-2}$. Note that doping of VO_2 by ion implantation to a concentration of at least 1 at.% would require an ion fluence of roughly $N_I = 5 \times 10^{15}\,\mathrm{cm}^{-2}$, which is far beyond the amorphization fluence. However, the doping

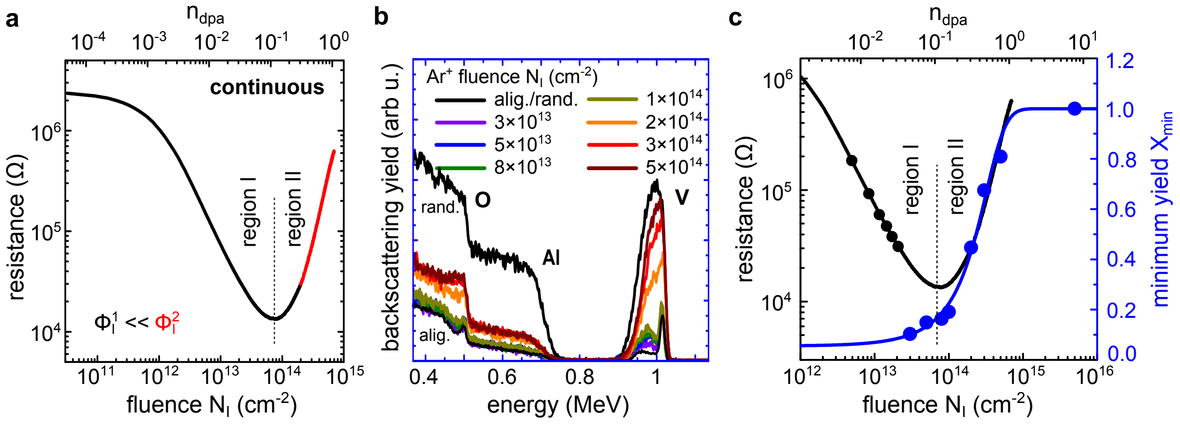

Figure 5.4.: (a) Continuous in-situ measurement of the resistance of a ∼ 100 nm VO_2 thin film on c-Al_2O_3 during 75 keV Ar^+ irradiation at $T = -30\,°C$. The flux was kept as low as possible and constant at $\Phi_I^1 = 6 \times 10^{10}\,cm^{-2}$, and $\Phi_I^2 = 1.3 \times 10^{12}\,cm^{-2}$, for fluences lower and higher than $N_I = 2 \times 10^{14}$, respectively. Two fluence regions can be distinguished: I) reduction of the resistance due to point defect formation. II) increase of the resistance due to defect accumulation and amorphization. **(b)** 1.4 MeV RBS spectra of VO_2 thin films, which were irradiated with 75 keV Ar^+ at room temperature to various ion fluences, measured along the b_{M1} direction. A random spectrum (black line) is given for comparison. **(c)** Resistance and minimum yield X_{min} as a function of the ion fluence N_I.

concentrations reached in region I are very small and do not significantly effect the IMT by electronic doping (compare section 2.1.4) and all occurring effects can be primarily attributed to lattice disorder.

Successive ion irradiation

The effect of ion irradiation on the temperature-dependent electrical properties of VO_2, especially the IMT, can only be investigated when the continuous ion irradiation is interrupted at a certain ion fluence. At that fluence a subsequent thermal cycle has to be performed to determine the phase transition temperature. Figure 5.5a shows the resistance R of an approximately 100 nm thin VO_2 film on Al_2O_3 measured in-situ during the irradiation in six successive steps of $N_I = 2 \times 10^{13}\,cm^{-2}$ each. Before ion irradiation and between all irradiation steps two consecutive heating cycles were conducted, respectively. The temperature in the first cycle reached a maximum value of approximately 93 °C and in the second cycle 90°C. The slightly lower maximum temperature was chosen to minimize annealing in the second cycle. The inset of figure 5.5a shows the temporal dynamics of R during and after the first irradiation step. As expected, R decreases due to defect formation during ion irradiation. After the beam is shut off, only a slight increase of R is observed indicating that most of the defects that remain in the film are stable at $-30\,°C$. Note that the formation of stable irradiation defects often proceeds via a dynamic annealing process, involving migration, recombination and clustering of mobile point defects during irradiation.[284] However, strong annealing of irradiation defects, which manifests in a considerable resistance increase, is observed during the first heating cycle after each irradiation step. This results in a large resistance jump between successive irradiations, as shown in figure 5.5a.

To account for the strong annealing effect and to determine a reasonable number of displaced lattice atoms, which remain in the VO_2 film after thermal cycling, an effective ion fluence N_I^* is assigned, as shown in figure 5.5b. For this purpose, the resistance at a temperature of $-30\,°C$ after each thermal cycling was compared with the in-situ resistance measured during

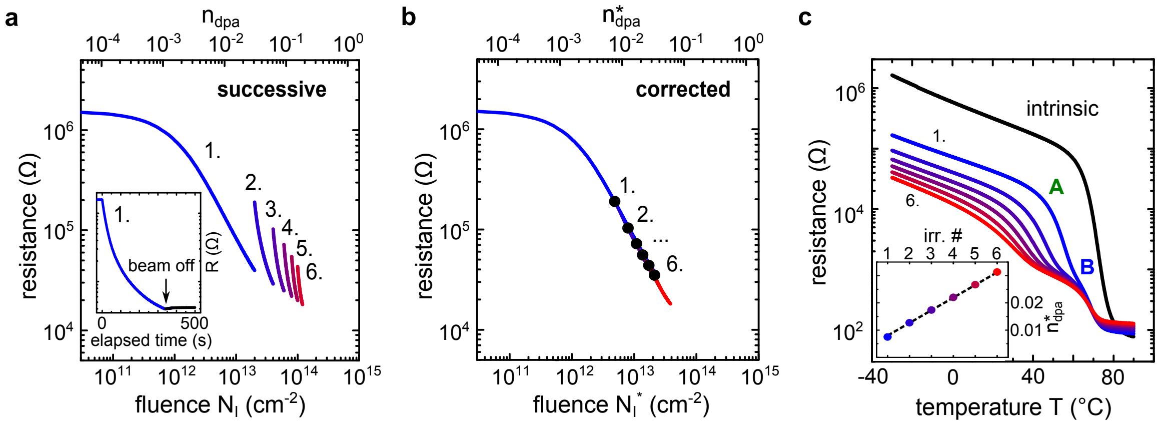

Figure 5.5.: (a) Successive in-situ measurement of the resistance R of a VO_2 thin film during 75 keV Ar^+ irradiation at $T = -30°C$. The irradiation was performed in steps of $N_I = 2 \times 10^{13}$ cm^{-2}. After each irradiation step, a temperature-dependent resistance measurement (thermal cycling) was performed. The inset shows the temporal dynamics of R during and after the first irradiation. **(b)** Same as (a) with effective ion fluence N_I^* (effective number of displacements per lattice atom n_{dpa}^*) corrected for annealing effects during thermal cycling. **(c)** Temperature-dependent resistance measurements of intrinsic and irradiated VO_2 after each irradiation step [compare (a)] For clarity, only the second of two heating cycles is shown, respectively. The inset shows n_{dpa}^* after each irradiation step and the subsequent thermal cycling (irr. #).

the corresponding irradiation step. The ion fluence, at which the same resistance value is found, is assumed to be N_I^*. For each irradiation and thermal cycling step ΔN is the fluence, whose effect is completely annealed: $\Delta N = N_I - N_I^*$. In this case an almost constant value of $\Delta N = (1.6 \pm 0.1) \times 10^{13}$ cm^{-2} was found for each irradiation step. That is, assuming that only point defects are created, roughly 80% of all defects are annealed during the thermal cycling. Interactions between isolated point defects can create defect complexes that have a lower formation energy than isolated point defects.[285] These defect complexes might have a different effect on the resistance. However, the effective number of displacements per lattice atoms n_{dpa}^* is roughly estimated using N_I^* and SRIM simulations. The value of n_{dpa}^* is estimated for the maximum of the simulated defect distribution (compare 2.3.1): $n_{\mathrm{dpa}}^* = N_0 N_I^* / N_{\mathrm{displ}}$. Here, n_{dpa}^* ranges from 0.007 to 0.031, as shown in the inset of figure 5.5c. Note that as a consequence of assumptions made for the SRIM simulations the value of N_{displ} and thus the value of n_{dpa}^* is uncertain and only a qualitative measure (compare 2.3.1).

Figure 5.5c shows the temperature-dependent resistance of the intrinsic and irradiated VO_2 film measured during the second heating cycle before ion irradiation and after each of the six irradiation steps. Strikingly, the resistance after each of the irradiation steps displays two distinct phase transitions A and B. The phase transition temperature of the former significantly decreases with increasing ion fluence, whereas the phase transition temperature of the latter is fixed at a certain temperature. The two phase transitions can be attributed to irradiated VO_2 regions located between the electrical contacts (region A) and small regions beneath the edges of the electrical contacts that contribute to the measured resistance but are shadowed from the ion beam (region B, see inset in figure 5.6a). The total resistance of the film can be written as resistances of region A and regions B connected in series: $R = qR_{\mathrm{A}} + 2(1-q)R_{\mathrm{B}}$, where q is the area fraction of region A with respect to the total area that contributes to the electrical transport. To decompose the contributions of region A and B, the resistor network model described previously was used, and the results are exemplarily shown in figure 5.6a for the resistance measured after the fifth irradiation ($n_{\mathrm{ndpa}}^* = 0.027$). Although a q value

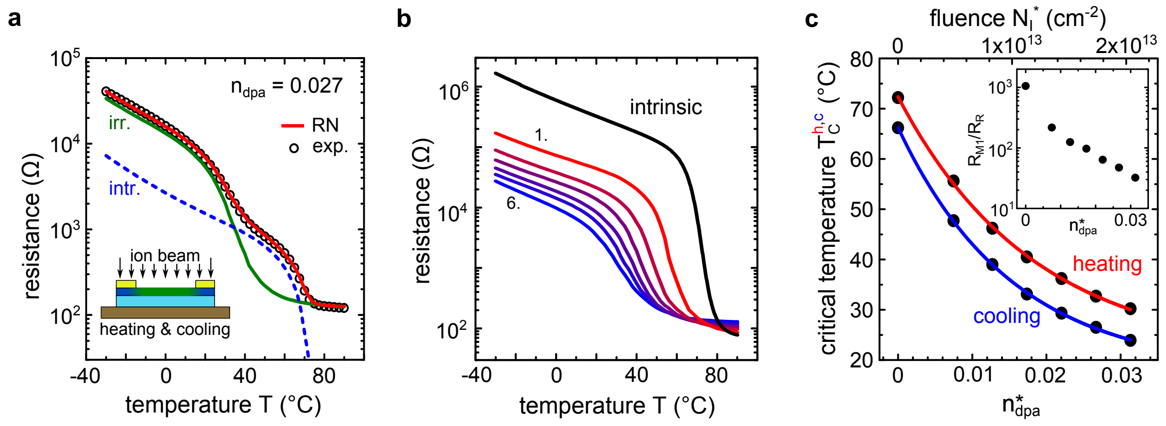

Figure 5.6.: Evaluation of the in-situ temperature-dependent resistance measurements. **(a)** Decomposition of the measured resistance into a fraction A corresponding to irradiated VO_2 (irr.) and a fraction B corresponding to parts of the VO_2 film covered by electrical contacts (intr.) using the resistor network model of VO_2. As an example, the evaluation of the resistance in the second heating cycle after the fifth irradiation ($n^*_{\text{dpa}} = 0.027$) is shown. **(b)** Extracted temperature-dependent resistance of the irradiated part of the VO_2 film for all irradiation steps. **(c)** Critical temperature $T_C^{h,c}$ of the heating (h) and cooling cycle (c) as a function of n^*_{dpa}. The inset shows the resistance ratio $R_{\text{M1}}/R_{\text{R}}$ across the IMT at T_C^h of intrinsic and irradiated VO_2. Error bars are of the size of the symbols.

of 99.8% was found, the high resistance in the insulating state of intrinsic VO_2 compared to the resistance of the metallic phase of irradiated VO_2 and a significant shift of the phase transition temperature of irradiated VO_2 lead to the appearance of the IMT of intrinsic VO_2 (compare dashed blue and solid green line in figure 5.6a).

The extracted temperature-dependent resistance of irradiated VO_2 is shown in figure 5.6b and the critical temperature $T_C^{\text{h,c}}$ determined for the heating (h) and cooling cycle (c) is given in figure 5.6c, respectively. Ion irradiation in the fluence region of point defect formation and subsequent thermal annealing to roughly 90 °C leads to a strong decrease of T_C. This effect is a result of irradiation damage, that is, the displacements of both oxygen and vanadium atoms from their lattice sites by nuclear collisions that lead to the formation of interstitial-vacancy complexes (Frenkel pairs) at low ion fluences.[44] The critical temperature is reduced by a combination of local strain induced by lattice disorder, and an increased number of vacancies, interstitials and defect complexes formed during annealing. For example the formation of oxygen vacancies introduces electrons, which are trapped by V^{4+} sites forming lower valence states $V^{(4-n)+}$, which introduce multiple donor levels below the conduction band.[286] Charge redistribution among the nearest neighboring vanadium atoms caused by an increasing number of localized defects and the presence of free charge carriers greatly effects the band structure of VO_2.[84,287] However, compressive strain is also known to a decrease the band gap by orbital shifting.[100,124] The narrowing of the band gap and the increased number of free carriers is also evident from the lowering of R and the reduction of the slope of $logR$ in the insulating state (see figure 5.6b). Further, ion irradiation leads to an increasing value of R in the metallic state, indicating that the mobility of free-carriers decreases as a result of an increasing number of lattice defects shortening the electronic mean free path length.[211,212]. The broadening of the phase transition width δT for increasing ion fluences can be attributed to the Gaussian depth distribution of lattice defects.[44]

The decrease of T_C is non-linear with n^*_{dpa} and one percent of displaced lattice atoms already leads to a decrease of T_C by $\Delta T_C = -22\,°C$ (see figure 5.6c). Thus, when comparing the number of displaced lattice atoms with the number of incorporated atoms for ion beam doping, lattice disorder is as effective in reducing T_C as doping with tungsten, which typically achieves ΔT_C values of $-20\,°\text{C/at.\%}$.[95,170] For practical applications the resistivity ratio is of importance. Although ion irradiation leads to a decrease of $R_{\text{M1}}/R_{\text{R}}$, a resistivity ratio of 32 is still present for the highest ion fluence used (see inset figure 5.6c). For this fluence the phase transition temperatures of irradiated and intrinsic VO_2 are separated by more than 40 °C. Thus, defect engineering by means of ion irradiation is a promising method to fabricate inherently flat VO_2 samples with locally controllable phase transition temperatures.

5.3. Effect of the defect density on the IMT of VO_2

Ion irradiation with an ion fluence on the order of $10^{13}\,\text{cm}^{-2}$ and ion energies in the range of 10-500 keV corresponds to the incorporation of less than 0.01 at% of the ion species used. At those concentrations no significant effect of electronic doping on the IMT of VO_2 is expected (compare section 2.1.4). However, the amount and local density of defects critically depends on the ion mass m_I. Although the amount of defects created can be adjusted by the choice of the ion fluence, the density of defects within a single collision cascade is fixed by the ion species and ion energy. To compare the effect of ion irradiation with different ions on the IMT of VO_2, the successive ion irradiation experiment described in the previous section was repeated with 12 representative ion species with ion masses m_I ranging from 14 (N) to 209 amu (Bi). The ion energy E_0, ion fluence N_I, and ion flux Φ_I were carefully adjusted to ensure a comparable irradiation depth with emphasis on the formation of a comparable amount of lattice defects created with a comparable rate.

The ion energy E_0 required to implant the different ion species into VO_2 at a given depth of $R_P = 50\,\text{nm}$ was calculated using SRIM full-cascade simulations[204] to ensure comparable implantation profiles (see figure 5.7a). This also ensures comparable defect distributions centered at a depth of approximately 33 nm (see inset in figure 5.7a). Note, that with increasing m_I the FWHM of both distributions slightly decrease. The number of displaced lattice atoms per unit depth in the maximum of the defect distribution N_{displ} was simulated for each combination of E_0 and m_I, as shown in figure 5.7a (green points, right scale). N_{displ} follows the same mass dependence as E_0. To ensure the formation of a comparable amount of lattice defects the ion fluence $N_I(m_I)$ used for each ion species was determined from the n_{dpa} value obtained for an Ar^+ ion fluence of $N_I(m_{\text{Ar}}) = 1 \times 10^{13}\,\text{cm}^{-2}$:

$$N_I(m_I) = \frac{N_I(m_{\text{Ar}})N_{\text{displ}}(m_{\text{Ar}})}{N_{\text{displ}}(m_I)} = n_{\text{dpa}}(m_{\text{Ar}})\frac{N_0}{N_{\text{displ}}(m_I)}, \tag{5.2}$$

where N_0 is the atomic density of VO_2. The obtained values of $N_I(m_I)$ are summarized in figure 5.7b. However, in a pre-experiment it turned out that especially the fluences for heavy ions are overestimated and thus, slightly lower fluences were used (figure 5.7b, red points). These ion fluences are motivated by a linear extrapolation of N_{displ} obtained from light ions (red dashed line in figure 5.7a). To ensure a comparable rate of lattice defect formation, the ion flux Φ_I (beam current) was adjusted to achieve a constant irradiation duration of three minutes. A table summarizing the values of E_0, N_I and Φ_I is given in the appendix A.3.

Successive ion irradiation for each ion species was performed in twelve steps at a temperature of $-30\,°\text{C}$. Each irradiation step was followed by thermal cycling to determine the critical

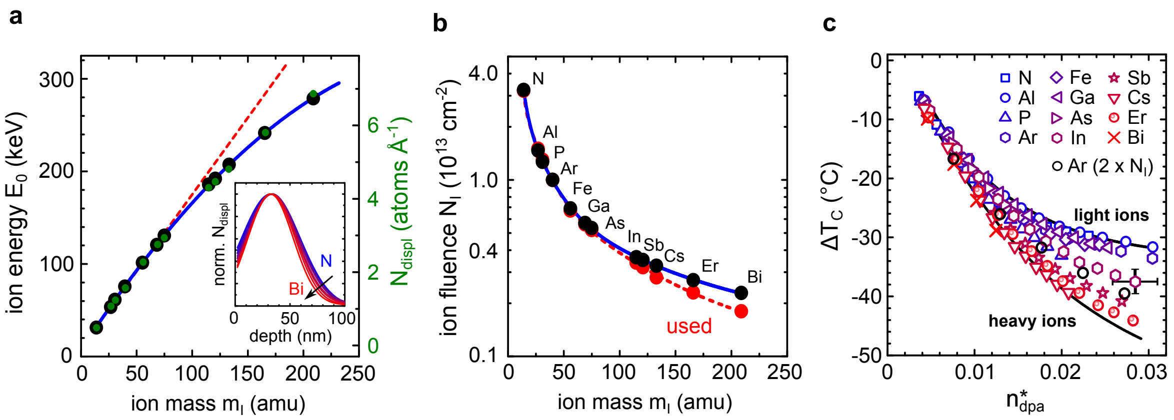

Figure 5.7.: **(a)** Energy E_0 required to implant ions with mass m_I into VO$_2$ at a given depth of $R_P = 50\,\text{nm}$ (black data points, left scale). Number of displaced lattice atoms per ion and unit depth N_{displ} taken from the maximum of the defect distribution calculated for each combination of m_I and E_0 (green data points, right scale). The blue curve is a guide to the eye. Linear extrapolation of N_{displ} using only values of light ions up to $m_I \leq 75\,\text{amu}$ (dashed red line). The inset shows the normalized defect distributions for the irradiation with different ion species from light to heavy ions (blue to red color coded). **(b)** Ion fluence N$_I$ that results in a comparable n_{dpa} value (black data points). However, in the experiment a lower value of N_I was used for heavy ions with $m_I > 100\,\text{amu}$ (red data points). **(c)** Change of the critical temperature ΔT_C^h of irradiated VO$_2$ with respect to T_C^h of intrinsic VO$_2$ as a function of n_{dpa}. For each ion species twelve irradiation and thermal cycle steps were performed using the ion energy and ion fluence given in (a) and (b). The color of the symbols from blue to red corresponds to the ion mass from light ions (N) to heavy ions (Bi). Results from figure 5.6c are shown for comparison (Ar, $2 \times N_I$, black circles). For clarity, error bars are only given for one representative data point and are typical after 12 irradiation steps. Note, that the error is much smaller for the first irradiation step.

temperature T_C^h. Figure 5.7c summarizes the change of the critical temperature ΔT_C^h for each irradiation step with respect to intrinsic VO$_2$ as a function of n^*_{dpa}. For clarity, only the values obtained in the heating cycle are depicted. According to the previous section, n^*_{dpa} was estimated by comparing the resistivity after thermal cycling at a temperature of $-30\,°\text{C}$ to the in-situ measured resistivity during the corresponding irradiation step. Strikingly, the critical temperature decreases with increasing amount of lattice defects independent of the ion species itself for low ion fluences. In agreement with the previous section, 1% of lattice displacements ($n^*_{\text{dpa}} = 0.01$) lead to a reduction of T_C^h by $\Delta T_C^h = -20 \pm 2\,°\text{C}$. However, with increasing n^*_{dpa} the decrease of T_C^h is significantly more pronounced for heavy ions compared to light ions. As an example: At an n^*_{dpa} value of 0.03 light ions like N$^+$ and Al$^+$ decrease T_C^h by $\Delta T_C^h \sim -30\,°\text{C}$, whereas heavy ions like Cs$^+$, Er$^+$, and Bi$^+$ at least reach values of $\Delta T_C^h \sim -45\,°\text{C}$. This effect can be attributed to a different density of point defects within a single collision cascade created by different ions and an increase in the defect clustering efficiency with increasing local density of ion beam induced mobile point defects.[288] The amount of transferred energy within a binary collision of ion and target atom is proportional to the ion mass, and ion energy. Therefore, heavy ion irradiation with high energy results in a dense collision cascade with many secondary knock-on atoms, whereas light ion irradiation with low energy results in the displacement of single lattice atoms along the ion trajectory with relatively dilute collision cascades (compare figure 5.8a).

Simulations show, that ion irradiation with light ions and with the fluences used lead to a lateral homogeneous distribution of lattice defects. In contrast, ion irradiation with heavy ions results in a lateral heterogeneous distribution of lattice defects with regions of much higher

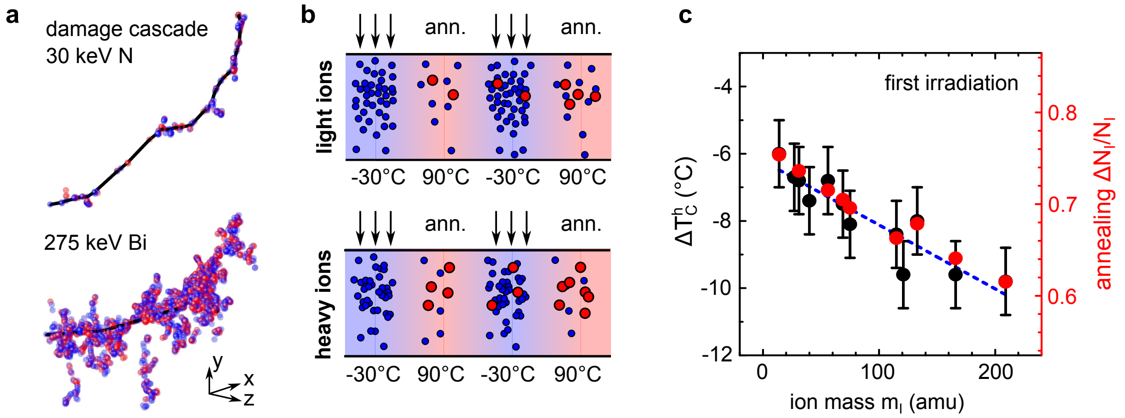

Figure 5.8.: **(a)** Simulated binary collision cascade for the irradiation of VO_2 with 30 keV N^+ and 275 keV Bi^+ using SRIM full-cascade simulations,[204] respectively. **(b)** Simplified model of ion beam induced defect formation in VO_2 for successive ion irradiation with light and heavy ions. The lateral defect distribution caused by light ion irradiation is almost homogeneous, whereas heavy ion irradiation results in a high local density of point defects (blue dots) caused by the dense collision cascade. Stable defect clusters (red dots) are most likely formed in regions of high point defect density during the annealing step (ann.). **(c)** ΔT_C^h for the first irradiation step as a function of ion mass (black circles, left scale). Relative fluence, whose effect is completely annealed during the first thermal cycling: $\Delta N_I/N_I$ (red circles, right scale).

defect density. This is schematically depicted on the left-hand side of figure 5.8b. It is likely that the competing processes of defect recombination and defect transformation into stable defect complexes depend on the defect density.[284] A strong effect of the collision cascade density on the ion beam induced defect formation process was also found for other material systems, such as silicon carbide (SiC),[289] gallium nitride,[288] and metals.[290]

A significant difference of the effect of Ar^+ irradiation on T_C^h is found when different fluence steps are used (black circles and purple hexagons in figure 5.7c correspond to $N_I = 1 \times 10^{13}$ and $2 \times 10^{13}\,\mathrm{cm}^{-2}$ fluence steps, respectively). That is, the amount of stable defects after a thermal treatment depends on the initial defect density. Further, the relative fluence, whose effect is completely annealed after the first thermal cycling step: $\Delta N_I/N_I$ shows a considerable m_I dependence (see figure 5.8c). It seems that the higher m_I the less defects are annealed, which results in a decrease of ΔT_C^h. A similar trend was observed by Aji *et al.*[289] for the irradiation of silicon carbide. However, it is not straightforward to quantify the annealing of defects by the recovery of resistivity when different defect types are present, because the contributions of different defects to the free-carrier concentration and to carrier scattering is unclear. It is likely that a larger number of stable defect complexes is formed for the sample irradiated with heavy ions. These defects alter the resistivity of VO_2 and are not taken into account when calculating ΔN_I and n^*_{dpa}.

In summary, although a comparable number of point defects can be created for the irradiation of VO_2 with different ion species, the amount of stable defects after a thermal treatment critically depends on the local density of defects. In a simplified model most of the defects anneal out in regions of low defect density. Therefore, repetitive ion irradiation with light ions and repetitive thermal treatment leads to a low number of stable defects. Heavy ion irradiation creates local regions of high defect density and favors the formation of stable defect complexes during thermal treatment. Thus, repetitive heavy ion irradiation and repetitive thermal treatment yields a higher number of stable defects, which results in a larger value of ΔT_C (compare model in figure 5.8b). That is, although the critical temperature of VO_2 can

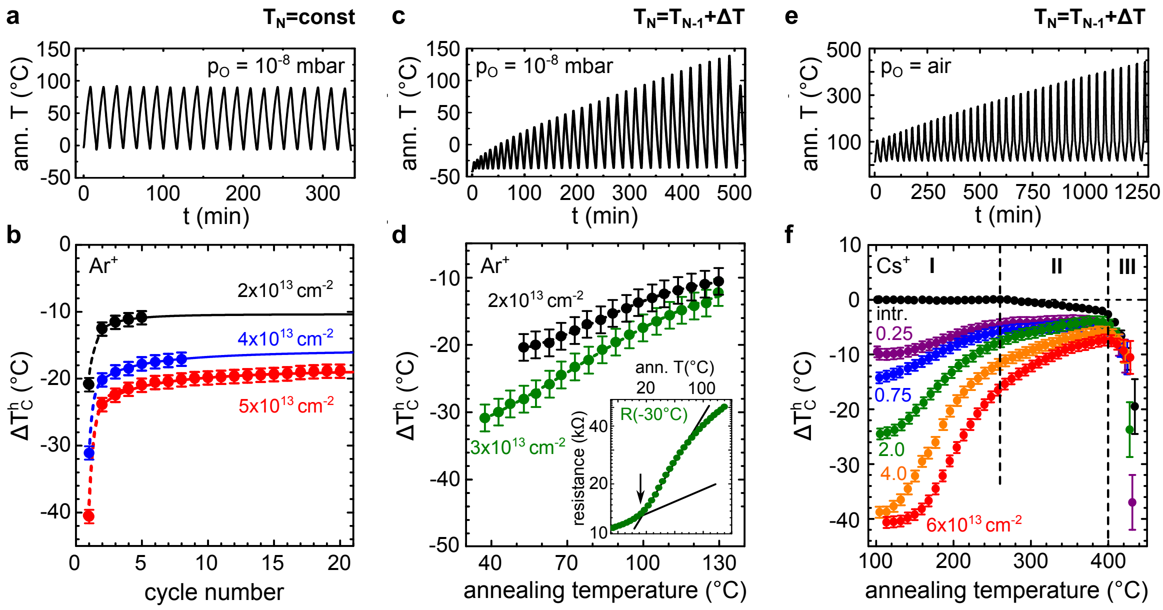

Figure 5.9.: (a-d) Thermal annealing performed in the irradiation chamber directly after 75 keV Ar^+ irradiation of approximately 100 nm VO_2 films. Critical temperatures are obtained from in-situ electrical measurements. **(a,c)** Time-temperature curve for the thermal treatment with fixed maximum temperature of 90 °C (a, T_N = const.) and with successively increasing maximum temperature of $\Delta T = 5\,°C$ (c, $T_N = T_{N-1} + \Delta T$). **(b)** ΔT_C^h obtained from each heating cycle as function of the cycle number (compare a). **(d)** ΔT_C^h as a function of the maximum temperature reached until the time at which T_C was determined, respectively (compare c). **(e-f)** Thermal annealing performed in air directly after 190 keV Cs^+ irradiation of approximately 100 nm VO_2 films at room temperature. Critical temperatures are obtained from in-situ reflectance measurements at $\lambda_0 = 4\,\mu m$. **(e)** Time-temperature curve of the thermal treatment with successively increasing maximum temperature of $\Delta T = 10\,°C$. **(f)** ΔT_C^h as a function of the annealing temperature for various Cs^+ ion fluences.

be precisely adjusted by ion irradiation, the value of T_C critically depends on the ion species used and the sequence of irradiation and annealing steps.

5.4. Thermal stability of irradiation induced defects

One of the main challenges in VO_2 device fabrication that utilizes the reduction of the critical temperature by ion beam induced defect formation is the thermal stability of irradiation defects. If defects recombine or transform during device operation the critical temperature will be changed, which might lead to a significant reduction of device performance.

The thermal stability of irradiation defects was investigated by in-situ electrical measurements during a thermal treatment within the irradiation chamber directly after ion irradiation (figs. 5.9a-d). Several samples were irradiated at $T = -30\,°C$ with 75 keV Ar^+ ions and N_I ranging from 2×10^{13} to $5 \times 10^{13}\,cm^{-2}$. Thermal annealing for up to 20 cycles was performed with a constant maximum temperature of $T_N = 90\,°C$ and heating/cooling rates of approximately $\pm 10\,°C\,min^{-1}$ (compare fig 5.9a). Note that after reaching T_N the samples were immediately cooled limiting the time spent in the high temperature interval from 85 − 90°C to approximately one minute. The critical temperature T_C^h was determined from the temperature-dependent resistivity in the heating branch of each cycle as described previously.

Figure 5.9b shows the change of T_C^h with respect to intrinsic VO_2 (ΔT_C^h) as a function of the cycle number for various N_I. A dramatic increase of ΔT_C^h is observed after the first annealing cycle, which reflects the strong annealing and transformation of point defects by thermal annealing. Note that the first value of ΔT_C^h is obtained from the first heating branch before the annealing temperature is reached. Therefore, this value is not taken into account in the following analysis. All other values of ΔT_C^h represent the state of the sample after the previous annealing cycle. ΔT_C^h increases with increasing cycle number N (total annealing time: $t \propto N$) and is almost constant after a few cycles for all N_I. Because of the multitude of recombination and transformation processes taking place simultaneously but on different timescales, the defect annealing kinetics cannot be described by a simple exponential decay. Especially, the number of possible defect complexes with different activation energies can be significant. However, ΔT_C^h can be fitted using a stretched exponential function (Kohlrausch function), which is often used to empirically describe annealing effects in disordered materials:[285,291,292]

$$\Delta T_C^h(t) = \Delta T_C^h(0) \exp\left[-\left(\frac{t}{\tau}\right)^{\beta}\right] + \Delta T_C^h(\infty), \tag{5.3}$$

where τ is a characteristic relaxation time, $\Delta T_C^h(0)$ and $\Delta T_C^h(\infty)$ are the values obtained before annealing and for thermal equilibrium at the annealing temperature, and $0 < \beta < 1$ is the stretch exponent related to the number of interacting processes. A β value of 0.3 ± 0.1 was obtained for the sample irradiated with $N_I = 5 \times 10^{13}\,\mathrm{cm}^{-2}$, consistent with a large deviation from a single exponential decay. The characteristic relaxation time is on the order of a minute, and the value of $T_C^h(\infty)$ was found to be $-(10.4 \pm 0.3)$, $-(15.6 \pm 0.6)$, and $-(17.8 \pm 0.4)$ °C for $N_I = 2$, 4, and $5 \times 10^{13}\,\mathrm{cm}^{-2}$, respectively. That is, depending on the amount of initial point defects ($\propto N_I$) and the annealing temperature, a certain amount of stable defects remain within the $\mathrm{VO_2}$ films. These defects lead to a permanent reduction of T_C, as long as the annealing temperature is not exceeded during device operation.

Isochronal thermal annealing with successive increasing maximum temperature was performed within the irradiation chamber directly after irradiation at −30 °C (compare figs. 5.9c,d). In each cycle, the annealing temperature was increased by $\Delta T = 5$ °C. Figure 5.9d shows ΔT_C^h as a function of the annealing temperature obtained from the heating branch, which follows the thermal cycle in which the annealing temperature is reached. With increasing annealing temperature ΔT_C^h continuously decreases and no saturation is reached up to the maximum temperature of 130 °C, which is mainly limited by the stability of electrical contacts. Unfortunately the lowest annealing temperature for which ΔT_C^h can be evaluated is determined by T_C^h: $T > T_C^h$. Thus, ΔT_C^h of as implanted samples cannot be obtained without a thermal treatment. However, the inset of figure 5.9d shows the low temperature resistance at $T = -30$ °C after each thermal cycle of the sample irradiated with $N_I = 3 \times 10^{13}\,\mathrm{cm}^{-2}$. At $T \sim 20$ °C the slope of the resistance drastically increases, which indicates a change of the recombination or transformation kinetics of defects. Assuming that the defect mobility is different in insulating and metallic $\mathrm{VO_2}$, the different kinetics in the region below and above this temperature most likely indicate the phase transition ($\Delta T_C^h \sim 50$ °C). Obviously, annealing and transformation of irradiation defects is favored in the metallic phase of $\mathrm{VO_2}$.

Thermal annealing of irradiated $\mathrm{VO_2}$ was further investigated in the temperature interval from 100 to 500 °C by means of in-situ reflectance measurements during a temperature treatment in air. Various approximately 100 nm $\mathrm{VO_2}$ films were irradiated with 190 keV $\mathrm{Cs^+}$ ions in the fluence range from $N_I = 0.25\times$ to $6 \times 10^{13}\,\mathrm{cm}^{-2}$ at room temperature. Isochronal thermal annealing was performed with a successively increasing annealing temperature of $\Delta T = 10$ °C,

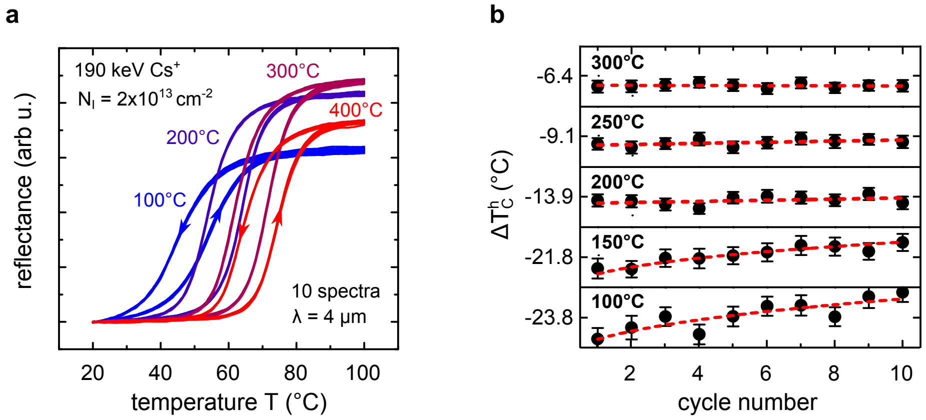

Figure 5.10.: **(a)** Temperature-dependent reflectance at 4 µm of a VO_2 thin film sample that was annealed at various annealing temperatures after ion irradiation. The sample was irradiated with 190 keV Cs^+ and an ion fluence of $N_I = 2 \times 10^{13}\,\mathrm{cm}^{-2}$ at room temperature. For each annealing temperature 10 consecutive thermal cycles to a maximum temperature of 100 °C are shown. **(b)** Critical temperature shift with respect to intrinsic VO_2 obtained from the heating cycle ΔT_C^h as a function of the cycle number. Red dashed lines are stretched exponential function fits. The temperature axis of each plot shows a temperature interval of ±0.3 °C around the indicated value of ΔT_C^h.

a heating/cooling rate of approximately ±10 °C and an annealing duration of roughly 4 min at the annealing temperature in each cycle (compare figure 5.9e). Figure 5.9f shows ΔT_C^h obtained from the reflectance derivative[242] with respect to untreated intrinsic VO_2 as a function of the annealing temperature for intrinsic and various irradiated VO_2 samples. Obviously, three different temperature regions of the thermal treatment can be clearly distinguished: (Region I) For annealing temperatures up to 260 °C no change of the critical temperature of intrinsic VO_2 is observed (black dots in figure 5.9f). In this interval ΔT_C^h of irradiated VO_2 rapidly increases especially at temperatures of approximately 200 °C, which can be associated with annealing of point defects but also the dissociation of point defect complexes with low dissociation energy. (Region II) In the temperature interval ranging from 260 to 400 °C a slight decrease of T_C^h of intrinsic VO_2 can be observed. The reduction of T_C^h is caused by the onset of oxidization of VO_2, which is in good agreement with thermogravimetric investigations of VO_2 nanoparticles by Li *et al.*[293]. In this temperature range, the increase of ΔT_C^h of irradiated VO_2 by thermal annealing is significantly reduced compared to region I. However, the critical temperature of irradiated VO_2 is still significantly lower compared to intrinsic VO_2. (Region III) A sudden decrease of ΔT_C^h at roughly 400 °C for all samples marks the formation temperature of V_6O_{13}, which has a much lower phase transition temperature compared to VO_2, and further oxidation of the samples towards V_2O_5 occurs.[294,295] On the one hand, the intrinsic properties cannot be restored by thermal annealing in air. On the other hand, the critical temperature of irradiated VO_2 can be adjusted by thermal annealing to a certain value.

To demonstrate the stability of the criticial temperature of annealed VO_2 samples during device operation, figure 5.10 shows 10 cycles of the temperature-dependent reflectance of a VO_2 sample at a fixed wavelength of $\lambda_0 = 4\,\mu m$ measured directly after a thermal treatment at various annealing temperatures. An approximately 100 nm VO_2 film on Al_2O_3 was irradiated with 190 keV Cs^+ and an ion fluence of $N_I = 2 \times 10^{13}\,\mathrm{cm}^{-2}$ and annealed for 10 minutes in air at successively increasing temperatures in the temperature range from 100 to 400 °C. In between two annealing steps the temperature-dependent reflectance was measured for 10 cycles. At first glance, there is no difference between each of the 10 cycles, measured after each of the thermal treatments, respectively. A closer inspection of the critical temperature reveals a slight shift of ΔT_C^h for annealing temperatures up to 150 °C and no change of ΔT_C^h for thermal annealing of the samples above 150 °C (compare figure 5.10b). However, even for the low annealing temperatures the temperature shift decreases with each cycle and is in total as small as 0.5 and 0.3 °C for the first 10 cycles after the annealing at 100 and 150 °C, respectively. Thus, the phase transition temperature of VO_2 can be adjusted and stabilized by ion irradiation and post-irradiation thermal annealing in the temperature range above the temperature of device operation and below the temperature of severe oxidization. Note that the reduction of lattice defects by thermal annealing up to 300 °C results in an increase of the reflectance amplitude across the IMT (compare figure 5.10a). Whereas oxidization of VO_2 at 400 °C leads to a decrease of the reflectance amplitude. In this thesis, all devices were annealed at 100 °C for up to 1 h prior to characterization, to maintain a large critical temperature shift.

5.5. Effects of ion irradiation on the structural phase transition

Ion irradiation and a thermal treatment leads to the formation of stable defects that alter the phase transition temperature of VO_2. However, the physical mechanism of the temperature shift remains unclear. On the one hand electronic doping caused by charged defects might play the crucial role in destabilizing the insulating phase of VO_2. On the other hand, point defects and defect complexes lead to a distortion and strain in the VO_2 lattice, which might significantly contribute to the reduction of the phase transition temperature. However, the electronic structure of VO_2 is closely entangled with its structural properties. For example, Aetukuri *et al.*[100] and Fan *et al.*[124] recently demonstrated that the orbital occupancy is strongly affected by strain, which changes the electron-electron correlation and drives the phase transition. Complementary, Tan *et al.*[84] verified that electronic doping induces a local structural distortion in the vicinity of the dopants caused by charge transfer, which lowers the IMT temperature.

To investigate the effects of strain induced by ion irradiation on the structural phase transition of VO_2 temperature-dependent X-ray diffraction and Raman spectroscopy was employed as a function of ion fluence.

5.5.1. Ion beam induced strain in VO_2 films

Figure 5.11a shows coupled θ - 2θ XRD patterns obtained at room temperature from irradiated VO_2 films grown on Al_2O_3. The approximately 100 nm thin VO_2 films were irradiated with 190 keV Cs^+ and various ion fluences up to $2 \times 10^{13}\,\mathrm{cm}^{-2}$ at room temperature. Prior to the XRD measurements, all samples were annealed at 100 °C for 30 min in air.

Ion irradiation with an increasing ion fluence leads to a shift of the $(0\,2\,0)_{\mathrm{M1}}$ reflection of VO_2 towards lower values of 2θ and a significant broadening of this reflection with an increase of the FWHM from 0.23 ° to 0.36 °. In comparison, the $(0\,0\,0\,12)$ reflection of the Al_2O_3 substrate is at the same 2θ value with no reflection broadening for all samples. That is, the ion irradiation only affects the VO_2 layer. The shift of the $(0\,2\,0)_{\mathrm{M1}}$ reflection corresponds to an increase of the out-of-plane lattice parameter b_{M1} from ~ 4.517 Å obtained from intrinsic VO_2 to ~ 4.552 Å determined for the sample irradiated with the highest ion fluence (compare figure 5.11c). According to equation 5.1, the increase of b_{M1} corresponds to a change of the

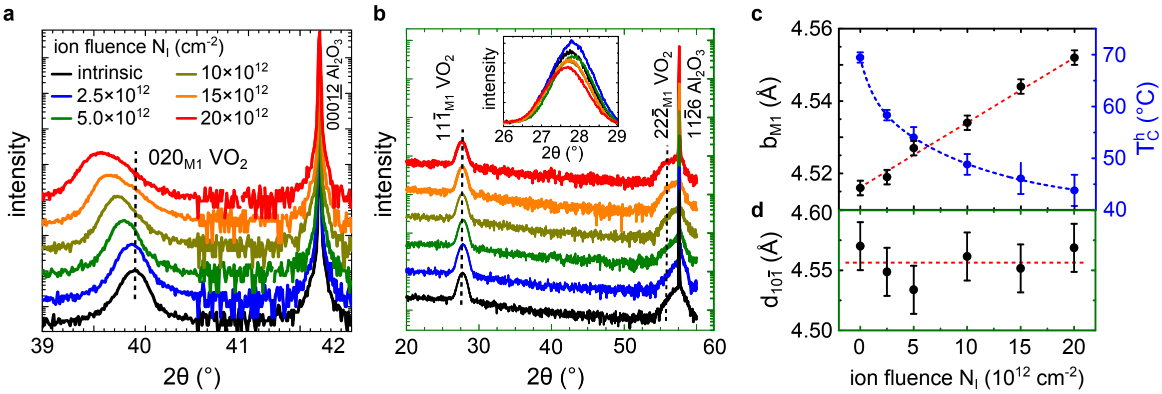

Figure 5.11.: In-plane **(a)** and off-axis **(b)** $\theta - 2\theta$ XRD pattern of an intrinsic and various irradiated VO_2 thin films grown on Al_2O_3 substrates. Ion irradiation was performed using 190 keV Cs^+ with ion fluences up to $N_I = 2 \times 10^{13}\,\mathrm{cm}^{-2}$ at room temperature. Off-axis scans were performed at a sample inclination angle of $\Psi = 44.3°$. The $(1\,1\,\bar{1})_{\mathrm{M1}}$ reflection of VO_2 is highlighted in the inset of (b). **(c)** Comparison of the determined b_{M1} lattice parameter and T_C obtained from figure 5.12c as function of the ion fluence N_I. **(d)** Lattice plane spacing $d_{1\,0\,\bar{1}}$ of the $(1\,0\,\bar{1})_{\mathrm{M1}}$ plane as a function of N_I. Dashed lines in (c) and (d) are guides to the eye.

out-of-plane strain state of the sample from slightly compressive ($\eta_a = -0.2\%$) to tensile ($\eta_a = 0.6\%$) strained. The origin of the lattice expansion is most likely an increase of the defect density and especially the formation of interstitial defects caused by ion irradiation. The clear broadening of the $(0\,2\,0)_{\mathrm{M1}}$ reflection can be attributed to the depth distribution of lattice defects. In contrast, the $(1\,1\,\bar{1})_{\mathrm{M1}}$ reflection does not significantly shift during ion irradiation (compare figure 5.11b). The in-plane lattice plane spacing $d_{1\,0\,\bar{1}}$ was calculated from the $(0\,2\,0)_{\mathrm{M1}}$ and $(1\,1\,\bar{1})_{\mathrm{M1}}$ reflection and is shown in figure 5.11d as a function of ion fluence. Despite strong fluctuations, the value of $d_{1\,0\,\bar{1}}$ is constant for all ion fluences, which might be attributed to a strong clamping[271] of the VO_2 film to the Al_2O_3 substrate and stress relaxation via out-of-plane lattice expansion.

The critical temperature of the structural phase transition of intrinsic and irradiated VO_2 thin films was determined from temperature-dependent coupled θ - 2θ XRD measurements. Figure 5.12a shows the XRD intensity as a function of diffraction angle 2θ (horizontal axis) and temperature (vertical axis) obtained from the intrinsic VO_2 film during a heating cycle. As the temperature is increased, the $(0\,2\,0)_{\mathrm{M1}}$ reflection of monoclinic VO_2 continuously transforms into the $(1\,0\,0)_{\mathrm{R}}$ reflection of rutile VO_2 in a small temperature interval around a temperature of approximately $T_C^h = 70\,°\mathrm{C}$ (compare figure 5.12c), which is consistent with atomic structure models (compare section 2.1.1), electrical (compare section 5.1.3), and optical measurements (compare section 5.1.5). The transformation can be seen by a slight shift of the 2θ value of the VO_2 reflection and an increase of its XRD intensity. For comparison, the $(0\,0\,0\,12)$ reflection of the Al_2O_3 substrate at $2\theta = 41.69°$ remains constant throughout the entire measurement. It is very important to simultaneously measure a substrate reflection for temperature-dependent XRD measurements to rule out effects caused by a thermal angle drift. Note, the large angle difference of film and substrate reflection (compare figure 5.11b) prevents a reliable temperature-dependent laboratory-based XRD measurement of the $(1\,1\,\bar{1})_{\mathrm{M1}}$ reflection. Figure 5.12b shows the contour plot of the XRD intensity obtained from the VO_2 film irradiated with an ion fluence of $N_I = 1 \times 10^{13}\,\mathrm{cm}^{-2}$. For this ion fluence the structural transition is clearly at a considerably lower temperature of approximately $T_C^h = 50\,°\mathrm{C}$. No transient phase, such as the M_2 phase, which was observed by Okimura *et al.*[296] in epitaxially strained VO_2

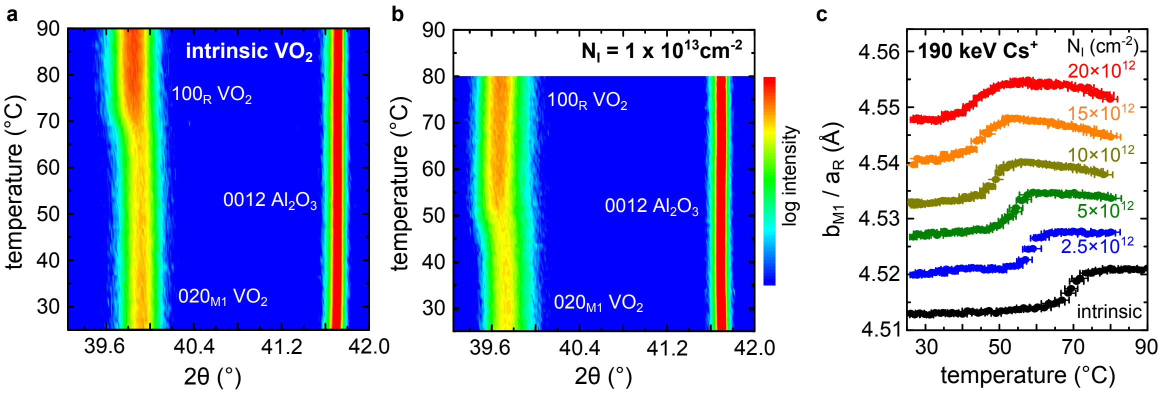

Figure 5.12.: Temperature-dependent $\theta - 2\theta$ XRD of intrinsic and irradiated VO$_2$. **(a,b)** XRD intensity as a function of diffraction angle 2θ and temperature obtained from an intrinsic (a) and an irradiated (b) VO$_2$ thin film on Al$_2$O$_3$ during a heating cycle, respectively. **(c)** Out-of-plane lattice parameter of intrinsic and irradiated VO$_2$ as a function of temperature. Ion irradiation was performed using 190 keV Cs$^+$ with ion fluences up to $N_I = 2 \times 10^{13}\,\mathrm{cm}^{-2}$ at room temperature.

films, is present in the irradiated films. The M2 phase is usually an indication for tensile strain along the c$_R$ axis of VO$_2$.[125] Since the c$_R$ axis is oriented parallel to the film plane, the absence of the M2 phase is in perfect agreement with the observed constant in-plane lattice plane spacing $d_{10\bar{1}}$. Furthermore, no indication of a residual intrinsic VO$_2$ layer is found. In contrast to optical measurements, the reflected XRD intensity is a superposition of the relative contributions of all individual layers within the X-ray penetration depth, which is typically on the order of several microns. Thus, an intrinsic layer underneath the irradiated layer would lead to the observation of a second phase transition taking place individually at approximately 70 °C. From point of XRD it must be concluded that the entire VO$_2$ layer is affected by ion irradiation.

Figure 5.12c summarizes the temperature dependence of the out-of-plane lattice parameters b_{M1} and a_R, obtained from the $(0\,2\,0)_{\mathrm{M1}}$ and $(1\,0\,0)_{\mathrm{R}}$ reflection for intrinsic and ion irradiated VO$_2$ for all ion fluences, respectively. At the transition from a monoclinic to a rutile structure, the VO$_2$ lattice expands by less than 0.01 Å for all films. The determined expansion along the out-of-plane lattice direction is in perfect agreement with XRD results obtained by Yang *et al.*[297] for intrinsic VO$_2$. Thus, it might be concluded that ion irradiation does not alter the structural phase transition process itself but only shifts its temperature. The ion beam induced lattice expansion is as large as 0.035 Å measured for the highest ion fluence of $N_I = 2 \times 10^{13}\,\mathrm{cm}^{-2}$ with respect to the intrinsic VO$_2$ film, shifting both the b$_{\mathrm{M1}}$ and a$_{\mathrm{R}}$ lattice parameter equally. The temperature T_C^h of the structural phase transition was determined from gaussian fitting of the derivative of the out-of-plane lattice parameter. The obtained values of T_C^h are depicted as a function of N_I in figure 5.11c. Assuming that the in-plane lattice parameter c$_{\mathrm{R}}$ is constant, T_C^h follows the same $\mathrm{c_R}/\mathrm{a_R} \propto 1/\mathrm{b_{M1}}$ dependence as was obtained by Aetukuri *et al.*[100] and Fan *et al.*[124] for epitaxially strained VO$_2$ films (compare figure 2.5b).

5.5.2. Irradiation induced phonon softening

Temperature-dependent Raman spectroscopy was employed to further study the influence of ion irradiation on the structural properties of VO$_2$, in particular on the phonon modes corresponding to V-V and V-O lattice vibrations. Previous reports on temperature-dependent Raman spectroscopy of VO_2 thin films[167,271,296,298–306] and VO_2 nanostructures[307–311] mainly focused on the structural dynamics of VO_2 across the IMT. Further, Raman spectroscopy was previously employd to study the effects of hydrostatic pressure[312] and epitaxial strain[266,271,296,304,309] on the structural properties of VO_2.

Figures 5.13a and 5.13b show the Raman spectra obtained at several temperatures across the IMT during a heating cycle from an intrinsic (figure 5.13a) and an irradiated VO_2 thin film (figure 5.13b), respectively. Each spectrum was accumulated over a temperature interval of approximately 5 °C during a slow temperature ramp with a heating rate of less than 0.1 °C/min. Both films have a comparable thickness of $\sim 100\,\mathrm{nm}$ and were grown on Al_2O_3 substrates. Ion irradiation was performed using 75 keV Ar^+ ions at an ion fluence of $N_I = 3 \times 10^{13}\,\mathrm{cm}^{-2}$ at room temperature. Prior to Raman spectroscopy the irradiated VO_2 film was annealed at 100 °C for 30 min in air.

At room temperature both samples display several sharp Raman peaks, which correspond to the monoclinic M1 phase of VO_2 (compare figure 5.13a,b). No other structural phases can be identified. The peaks at approximately 195 (noted ω_{V1}) and $224\,\mathrm{cm}^{-1}$ (ω_{V2}) can be assigned to V-V vibration modes, whereas all higher-frequency modes are related to V-O vibrations.[299,304,312,313] Especially the intense Raman peak at approximately $615\,\mathrm{cm}^{-1}$ is often used as a fingerprint to identify the structural phase of VO_2 and corresponds to oxygen ions connecting the different V chains along the c_R-axis.[299,312] Additional peaks located at 415, 575 and $748\,\mathrm{cm}^{-1}$ originate from the Al_2O_3 substrate.[300] As the temperature is increased, all Raman modes corresponding to the M1 phase gradually disappear over a temperature interval of approximately 25 °C starting at 55 °C and 40 °C for intrinsic and irradiated VO_2, respectively. At temperatures above 80 and 60 °C, respectively, both samples are entirely in the rutile R phase. Two very broad Raman peaks centered at approximately 400 and $565\,\mathrm{cm}^{-1}$ can be distinguished, which were assigned to phonon modes with A_{1g} and E_g symmetry previously.[299]

The fraction of M1 phase (m) at any temperature T in both samples was estimated by fitting each of the spectra with a weighted superposition of spectra taken at room temperature of apprixomately 25 °C and ~ 100 °C, which are suppossed to represent the pure M1 and R phase, respectively:[305]

$$F(T) = c[mF(\sim 25\,°\mathrm{C}) + (1-m)F(\sim 100\,°\mathrm{C})], \tag{5.4}$$

where $F(T)$ is the experimental Raman spectrum at T and c a constant that takes into account intensity variations for different measurements. Despite slight shifts of the Raman peaks with temperature, all spectra were fitted very well. In perfect agreement with XRD measurements, this indicates the absence of transitional phases, such as the monoclinic M2 and triclinic T phase. Figure 5.13e shows the M1 fraction (m) for both samples as a function of temperature in the heating cycle. The phase transition temperature T_C^h of VO_2 deduced from Raman spectroscopy is defined as the temperature at which 50% of the intensity of the Raman signal originates from the M1 phase. For the intrinsic sample a value of $T_C^h = 64\,°\mathrm{C}$ was found, which is clearly lower than the previously determined value of approximately $T_C^h = 70\,°\mathrm{C}$ (compare sections 5.1.3, 5.1.5 and 5.5.1), most likely caused by laser induced heating during the Raman measurement. However, in accordance with the previous sections, the phase transition temperature of the irradiated sample is clearly lowered ($T_C^h = 48\,°\mathrm{C}$).

In order to extract structural details, figure 5.13c shows the temperature dependence of

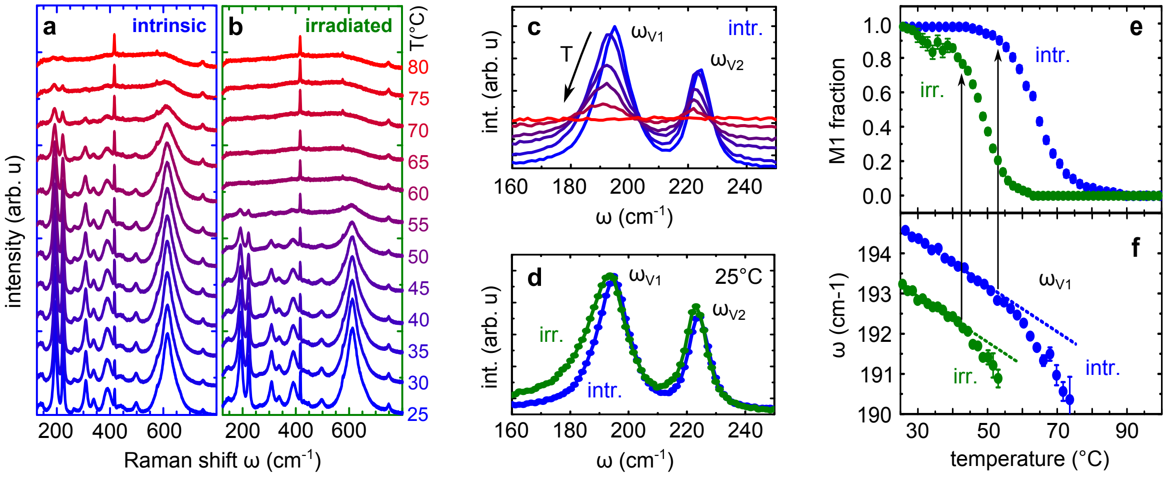

Figure 5.13.: (a,b) Temperature-dependent Raman spectra of an intrinsic (a) and an irradiated VO_2 film grown on Al_2O_3 (b). Irradiation was performed with 75 keV Ar^+ with an ion fluence of $N_I = 3\times10^{13}\,\mathrm{cm}^{-2}$. **(c,d)** Temperature-dependent Raman spectra of intrinsic VO_2 (c) and comparison of Raman spectra of intrinsic (int.) and irradiated (irr.) VO_2 obtained at room temperature (d) around the ω_{V1} and ω_{V1} phonon mode, respectively. **(e)** Temperature dependence of the monoclinic M1 fraction of intrinsic and irradiated VO_2 deduced from fitting Raman data. **(f)** Comparison of the temperature-dependent Raman shift of the ω_{V1} phonon mode, which corresponds to V-V vibrations, of intrinsic and irradiated VO_2. Arrows indicate the onset of the IMT.

the normalized ω_{V1} and ω_{V2} Raman peak of the intrinsic VO_2 film. Across the IMT both Raman peaks do not only gradually vanish but simultaneously shift in frequency and broaden. The Raman peak position of the ω_{V1} phonon mode at each temperature was obtained from Lorentzian line fits after background subtraction and is shown in figure 5.13f as blue dots. The peak position linearly decreases with increasing temperature at a rate of $-0.06\,\mathrm{cm}^{-1}\mathrm{K}^{-1}$, as a result of thermal lattice expansion.[304] At the onset of the IMT, which is marked with an arrow in figure 5.13f, phonon softening due to the transition from monoclinic M1 to rutile R leads to a strong decrease of the ω_{V1} phonon frequency.[304,313] Furthermore, figure 5.13d compares the line shapes of the V-V phonon modes of the intrinsic and irradiated VO_2 film at room temperature. The ω_{V1} Raman peak of the intrinsic VO_2 film has a FWHM of $12.7\,\mathrm{cm}^{-1}$ and is clearly broadened upon ion irradiation (FHWM= $16.5\,\mathrm{cm}^{-1}$). The broadening mainly affects the low-frequency side of the Raman peak. Although the Raman peak positions of the intrinsic and irradiated VO_2 film show a similar temperature-dependent behavior, the frequency of the ω_{V1} phonon mode at room temperature is clearly red-shifted from 194.6 to $193.2\,\mathrm{cm}^{-1}$ upon ion irradiation (see figure 5.13f).

To verify the red-shift of the phonon modes, Raman spectroscopy was conducted at a fixed temperature of −75 °C for intrinsic and various irradiated VO_2 films. Ion irradiation was performed using 190 keV Cs^+ ions at various ion fluences ranging from $N_I = 5\times10^{12}$ to $2\times10^{13}\,\mathrm{cm}^{-2}$ at room temperature. Note that these are the samples used previously for XRD measurements. Figure 5.14a shows the obtained low-temperature Raman spectra in the vicinity of the ω_{V1} and ω_{V2} phonon modes. The ω_{V1} phonon mode of the intrinsic VO_2 film is centered at a frequency of approximately $200.0\,\mathrm{cm}^{-1}$, which is in perfect agreement with the peak position found at room temperature and the linear decrease of this peak position due to thermal lattice expansion obtained previously (compare figure 5.13f). The spectral line width is $7.7\,\mathrm{cm}^{-1}$, which is smaller than the line width at room temperature, because of suppressed thermal broadening. Upon ion irradiation the Raman peak position of the ω_{V1} phonon mode

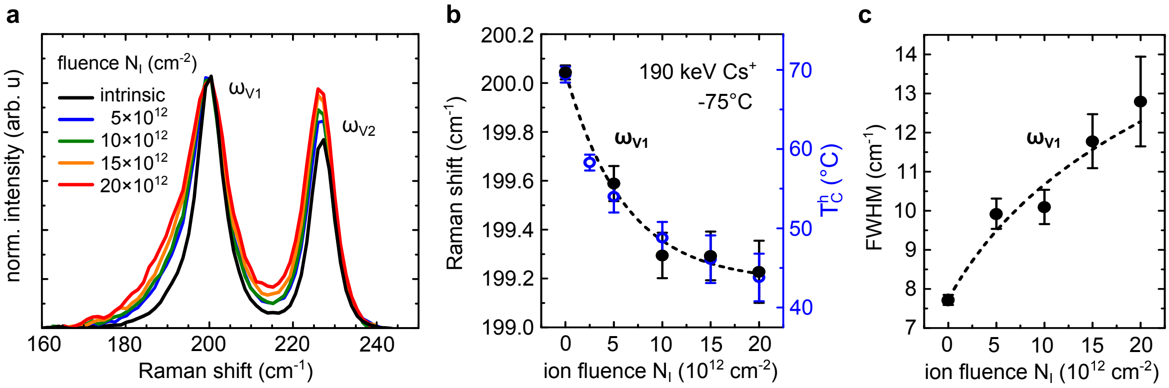

Figure 5.14.: **(a)** Raman spectra taken around the ω_{V1} and ω_{V2} phonon mode of intrinsic and various irradiated $\mathrm{VO_2}$ films obtained at $-75\,°\mathrm{C}$. Ion irradiation was performed using 190 keV Cs^+ with ion fluences up to $N_I = 2 \times 10^{13}\,\mathrm{cm}^{-2}$ at room temperature. Peak position **(b)** and FWHM **(c)** of the ω_{V1} Raman peak as a function of N_I. The dashed lines are plotted to guide the eye.

continuously red-shifts to lower frequencies with increasing ion fluence and reaches a value of approximately $199.2\,\mathrm{cm}^{-1}$ for irradiation at an ion fluence of $N_I = 2 \times 10^{13}\,\mathrm{cm}^{-2}$ (see figure 5.14b). At the same time the line width increases with increasing ion fluence and reaches a value of roughly $13\,\mathrm{cm}^{-1}$ for the highest ion fluence used (see figure 5.14c). Further, the fluence dependence of the ω_{V1} phonon mode is in perfect agreement with the ion fluence dependence of the strucutral phase transition temperature T_C^h obtained from XRD measurements (blue data points in 5.14b, compare also section 5.5.1).

A significant blue-shift of the ω_{V1} and ω_{O} phonon modes was found by Shibuya *et al.*[304] for epitaxially strained $\mathrm{VO_2}$ films. In their combined XRD and Raman study of 80 nm $\mathrm{VO_2}$ films grown on (0 0 1) magnesium fluoride ($\mathrm{MgF_2}$) they demonstrated that the lattice mismatch between $\mathrm{VO_2}$ and $\mathrm{MgF_2}$ leads to a significant reduction of the phase transition temperature caused by tensile strain along $\mathrm{a_r}$ and compressive strain along $\mathrm{c_r}$. The blue-shift was attributed to bond-stiffening caused by compressive strain along the $\mathrm{c_R}$ axis. In contrast, Zhang *et al.*[159] observed a considerable red-shift of the V-V and V-O phonon modes and a significant reduction of the phase transition temperature in oxygen deficient $\mathrm{VO_2}$. In their study oxygen vacancies were formed by thermal annealing of $\mathrm{VO_2}$ at a low-oxygen partial pressure. The reduction of the phase transition temperature and the bond softening were attributed to a reduction of the oxidization state of vanadium from V^{4+} to V^{3+}. A comparable red-shift of the phonon modes is also observed in other transition metal oxides if the oxidization state of the metal decreases without changing the coordination.[314] Thus, the red-shift and broadening of the Raman modes upon ion irradiation might be attributed to the presence of an increasing amount of V^{3+} states. First in-situ XPS measurements of ion irradiated $\mathrm{VO_2}$ films seem to confirm the reduction of the oxidization state of the vanadium lattice atoms upon ion irradiation (compare appendix A.4). Nevertheless, XPS is a surface sensitive method and the results might not be comparable. However, the perfect agreement of the fluence dependence of the ω_{V1} phonon mode and of T_C^h (compare figure 5.14b) indicates that charge redistribution between irradiation defects and vanadium lattice atoms and consequent reduction of the vanadium oxidization state might play a crucial role in the decrease of the phase transition temperature of irradiated $\mathrm{VO_2}$.

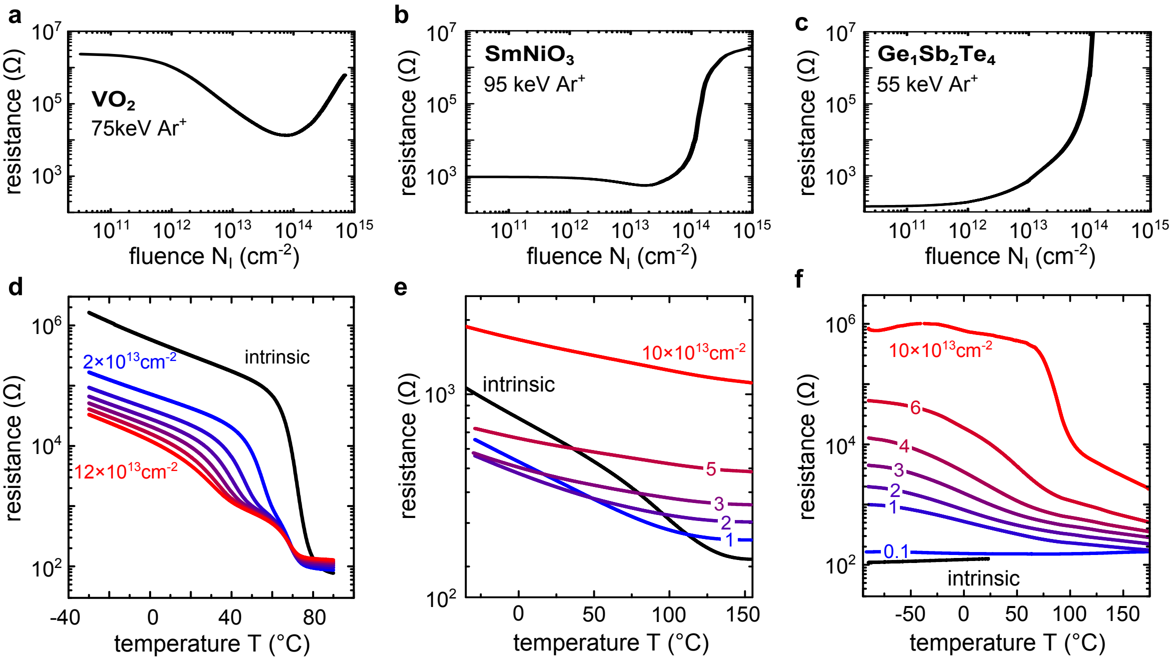

Figure 5.15.: (a-c) In-situ resistance measurement during Ar^+ ion bombardment of an approximately 100 nm thin VO_2 (a), $SmNiO_3$ (b), and $Ge_1Sb_2Te_4$ film at $T = -30\,°C$. Each of the ion energies was chosen in order to ensure a comparable implantation profile. **(d-f)** Temperature-dependent resistance measurements of an intrinsic and a successively irradiated VO_2 (d) $SmNiO_3$ (e) and $Ge_1Sb_2Te_4$ (f) film after several implantation steps to a total ion fluence as indicated.

5.6. Applicability to other material systems

The concept of defect engineering by means of ion irradiation is not limited to VO_2. In general, the formation of irradiation defects can be observed in almost all materials. However, the modification of materials that exhibit an electronic phase transition, such as the vanadium oxides VO_x,[44,315] rare-earth nickelates $RNiO_3$,[56,316–319] and GeSbTe compounds along the pseudo-binary GeTe - Sb_2Te_3 line[320] is of particular interest. Typically, the phase transition in these materials is accompanied by dramatic changes of the electrical and optical properties.[44,56,315,321,322] Although the origin of the phase transition is significantly different, the ion beam can be used to locally modify or trigger the phase transition.

Figure 5.15 shows a comparison of the effect of Ar^+ ion irradiation on the electrical properties of VO_2, $SmNiO_3$ and $Ge_1Sb_2Te_4$ (GST) thin films. In-situ resistance measurements of the approximately 100 nm films were performed during ion irradiation at a temperature of $-30\,°C$ (compare figures 5.15a-c). Note that an ion energy of 75, 95 and 55 keV was chosen for the irradiation of the VO_2, $SmNiO_3$ and GST film, respectively, in order to ensure a comparable defect distribution. Temperature-dependent resistance measurements of VO_2, $SmNiO_3$ and GST films were performed prior to and after each of several successive irradiation steps (compare figures 5.15d-f). In this case, the Ar^+ ion irradiation was performed at $T = -30\,°C$ for VO_2 and $SmNiO_3$, and at $T = -90\,°C$ for GST.

As discussed previously, ion irradiation of VO_2 with an increasing ion fluence up to approximately $N_I = 1 \times 10^{14}\,cm^{-2}$ leads to a significant shift of the IMT transition temperature (see figure 5.15d). Further, a reduction of the resistance in the insulating state by almost two orders of magnitude is observed (compare figures 5.15a,d). In contrast to VO_2, the reversible IMT of intrinsic $SmNiO_3$ is less pronounced and takes place at approximately 100 °C (see figure 5.15e). Although ion irradiation with small ion fluences shifts the critical temperature dramatically, the striking feature is a rapid increase of the resistance by more than 3 orders of magnitude starting at an ion fluence of approximately $N_I = 1 \times 10^{14}\,\mathrm{cm}^{-2}$ (compare figures 5.15b,e). According to Shi *et al.*[323] and Li *et al.*[56] a change of the electron configuration of Ni^{3+} to Ni^{2+}, which might be induced by the formation of an increasing amount of irradiation defects and consequent charge redistribution, leads to a strong Coulomb repulsion and the emergence of a new highly insulating state. An even stronger increase of the resistance by more than 4 orders of magnitude is observed for the irradiation of GST with an ion fluence on the order of $N_I = 1 \times 10^{14}\,\mathrm{cm}^{-2}$ (see figure 5.15c). In the crystalline state, GST is metallic with a delocalized electron system caused by vacancy ordering.[320] Ion irradiation with an increasing ion fluence leads to an increasing amount of lattice distortions, and especially the formation and redistribution of cation vacancies, in the GST film. Using density functional theory, Kolobov *et al.*[324] demonstrate that slight distortions in the crystalline phase may trigger a collapse of long-range order, generating an amorphous phase. According to Wang *et al.*[320] electron localization caused by lattice disorder (Anderson localization[320,325]) drives a phase transition from metallic to highly insulating (compare figure 5.15c,f). The disordered/amorphous phase is stable up to elevated temperatures of approximately 100 °C, as can be seen from figure 5.15f. Above this temperature GST crystallizes into a metastable cubic (rock-salt-like) structure. At temperatures as low as roughly 250 °C GST crystallizes in the stable hexagonal metallic phase, which makes this material easily reconfigurable.[324]

5.7. Summary

Phase pure VO_2 thin films were grown on $\mathrm{Al}_2\mathrm{O}_3$ substrates using reactive rf sputtering. The structural properties of as-grown films were investigated by electron microscopy and X-ray diffraction. All films are composed of highly oriented columnar grains with six-fold domain symmetry. Epitaxial strain is relaxed most likely via the formation of dislocations. The IMT characteristics of as grown VO_2 films were examined using temperature-dependent resistance and reflectance measurements. Although the domain structure of the VO_2 films leads to a broadening of the phase transition, a resistivity change of three orders of magnitude and a critical temperature of the IMT close to the bulk value[160] of approximately 67 °C indicate a high film quality. The resistance change is well described using a resistor network model that takes into account the contributions of individual VO_2 domains. The only free parameter in this model is the temperature-dependent metallic fraction, which is estimated using a thermal equilibrium model.

Noble gas ion irradiation of VO_2 films was performed in order to investigate the effect of ion irradiation on the IMT separated from doping effects. At room temperature 75 keV Ar^+ ion irradiation with ion fluences exceeding $N_I = 1 \times 10^{15}\,\mathrm{cm}^{-2}$ ($n_{dpa} \sim 1$, $c_{\mathrm{Ar}} < 0.2\,\mathrm{at.\%}$) results in a complete amorphization of the VO_2 lattice. Amorphous VO_2 does not feature an IMT. Elevated irradiation temperatures result in a metalization of VO_2 films, most likely due to enhanced oxygen out-diffusion of displaced oxygen atoms.

In-situ electrical measurements at a fixed temperature during ion irradiation indicated that point defect formation at low ion fluences can be used to alter the properties of the IMT of VO_2. When VO_2 films were irradiated with 75 keV Ar^+ ions in steps of $N_I = 2 \times 10^{13}\,\mathrm{cm}^{-2}$, the critical temperature of the phase transition decreased, reaching almost room temperature for $N_I = 1 \times 10^{14}\,\mathrm{cm}^{-2}$. This effect is a result of the displacements of both oxygen and vanadium from their lattice sites by nuclear collisions that lead to the formation of interstitial-vacancy complexes. Temperature-dependent XRD and Raman spectroscopy revealed that ion irradiation of thin VO_2 films induces tensile-strain along the out-of-plane a_R direction and leads to bond-softening most likely caused by a reduction of the oxidization state of vanadium lattice atoms. Thus, the critical temperature is reduced by a combination of local strain and the reduction of the vanadium oxidization state by neighboring charged lattice defects.

A moderate heat treatment was inevitable to determine the phase transition temperature. Strong annealing of point defects and the formation of stable defect complexes at temperatures starting well below 100 °C was observed. A remaining displacement of roughly 1 % of all lattice atoms after moderate annealing results in a reduction of the critical temperature T_C by $\Delta T_C = -20 \pm 2\,°C$. A comparable reduction of T_C is reported for tungsten doped VO_2 thin films ($c_W \sim 1$ at.%). The amount of stable defects after a thermal treatment critically depends on the initial local defect density, which is determined by the defect density created within a single damage cascade and the number of overlapping cascades. Heavy ion irradiation results in a dense collision cascade with many displaced lattice atoms, whereas light ion irradiation results in the displacement of single lattice atoms along the ion trajectory. Consequently, the decrease of T_C with increasing ion fluence is significantly more pronounced for heavy ion irradiation (e.g. Er^+, $\Delta T_C \sim -45\,°C$ at $n^*_{dpa} \sim 0.03$) compared to light ion irradiation (e.g. N^+, $\Delta T_C \sim -30\,°C$ at $n^*_{dpa} \sim 0.03$).

The effect of ion irradiation on the IMT of other phase change and phase transition materials, such as $SmNiO_3$ and GST, was investigated. It was demonstrated that the formation of a small amount of irradiation defects strongly affects the electron-electron correlation and induces disorder-driven transitions. The accompanied drastic changes in electrical resistance and optical properties can be exploited in device fabrication, especially when the ion beam is used to structure these materials laterally.

6 Defect engineered VO_2 metasurfaces

An ultra-thin film of VO_2 on a sapphire substrate can be tuned into a near-perfect absorption, non-reflecting state by varying the temperature in the vicinity of the IMT.[38,44,76] The IMT in VO_2 is particularly interesting because it occurs gradually over a range of temperatures. In close proximity to its phase transition, an intrinsic VO_2 film comprises randomly distributed islands of the metallic and insulating phase with sub-wavelength dimensions.[63] Optically, the resulting effective medium behaves as a tunable disordered metamaterial with giant optical absorption in a small infrared wavelength band (compare section 3.5).[38,44] However, the intrinsic transition temperature of VO_2 of approximately 70 °C limits the utility of this material for device fabrication.

In this thesis, ion irradiation is demonstrated to modify the thermally driven IMT of VO_2 via the intentional creation of structural defects and lattice damage. Unlike existing means to modify the IMT of VO_2 via doping during growth,[95] or via strain engineering,[163,166,326] ion irradiation can be combined with lithographic patterning to locally adjust the IMT. The shape, temperature, and persistence of the phase coexistence regions can be controlled by selectively irradiating appropriate regions of the VO_2 film on a nanometer scale. This allows to create complex optical metasurfaces with designer phase transitions. Parts of the results presented in this chapter are published in reference [44].

6.1. Optical properties of irradiated VO_2

The optical metasurfaces presented in this thesis are based on a local shift of the phase transition temperature of VO_2 by area-selective ion irradiation. Provided the induced shift is large enough, the phase transition from insulating to metallic in the irradiated VO_2 regions will be completed at a temperature lower than the phase transition temperature of intrinsic VO_2. Thus, a thermally switchable optical three state system can be realized: I) The entire film is insulating. II) Irradiated regions are yet metallic and intrinsic regions are still insulating. III) The entire film is metallic. A change of the optical properties by ion irradiation is not desirable for this kind of metasurfaces but almost inevitable. A local change of the optical properties can also be exploited.[327] However, those devices usually cannot be significantly tuned by an external stimulus.

Temperature-dependent variable angle spectroscopic ellipsometry was employed to compare the optical properties of intrinsic and ion irradiated VO_2 ($190\,\mathrm{keV}$ Cs^+, $N_I = 2 \times 10^{13}\,\mathrm{cm}^{-2}$) in both the insulating M1 and the metallic R phase (see figures 6.1a,b). Ion irradiation clearly changes the real n and imaginary part κ of the complex refractive index in both phases of VO_2 throughout the entire spectral region from UV-VIS-NIR (figure 6.1a) to mid-IR (figure 6.1b). A significant red-shift of the spectral features of n and κ associated with interband transitions is observed for irradiated VO_2 in the UV-VIS spectral region in figure 6.1a. A direct assignment of the electronic transitions is possible in the real part of the optical conductivity

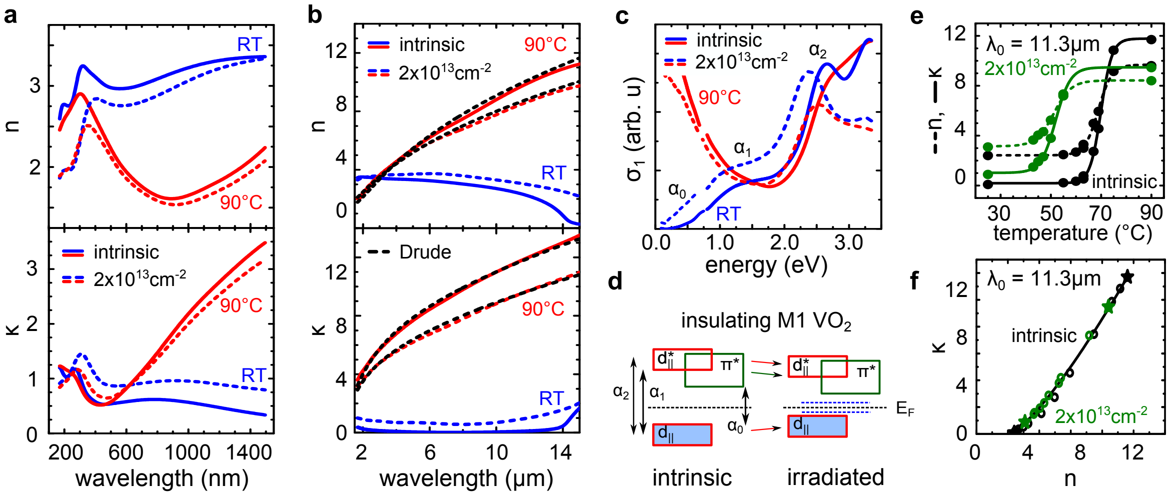

Figure 6.1.: (a, b) Real n and imaginary part κ of the refractive index of intrinsic (solid lines) and irradiated (dashed lines) VO_2 thin films in the UV-VIS-NIR (a), and in the mid-IR spectral range (b), determined by spectroscopic ellipsometry at room temperature (RT, blue) and 90 °C (red), respectively. Ion irradiation was performed with 190 keV Cs^+ and an ion fluence of $N_I = 2 \times 10^{13}\,\text{cm}^{-2}$ at room temperature. Black dashed lines in (b) are Drude model fits. **(c)** Real part of the optical conductivity σ_1 calculated from refractive index data given in (a) and (b). Features, that correspond to optical transitions in the M1 phase are labeled according to (d) and figure 2.3b. **(d)** Schematic of the electronic band structure of intrinsic and irradiated VO_2. **(e, f)** Temperature-dependence (e) and contour plot (f) of the n (dashed lines in e) and κ values (solid lines in e) of intrinsic (black) and irradiated (green) VO_2 thin films at $\lambda_0 = 11.3\,\mu$m. The effective medium approximation of intrinsic refractive index values is given as a solid line in (f).

σ_1, which is plotted as a function of photon energy $\hbar\omega$ in figure 6.1c (compare also section 2.1.2). Solid and dashed lines represent σ_1 of intrinsic and irradiated VO_2, respectively, in both the M1 (blue) and R phase (red). All features of σ_1 in the M1 phase can be assigned to optical transitions from the filled $d_{||}$ band to both the empty π^* (α_1) and the empty $d_{||}^*$ band (α_2) across the optical band gap (α_0, compare figure 6.1d). In the M1 phase, ion irradiation with the parameters given above reduces the band gap energy α_0 from approximately 0.5 eV to roughly 0.1 eV, and shifts down the energy for the electronic transitions α_1 and α_2 by roughly the same value of 0.4 eV. The corresponding change of the electronic band structure near the Fermi energy is schematically depicted in figure 6.1d. The band gap energy of VO_2 is reduced by the formation of multiple states within the band gap, a downshift of the π^* band with respect to E_F, and a reduced splitting of the $d_{||}$ band. The formation of a large number of electronic states within the band gap of VO_2 induced by ion irradiation is evident from a non-zero value of κ in the mid-IR (compare dashed blue curve in figure 6.1b). According to Zhang *et al.*[328] and Tan *et al.*[84] a weakening of the vanadium-vanadium interaction by charge carrier doping leads to the observed downshift of the conduction band formed by π^* and $d_{||}^*$ bands and the upshift of the valance band $d_{||}$. In contrast, Aetukuri *et al.*[100] and Fan *et al.*[326] consistently report an increased splitting of the $d_{||}$ and $d_{||}^*$ band for purely strained VO_2 films, which show a reduced phase transition temperature. That is, electronic doping by charged defects is crucial to explain the observed optical conductivity of ion irradiated VO_2. The optical conductivity of VO_2 in the metallic R phase at low photon energies is dominated by a Drude tail caused by intraband transitions (compare figure 6.1c), which results in a large value of κ especially in the mid-IR spectral region (compare figure 6.1b). Ion irradiation leads to a decrease of σ_1 in this spectral region and consequently results in a reduction of κ in the mid-IR. Further details are obtained by fitting the mid-IR refractive index data of intrinsic and irradiated R VO_2 with a simple Drude model (black dashed lines in figure 6.1b):

$$\tilde{n}(\omega)^2 = \epsilon(\omega) = \epsilon_\infty \left(1 - \frac{\omega_p^2}{\omega(\omega + \mathrm{i}\Gamma)}\right), \tag{6.1}$$

where ϵ_∞ is the high-frequency dielectric constant, ω_p is the screened plasma frequency, and Γ is a scattering rate. The scattering rate is related to the mobility μ of the charge carriers through $\Gamma = e/m^*\mu$, where e is the elementary charge and m^* is the effective mass of the electron. The formation of lattice defects limits the mean free path of charge carriers and increases the scattering rate of free electrons from $\Gamma = 0.59\,\mathrm{eV}$ for intrinsic VO_2 to $\Gamma = 0.86\,\mathrm{eV}$ for irradiated VO_2. The plasma frequency is related to the free carrier concentration N through $N = \epsilon_0\epsilon_\infty\omega_p^2 m^*/e^2$, where ϵ_0 is the vacuum permittivity. Although ω_p increases slightly from 1.39 eV to 1.47 eV upon ion irradiation, a decreasing value of ϵ_∞ from 7.7 eV to 6.3 eV results in an almost constant value of the free carrier concentration, assuming that m^* is constant. Thus, the change of n and κ due to ion irradiation cannot be attributed to a change of free carrier concentration and is most likely related to an increased scattering rate of charge carriers on irradiation defects. The determined values of ω_p and ϵ_∞ of intrinsic VO_2 are in good agreement with previously reported values.[274,329]. The reported values of m^* differ greatly and range from $1.5\,m_0$ to $23\,m_0$,[177,329–331] which results in an estimated free carrier concentration on the order of 10^{21} to $10^{22}\,\mathrm{cm}^{-3}$ for both intrinsic and irradiated metallic VO_2.

In summary, besides the shift of the phase transition temperature, ion irradiation lowers the considerable change of the complex refractive index across the phase transition of VO_2, especially in the mid-IR spectral region. As an example, figure 6.1e shows the temperature dependent values of n and κ for intrinsic and irradiated VO_2 at a fixed wavelength of $\lambda_0 = 11.3\,\mu$m. For this wavelength the complex refractive index of intrinsic VO_2 changes from $\tilde{n} = 2.4 + 0.1\,\mathrm{i}$ to $\tilde{n} = 9.6 + 11.7\,\mathrm{i}$ across the IMT. The change of the complex refractive index (n and κ, respectively) of irradiated VO_2 is noticeable smaller (from $\tilde{n} = 3.1 + 0.9\,\mathrm{i}$ to $\tilde{n} = 8.4 + 9.4\,\mathrm{i}$). However, these differences almost not affect the effective optical properties attainable in the temperature region of phase coexistence of metallic and insulating VO_2. Although the start and end values are different, the effective refractive index trajectory of irradiated VO_2 matches the effective refractive index trajectory obtained for intrinsic VO_2 in the vicinity of the IMT (compare figure 6.1f). Note that different metallic fractions are necessary to obtain comparable effective index values for intrinsic and irradiated VO_2.

6.2. Maintaining the VO_2 disordered metasurface

An ultra-thin film of intrinsic vanadium dioxide in its transitional state behaves optically like a disordered metasurface when deposited on a metallic substrate, such as Al_2O_3 in its reststrahlen band region.[38,44,76] The combination of effective optical properties of VO_2 associated with the phase coexistence of insulating and metallic domains and metal-like optical properties of the substrate lead to the occurrence of an ultrahin-film interference (compare section 3.5). As discussed previously, a 100 nm intrinsic VO_2 film on Al_2O_3 can be tuned in and out of a zero-reflection state at $\lambda_0 = 11.3\,\mu$m by changing the temperature in close proximity to the phase transition temperature (compare figures 6.2a I, 6.2c black curve, and section 5.1.5).

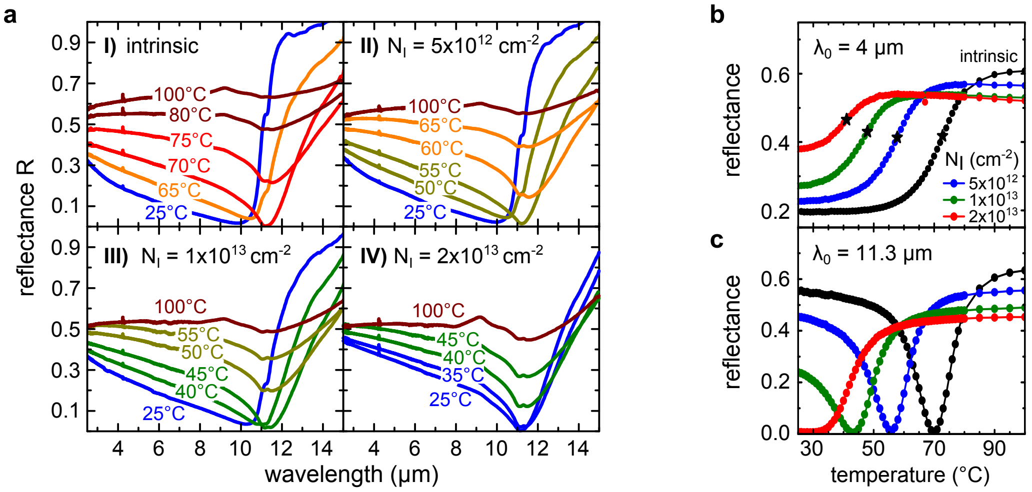

Figure 6.2.: **(a)** Temperature-dependent reflectance spectra of intrinsic (I) and various irradiated regions (II-IV) of an approximately 100 nm thin VO_2 film on Al_2O_3 substrate. Ion irradiation was performed through an apperture of $2 \times 2\,mm^2$ using 190 keV Cs^+ with ion fluences up to $N_I = 2 \times 10^{13}\,cm^{-2}$ at room temperature. **(b,c)** Temperature-dependent reflectance at a fixed wavelength of $\lambda_0 = 4$ (b) and $11.3\,\mu m$ (c). The critical temperature of the IMT (black stars) is slightly higher than the temperature of minimal reflectance.

To investigate how ion irradiation affects the occurrence of this zero-reflection state, different $2 \times 2\,mm^2$ regions of an approximately 100 nm thin VO_2 film on Al_2O_3 were irradiated with 190 keV Cs^+ ions and with various ion fluences up to $N_I = 2 \times 10^{13}\,cm^{-2}$ through a copper aperture at room temperature. The effective optical properties of the intrinsic and irradiated VO_2 regions were studied via temperature-dependent mid-IR reflectance measurements using a mid-IR microscope attached to a Fourier transform infrared spectrometer. Figure 6.2a compares the obtained reflectance spectra during a heating cycle, respectively. The spectra of irradiated VO_2 regions (figures 6.2a II-IV) qualitatively resemble the spectra of intrinsic VO_2 (figure 6.2a I) throughout the entire mid-IR. A comparable reflectance minimum of $R_{min} < 0.01$ is reached at $\lambda_{min} = 11.3\,\mu m$ in all regions independent of the respective ion fluence. The temperature T_{min} at which the reflectance minimum occurs decreases with increasing ion fluence and reaches room temperature for $N_I = 2 \times 10^{13}\,cm^{-2}$. Note that the reflectance curve obtained at room temperature for this ion fluence is comparable to the reflectance curve measured at 70 °C for intrinsic VO_2.

Figures 6.2b and 6.2c compare the temperature dependent reflectance of intrinsic and irradiated VO_2 regions at a fixed wavelength of $\lambda_0 = 4.0$ and $11.3\,\mu m$, respectively. Note, ion irradiation with an increasing ion fluence results in a strong decreased reflectance change at $4\,\mu m$ across the phase transtion, which is in agreement with the previously discussed refractive index change. The critical temperature of the phase transition in the heating cycle T_C^h was determined from the reflectance derivative at $\lambda_0 = 4.0\,\mu m$ (marked with black stars in figure 6.2b). The critical temperature decreases from $T_C^h \sim 73\,°C$ for intrinsic VO_2 regions to $T_C^h \sim 41\,°C$ for VO_2 regions irradiated with an ion fluence of $N_I = 2 \times 10^{13}\,cm^{-2}$, which is in agreement with previous sections. Note, a strong sample to sample variation of T_C^h is observed, most likely due to a varying film quality and different film thicknesses. However, the temperature at which the reflectance minimum occurs decreases much stronger from $T_{min} \sim 70\,°C$ to room temperature (compare figure 6.2c). The reason is that zero-reflection at a given wavelength occurs for a specific effective refractive index of the VO_2 film and not at a fixed temperature

($\tilde{n} = 3.8 + 2.3\mathrm{i}$ at $\lambda_0 = 11.3\,\mu$m, compare section 3.5). The temperature dependent effective refractive index depends on the complex refractive index of both insulating and metallic VO_2 and the temperature dependent metallic fraction. As demonstrated previously, the reflectance minimum occurs at a metallic fraction of 32 % for intrinsic VO_2 (compare section 3.5). Ion irradiation with an increasing ion fluence changes the complex refractive index in such a way that a decreasing metallic fraction is sufficient to obtain the specific effective refractive index and thus, zero reflectance. Strikingly, ion irradiation with $N_I = 2 \times 10^{13}\,\mathrm{cm}^{-2}$ results in a complex refractive index of the insulating state which already meets the requirements for zero-reflection at $\lambda_0 = 11.3\,\mu$m. That is, a reflectance minimum is observed when the irradiated VO_2 film is in the insulating phase and persists until the onset of the IMT. Although ion irradiation changes the optical properties somewhat, the zero-reflection state is maintained. Individual irradiated regions of a VO_2 thin film on an Al_2O_3 substrate remain disordered metasurfaces with adjusted temperature at which the reflectance minimum occurs.

6.3. Isotropic metasurfaces: checkerboard pattern

Isotropic metasurfaces composed of irradiated and intrinsic VO_2 regions in a square checkerboard arrangement were fabricated by irradiating a 100 nm thin VO_2 film on c-plane Al_2O_3 with 190 keV Cs^+ ions through a PMMA mask, which was defined by electron-beam lithography (compare figure 6.3a). The mask is approximately 300 nm thick, which is sufficient to prevent ions from penetrating through the covered regions. The period of the unit cell of the pattern is 500 nm and thus, substantially smaller than the wavelength of mid-IR light. The edge length a of masked regions within the unit cell was varied in order to achieve various duty cycles F of the pattern. Each pattern covers a region of $100 \times 100\,\mu$m and the distance between the patterns is $500\,\mu$m. An ion fluence $N_I = 1 \times 10^{13}\,\mathrm{cm}^{-2}$ was used for ion irradiation at room temperature. The fluence is sufficient to decrease the critical temperature of the IMT of the irradiated VO_2 regions by roughly 20 °C (compare figure 6.2d). In the temperature interval, in which irradiated VO_2 regions of the pattern are yet metallic but intrinsic VO_2 regions are still insulating, phase coexistence is artificially introduced. For comparison, intrinsic and fully irradiated regions on the sample were defined by completely covering and not covering parts of the sample with PMMA.

The effective optical properties of the checkerboard structure ($F = 0.5$) were investigated by measuring the temperature-dependent reflectance in the central part ($50 \times 50\,\mu\mathrm{m}^2$) of the pattern using the mid-IR microscope. Selected reflectance spectra obtained during a heating cycle are shown in figure 6.3b. At low temperatures, both intrinsic and irradiated regions of the pattern are in the insulating state and the entire pattern is basically transparent. As discussed previously, the reflectance spectrum is dominated by the onset of metallic reflectance of the Al_2O_3 substrate (compare sections 3.5 and 5.1.5). As the temperature is increased, irradiated regions of the pattern undergo the IMT first and consequently, a reflectance minimum appear at $\lambda_{\mathrm{min}} = 11.3\,\mu$m. This reflectance minimum, which was previously observed for intrinsic and fully irradiated VO_2 samples, occurs at a temperature of approximately $T_{\mathrm{min}} \sim 60\,°\mathrm{C}$. At this temperature, the effective optical properties of the checkerboard structure match the ultrathin-film interference condition (compare section 3.5). At high temperatures, intrinsic and irradiated regions of the pattern are both in the metallic phase, which leads to high reflectance values throughout the entire mid-IR.

In particular, the reflectance of the pattern at $\lambda_{\mathrm{min}} = 11.3\,\mu$m as a function of temperature

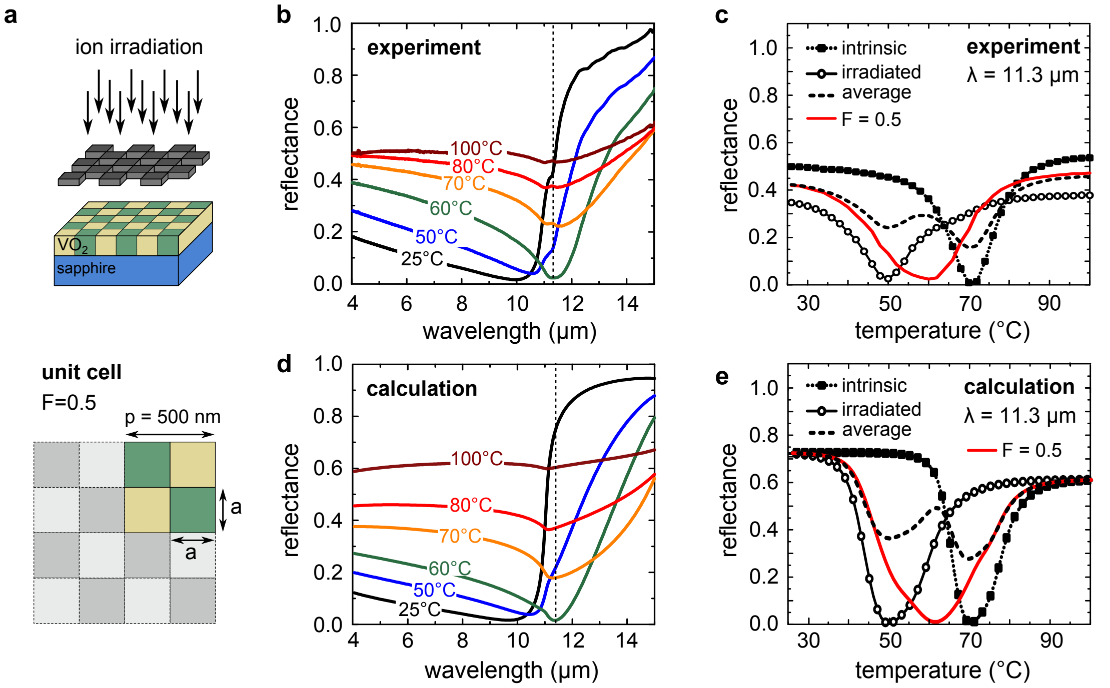

Figure 6.3.: **(a)** Schematic drawing of ion irradiation through a mask to create a checkerboard irradiation pattern and definition of the unit cell of the resulting checkerboard pattern. **(b)** Measured temperature-dependent reflectance spectra of the checkerboard structure (duty cycle $F = 0.5$, $p = 500\,\mathrm{nm}$, and $a = 250\,\mathrm{nm}$) created within a 100 nm thin VO$_2$ film on Al$_2$O$_3$. **(c)** Measured reflectance of intrinsic, checkerboard structure ($F = 0.5$) and completely irradiated VO$_2$ films as a function of temperature at $\lambda_0 = 11.3\,\mu\mathrm{m}$. **(d,e)** Calculated reflectance for the sample measured in (b,c) using Fresnel equations and effective medium approximation.

shows that the checkerboard structure ($F = 0.5$) with its subwavelength features posses effective optical properties that cannot be trivially deduced by averaging the reflectance of intrinsic and fully irradiated VO$_2$ regions of the sample (compare figure 6.3c). The reflectance minimum of intrinsic and fully irradiated regions is observed independently at approximately $T_{\mathrm{min}} \sim 70$ and $\sim 50\,^\circ\mathrm{C}$ with a full width at half-minimum (FWHM) of ~ 12 and $\sim 15\,^\circ\mathrm{C}$, respectively, which is in good agreement with previously obtained results (compare figure 6.2c). In contrast, the checkerboard structure appears to have a single effective reflectance minimum at approximately $\sim 60\,^\circ\mathrm{C}$, with a much larger FWHM of $> 25\,^\circ\mathrm{C}$. Usually, the reflectance minimum occurs in the vicinity of the IMT of VO$_2$. Therefore, it seems as if the checkerboard structure undergoes a single effective phase transition.

Because of the subwavelength dimensions of the intrinsic and irradiated regions of the checkerboard structure, the patterned VO$_2$ film can be treated as an effective medium that has a well-defined temperature- and wavelength-dependent complex refractive index:[44]

$$\tilde{n}_{\mathrm{eff}}^{\mathrm{check}}(T) = \sqrt{\tilde{n}_{\mathrm{eff}}^{\mathrm{int}}(T)\tilde{n}_{\mathrm{eff}}^{\mathrm{irr}}(T)}, \tag{6.2}$$

where $\tilde{n}_{\mathrm{eff}}^{\mathrm{int}}(T)$ and $\tilde{n}_{\mathrm{eff}}^{\mathrm{irr}}(T)$ are the temperature-dependent effective complex refractive indices of intrinsic and irradiated VO$_2$ regions. The effective refractive indices of these regions are calculated from the refractive indices of insulating and metallic VO$_2$, extracted from the measurements of intrinsic VO$_2$ of Qazilbash *et al.*[63], using Lichteneckers effective medium approximation (compare section 3.5). The temperature-dependent metallic fraction in the intrinsic and irradiated regions of the pattern was estimated by fitting the reflectance spectra obtained from intrinsic and fully irradiated VO_2 regions on the sample, respectively. Reflectance spectra of the checkerboard pattern were calculated for various temperatures using $\tilde{n}_{\text{eff}}^{\text{check}}(T)$ and Fresnel equations. A detailed description of the calculations can be found in section 3.5. The obtained reflectance spectra, which are shown in figure 6.3d, are in good agreement with the measured spectra (compare figure 6.3b). The wavelength, temperature and FWHM of the reflectance minimum is predicted correctly (compare figures 6.3c and 6.3e). Differing absolute reflectance values are most likely caused by neglecting the refractive index change caused by ion irradiation induced defects for the irradiated regions and a different optical quality of the intrinsic VO_2 sample compared to that in reference [63].

The results demonstrate that artificial phase coexistence can be introduced by area-selective ion irradiation. The temperature range of phase coexistence can be greatly increased compared to intrinsic VO_2, because the metallic fraction will remain roughly constant in the temperature range between the individual phase transition temperatures of intrinsic and irradiated VO_2 regions. Thus, the optical properties of a patterned VO_2 thin film can be tuned in and out of an artificially designed effective medium state over a desired range of temperatures. In contrast, when T_{min} of a VO_2 film is adjusted by ion irradiation without patterning, a specific metallic fraction is reached only at a certain temperature. The metallic fraction and consequently, the zero-reflection state does not persist over a range of temperatures. Note that a vertical distribution of phase transition temperatures, which can be achieved for example by doping during growth,[242] results in a similar persistent artificial phase coexistence state with comparable effective optical properties (compare section 3.7).

The metallic fraction of the checkerboard structure in the temperature range of artificial phase coexistence can be adjusted by changing the duty cycle F of the pattern (compare figure 6.4a). Several checkerboard-like structures with the same period of the unit cell ($p = 500\,\text{nm}$) but varying area fractions ($f = 0.25$, 0.5, and 0.75) of masked regions within the unit cell ($a = \sqrt{1/2} \times 250\,\text{nm}$, $a = 250\,\text{nm}$, and $a = \sqrt{3/2} \times 250\text{nm}$, compare figure 6.3a) were fabricated on the sample used in figure 6.3. Independent of F, a reflectance minimum is observed at a wavelength of $\lambda_{\text{min}} = 11.3\,\mu\text{m}$ for all patterned VO_2 regions. Figure 6.4b compares the measured reflectance of the differently patterned VO_2 regions with varying values of F at $11.3\,\mu\text{m}$ as a function of temperature. In perfect agreement with calculations presented in section 3.5, the temperature at which the reflectance minimum occurs can be continuously tuned between T_{min} of intrinsic and fully irradiated VO_2 regions by adjusting F (compare figure 6.4c).

One requirement for the applicability of ion-beam engineered VO_2 metasurfaces is its stability. An extensive thermal stability test was performed with the checkerboard sample ($F = 0.5$). The sample was repeatedly cycled through the IMT in the temperature range from 30 to 100 °C with a heating and cooling rate of approximately 0.5 °C/min, respectively. The temperature-dependent reflectance at $\lambda_{\text{min}} = 11.3\,\mu\text{m}$ was measured before cycling, and after 200 and 400 cycles (compare figure 6.4d). Although the absolute values differ slightly, predominantly caused by a different placement of the sample under the IR-microscope, the point of minimum reflectance at $\lambda_{\text{min}} = 11.3\,\mu\text{m}$ remains constant at $T_{\text{min}} \sim 60\,°\text{C}$, indicating good thermal stability of the checkerboard patterned sample.

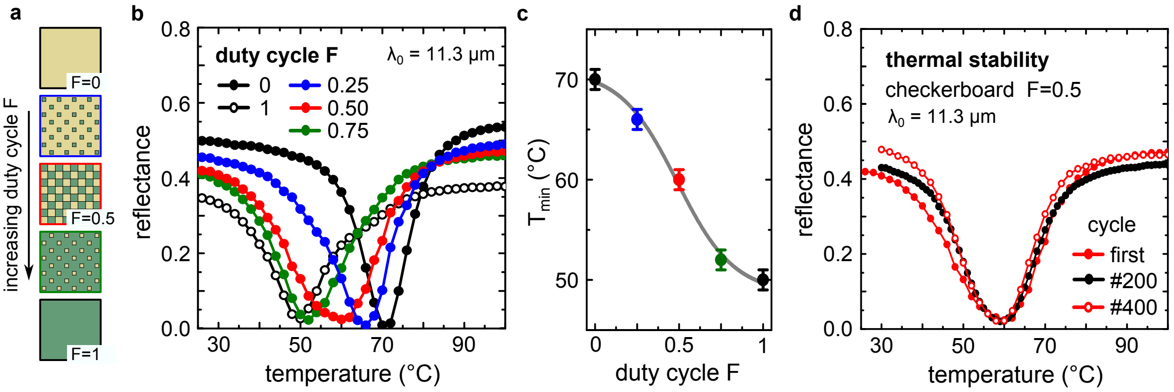

Figure 6.4.: **(a)** Schematic drawing of the checkerboard pattern with increasing duty cycle F. **(b)** Reflectance of various checkerboard patterned 100 nm thin VO_2 films on Al_2O_3 as a function of temperature at a fixed wavelength of 11.3 μm. **(c)** Temperature T_{min} at which the reflectance minimum occurs as a function of F. **(c)** Thermal stability test of the checkerboard structure ($F = 0.5$). The reflectance was measured as a function of temperature in the first heating cycle, and after 200 and 400 cycles, respectively.

6.4. Anisotropic metasurfaces: grid pattern

Optical functionality can be achieved by realizing anisotropic VO_2 metasurfaces with temperature-tunable dichroism. Dichroic materials are those in which light of different polarization states is absorbed by a different amount. Anisotropic phase coexistence has been observed for ultra-thin VO_2 films on TiO_2 substrates and occurs naturally due to anisotropic epitaxial strain.[66] The thickness-dependent strain induces a stripe phase pattern in the VO_2 thin films in the vicinity of the IMT.[66,332] However, strain engineered dichroism is limited to particular substrates and provides little control over the degree of anisotropy.

According to the natural model a periodic structure consisting of parallel ridges with a width of 0.5 μm and a period of $p = 1\,\mu$m was fabricated by irradiating a suitably PMMA masked 100 nm thin VO_2 film on Al_2O_3 with 190 keV Cs^+ ions at an ion fluence of $N_I = 2 \times 10^{13}\,\mathrm{cm}^{-2}$ (compare figure 6.5a). The temperature-dependent reflectance of this pattern was investigated using a mid-IR micsrocope and linear polarized incident light. The reflectance of the anistropic VO_2 structure depends on the incident polarization over most of the mid-IR wavelength region in the temperature range of artificial phase coexistence. As an example figure 6.5b shows the reflectance of light that is polarized parallel ($E_{||}$, red solid curve) and perpendicular ($E_\perp$, black solid curve) to the ridges of the structures at a fixed temperature of 60 °C. At this temperature a reflectance minimum caused by ultrathin-film interference is only observed for parallel polarized light at a wavelength of approximately $\lambda_{\mathrm{min}} = 11\,\mu$m, indicating a large degree of dichroism.

Figure 6.5c shows the measured polarization-dependent reflectance at $\lambda_0 = 11\,\mu$m as a function of increasing temperature and figure 6.5d summarizes the reflectance of light polarized parallel ($E_{||}$, red open circles) and perpendicular to the ridges ($E_\perp$, black open circles) as a function of temperature, respectively (right axis). The reflectance is small from 40 to 70 °C for light polarized parallel to the ridges, and a value of $R^{||}_{\mathrm{min}} = 0.009$ is reached at a temperature of $T^{||}_{\mathrm{min}} = 45\,°\mathrm{C}$. At the same temperature, the reflectance for light polarized perpendicular to the ridges is $R^{\perp}_{45\,°\mathrm{C}} = 0.17$. Although a comparable reflectance minimum occurs for orthogonal polarization, it appears at much higher temperatures between 70 and 75 °C and is less pronounced. As a consequence, in the temperature range of artificial phase coexistence

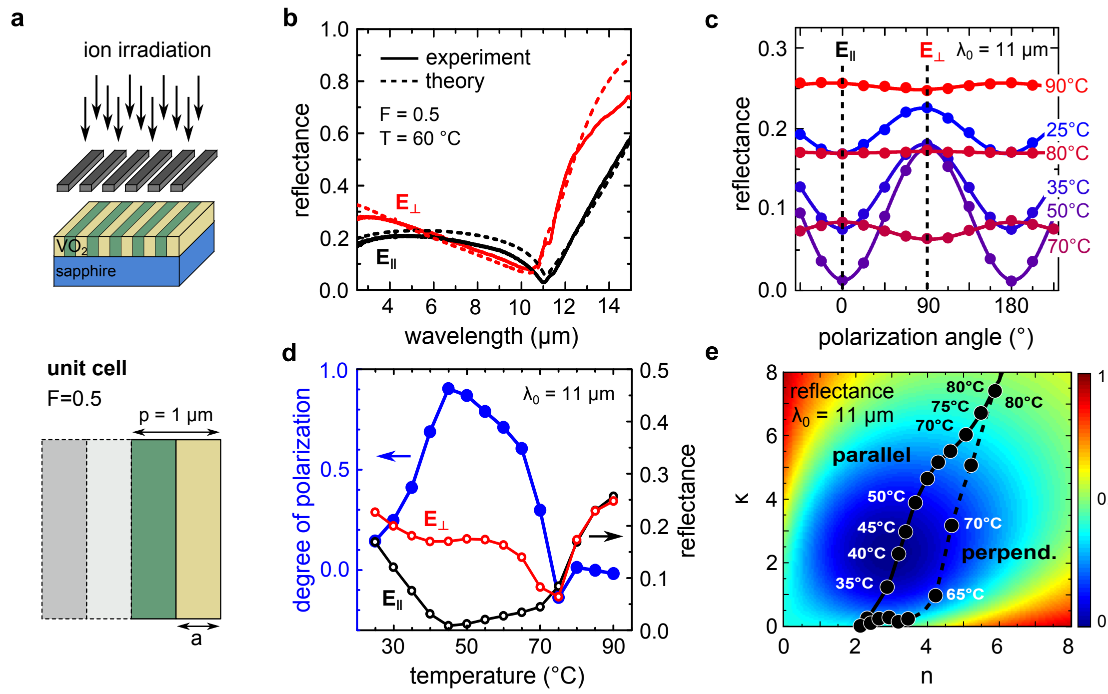

Figure 6.5.: **(a)** Schematic drawing of ion irradiation through a mask to create a striped irradiation pattern and definition of the unit cell of the resulting anisotropic structure. **(b)** Measured (solid lines) and calculated (dashed lines) reflectance of the anisotropic structure (duty cycle $F = 0.5$, $p = 1\,\mu$m) created within a 100 nm thin VO_2 film on Al_2O_3 at a fixed temperature of 60 °C. The incident light is polarized parallel ($E_{||}$, black curves) and perpendicular ($E_{\perp}$, red curves) to the ridges of the structure, respectively. **(c)** Evoulution of the polarization-dependent reflectance at $\lambda_0 = 11$ mum for increasing temperatures between 25 °C and 90 °C. **(d)** Degree of polarization (left axis), and reflectance for both polarizations of incident light (right axis) as a function of temperature. **(e)** Calculated map of the reflectance at $\lambda_0 = 11\,\mu$m as a function of the real n and imaginary part κ of the complex refractive index of an arbitrary 100 nm thin film on Al_2O_3. The solid and dashed line marks the calculate temperature-dependent effective complex refractive index of a stripe patterned VO_2 film for light that is polarized parallel and perpendicular to the ridges, respectively.

unpolarized light, which is reflected from the patterned VO_2 film, becomes highly polarized with a degree of linear polarization of roughly 90 % (compare figure 6.5, blue data points, left axis), defined as intensity of light reflected with the preferential polarization minus the intensity of light reflected perpendicular to it divided by the sum of both.[333] The polarization dependence almost completely vanishes above 75 °C, as both regions become metallic. Therefore, the anisotropic VO_2 structure can be tuned in and out of a highly polarizing state by tuning the temperature in the vicinity of the effective IMT temperature.

In agreement with the previous section, the striped VO_2 pattern can be treated as an effective medium with well-defined temperature- and wavelength-dependent complex refractive index. When the wavelength is sufficiently large, $\lambda_0 >> p$, the effective complex refractive index in the direction parallel ("ordinary") and perpendicular to the ridges ("extraordinary") can be expressed as:[187]

$$\begin{aligned}\tilde{n}_{\mathrm{o}}(T) &= \left[(1-F)\,\tilde{n}_{\mathrm{eff}}^{\mathrm{int}^2}(T) + F\,\tilde{n}_{\mathrm{eff}}^{\mathrm{irr}^2}(T)\right]^{1/2}\\ \tilde{n}_{\mathrm{e}}(T) &= \frac{\tilde{n}_{\mathrm{eff}}^{\mathrm{int}}(T)\,\tilde{n}_{\mathrm{eff}}^{\mathrm{irr}}(T)}{\left[F\,\tilde{n}_{\mathrm{eff}}^{\mathrm{int}^2}(T) + (1-F)\,\tilde{n}_{\mathrm{eff}}^{\mathrm{irr}^2}(T)\right]^{1/2}},\end{aligned} \tag{6.3}$$

respectively, where F is the duty cycle (area coverage of irradiated VO_2 regions), and $\tilde{n}_{\text{eff}}^{\text{int}}(T)$ and $\tilde{n}_{\text{eff}}^{\text{irr}}(T)$ are the temperature-dependent effective complex refractive indices of intrinsic (int) and fully irradiated (irr) VO_2 regions discussed previously (compare section 6.3). The calculated effective index trajectories are depicted in figure 6.5e onto the reflectance map in n-κ space for a 100 nm thin film of arbitrary refractive index on an Al_2O_3 substrate at $\lambda_0 = 11\,\mu$m (compare section 3.5). At temperatures lower than 25 °C and higher than 75 °C, the refractive index values for parallel and perpendicular polarized light are basically the same, whereas for intermediate temperatures a huge difference is observed, because of the artificially induced anisotropy. The calculated index trajectory for parallel polarized light almost crosses the point of zero reflection at a temperature of approximately 40 °C, which is qualitatively in agreement with the measured reflectance. In contrast, the index trajectory for perpendicular polarized light passes the point of zero reflection in some distance at a temperature between 65 and 70 °C, which lead to a higher value of minimal reflection observed for this polarization. Calculated reflectance spectra for a temperature of 60 °C are shown in figure 6.5b as dashed lines and are in good agreement with the experimental data. Differing absolute reflectance values are most likely attributed to irradiation induced changes of the refractive index of irradiated VO_2 regions, which are neglected in the calculations.

The results demonstrate that a defect engineered, anisotropically structured VO_2 film can be tuned into a form birefringente state with birefringence values as large as $\Delta n = n_e - n_o \sim 0.8$ in the temperature range of artificial phase coexistence ($\lambda_0 = 11\,\mu$m, $T \sim 60$ °C). In contrast, typical values achievable using, for example, the Kerr effect are not greater than $\sim 10^{-4}$ [334]. Note, birefringence refers to the real part of the complex refractive index. The large difference of κ_e and κ_o, which occurs in this temperature range, leads to a strong dichroic behavior ($\Delta k = k_e - k_o sim - 4.9$ with $k_e = 0.15$ at $\lambda_0 = 11\,\mu$m, $T \sim 60$ °C).

6.5. Near-field imaging of artificial phase coexistence

Although far-field measurements can probe the effective optical properties of the isotropic and anisotropic metasurfaces, the subwavelength structures of ion-beam patterned VO_2 films itself cannot be resolved due the the diffraction limit. To explore the limits of area-selective ion irradiation, such as the sharpness of the boundary between intrinsic and irradiated VO_2 regions, scattering-type scanning near-field optical microscopy at a CO_2 laser wavelength of 10.9 μm was employed.

Near-field and AFM topography images of the anisotropic ridge structure, which was described in detail in the previous section, were recorded simultaneously at increasing temperatures ranging from −30 to 80 ° C (see figure 6.6a). The near-field images contain highly localized information about the dielectric function of the patterned VO_2 film, especially the local charge distribution, and provide a contrast between the insulating and metallic VO_2 phase.[335] Insulating regions cause a low scattering amplitude and appear dark blue, whereas metallic regions give rise to a high scattering amplitude and appear bright yellow in the near-field images. At low temperatures, both the intrinsic and irradiated VO_2 regions are in the insulating state (e.g. 6.6a, −40 °C). Due to a different defect density caused by ion irradiation, intrinsic regions appear slightly darker. As the temperature is increased, the irradiated areas undergo the IMT first, and thus, those regions appear brighter. Note that the irradiated ridges appear slightly darker than the fully irradiated surrounding of the pattern at a fixed temperature (e.g.

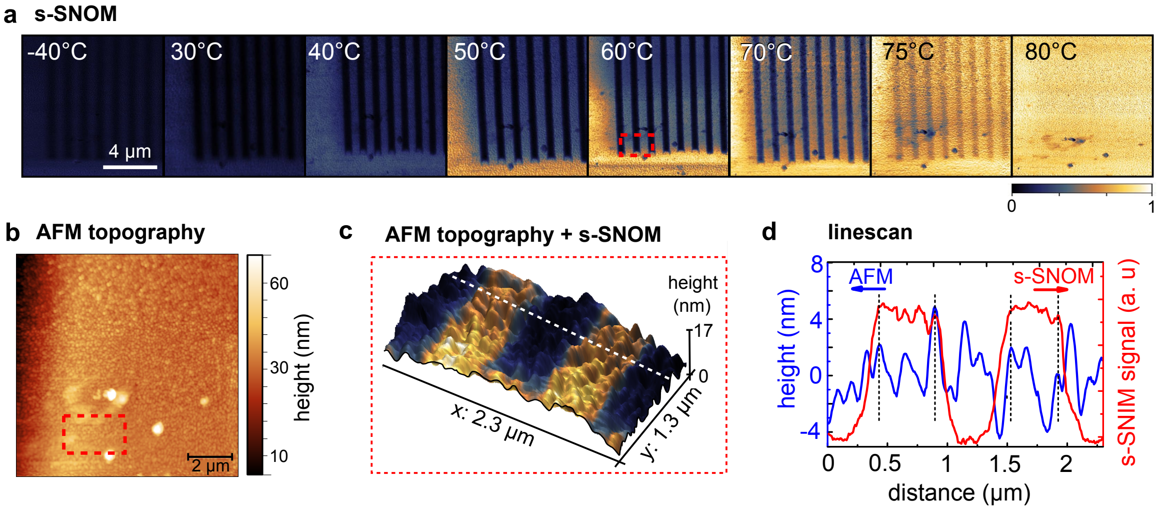

Figure 6.6.: (a) s-SNOM images of the scattering amplitude of the anisotropic ridge structure described in section 6.4 at $\lambda_0 = 10.9\,\mu$m for increasing temperatures. **(b)** Atomic force microscopy topography images of the area investigated in (a). **(c)** Topography of the sample measured by AFM [zoom-in, correspongind to the red dashed area in (a) and (b)] overlaid with the color map of the near-field scattering amplitude that was measured simultaneously at 60 °C. **(d)** Line scan of the AFM topography (blue curve) and near-field amplitude (red curve) taken at the line indicated in figure (c). Parts of the figure were published in [44].

6.6a, 60 °C). This behavior might be attributed to a different phase transition temperature of those regions and is most likely caused by strain relaxation and defect migration towards the adjacent intrinsic ridges. For increasing temperatures above 60 °C, the contrast between intrinsic and irradiated ridges decreases and vanishes completely at temperatures above 80 °C, which is in agreement with the reflectance measurements (compare figures 6.5c and 6.5d). At this temperature, the entire structure is in the metallic phase.

Figure 6.6b shows the AFM topography image of the patterned VO_2 area. Note the striking dirt particles which appear bright in the AFM image and dark in the s-SNOM images (compare 6.6a). The VO_2 film consists of tightly packed grains with an average diameter of ~ 100 nm. No indication of a height modulation caused by ion irradiation was found. Figure 6.6c compares a near-field image obtained at 60 °C with the simultaneously acquired topography information. The 3D topographic image is overlayed with the color map of the near-field scattering amplitude. The measured region corresponds to the red marked area in figures 6.6a and 6.6b. A representative line scan through the ridges is shown in figure 6.6d. Obviously, the spatial boundary between the metallic (irradiated) and insulating (intrinsic) VO_2 regions is not sharp but follows the grain boundaries. Strain relaxation in thin films tends to terminate at grain boundaries and the defect mobility into adjacent grains is strongly reduced. Therefore, the best spatial resolution with area-selective ion irradiation is reached when the grain size matches the lateral straggle of ions in the VO_2 film plane. The lateral straggle was determined using SRIM simulations and is on the order of 10 nm.

6.6. Area-selective defect engineering using the focused ion beam

Instead of an elaborate e-beam masking of VO_2, a focused ion beam can be used to locally modify the phase transition temperature of individual VO_2 regions (direct writing of an irradiation pattern, compare figure 6.7a). A common FIB system is restricted to gallium ions with a maximum energy of 30 keV. This energy limits the penetration depth of Ga^+ ions in VO_2 to approximately 16 nm. As a consequence, the defect distribution is very narrow and only affects the near-surface layer up to a depth of 20 nm with a defect concentration maximum at a depth of roughly 10 nm. First experiments were performed using two rather thick VO_2 films grown on Al_2O_3 with a thickness of 80 and 100 nm. Various $100 \times 100\,\mu$m VO_2 regions were irradiated at normal incidence with 30 keV Ga^+ and various ion fluences ranging up to $1.2 \times 10^{14}\,\mathrm{cm}^{-2}$ for the 80 nm film and up to $3.3 \times 10^{14}\,\mathrm{cm}^{-2}$ for the 100 nm thick VO_2 film. Platinum crosses were deposited prior to the irradiation to find the irradiated regions in the mid-IR microscope. After FIB irradiation, both samples were annealed for 30 min at 100 °C in air.

Figure 6.7b shows the reflectance of various irradiated regions of both samples at a fixed wavelength of $4\,\mu$m as a function of temperature measured during the heating cycle. In agreement with previous results, FIB irradiation with an increasing ion fluence decreases the critical temperature of the IMT of irradiated VO_2 regions with respect to intrinsic VO_2 (marked with open circles in figure 6.7b). However, the decrease is as small as $\sim -10\,°\mathrm{C}$ for the 80 nm VO_2 film and seems to saturate at $N_I = 8 \times 10^{13}\,\mathrm{cm}^{-2}$. A saturation of the critical temperature decrease is also found for the thicker VO_2 film at the same ion fluence, but the critical temperature change is only $\sim -5\,°\mathrm{C}$. Furthermore, FIB irradiation with an increasing ion fluence above $N_I = 1 \times 10^{14}\,\mathrm{cm}^{-2}$ results in a gradual increase of the critical temperature for this sample. Due to the limited range of Ga^+ ions, both VO_2 films consists of a thin irradiated ($d_2 \sim 20$ nm) and a thick intrinsic layer ($d_1 \sim 60$ nm and ~ 80 nm, respectively). The resulting two-layer system can be treated as a single homogeneous effective layer in the mid-IR with effective phase transition. The critical temperature of the effective IMT primarily depends on the layer thickness fraction $D = d2/(d1 + d2)$ (compare section 3.7). The critical temperature of the irradiated layer must be significantly lower. It is most likely that ion irradiation with fluences above $1.5 \times 10^{14}\,\mathrm{cm}^{-2}$ leads to a partial amorphization of the surface near layer. Since amorphous VO_2 regions do not feature an IMT, the critical temperature shifts back towards the intrinsic values. To directly measure the critical temperature of the IMT of irradiated regions, future experiments will be performed with VO_2 films that have a film thickness on the order of the penetration depth.

A FIB system can be used to directly write complex irradiation patterns with reduced phase transition temperature into VO_2 films (compare figure 6.7d). In contrast to masked ion irradiation, regions irradiated with different ion fluences can be easily combined to create complex irradiation patterns, like structures that involve phase transition temperature gradients. Such VO_2 structures will be investigated in a joined project with the European Synchrotron Radiation Facility (ESRF) Grenoble using full field diffraction X-Ray Microscopy and near-field imaging techniques as a function of temperature.

6.7. Summary

The optical properties of intrinsic and homogeneously irradiated VO_2 thin films were investigated via temperature-dependent spectroscopic ellipsometry measurements spanning the spectral region from UV/VIS to mid-IR wavelengths. Ion irradiation affects the refractive index of both insulating and metallic VO_2 due to increased scattering at irradiation defects and especially decreases the amplitude of the refractive index change across the IMT. However,

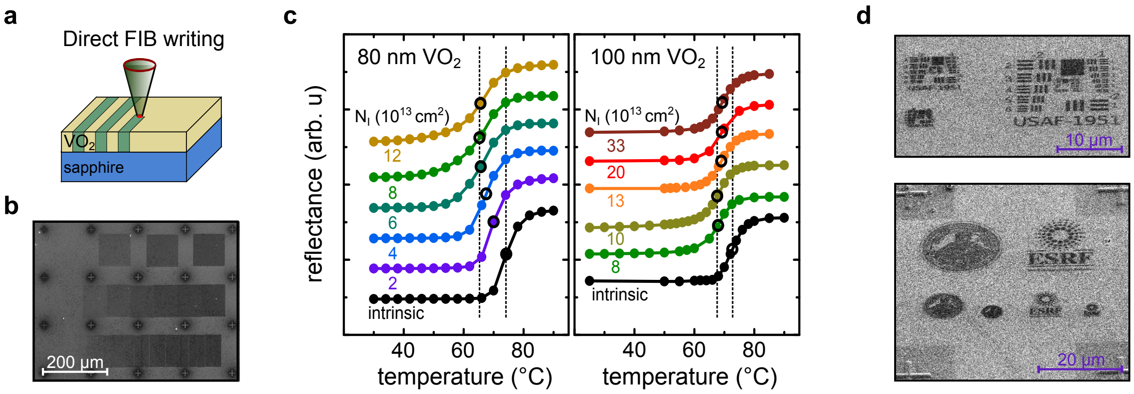

Figure 6.7.: **(a)** Schematic drawing of direct writing of an irradiation pattern using a focused ion beam. **(b)** SEM image of fully irradiated VO_2 regions using 30 keV Ga^+ ions and various ion fluences. Platinum crosses are deposited within the FIB system to find the irradiated regions in the mid-IR microscope. **(c)** Comparison of the temperature dependent reflectance of FIB irradiated VO_2 films with different thicknesses of 80 and 100 nm and for various ion fluences, respectively. **(d)** SEM image of a FIB patterned VO_2 film, which will be investigated using full field diffraction X-Ray Microscopy and near-field imaging. The test structures shown are an USAF 1951 resolution test and logos of the FSU Jena and the ESRF Grenoble. Note, the resolution of the SEM images in (b) and (d) is low and the contrast was not optimized in order to minimize the interaction time of sample and electron beam.

the effective optical properties of intrinsic and irradiated VO_2 films in the temperature range of phase coexistence, which can be successfully modeled by effective medium theory, are quite similar. Temperature-dependent mid-IR reflectance spectra of thin VO_2 films on Al_2O_3 were measured using a mid-IR microscope attached to an FTIR spectrometer. An ultra-thin film of VO_2 on Al_2O_3 can be tuned in and out of a zero-reflectance state, which is caused by ultra-thin film interference, by tuning the temperature in the vicinity of the IMT. Although the temperature at which the reflectance minimum occurs, can be significantly tuned by ion irradiation, its wavelength is not affected.

Isotropic and anisotropic metasurfaces composed of irradiated and intrinsic VO_2 regions in a square checkerboard and stripe pattern arrangement, respectively, were successfully fabricated using ion irradiation through e-beam defined irradiation masks. In a temperature region, were irradiated VO_2 is yet metallic, whereas intrinsic regions are still insulating, persistent phase coexistence is artificially introduced. Isotropic metasurfaces show a single effective phase transition at a temperature in between the phase transition temperature of intrinisc and irradiated VO_2. The temperature of the effective phase transition was adjusted, by changing the duty cycle of the pattern. Anisotropic VO_2 metasurfaces are demonstrated to be tunable reflection polarizes based on thermally triggered dichroism. Preferential absorption of light that is polarized parallel to the ridges of the pattern lead to a degree of linear polarization of 90 % within the temperature range of artificial phase coexistence. This behavior was successfully described using effective medium theory and extremely large values of form birefringence and optical dichroism ($\Delta n \sim 0.8$ and $\Delta k \sim\ -4.9$, respectively) were determined.

Temperature-dependent scattering-type SNOM was employed to study the near-field optical properties of the anisotropic metasurfaces. The scattering amplitude is sensitive to the different dielectric properties of insulating and metallic regions. The ridge pattern was successfully resolved in sSNOM images, whereas no indication of morphology changes were detected by AFM in the patterned region. Thus, VO_2 metasurfaces fabricated by ion irradiation are inherently flat. However, the domain size of the VO_2 film limits the resolution, that can be

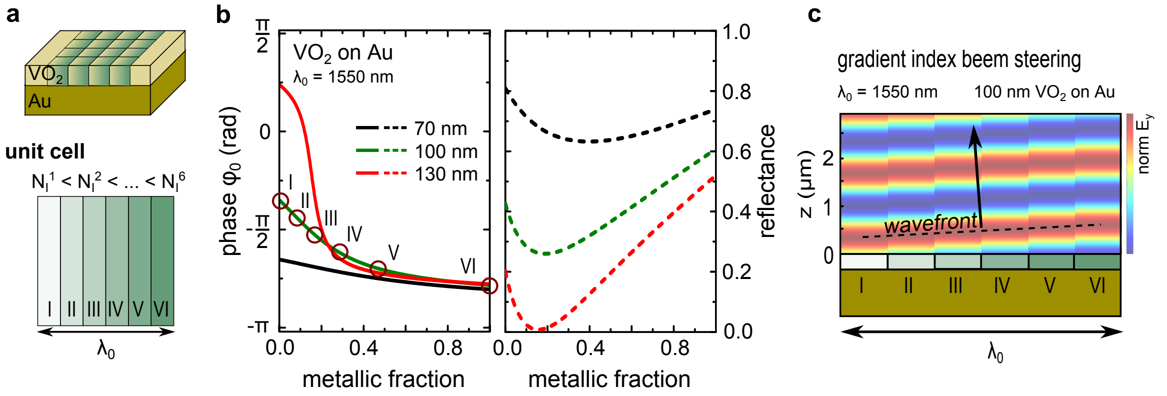

Figure 6.8.: **(a)** Schematic drawing of a gradient patterned VO_2 film on a Au substrate and definition of the unit cell of the gradient pattern comprising VO_2 regions (I-VI) irradiated with an increasing ion fluences from left to right. **(b)** Calculated reflection phase ϕ_0 (left figure) and calculated reflectance (right figure) of a homogeneous VO_2 film with various film thicknesses deposited on a Au substrate as a function of the metallic fraction in the VO_2 film. Values were calculated for a wavelength of $\lambda_0 = 1550\,\mathrm{nm}$. **(c)** Reflected E_y field patterns of 100 nm thin VO_2 films on gold calculated for the metallic fractions (I-VI) marked in figure (b). Light is incident normal to the sample surface at a wavelength of $\lambda_0 = 1550\,\mathrm{nm}$. The black dashed line highlights the wavefront of reflected light.

obtained by ion beam patterning of these metasurfaces.

Spatially selective ion irradiation was also demonstrated using a FIB system. The unprecedented flexibility in mask-free patterning is particular promising for films that match the penetration depth of 30 keV Ga^+ ions commonly used in FIB systems. The results demonstrate that nanoscale defect engineering using area-selective ion irradiation represents a new paradigm to create active photonic structures and devices, such as reflection polarizers and beam steering surfaces.

6.8. Outlook: Gradient index metasurfaces

Ultrathin metasurfaces with a spatial gradient of material properties, such as dense arrangements of resonant optical antennas with subwavelength spatial varying size or geometry of their building blocks, were found to exhibit extraordinary light-manipulation abilities that can be utilized for beam steering and focusing devices.[2,14,336] In those devices the properties of reflected and refractive light beams are controlled by locally manipulating the amplitude and phase of the light wave.[2] The phase of light waves reflected from a substrate can also be controlled by using a suitable coating with spatial refractive index variations. A refractive index gradient in a thin VO_2 film can be obtained by locally adjusting the phase transition temperature in such a way that a spatial metallic fraction gradient is achieved at a certain temperature (compare figure 6.8a). The unit cell of such a pattern might comprise various stripes of VO_2, which are irradiated with an increasing ion fluence. In contrast to index gradients fabricated by varying the building blocks of plasmonic antenna,[336] the index gradient in VO_2 can be dynamically tuned by temperature. At low (high) temperatures all stripes are in the insulating (metallic) state, whereas at intermediate temperatures a metallic fraction gradient appears.

To theoretically demonstrate that a properly designed ion beam patterned VO_2 metasurface can be used to dynamically steer light beams, the reflection phase ϕ_0 and reflectance of thin VO_2 films on gold substrates were calculated at a fixed wavelength of 1550 nm as a function of the metallic fraction f using Fresnel equations and effective medium theory (compare figure 6.8b). The largest modulation of ϕ_0 can be observed for a 130 nm VO_2 film. The reflection phase is $\sim \pi/4$ for insulating VO_2 ($f = 0$) and gradually decreases to $\sim -3/4\pi$ for metallic VO_2 ($f = 1$). However, the strong phase modulation is connected to the ultrathin-film interference condition at 1550 nm, which is perfectly matched for this VO_2 film thickness. Consequently, almost no light will be reflected from parts of the pattern, especially when the metallic fraction is roughly $f = 0.15$ (compare figure 6.8b, red dashed curve in the right figure). A 100 nm thin VO_2 film shows an average reflectance of $\sim 40\,\%$ and a maximum phase shift of 1.4 rad between insulating and metallic regions of the gradient pattern. Figure 6.8c combines the calculated reflected E-field patterns of six different 100 nm thin VO_2 films with different metallic fractions (I-VI) as indicated in figure6.8b on gold. Assuming that each pattern has a width of 250 nm ($p \sim \lambda$), the maximum phase shift of 1.4 rad between the outer regions corresponds to a steering angle of roughly 12 ° (compare figure 6.8c). Note that the intensity variations of the reflected beam may reduce the attainable steering angle and distorts the beam profile. Although much higher reflectance values can be achieved by using thinner films, the attainable phase shift, and thus the ability to steer light beams, decreases accordingly (compare figure 6.8b). Kaplan *et al.*[337] demonstrated that the steering angle and reflectance can be greatly enhanced by incorporating plasmonic antenna on top of the VO_2 gradient index pattern. However, these structures are no longer inherently flat.

7 | Epsilon-near-zero substrate engineering

Most of the VO_2 based optical metasurfaces demonstrated in the previous chapter are based on the complete suppression of light reflection. The reflection is effectively suppressed by utilizing destructive interference of light which occurs for ultra-thin absorbing films, such as VO_2 in the vicinity of the IMT, deposited on low index substrates like metals or polar materials featuring phonon resonances, such as Al_2O_3 (compare section 3.5.2). The effective optical properties of VO_2 metasurfaces arise from artificial phase coexistence induced by ion beam patterning of thin VO_2 films. However, the wavelength at which the reflection can be fully suppressed is primarily determined by the nature of the substrates and is pinned to particular values near plasma or phonon resonances. The former are typically located in the UV/VIS and the latter in the infrared spectral region. In the past, VO_2 has been used to demonstrate ultra-thin film absorbers using substrates such as Al_2O_3 [38, 44] and noble metals [75]. However, these substrate choices tie the wavelength of operation to particular narrow bands.[76]

Chapter 3 demonstrates theoretically that completely suppressed reflection using ultra-thin VO_2 films with thicknesses much smaller than the wavelength of light can be only obtained within a spectral region were the real part of the refractive index of the substrate is $n \lesssim 1$, which is characteristic of materials with permittivity close to zero. This condition is experimentally verified in this chapter by measuring the temperature dependent reflectance of vanadium dioxide films deposited on several epsilon-near-zero (ENZ) materials having vanishingly small dielectric permittivity, including aluminum-doped zinc oxide (AZO). Aluminum-doped zinc oxide is one of the transparent conductive oxides that have emerged recently as alternative plasmonic materials.[34,37,338–340] By tailoring the plasma frequency of AZO using ion beam aluminum doping, the epsilon-near-zero point is tuned, thus suppressed reflection is achieved at wavelength that continuously span the near- and mid-infrared wavelength range. This especially closes the spectral gap, which is not accessible by using noble metal and polar dielectric substrates. The results presented in this chapter are published in reference [76].

7.1. Low index substrates

Noble metals, such as silver and gold, transition metal nitrides, highly doped semiconductors, especially oxide semiconductors like AZO, and polar dielectrics behave like ENZ materials near their plasma frequencies or phonon resonance frequencies.[76,341,342] At these frequencies the real part n of the complex refractive index becomes significantly smaller than unity, provided the material is low loss near the ENZ condition.

The optical properties of polar dielectric materials in the vicinity of a phonon resonances can be described using a Lorentz oscillator model (ϵ_{L}):[76]

$$\tilde{n}_{\mathrm{L}}^2 = \epsilon_{\mathrm{L}} = \epsilon_\infty \left(1 + \frac{\omega_{\mathrm{LO}}^2 - \omega_{\mathrm{TO}}^2}{\omega_{\mathrm{TO}}^2 - \omega^2 - \mathrm{i}\omega\gamma}\right), \tag{7.1}$$

where ϵ_∞ is the background permittivity, ω_{LO} and ω_{TO} are the longitudinal optical (LO) and travers optical (TO) phonon frequencies, respectively, and γ is a damping factor related to the phonon lifetime (optical losses). Figure 7.1a shows the real and imaginary parts of the complex refractive index for a polar dielectric material with different values of γ. The spectral region of $\kappa > n$ is called the reststrahlen band and corresponds to the region of negative permittivity, which typically expands from ω_{LO} to ω_{TO}. Negative permittivity values in polar dielectrics are a result of the coherent oscillation of vibrating bound charges on the atomic lattice. Values of $n \leq 1$ can be found within and just before the reststrahlen band region, starting at $\Omega_{\mathrm{L}}^2 \sim (\omega_{\mathrm{TO}}^2 - \epsilon_\infty\omega_{\mathrm{LO}}^2)(\epsilon_\infty)^{-1}$, for low-loss polar dielectric materials ($\gamma << \omega_{\mathrm{TO}}$, compare figure 7.1a). The slow scattering rates of optical phonons of polar materials, which typically occur on the time scale of picoseconds compared to the faster scattering rate of free-charge-carrier plasmons in highly doped semiconductors, results in low optical losses. As a consequence, very low values of $n \lesssim 0.1$ can be reached employing materials, such as hexagonal boron nitride (hBN), $\mathrm{Al_2O_3}$ and ZnO (compare figure 7.1c). However, the supply of polar materials with suitable phonon resonances limits the wavelength at which $n < 1$ can be realized to infrared wavelength $\lambda_0 > 6\,\mu$m.[341]
The optical properties of metals, doped semiconductors, and conducting oxides, are dominated by the free carrier contribution, which can be described by the Drude model:[76]

$$\tilde{n}_{\mathrm{D}}^2 = \epsilon_{\mathrm{D}} = \epsilon_\infty \left(1 - \frac{\omega_p^2}{\omega(\omega + \mathrm{i}\Gamma)}\right), \tag{7.2}$$

where Γ is a damping factor associated with the charge carrier mobility, and ω_p is the screened plasma frequency, which is related to the free carrier concentration N through: $\omega_p^2 = Ne^2/(\epsilon_0\epsilon_\infty m^*)$. Here e is the elementary charge and m^* is the effective mass. Figure 7.1b shows n and κ for Drude-like materials with different values of Γ. Optical properties typically consistent with metals ($\kappa > n$) are found at wavelengths associated with negative permittivity, which results from the collective oscillations of free carriers.[343] Especially for weakly damped systems with high carrier mobility ($\Gamma << \omega_p$), characteristically low n values of ≤ 1 can be found in the vicinity of the crossover wavelength starting at $\Omega_{\mathrm{D}}^2 \sim \epsilon_\infty\omega_p^2(\epsilon_\infty - 1)^{-1}$.

Typically, the plasma resonance of conventional metals is located in the ultraviolet or visible, because of the very large free carrier concentration ($N \sim 10^{23}\,\mathrm{cm}^{-3}$). Due to the high conductivity in these materials, the region of $n < 1$ extends far beyond the visible [$\lambda_{\mathrm{Au}}(n = 1) \sim 2.2\,\mu$m, $\lambda_{\mathrm{Ag}}(n = 1) \sim 2.6\,\mu$m, compare figure 7.1c]. But although they are ideal substrates for the visible,[73,75] they cannot be used as substrate materials for ultra-thin $\mathrm{VO_2}$ coatings to achieve completely suppressed reflection at longer wavelength, such as the near- and mid-IR, because in this spectral region the vast majority of metals have extinction coefficients $\kappa >> 1$ (compare figure 7.1c and section 3.5.2).[76]
Doped semiconductors, transparent conducting oxides (TCOs) and nitrides offer great potential to circumvent the limitations of metals by modifying their intrinsic free-carrier concentration through impurity doping.[34,37,338–340,343] Typically, very low values of n can be reached by

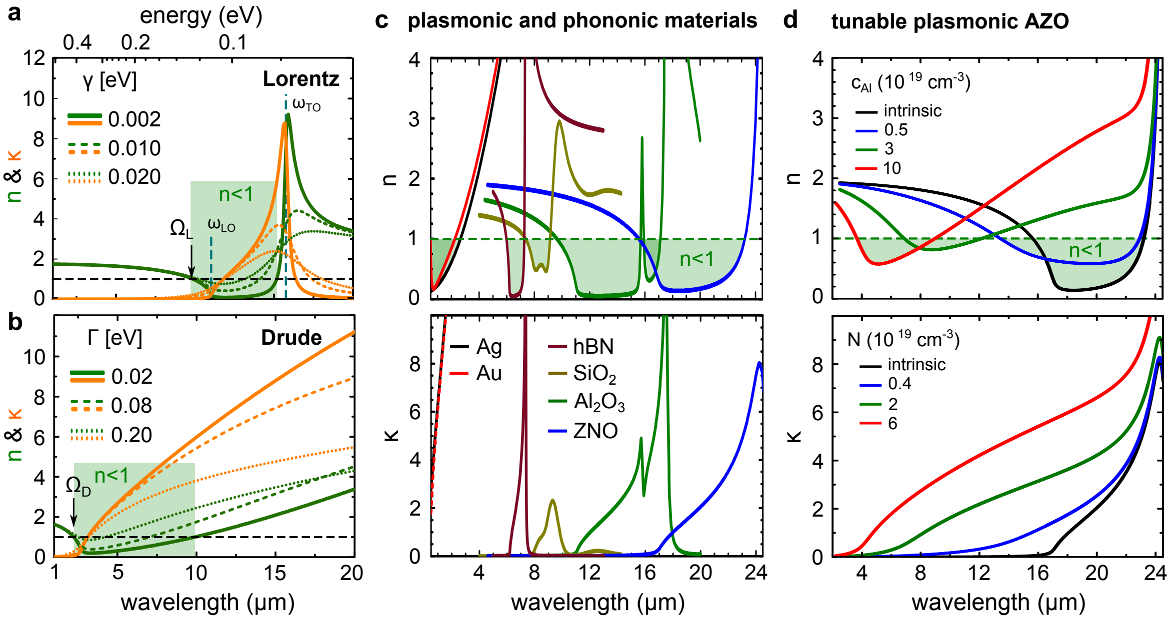

Figure 7.1.: Epsilon-near-zero substrate materials **(a)** Lorentz oscillator model for polar dielectric materials and Drude model refractive indices n and κ for various damping constants γ and Γ, respectively. The model parameter values are $\omega_p = 0.46\,\text{eV}$, $\epsilon_\infty = 5$, $\omega_{\text{TO}} = 0.079\,\text{eV}$, and $\omega_{\text{LO}} = 0.112\,\text{eV}$. **(b)** Real and imaginary parts, n and κ, of the refractive index of plasmonic (Ag [344], Au [344]) and phononic materials (hBN [345], SiO_2 [230], Al_2O_3, and ZnO). **(d)** Real and imaginary parts, n and κ, of the refractive index of aluminum-doped ZnO for various values of the free carrier concentrations N. The spectral region of $n < 1$ is highlighted in (b) and (c).

doping traditional semiconductors, because of a combination of high carrier mobility and very low effective mass.[346] However, the achievable free carrier concentration is orders of magnitude smaller compared to that of metals due to solid-solubility limits. In contrast, oxide semiconductors such as ZnO can be heavily doped, e.g. with aluminum, without significant alteration of their structural properties, reaching carrier concentrations on the order of $N \sim 10^{21}\,\text{cm}^{-3}$, which leads to plasma frequencies in the near- and mid-IR.[35,76]
In this thesis, 400 nm thick AZO layers with aluminum concentrations ranging from $c_{\text{Al}} \sim 10^{18}$ to $\sim 10^{21}\,\text{cm}^{-3}$ were fabricated by Al^+ ion implantation of ZnO single crystals. In order to achieve homogeneous box-like aluminum implantation profiles multiple ion implantation steps with suitable ion energies and ion fluences were performed (compare section 4.2 and appendix A.2). Figure 7.1d shows the real n and imaginary part κ of the complex refractive index of various AZO samples, as measured by spectroscopic ellipsometry. The effective optical properties of all samples are well described by a combination of a single Lorentz oscillator and a Drude term, which take into account the contributions of both the phonon resonance and free-charge carriers:[76]

$$\tilde{n}^2(\omega) = \epsilon(\omega) = \epsilon_{\text{L}} + \epsilon_{\text{D}} - \epsilon_\infty = \epsilon_\infty \left(1 + \frac{\omega_{\text{LO}}^2 - \omega_{\text{TO}}^2}{\omega_{\text{TO}}^2 - \omega^2 - i\omega\gamma} - \frac{\omega_p^2}{\omega(\omega + i\Gamma)}\right). \qquad (7.3)$$

An increasing aluminum doping concentration changes the optical properties from phonon dominated for concentrations up to $c_{\text{Al}} = 5 \times 10^{18}\,\text{cm}^{-3}$ (blue curve in figure 7.1d), to Drude-like behavior for aluminum concentrations starting at $c_{\text{Al}} = 3 \times 10^{19}\,\text{cm}^{-3}$ (green curve in figure 7.1d), caused by the increasing number of free-charge carriers in the AZO layer. A fit to the experimental data for the sample with a nominal aluminum concentration of $c_{\mathrm{Al}} \sim 1 \times 10^{20}\,\mathrm{cm}^{-3}$ yields $\epsilon_\infty = 3.65$, $\omega_{\mathrm{TO}} = 0.051\,\mathrm{eV}$, $\omega_{\mathrm{LO}} = 0.074\,\mathrm{eV}$, $\gamma = 0.06\,\mathrm{eV}$, $\Gamma = 0.071\,\mathrm{eV}$, and a screened plasma frequency of $\omega_p = 0.28\,\mathrm{eV}$. The free-carrier concentration for this sample was estimated from the plasma frequency using an effective electron mass of $m^* = 0.3\,m_0$ [347] and is approximately $N \sim 6 \times 10^{19}\,\mathrm{cm}^{-3}$. Thus, the fraction of aluminum dopants, which are incorporated in the ZnO lattice and contribute an electron to the conduction band, is roughly 60 %. Samples doped with higher amounts of aluminum (not shown) have a significantly reduced free-carrier concentration, most likely due to a dramatically increased amount of irradiation defects, which remain in the sample after thermal annealing.

Optical properties typically associated with metals ($\kappa > n$) can be observed for the AZO sample doped with $c_{\mathrm{Al}} \sim 1 \times 10^{20}\,\mathrm{cm}^{-3}$ above the crossover wavelength of $\lambda \sim 4.4\,\mu\mathrm{m}$. The spectral region of $n < 1$ extends from 3.7 to 9.2 μm (compare figure 7.1d). In contrast to the extinction coefficient of noble metals (compare figure 7.1c), κ of the AZO sample remains small in this spectral region. Wang *et al.*[21] and Kim *et al.*[348] reported crossover wavelengths as small as 1.3 μm for thick sputtered AZO films deposited on silicon and glass substrates, respectively. Thus, AZO is a suitable substrate material to achieve suppressed reflection in the spectral gap between the visible and the infrared.[76]

7.2. Suppressed reflection on low index substrates

To demonstrate that suppressed reflection of light using ultra-thin absorbing coatings occurs on low index substrates ($n < 1$), VO_2 films were deposited on various substrate materials including AZO, which is dominated by a plasma resonance, SiO_2 and Al_2O_3, both featuring a prominent phonon resonance, and intrinisc ZnO, which is completely transparent in the mid-IR. Figure 7.2a-d summarizes the temperature-dependent reflectance of all samples during a heating cycle, respectively. Figure 7.2a shows the temperature-dependent reflectance of an approximately 100 nm thin VO_2 film grown on the AZO sample with $N \sim 6 \times 10^{19}\,\mathrm{cm}^{-3}$. Note, the film thickness in the near and mid-IR is much smaller than the wavelength of light ($\delta = 1/20$ at $5\,\mu\mathrm{m}$). At low temperatures (30 °C, blue curve), when the VO_2 film is insulating and basically transparent, the reflectance spectra is dominated by the reflectivity of the AZO substrate, which starts to be highly reflective at wavelength larger than the crossover wavelength of 4.4 μm. At elevated temperatures, phase coexistence of metallic and insulating domains makes the VO_2 film absorbing. Due to ultra-thin film interference, a reflectance minimum with $R_{\mathrm{min}} = 0.01$ is observed at $\lambda_{\mathrm{min}} = 5.0\,\mu\mathrm{m}$, and $T_{\mathrm{min}} = 70\,°\mathrm{C}$. The complex refractive index value of AZO is $\tilde{n} = 0.56 + 1.09\mathrm{i}$ at this wavelength, which is in perfect agreement with the theoretical predictions (compare section 3.2).

Figure 7.2b shows the temperature-dependent reflectance of a 200 nm thin VO_2 film deposited on SiO_2. The thickness was chosen in order to match the reduced thickness of VO_2 on AZO ($\delta \sim 1/19$ at $\lambda_0 = 8.8\,\mu\mathrm{m}$). At low temperatures, the reflectance spectrum features a narrow band with high reflectance values caused by the dominant reststrahlen band of the SiO_2 substrate that extends from 7.9 to 9.2 μm (compare figure 7.1c). As the temperature is increased, ultra-thin film interference causes a minimum in reflectance within this band. The reflectance minimum with $R_{\mathrm{min}} = 0.005$ occurs at $\lambda_{\mathrm{min}} = 8.8\,\mu\mathrm{m}$ and $T_{\mathrm{min}} = 73\,°\mathrm{C}$. At this wavlength the complex refractive index of the substrate is $\tilde{n} = 0.47 + 1.19\mathrm{i}$. The temperature-dependent reflectance of a 100 nm thin VO_2 film ($\delta = 1/30$ at $\lambda_0 = 11.3\,\mu\mathrm{m}$) deposited on Al_2O_3 was discussed in detail previously (compare sections 3.5 and 5.1.5) and is

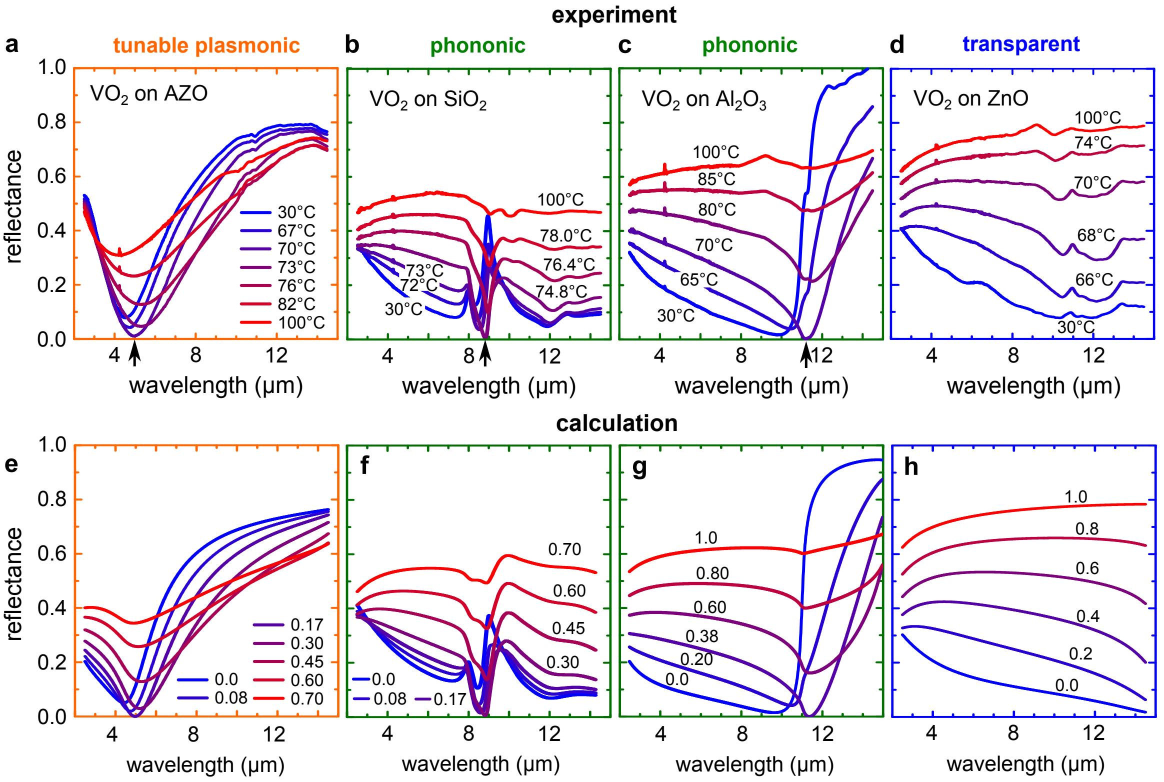

Figure 7.2.: (a-d) Measured temperature-dependent mid-IR reflectance of an ultra-thin VO_2 film ($d << \lambda_0$) grown on AZO with $N \sim 6 \times 10^{19}\,\mathrm{cm}^{-3}$ (a), SiO_2 (b), Al_2O_3 (c), and ZNO (d), respectively. All spectra are measured during a heating cycle. The reflectance minimum is marked with an arrow. **(e-h)** Calculated reflectance of the samples described in (a)-(d) as a function of the fraction of metallic phase in the VO_2 film.

shown in figure 7.2c for the sake of completeness. A reflectance minimum with $R_{\mathrm{min}} = 0.003$ is found at $\lambda_{\mathrm{min}} = 11.3\,\mu\mathrm{m}$ and $T_{\mathrm{min}} = 70\,°\mathrm{C}$ within the reststrahlen band of the Al_2O_3 substrate that extens from 10.9 to $15.8\,\mu\mathrm{m}$ (compare figure 7.1c). The complex refractive index of the substrate is $\tilde{n} = 0.09 + 0.49\mathrm{i}$ (compare figure 7.1c).

No reflectance minimum is observed in the entire mid-IR for a 100 nm thin VO_2 film deposited on ZnO, because the real part of the complex refractive index of ZnO is $n > 1$ for wavelength up to $15.5\,\mu\mathrm{m}$ (compare figure 7.1c). Note, the lower high-temperature reflectance of VO_2 films grown on AZO and SiO_2 substrates compared to the high-temperature reflectance of VO_2 films deposited on Al_2O_3 and ZnO substrates, which might be attributed to a lower film quality, especially with many extended defects and void formation at the interface, which was observed using STEM (see appendix A.2).

Figures 7.2e-h summarize the calculated reflectance of ultra-thin VO_2 films deposited on AZO, SiO_2, Al_2O_3, and ZnO, respectively, as a function of the metallic fraction f within the VO_2 films. At low temperatures, when VO_2 is in the insulating state, the metallic fraction is zero and at high temperatures, when VO_2 is entirely in the metallic state, f equals unity. All reflectance spectra are calculated using Fresnel equations and metallic fraction-dependent effective refractive indices of VO_2. The effective refractive indices are estimated from the refractive indices of insulating and metallic VO_2, extracted from the measurements of intrinsic VO_2 of Qazilbash *et al.*[63], using Lichteneckers effective medium approximation (compare section 3.5). In all cases, the calculated reflectance is in very good agreement with the experimental data and the wavelength of all reflectance minima is correctly predicted.

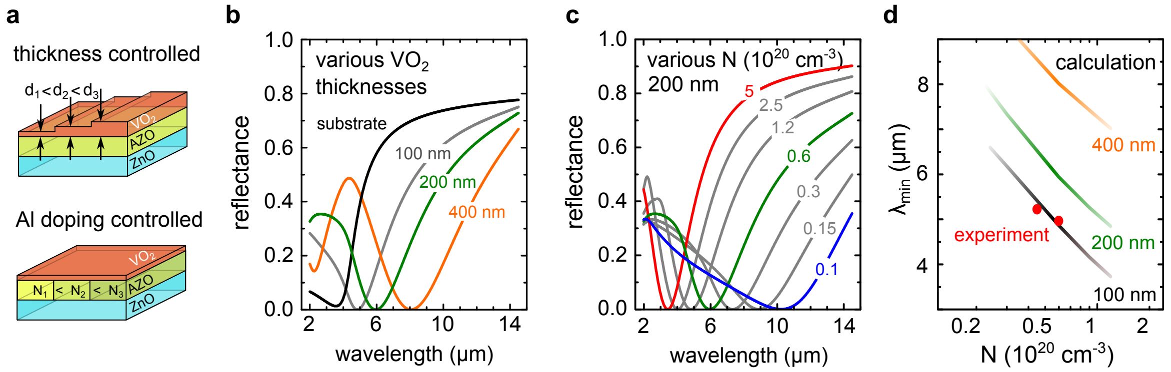

Figure 7.3.: **(a)** The wavelength of completely suppressed reflection of light can be adjusted by varying the VO_2 film thickness or by changing the aluminum dopant concentration of the AZO substrate. **(b)** Calculated reflectance of ultra-thin VO_2 films deposited on an AZO substrate with fixed free-carrier concentration $N \sim 6 \times 10^{19}\,\mathrm{cm}^{-3}$ for various VO_2 film thicknesses. **(c)** Calculated reflectance of a 200 nm thin VO_2 film deposited on AZO substrates with various free-carrier concentrations N. **(d)** Comparison of the experimental and calculated λ_{min}.

However, note that the measured high-temperature reflectance of VO_2 films deposited on AZO and SiO_2 is in agreement with the calculated reflectance for a metallic fraction of only $f \sim 0.7$. This discrepancy might be attributed to a large number of structural defects affecting the optical properties of VO_2. The calculations also underestimate the reflectance of VO_2 on AZO at short wavelengths, which might be caused by both the quality of the VO_2 film and the assumption of a semi-infinite substrate, which was made for the calculations. However, this assumption is only critical for wavelengths at which the AZO substrate is transparent ($\lambda_0 \lesssim 4\,\mu\mathrm{m}$) and does not affect the minimum reflectance point which occurs at a wavelength at which the AZO substrate is opaque.

The results demonstrate that ultra-thin coatings of VO_2 on low index substrates can efficiently suppress light reflection at a wavelength at which the substrate has an index of refraction $n < 1$, provided the extinction coefficient is small (compare also section 3.5).

7.3. Zero reflectance wavelength agility

The wavelength of zero reflection for ultra-thin VO_2 coatings on AZO substrates can be tuned over a broad wavelength range either by adjusting the thickness of the VO_2 film (compare figures 7.3a,b) or by changing the free-carrier concentration of the AZO substrate (compare figures 7.3a,c). Figure 7.3b shows the calculated reflectance of ultra-thin VO_2 coatings on an AZO substrate for various thicknesses of the VO_2 film up to 400 nm. For clarity, the reflectance spectra are given for a metallic fraction at which the reflectance minimum occurs. The minimum reflectance wavelength shifts from $\lambda_{\mathrm{min}} = 5\,\mu\mathrm{m}$ to approximately $8\,\mu\mathrm{m}$ by increasing the VO_2 film thickness from 100 to 400 nm for a given free-carrier concentration of the AZO substrates of $N = 6 \times 10^{19}\,\mathrm{cm}^{-3}$ (compare figures 7.3b,d). A similar wavelength shift is obtained by maintaining the VO_2 film thickness constant at 200 nm and adjusting the free-carrier concentration of the AZO substrate (compare figures 7.3c,d). Changing N from 0.1×10^{20} to $5 \times 10^{20}\,\mathrm{cm}^{-3}$, accessible by impurity doping,[35,37,348] results in the tuning of λ_{min} from approximately 10.5 to approximately $3.5\,\mu\mathrm{m}$. The experimentally obtained reflectance minima at $\lambda_{\mathrm{min}} = 5.3$ and $5.0\,\mu\mathrm{m}$ for approximately 100 nm thin VO_2 films on AZO substrates with $N \sim 4.5 \times 10^{19}\,\mathrm{cm}^{-3}$ (not shown) and $N \sim 6.0 \times 10^{19}\,\mathrm{cm}^{-3}$ (compare figure 7.2a) are in good agreement with the calculations. The results demonstrate that, depending on the VO_2 film thickness and the doping concentration of the AZO substrate, the wavelength of minimal reflection can be precisely tuned between the phonon resonance of intrinsic ZnO and the highest plasma wavelength achievable in doped ZnO.[76]

7.4. Summary

Thin VO_2 films were successfully grown on various plasmonic and phononic substrates, such as AZO, SiO_2, Al_2O_3 and ZnO. It was experimentally demonstrated that almost completely suppressed reflection of light only occurs at wavelengths at which the substrate has a low refractive index ($n \leq 1$) and small optical losses. Values of $n \leq 1$ are most commonly found in metals and polar dielectric substrates close to plasmonic and phononic resonances, where the real permittivity is close to zero (epsilon-near-zero). Although the ENZ condition can be achieved over a wide range of wavelengths by using metals and classical semiconductor materials, suppressed reflection cannot be attained with these substrate materials in the near- and mid-IR spectral region. This limitation was circumvented by adjusting the plasma frequency of AZO using ion beam aluminum doping. Experimentally, a free-carrier concentration of $N \sim 6 \times 10^{19}\,\mathrm{cm}^{-3}$, which corresponds to a crossover wavelength of approximately $4.4\,\mu$m, was achieved for AZO samples homogeneously doped with an aluminum concentration of $c_{\mathrm{Al}} = 1 \times 10^{20}\,\mathrm{cm}^{-3}$ after a thermal annealing treatment. It was demonstrated experimentally and theoretically that the wavelength of suppressed reflection in a system comprising an ultra-thin VO_2 coating deposited on an AZO substrate can be tuned over the entire mid-infrared range by changing the free-carrier concentration of the AZO substrate.

8 | Summary and conclusion

Active, widely tunable optical materials have enabled rapid advances in photonics and optoelectronics, especially in the emerging field of meta-devices.[44] Of the tunable optical materials, one of the most prolifically studied is VO_2, which undergoes a reversible IMT as the temperature reaches a critical temperature of approximately 67 °C.[44,160] Due to the dramatic change of the optical properties accompanying the IMT, thin VO_2 films are increasingly used as tunable spacing layers to achieve dynamic control of the optical properties of existing plasmonic metasurface devices. It was recently demonstrated that an ulra-thin VO_2 film with thickness much smaller than the wavelength of incident light can be tuned into a near-perfect absorption state by varying the temperature in close proximity to the IMT when deposited on a metal-like substrate.[38] To successfully transform these metafilms into inherently flat, active tunable metasurfaces, several key challenges were identified and have to be addressed: i) The necessary conditions for perfect absorption and suppressed light reflection in systems comprising ultra-thin absorbing coatings on metal-like substrates have to be explored. Based on these results, suitable substrates have to be found to control the wavelength at which VO_2-based devices operate. ii) The phase transition temperature of VO_2 has to be adjusted locally to room temperature. iii) Patterned artificial phase coexistence of metallic and insulating domains has to be achieved in VO_2 films to allow the fabrication of functional optical metasurfaces.

To address the first key challenge, this thesis derives a methodical strategy to design highly absorbing anti-reflection coatings using utlra-thin films on metal-like substrates. This strategy is based on the calculation of the reflection of light from and transmission of light through multilayer systems using Fresnel equations. A suitable representation of the giant parameter space, which includes the wavelength and incident angle of light, as well as the film thickness and complex refractive indices of film and substrate, was introduced. This representation has allowed finding the requirements for possible film substrate combinations regarding their refractive indices. It was demonstrated that ultra-thin coatings, with a thickness much smaller than the wavelength of incident light ($d << \lambda, \delta < 1/10$) can completely suppress light reflection provided the index of refraction of the substrate is $n_s \lesssim 1$ and the extinction coefficient of the substrate is small (small optical losses). The $n_s < 1$ condition requires ENZ materials, which ties the material choice of the substrate to low-loss plasmonic and phononic materials. Further, the extinction coefficient of the coating material must be smaller than or equal to its real part of the complex refractive index: $\kappa_f \leq n_f$.
The strategy was verified both experimentally and theoretically by using ultra-thin VO_2 films deposited on various plasmonic and phononic substrates. The temperature-dependent refractive index of VO_2 was determined throughout the spectral region from UV-VIS-NIR to mid-IR wavelengths using spectroscopic ellipsometry. The reversible IMT in VO_2 provides access to a broad range of complex refractive-index values (from $\kappa_f \sim 0$ to $\kappa_f > n_f$), especially in the mid-IR, due to naturally occurring phase coexistence. The effective optical properties in the vicinity of the phase transition were successfully described using Lichteneckers effective

medium theory with a wavelength dependent exponent k. The temperature-dependent reflectance of all samples was measured using mid-IR microscopy in combination with a FTIR spectrometer and calculated using Fresnel equations and a thermal equilibrium model. In agreement with results obtained by Kats *et al.*[38], it was demonstrated that a 100 nm thin VO_2 film deposited on an Al_2O_3 substrate can be tuned into a near-zero reflection state by tuning the temperature in the vicinity of the IMT. Near-zero reflection with $R = 0.005$ was observed within the reststrahlen band of the sapphire substrate at a wavelength of $11.3\,\mu$m. At this wavelength the film thickness is less than one hundredth of the wavelength and the refractive index of the Al_2O_3 substrate is $\tilde{n_s} = 0.09 + 0.49i$, which is in perfect agreement with the developed strategy. It was calculated that approximately 93 % of the incident light is absorbed within the VO_2 film and the remaining light is absorbed within the first microns of the opaque substrate. A comparable reflectance minimum was observed for a 200 nm VO_2 film deposited on a SiO_2 substrate at $8.8\,\mu$m. The refractive index of SiO_2 at this wavelength is $\tilde{n_s} = 0.47 + 1.19i$. The wavelength at which suppressed reflection occurs is determined by the phonon resonances of the Al_2O_3 and SiO_2 substrates and can be adjusted only slightly by the VO_2 film thickness. In agreement with the strategy, no reflectance minimum was found in the mid-IR for ultra-thin VO_2 films on ZnO substrates, because the real part of the complex refractive index of ZnO is $n > 1$ for wavelength up to $15.5\,\mu$m. Further, although the index of refraction of noble metals is $n < 1$, suppressed reflection using ultra-thin VO_2 films cannot be achieved over a large wavelength range, due to inherent high losses in the metal substrates. Wavelength agility of the point of zero reflection was theoretically and experimentally demonstrated by using ultra-thin VO_2 coatings on AZO substrates. An ENZ condition, consistent with $n_s < 1$, was achieved over a wide wavelength region by adjusting the free-carrier concentration of the AZO substrates. Aluminum ion implantation and post implantation annealing was successfully used to tailor the free carrier concentration of the AZO substrates. The wavelength at which minimal reflection occurs was continuously tuned over the entire mid-IR wavelength range. It can be anticipated that the development of new low-loss ENZ substrates will enable efficient single-layer ultrahin absorbers and antireflection coatings in the near- and mid-IR. The understanding and control of suppressed reflection of light using ultra-thin absorbing coatings is a key requirement for the fabrication of VO_2 metasurfaces.

To address the second key challenge, a setup to measure the electrical properties of solid materials in-situ during ion irradiation as a function of temperature was developed, installed, and established to address the second key challenge. The experiments performed with this setup provide a means to investigate the effects of ion beam induced defect formation on the insulator-metal transition of VO_2. Ion irradiation experiments were performed as a function of ion species, ion energy, ion fluence, and irradiation temperature. Besides in-situ electrical measurements, the structural, optical, and electrical properties of VO_2 thin films were investigated as a function of temperature prior to and after ion irradiation. The experimental results described in the following are key to an efficient modification of the phase transition temperature of VO_2 using ion irradiation.

The ion irradiation experiments were performed using VO_2 thin films grown on Al_2O_3. Electron microscopy and temperature-dependent X-ray diffraction were employed to study the structural properties of as-grown films. The VO_2 films were found to be phase-pure and composed of highly oriented columnar grains with six-fold domain symmetry. The temperature-dependent electrical and optical properties of VO_2 were investigated using 4-wire resistance and mid-infrared reflectance measurements. In contrast to bulk VO_2, the IMT of VO_2 films is broadened due to the domain structure. A resistance change of three orders of magnitude across the IMT and a bulk-like critical temperature of the IMT were observed, indicating high film quality. A high film quality is necessary to separate the effects of ion beam induced defects from defects initially present in the VO_2 films, especially with regard to their possible interaction. Rutherford backscattering spectrometry in channeling geometry was used to investigate the evolution of irradiation induced damage formation in the VO_2 films. At room temperature 75 keV Ar^+ ion irradiation with ion fluences exceeding $N_I = 1 \times 10^{15}\,\mathrm{cm}^{-2}$ ($n_{dpa} \sim 1$) resulted in a complete amorphization of the VO_2 lattice. Amorphous VO_2 does not feature an IMT. Elevated irradiation temperatures caused a metallization of VO_2 films, most likely due to enhanced oxygen out-diffusion of displaced oxygen atoms. Consequently, the in-situ irradiation experiments performed in this thesis as a function of ion species and ion fluence focus on low fluence ion irradiation for which the formation of only a minor amount of lattice displacements was observed ($n_{dpa} \leq 0.03$). Independent of the ion species, low fluence ion irradiation led to a significant decrease of the phase transition temperature. It was found that persistent lattice damage with roughly 1 % of all lattice atoms displaced, results in a reduction of the critical temperature T_C by $\Delta T_C = -20 \pm 2\,^\circ\mathrm{C}$. Temperature-dependent XRD and Raman spectroscopy revealed that ion irradiation of VO_2 induces tensile strain along the out-of-plane a_R direction and leads to V-V bond-softening most likely caused by a reduction of the oxidization state of vanadium lattice atoms. Thus, the reduction of the phase transition temperature is a consequence of the displacement of both oxygen and vanadium from their lattice sites by nuclear collisions, which results in lattice strain and the presence of V^{3+} states locally triggering an early onset of the phase transition. Strong annealing of point defects was observed starting at temperatures at which VO_2 is in the metallic phase. The amount of stable defects that remain in the VO_2 films after moderate heat treatment critically depends on the initial local defect density and thus, is strongly dependent on the ion species and ion fluence used for ion irradiation. The dense collision cascades of heavy ion irradiation locally produce a high amount of lattice atom displacements, whereas light ion irradiation results in the displacement of single lattice atoms along the ion trajectory. It was demonstrated that a combination of ion irradiation and moderate annealing leads to a persistent reduction of the phase transition temperature of VO_2. Since the amount of lattice defects can be precisely tuned by choosing appropriate irradiation and annealing conditions, the phase transition temperature of VO_2 can be engineered at will (defect engineering) down to room temperature. First irradiation experiments were conducted using other phase change and phase transition materials, such as samarium nickelate and germanium antimony telluride (GST). In agreement with the results presented for VO_2, it was demonstrated that the formation of a small amount of irradiation defects strongly affects these materials. Future studies should further develop the existing in-situ irradiation setup and use pulsed ion beams to achieve a temporal resolution of the effects of ion beam induced lattice disorder. The pulsed ion beam method was already successfully applied to investigate the lifetimes, interaction rates, and diffusion lengths of point defects in crystalline solids.[284,349–351] Small scale devices with high crystal quality should be used. The small surface area of such devices dramatically reduce the amount of impinging ions down to ion impacts easily separable in time. The high crystalline quality is required to investigate the effect of a very small amount of lattice defects. Thus, the effect of disorder induced by a single ion on the transport properties of materials with strongly-correlated electron systems and disorder driven phase transitions might be investigated. Such experiments could potentially help to gain insight into the underlying physics of short-range (local) and long-range (global) correlations. Small amounts of disorder may disrupt long-range electronic correlations triggering a global phase transition, but may have only minor effect on the local correlations.[211]

To address the third key challenge, 100 nm thin VO_2 films were irradiated through lithographically patterned poly(methyl methacrylate) (PMMA) masks. The phase transition temperature was only modified in those regions of the films that were not covered by PMMA. In a temperature region, in which irradiated VO_2 is yet metallic, whereas intrinsic regions are still insulating, persistent phase coexistence was artificially introduced. The results address the third key challenge and demonstrate the possibility to pattern inherently flat VO_2 metasurfaces by ion-beam defect engineering. Using this robust technique, isotropic and anisotropic metasurfaces composed of irradiated and intrinsic VO_2 regions in a square checkerboard and stripe pattern arrangement, respectively, were successfully fabricated. The effective optical properties of these metasurfaces were investigated using temperature-dependent reflectance measurements. It was found that isotropic metasurfaces undergo a single effective phase transition at a temperature in between the phase transition temperatures of intrinsic and irradiated VO_2 regions. Extremely large values of the form birefringence and optical dichroism ($\Delta n \sim 0.8$ and $\Delta k \sim -4.9$) were obtained for the anisotropic metasurfaces in the temperature range of phase coexistence. Preferential absorption of light polarized parallel to the ridges of the pattern due to the large optical dichroism lead to a degree of polarization of 90 %. Thus, the anisotropic VO_2 metasurfaces can be described as tunable reflection polarizers. It was experimentally demonstrated that all VO_2 metasurfaces can be tuned in and out of their effective medium states by tuning the temperature, and the effective optical properties were successfully adjusted by changing the duty cycle of irradiated regions within the pattern. The temperature-dependent effective optical properties of both types of metasurfaces were successfully described using effective medium theory. The patterns of the metasurfaces were experimentally resolved using temperature-dependent scattering-type scanning near-field optical microscopy measurements. It was found that the border between intrinsic and irradiated regions follows the domain boundaries. Thus, the feature size, which can be achieved by patterned ion irradiation is mainly limited by the domain size of the VO_2 films.

The possibility to engineer the phase transition of VO_2 on a subwavelength scale by local ion irradiation greatly expands the utility of this material, enabling new types of tunable optical meta-devices. In contrast to other methods, ion beams can be focused down to a spot size of a few nanometers, which allows the fabrication of small-scale structures. This offers great opportunities to circumvent the diffraction limited structuring of materials that are usually patterned via intense laser light, such as GST thin films. Furthermore, ion beam patterned metasurfaces remain inherently flat and might potentially serve as highly functional building platforms for bottom-up nanofabrication, or can even be used to create stacked metasurfaces. Area-selective ion irradiation of phase change materials was introduced in this thesis. The theoretical investigations and experimental results presented here provide a valuable contribution to design inherently flat optical metasurfaces by engineering the IMT of phase change and phase transition materials.

Bibliography

[1] K. Horie, H. Ushiki, *et al.*, *Molecular photonics: fundamentals and practical aspects* (John Wiley & Sons, 2008).

[2] N. Yu and F. Capasso, Nature Materials **13**, 139 (2014).

[3] D. R. Smith, J. B. Pendry, and M. C. Wiltshire, Science **305**, 788 (2004).

[4] J. B. Pendry, D. Schurig, and D. R. Smith, Science **312**, 1780 (2006).

[5] A. V. Kildishev, A. Boltasseva, and V. M. Shalaev, Science **339**, 1232009 (2013).

[6] R. A. Shelby, D. R. Smith, and S. Schultz, Science **292**, 77 (2001).

[7] V. M. Shalaev, Nature Photonics **1**, 41 (2007).

[8] J. B. Pendry, Physical Review Letters **85**, 3966 (2000).

[9] N. Fang, H. Lee, C. Sun, and X. Zhang, Science **308**, 534 (2005).

[10] X. Zhang and Z. Liu, Nature Materials **7**, 435 (2008).

[11] W. Cai, U. K. Chettiar, A. V. Kildishev, and V. M. Shalaev, Nature Photonics **1**, 224 (2007).

[12] O. Hess, J. B. Pendry, S. A. Maier, R. F. Oulton, J. Hamm, and K. Tsakmakidis, Nature Materials **11**, 573 (2012).

[13] N. Landy, S. Sajuyigbe, J. Mock, D. Smith, and W. Padilla, Physical Review Letters **100**, 207402 (2008).

[14] D. Lin, P. Fan, E. Hasman, and M. L. Brongersma, Science **345**, 298 (2014).

[15] B. Walther, C. Helgert, C. Rockstuhl, F. Setzpfandt, F. Eilenberger, E.-B. Kley, F. Lederer, A. Tünnermann, and T. Pertsch, Advanced Materials **24**, 6300 (2012).

[16] N. Yu, P. Genevet, M. A. Kats, F. Aieta, J.-P. Tetienne, F. Capasso, and Z. Gaburro, Science **334**, 333 (2011).

[17] X. Ni, S. Ishii, A. V. Kildishev, and V. M. Shalaev, Light: Science & Applications **2**, e72 (2013).

[18] M. Khorasaninejad, W. T. Chen, R. C. Devlin, J. Oh, A. Y. Zhu, and F. Capasso, Science **352**, 1190 (2016).

[19] F. Aieta, P. Genevet, M. A. Kats, N. Yu, R. Blanchard, Z. Gaburro, and F. Capasso, Nano Letters **12**, 4932 (2012).

[20] N. Yu, F. Aieta, P. Genevet, M. A. Kats, Z. Gaburro, and F. Capasso, Nano Letters **12**, 6328 (2012).

[21] D. Wang, Y. Gu, Y. Gong, C.-W. Qiu, and M. Hong, Optics Express **23**, 11114 (2015).

[22] J. Hao, J. Wang, X. Liu, W. J. Padilla, L. Zhou, and M. Qiu, Applied Physics Letters **96**, 251104 (2010).

[23] X. Shen, Y. Yang, Y. Zang, J. Gu, J. Han, W. Zhang, and T. Jun Cui, Applied Physics Letters **101**, 154102 (2012).

[24] Y. Cui, Y. He, Y. Jin, F. Ding, L. Yang, Y. Ye, S. Zhong, Y. Lin, and S. He, Laser & Photonics Reviews **8**, 495 (2014).

[25] N. Liu, M. Mesch, T. Weiss, M. Hentschel, and H. Giessen, Nano Letters **10**, 2342 (2010).

[26] C. Wu, I. Burton Neuner, G. Shvets, J. John, A. Milder, B. Zollars, and S. Savoy, Physical Review B **84**, 075102 (2011).

[27] X. Liu, T. Tyler, T. Starr, A. F. Starr, N. M. Jokerst, and W. J. Padilla, Physical Review Letters **107**, 045901 (2011).

[28] A. Kabiri, E. Girgis, and F. Capasso, Nano Letters **13**, 6040 (2013).

[29] G. V. Naik and A. Boltasseva, Metamaterials **5**, 1 (2011).

[30] P. R. West, S. Ishii, G. V. Naik, N. K. Emani, V. M. Shalaev, and A. Boltasseva, Laser & Photonics Reviews **4**, 795 (2010).

[31] S. Xiao, V. P. Drachev, A. V. Kildishev, X. Ni, U. K. Chettiar, H.-K. Yuan, and V. M. Shalaev, Nature **466**, 735 (2010).

[32] M. I. Shalaev, J. Sun, A. Tsukernik, A. Pandey, K. Nikolskiy, and N. M. Litchinitser, Nano Letters **15**, 6261 (2015).

[33] M. Decker, I. Staude, M. Falkner, J. Dominguez, D. N. Neshev, I. Brener, T. Pertsch, and Y. S. Kivshar, Advanced Optical Materials **3**, 813 (2015).

[34] G. V. Naik, J. Kim, and A. Boltasseva, Optical Materials Express **1**, 1090 (2011).

[35] K. Ellmer, Nature Photonics **6**, 809 (2012).

[36] J. Kim, G. V. Naik, N. K. Emani, U. Guler, and A. Boltasseva, IEEE Journal of Selected Topics in Quantum Electronics **19**, 4601907 (2013).

[37] G. V. Naik, J. L. Schroeder, X. Ni, A. V. Kildishev, T. D. Sands, and A. Boltasseva, Optical Materials Express **2**, 478 (2012).

[38] M. A. Kats, D. Sharma, J. Lin, P. Genevet, R. Blanchard, Z. Yang, M. M. Qazilbash, D. Basov, S. Ramanathan, and F. Capasso, Applied Physics Letters **101**, 221101 (2012).

[39] M. A. Kats, R. Blanchard, P. Genevet, and F. Capasso, Nature Materials **12**, 20 (2013).

[40] H.-T. Chen, W. J. Padilla, J. M. Zide, A. C. Gossard, A. J. Taylor, and R. D. Averitt, Nature **444**, 597 (2006).

[41] N. I. Zheludev and Y. S. Kivshar, Nature Materials **11**, 917 (2012).

[42] J. Sautter, I. Staude, M. Decker, E. Rusak, D. N. Neshev, I. Brener, and Y. S. Kivshar, ACS Nano **9**, 4308 (2015).

[43] Q. Wang, E. T. Rogers, B. Gholipour, C.-M. Wang, G. Yuan, J. Teng, and N. I. Zheludev, Nature Photonics **10**, 60 (2016).

[44] J. Rensberg, S. Zhang, Y. Zhou, A. S. McLeod, C. Schwarz, M. Goldflam, M. Liu, J. Kerbusch, R. Nawrodt, S. Ramanathan, *et al.*, Nano Letters **16**, 1050 (2016).

[45] M. Seo, J. Kyoung, H. Park, S. Koo, H.-s. Kim, H. Bernien, B. J. Kim, J. H. Choe, Y. H. Ahn, H.-T. Kim, *et al.*, Nano Letters **10**, 2064 (2010).

[46] M. Goldflam, T. Driscoll, B. Chapler, O. Khatib, N. Marie Jokerst, S. Palit, D. Smith, B.-J. Kim, G. Seo, H.-T. Kim, *et al.*, Applied Physics Letters **99**, 044103 (2011).

[47] Y. H. Fu, A. Q. Liu, W. M. Zhu, X. M. Zhang, D. P. Tsai, J. B. Zhang, T. Mei, J. F. Tao, H. C. Guo, X. H. Zhang, *et al.*, Advanced Functional Materials **21**, 3589 (2011).

[48] M. A. Kats, R. Blanchard, P. Genevet, Z. Yang, M. M. Qazilbash, D. Basov, S. Ramanathan, and F. Capasso, Optics Letters **38**, 368 (2013).

[49] M. J. Dicken, K. Aydin, I. M. Pryce, L. A. Sweatlock, E. M. Boyd, S. Walavalkar, J. Ma, and H. A. Atwater, Optics Express **17**, 18330 (2009).

[50] J.-Y. Ou, E. Plum, L. Jiang, and N. I. Zheludev, Nano Letters **11**, 2142 (2011).

[51] J.-Y. Ou, E. Plum, J. Zhang, and N. I. Zheludev, Nature Nanotechnology **8**, 252 (2013).

[52] H. Tao, A. Strikwerda, K. Fan, W. Padilla, X. Zhang, and R. Averitt, Physical Review Letters **103**, 147401 (2009).

[53] Q. Zhao, L. Kang, B. Du, B. Li, J. Zhou, H. Tang, X. Liang, and B. Zhang, Applied Physics Letters **90**, 011112 (2007).

[54] D. H. Werner, D.-H. Kwon, I.-C. Khoo, A. V. Kildishev, and V. M. Shalaev, Optics Express **15**, 3342 (2007).

[55] Y. Yao, R. Shankar, M. A. Kats, Y. Song, J. Kong, M. Loncar, and F. Capasso, Nano Letters **14**, 6526 (2014).

[56] Z. Li, Y. Zhou, H. Qi, Q. Pan, Z. Zhang, N. N. Shi, M. Lu, A. Stein, C. Y. Li, S. Ramanathan, *et al.*, Advanced Materials **28**, 9117 (2016).

[57] Z. Yang, C. Ko, and S. Ramanathan, Annual Review of Materials Research **41**, 337 (2011).

[58] B. Gholipour, J. Zhang, K. F. MacDonald, D. W. Hewak, and N. I. Zheludev, Advanced Materials **25**, 3050 (2013).

[59] A.-K. U. Michel, P. Zalden, D. N. Chigrin, M. Wuttig, A. M. Lindenberg, and T. Taubner, ACS Photonics **1**, 833 (2014).

[60] I. Staude and C. Rockstuhl, Nature Materials **15**, 821 (2016).

[61] M. Wuttig and N. Yamada, Nature Materials **6**, 824 (2007).

[62] A. Crunteanu, J. Givernaud, J. Leroy, D. Mardivirin, C. Champeaux, J.-C. Orlianges, A. Catherinot, and P. Blondy, Science and Technology of Advanced Materials **11**, 065002 (2010).

[63] M. M. Qazilbash, M. Brehm, B.-G. Chae, P.-C. Ho, G. O. Andreev, B.-J. Kim, S. J. Yun, A. Balatsky, M. Maple, F. Keilmann, *et al.*, Science **318**, 1750 (2007).

[64] P. Němec, J. Přikryl, V. Nazabal, and M. Frumar, Journal of Applied Physics **109**, 073520 (2011).

[65] E. Abreu, M. Liu, J. Lu, K. G. West, S. Kittiwatanakul, W. Yin, S. A. Wolf, and R. D. Averitt, New Journal of Physics **14**, 083026 (2012).

[66] M. Liu, A. J. Sternbach, M. Wagner, T. V. Slusar, T. Kong, S. L. Bud'ko, S. Kittiwatanakul, M. Qazilbash, A. McLeod, Z. Fei, *et al.*, Physical Review B **91**, 245155 (2015).

[67] T. Ben-Messaoud, G. Landry, J. Gariépy, B. Ramamoorthy, P. Ashrit, and A. Haché, Optics Communications **281**, 6024 (2008).

[68] M. Soltani, M. Chaker, E. Haddad, R. Kruzelecky, and D. Nikanpour, Journal of Vacuum Science & Technology A **22**, 859 (2004).

[69] T. A. Miller, M. Rudé, V. Pruneri, and S. Wall, Physical Review B **94**, 024301 (2016).

[70] A. Pergament, G. Stefanovich, N. Kuldin, and A. Velichko, ISRN Condensed Matter Physics **2013** (2013).

[71] W.-T. Liu, J. Cao, W. Fan, Z. Hao, M. C. Martin, Y. Shen, J. Wu, and F. Wang, Nano Letters **11**, 466 (2010).

[72] J. Yoon, H. Kim, X. Chen, N. Tamura, B. S. Mun, C. Park, and H. Ju, ACS Applied Materials & Interfaces **8**, 2280 (2016).

[73] M. A. Kats, R. Blanchard, S. Zhang, P. Genevet, C. Ko, S. Ramanathan, and F. Capasso, Physical Review X **3**, 041004 (2013).

[74] M. A. Kats and F. Capasso, Laser & Photonics Reviews **10**, 699 (2016).

[75] J. Liang, L. Hou, and J. Li, Journal of the Optical Society of America B **33**, 1075 (2016).

[76] J. Rensberg, Y. Zhou, S. Richter, C. Wan, S. Zhang, P. Schöppe, R. Schmidt-Grund, S. Ramanathan, F. Capasso, M. A. Kats, *et al.*, Physical Review Applied **8**, 014009 (2017).

[77] F. F. Schlich and R. Spolenak, Applied Physics Letters **103**, 213112 (2013).

[78] J. W. Cleary, R. Soref, and J. R. Hendrickson, Optics Express **21**, 19363 (2013).

[79] J. Park, J.-H. Kang, A. P. Vasudev, D. T. Schoen, H. Kim, E. Hasman, and M. L. Brongersma, ACS Photonics **1**, 812 (2014).

[80] J. B. Goodenough, Journal of Solid State Chemistry **3**, 490 (1971).

[81] G. Villeneuve, A. Bordet, A. Casalot, J. Pouget, H. Launois, and P. Lederer, Journal of Physics and Chemistry of Solids **33**, 1953 (1972).

[82] C. Piccirillo, R. Binions, and I. P. Parkin, European Journal of Inorganic Chemistry **2007**, 4050 (2007).

[83] T. Hanlon, J. Coath, and M. Richardson, Thin Solid Films **436**, 269 (2003).

[84] X. Tan, T. Yao, R. Long, Z. Sun, Y. Feng, H. Cheng, X. Yuan, W. Zhang, Q. Liu, C. Wu, *et al.*, Scientific Reports **2**, 466 (2012).

[85] R. Binions, G. Hyett, C. Piccirillo, and I. P. Parkin, Journal of Materials Chemistry **17**, 4652 (2007).

[86] W. Burkhardt, T. Christmann, B. Meyer, W. Niessner, D. Schalch, and A. Scharmann, Thin Solid Films **345**, 229 (1999).

[87] H. Bruchlos and K.-D. Ufert, Crystal Research and Technology **12**, 153 (1977).

[88] N. Mlyuka, G. A. Niklasson, and C.-G. Granqvist, Applied Physics Letters **95**, 171909 (2009).

[89] C. J. Patridge, L. Whittaker, B. Ravel, and S. Banerjee, The Journal of Physical Chemistry C **116**, 3728 (2012).

[90] T. D. Manning, I. P. Parkin, C. Blackman, and U. Qureshi, Journal of Materials Chemistry **15**, 4560 (2005).

[91] C. Tang, P. Georgopoulos, M. Fine, J. Cohen, M. Nygren, G. Knapp, and A. Aldred, Physical Review B **31**, 1000 (1985).

[92] J. M. Booth and P. S. Casey, Physical Review Letters **103**, 086402 (2009).

[93] S.-Y. Hu, Shuanglinand Li, R. Ahuja, C. Granqvist, K. Hermansson, G. Niklasson, and R. Scheicher, Applied Physics Letters **101**, 201902 (2012).

[94] Y. Wu, L. Fan, Q. Liu, S. Chen, W. Huang, F. Chen, G. Liao, C. Zou, and Z. Wu, Scientific Reports **5**, 9328 (2015).

[95] K. Shibuya, M. Kawasaki, and Y. Tokura, Applied Physics Letters **96**, 022102 (2010).

[96] K. Shibuya, D. Okuyama, R. Kumai, Y. Yamasaki, H. Nakao, Y. Murakami, Y. Taguchi, T. Arima, M. Kawasaki, and Y. Tokura, Physical Review B **84**, 165108 (2011).

[97] X. Liu, S.-W. Wang, F. Chen, L. Yu, and X. Chen, Journal of Physics D: Applied Physics **48**, 265104 (2015).

[98] A. Moatti, R. Sachan, J. Prater, and J. Narayan, ACS Applied Materials & Interfaces (2017).

[99] M. Imada, A. Fujimori, and Y. Tokura, Reviews of Modern Physics **70**, 1039 (1998).

[100] N. B. Aetukuri, A. X. Gray, M. Drouard, M. Cossale, L. Gao, A. H. Reid, R. Kukreja, H. Ohldag, C. A. Jenkins, E. Arenholz, *et al.*, Nature Physics **9**, 661 (2013).

[101] M. Brahlek, L. Zhang, J. Lapano, H.-T. Zhang, R. Engel-Herbert, N. Shukla, S. Datta, H. Paik, and D. G. Schlom, MRS Communications **7**, 27 (2017).

[102] Y. Tokura and Y. Tomioka, Journal of Magnetism and Magnetic Materials **200**, 1 (1999).

[103] Y. Tokura and N. Nagaosa, Science **288**, 462 (2000).

[104] P. A. Lee, N. Nagaosa, and X.-G. Wen, Reviews of Modern Physics **78**, 17 (2006).

[105] U. Schwingenschlögl and V. Eyert, Annalen der Physik **13**, 475 (2004).

[106] H. Katzke, P. Tolédano, and W. Depmeier, Physical Review B **68**, 024109 (2003).

[107] F. Morin, Physical Review Letters **3**, 34 (1959).

[108] J. Feinleib and W. Paul, Physical Review **155**, 841 (1967).

[109] F. Chudnovskii, E. Terukov, and D. Khomskii, Solid State Communications **25**, 573 (1978).

[110] S. Kachi, K. Kosuge, and H. Okinaka, Journal of Solid State Chemistry **6**, 258 (1973).

[111] K. Nagasawa, Y. Bando, and T. Takada, Journal of Crystal Growth **17**, 143 (1972).

[112] D. Ruzmetov and S. Ramanathan, "Thin film metal oxides: fundamentals and applications in electronics and energy," (2010).

[113] W. Rosevear and W. Paul, Physical Review B **7**, 2109 (1973).

[114] T. Mitsuishi, Japanese Journal of Applied Physics **6**, 1060 (1967).

[115] D. Maurer and A. Leue, Materials Science and Engineering: A **370**, 440 (2004).

[116] V. Balakrishnan, C. Ko, and S. Ramanathan, Journal of Materials Research **27**, 1476 (2012).

[117] D. Kim and H. S. Kwok, Applied Physics Letters **65**, 3188 (1994).

[118] Y. Zhao, J. Hwan Lee, Y. Zhu, M. Nazari, C. Chen, H. Wang, A. Bernussi, M. Holtz, and Z. Fan, Journal of Applied Physics **111**, 053533 (2012).

[119] J. Jeong, N. Aetukuri, T. Graf, T. D. Schladt, M. G. Samant, and S. S. Parkin, Science **339**, 1402 (2013).

[120] C.-I. Li, J.-C. Lin, H.-J. Liu, M.-W. Chu, H.-W. Chen, C.-H. Ma, C.-Y. Tsai, H.-W. Huang, H.-J. Lin, H.-L. Liu, *et al.*, Chemistry of Materials **28**, 3914 (2016).

[121] Y. Zhou, X. Chen, C. Ko, Z. Yang, C. Mouli, and S. Ramanathan, IEEE Electron Device Letters **34**, 220 (2013).

[122] C. Griffiths and H. Eastwood, Journal of Applied Physics **45**, 2201 (1974).

[123] M. Liu, M. Wagner, J. Zhang, A. McLeod, S. Kittiwatanakul, Z. Fei, E. Abreu, M. Goldflam, A. J. Sternbach, S. Dai, *et al.*, Applied Physics Letters **104**, 121905 (2014).

[124] L. Fan, S. Chen, Z. Luo, Q. Liu, Y. Wu, L. Song, D. Ji, P. Wang, W. Chu, C. Gao, *et al.*, Nano Letters **14**, 4036 (2014).

[125] J. H. Park, J. M. Coy, T. S. Kasirga, C. Huang, Z. Fei, S. Hunter, and D. H. Cobden, Nature **500**, 431 (2013).

[126] S. Lysenko, F. Fernández, A. Rúa, J. Aparicio, N. Sepúlveda, J. Figueroa, K. Vargas, and J. Cordero, Journal of Applied Physics **117**, 184304 (2015).

[127] C. Chen, Y. Zhao, X. Pan, V. Kuryatkov, A. Bernussi, M. Holtz, and Z. Fan, Journal of Applied Physics **110**, 023707 (2011).

[128] D. McWhan, M. Marezio, J. Remeika, and P. Dernier, Physical Review B **10**, 490 (1974).

[129] A. Zylbersztejn and N. F. Mott, Physical Review B **11**, 4383 (1975).

[130] M. Korotin, N. Skorikov, and V. Anisimov, arXiv:cond-mat/0301347 (2003).

[131] L. Chen, X. Wang, D. Wan, Y. Cui, B. Liu, S. Shi, H. Luo, and Y. Gao, RSC Advances **6**, 73070 (2016).

[132] D. Kucharczyk and T. Niklewski, Journal of Applied Crystallography **12**, 370 (1979).

[133] V. Eyert, arXiv:cond-mat/0210558 (2002).

[134] J. B. Goodenough, Physical Review **117**, 1442 (1960).

[135] A. Haras, M. Witko, D. Salahub, K. Hermann, and R. Tokarz, Surface Science **491**, 77 (2001).

[136] M. Marezio, D. B. McWhan, J. Remeika, and P. Dernier, Physical Review B **5**, 2541 (1972).

[137] J. Pouget, H. Launois, J. d'Haenens, P. Merenda, and T. Rice, Physical Review Letters **35**, 873 (1975).

[138] H. Asayesh-Ardakani, W. Yao, A. Nie, P. M. Marley, E. Braham, R. F. Klie, S. Banerjee, and R. Shahbazian-Yassar, Applied Physics Letters **110**, 053107 (2017).

[139] S. Shin, S. Suga, M. Taniguchi, M. Fujisawa, H. Kanzaki, A. Fujimori, H. Daimon, Y. Ueda, K. Kosuge, and S. Kachi, Physical Review B **41**, 4993 (1990).

[140] D. Ruzmetov, S. D. Senanayake, V. Narayanamurti, and S. Ramanathan, Physical Review B **77**, 195442 (2008).

[141] A. Gray, J. Jeong, N. Aetukuri, P. Granitzka, Z. Chen, R. Kukreja, D. Higley, T. Chase, A. Reid, H. Ohldag, *et al.*, Physical Review Letters **116**, 116403 (2016).

[142] D. Ielmini and R. Waser, *Resistive Switching: From Fundamentals of Nanoionic Redox Processes to Memristive Device Applications* (John Wiley & Sons, 2015).

[143] X. He, Y. Zeng, X. Xu, C. Gu, F. Chen, B. Wu, C. Wang, H. Xing, X. Chen, and J. Chu, Physical Chemistry Chemical Physics **17**, 11638 (2015).

[144] N. Quackenbush, J. W. Tashman, J. A. Mundy, S. Sallis, H. Paik, R. Misra, J. A. Moyer, J.-H. Guo, D. A. Fischer, J. C. Woicik, *et al.*, Nano Letters **13**, 4857 (2013).

[145] M. M. Qazilbash, A. Schafgans, K. Burch, S. Yun, B. Chae, B. Kim, H.-T. Kim, and D. Basov, Physical Review B **77**, 115121 (2008).

[146] A. Cavalleri, T. Dekorsy, H. H. Chong, J.-C. Kieffer, and R. W. Schoenlein, Physical Review B **70**, 161102 (2004).

[147] V. R. Morrison, R. P. Chatelain, K. L. Tiwari, A. Hendaoui, A. Bruhács, M. Chaker, and B. J. Siwick, Science **346**, 445 (2014).

[148] D. Wegkamp, M. Herzog, L. Xian, M. Gatti, P. Cudazzo, C. L. McGahan, R. E. Marvel, R. F. Haglund Jr, A. Rubio, M. Wolf, *et al.*, Physical Review Letters **113**, 216401 (2014).

[149] M. Haverkort, Z. Hu, A. Tanaka, W. Reichelt, S. Streltsov, M. Korotin, V. Anisimov, H. Hsieh, H.-J. Lin, C. Chen, *et al.*, Physical Review Letters **95**, 196404 (2005).

[150] D. N. Basov, R. D. Averitt, D. Van Der Marel, M. Dressel, and K. Haule, Reviews of Modern Physics **83**, 471 (2011).

[151] T. Huffman, C. Hendriks, E. Walter, J. Yoon, H. Ju, R. Smith, G. Carr, H. Krakauer, and M. Qazilbash, Physical Review B **95**, 075125 (2017).

[152] J. D. Budai, J. Hong, M. E. Manley, E. D. Specht, C. W. Li, J. Z. Tischler, D. L. Abernathy, A. H. Said, B. M. Leu, L. A. Boatner, *et al.*, Nature **515**, 535 (2014).

[153] S. Ramanathan, Harvard University: Springer New York Dordrecht Heidelberg London (2010).

[154] B. T. OŠcallahan, A. C. Jones, J. H. Park, D. H. Cobden, J. M. Atkin, and M. B. Raschke, Nature Communications **6** (2015).

[155] S. Biermann, A. Poteryaev, A. I. Lichtenstein, and A. Georges, Physical Reviev Letters **94**, 026404 (2005).

[156] A. Liebsch, H. Ishida, and G. Bihlmayer, Physical Review B **71**, 085109 (2005).

[157] S. Lee, T. L. Meyer, C. Sohn, D. Lee, J. Nichols, D. Lee, S. S. A. Seo, J. W. Freeland, T. W. Noh, and H. N. Lee, APL Materials **3**, 126109 (2015).

[158] J. K. Kana, J. Ndjaka, G. Vignaud, A. Gibaud, and M. Maaza, Optics Communications **284**, 807 (2011).

[159] Z. Zhang, F. Zuo, C. Wan, A. Dutta, J. Kim, J. Rensberg, R. Nawrodt, H. H. Park, T. J. Larrabee, X. Guan, *et al.*, Physical Review Applied **7**, 034008 (2017).

[160] L. A. Ladd and W. Paul, Solid State Communications **7**, 425 (1969).

[161] Y. Muraoka, Y. Ueda, and Z. Hiroi, Journal of Physics and Chemistry of Solids **63**, 965 (2002).

[162] K. Nagashima, T. Yanagida, H. Tanaka, and T. Kawai, Physical Review B **74**, 172106 (2006).

[163] J. Cao, E. Ertekin, V. Srinivasan, W. Fan, S. Huang, H. Zheng, J. Yim, D. Khanal, D. Ogletree, J. Grossman, *et al.*, Nature Nanotechnology **4**, 732 (2009).

[164] J. Cao, Y. Gu, W. Fan, L. Chen, D. Ogletree, K. Chen, N. Tamura, M. Kunz, C. Barrett, J. Seidel, *et al.*, Nano Letters **10**, 2667 (2010).

[165] Y. Gu, J. Cao, J. Wu, and L.-Q. Chen, Journal of Applied Physics **108**, 083517 (2010).

[166] J. Cao and J. Wu, Materials Science and Engineering: R: Reports **71**, 35 (2011).

[167] M. Yang, Y. Yang, B. Hong, L. Wang, K. Hu, Y. Dong, H. Xu, H. Huang, J. Zhao, H. Chen, *et al.*, Scientific Reports **6** (2016).

[168] F. J. Wong, Y. Zhou, and S. Ramanathan, Journal of Crystal Growth **364**, 74 (2013).

[169] M. Nakano, K. Shibuya, D. Okuyama, T. Hatano, S. Ono, M. Kawasaki, Y. Iwasa, and Y. Tokura, Nature **487**, 459 (2012).

[170] Y. Wu, L. Fan, W. Huang, S. Chen, S. Chen, F. Chen, C. Zou, and Z. Wu, Physical Chemistry Chemical Physics **16**, 17705 (2014).

[171] S. Wang, M. Liu, L. Kong, Y. Long, X. Jiang, and A. Yu, Progress in Materials Science **81**, 1 (2016).

[172] S. Lee, T. L. Meyer, S. Park, T. Egami, and H. N. Lee, Applied Physics Letters **105**, 223515 (2014).

[173] P. Zhang, K. Jiang, Q. Deng, Q. You, J. Zhang, J. Wu, Z. Hu, and J. Chu, Journal of Materials Chemistry C **3**, 5033 (2015).

[174] C. Chen and Z. Fan, Applied Physics Letters **95**, 262106 (2009).

[175] Y. Cui, B. Liu, L. Chen, H. Luo, and Y. Gao, AIP Advances **6**, 105301 (2016).

[176] S. Zhang, I. S. Kim, and L. J. Lauhon, Nano Letters **11**, 1443 (2011).

[177] L. Fan, S. Chen, Y. Wu, F. Chen, W. Chu, X. Chen, C. Zou, and Z. Wu, Applied Physics Letters **103**, 131914 (2013).

[178] S. Rathi, I.-y. Lee, J.-H. Park, B.-J. Kim, H.-T. Kim, and G.-H. Kim, ACS Applied Materials & Interfaces **6**, 19718 (2014).

[179] K. Shibuya and A. Sawa, AIP Advances **5**, 107118 (2015).

[180] H. K. Raut, V. A. Ganesh, A. S. Nair, and S. Ramakrishna, Energy & Environmental Science **4**, 3779 (2011).

[181] O. Heavens, Reports on Progress in Physics **23**, 1 (1960).

[182] Z. Knittl, *Optics of thin films: an optical multilayer theory* (Wiley London:, 1976).

[183] O. S. Heavens, *Optical properties of thin solid films* (Courier Corporation, 1991).

[184] A. I. Lvovsky, *Fresnel equations* (Encyclopedia of Optical Engineering; Taylor & Francis: New York, 2013) pp. 1–6.

[185] J. Chilwell and I. Hodgkinson, Journal of the Optical Society of America A **1**, 742 (1984).

[186] C. C. Katsidis and D. I. Siapkas, Applied Optics **41**, 3978 (2002).

[187] P. Lalanne and M. Hutley, "Artificial media optical properties-subwavelength scale," (2003).

[188] O. Wiener, Physikalische Zeitschrift **5**, 332 (1904).

[189] K. Lichtenecker, Physik unserer Zeit **27**, 115 (1926).

[190] A. Goncharenko, V. Lozovski, and E. Venger, Optics Communications **174**, 19 (2000).

[191] H. Looyenga, Physica **31**, 401 (1965).

[192] J. M. Garnett, Philosophical Transactions of the Royal Society of London. Series A, Containing Papers of a Mathematical or Physical Character , 237 (1906).

[193] V. D. Bruggeman, Annalen der Physik **416**, 636 (1935).

[194] A. V. Goncharenko, Physical Review E **68**, 041108 (2003).

[195] D. Schmidt and M. Schubert, Journal of Applied Physics **114**, 083510 (2013).

[196] J. E. Spanier and I. P. Herman, Physical Review B **61**, 10437 (2000).

[197] G. Beydaghyan, C. Buzea, Y. Cui, C. Elliott, and K. Robbie, Applied Physics Letters **87**, 153103 (2005).

[198] I. Nerbø, S. Le Roy, M. Foldyna, M. Kildemo, and E. Søndergård, Journal of Applied Physics **108**, 014307 (2010).

[199] D. Schmidt, E. Schubert, and M. Schubert, Applied Physics Letters **100**, 011912 (2012).

[200] W. J. Weber, D. M. Duffy, L. Thomé, and Y. Zhang, Current Opinion in Solid State and Materials Science **19**, 1 (2015).

[201] W. Wesch and E. Wendler, "Ion beam modification of solids," (2016).

[202] M. Nastasi, J. Mayer, and J. K. Hirvonen, *Ion-solid interactions: fundamentals and applications* (Cambridge University Press, 1996).

[203] L. A. Giannuzzi *et al.*, *Introduction to focused ion beams: instrumentation, theory, techniques and practice* (Springer Science & Business Media, 2006).

[204] J. F. Ziegler, M. D. Ziegler, and J. P. Biersack, Nuclear Instruments and Methods in Physics Research Section B **268**, 1818 (2010).

[205] M. A. Nastasi and J. W. Mayer, *Ion implantation and synthesis of materials*, Vol. 80 (Springer, 2006).

[206] P. Jin, S. Nakao, and S. Tanemura, Thin Solid Films **324**, 151 (1998).

[207] K.-D. Ufert, Physica Status Solidi (a) **42**, 187 (1977).

[208] H. Hofsäss, P. Ehrhardt, H.-G. Gehrke, M. Brötzmann, U. Vetter, K. Zhang, J. Krauser, C. Trautmann, C. Ko, and S. Ramanathan, AIP Advances **1**, 032168 (2011).

[209] E. M. Heckman, L. P. Gonzalez, S. Guha, J. O. Barnes, and A. Carpenter, Thin Solid Films **518**, 265 (2009).

[210] H. Lim, N. Stavrias, B. C. Johnson, R. E. Marvel, R. F. Haglund, and J. C. McCallum, Journal of Applied Physics **115**, 093107 (2014).

[211] J. G. Ramirez, T. Saerbeck, S. Wang, J. Trastoy, M. Malnou, J. Lesueur, J.-P. Crocombette, J. E. Villegas, and I. K. Schuller, Physical Review B **91**, 205123 (2015).

[212] G. Khan, A. Kandasami, and B. Bhat, Radiation Physics and Chemistry **123**, 55 (2016).

[213] T. Tiedje, E. Yablonovitch, G. D. Cody, and B. G. Brooks, IEEE Transactions on Electron Devices **31**, 711 (1984).

[214] L. Hu and G. Chen, Nano Letters **7**, 3249 (2007).

[215] Y. M. Song, J. S. Yu, and Y. T. Lee, Optics Letters **35**, 276 (2010).

[216] M. Bernardi, M. Palummo, and J. C. Grossman, Nano Letters **13**, 3664 (2013).

[217] A. Polman, M. Knight, E. C. Garnett, B. Ehrler, and W. C. Sinke, Science **352**, aad4424 (2016).

[218] D. Rodrigo, O. Limaj, D. Janner, D. Etezadi, F. J. G. de Abajo, V. Pruneri, and H. Altug, Science **349**, 165 (2015).

[219] M. W. Knight, H. Sobhani, P. Nordlander, and N. J. Halas, Science **332**, 702 (2011).

[220] J. Mason, S. Smith, and D. Wasserman, Applied Physics Letters **98**, 241105 (2011).

[221] J. M. Lloyd, *Thermal imaging systems* (Springer Science & Business Media, 2013).

[222] J. A. Schuller, T. Taubner, and M. L. Brongersma, Nature Photonics **3**, 658 (2009).

[223] W. Streyer, S. Law, G. Rooney, T. Jacobs, and D. Wasserman, Optics Express **21**, 9113 (2013).

[224] K.-T. Lee, S. Seo, J. Y. Lee, and L. J. Guo, Advanced Materials **26**, 6324 (2014).

[225] H. Kocer, S. Butun, Z. Li, and K. Aydin, Scientific Reports **5**, 8157 (2015).

[226] E. Driessen and M. De Dood, Applied Physics Letters **94**, 171109 (2009).

[227] J. Monzón and L. Sánchez-Soto, Pure and Applied Optics: Journal of the European Optical Society Part A **1**, 219 (1992).

[228] A. P. Raman, M. A. Anoma, L. Zhu, E. Rephaeli, and S. Fan, Nature **515**, 540 (2014).

[229] A. C. Jones, B. T. OŠCallahan, H. U. Yang, and M. B. Raschke, Progress in Surface Science **88**, 349 (2013).

[230] J. Kischkat, S. Peters, B. Gruska, M. Semtsiv, M. Chashnikova, M. Klinkmüller, O. Fedosenko, S. Machulik, A. Aleksandrova, G. Monastyrskyi, *et al.*, Applied Optics **51**, 6789 (2012).

[231] D. M. Brown, E. T. Downey, M. Ghezzo, J. W. Kretchmer, R. J. Saia, Y. S. Liu, J. A. Edmond, G. Gati, J. M. Pimbley, and W. E. Schneider, IEEE Transactions on Electron Devices **40**, 325 (1993).

[232] J. I. Larruquert, A. P. Pérez-Marín, S. García-Cortés, L. Rodríguez-de Marcos, J. A. Aznárez, and J. A. Méndez, Journal of the Optical Society of America A **28**, 2340 (2011).

[233] H. B. Holl, Journal of the Optical Society of America A **57**, 683 (1967).

[234] X. Zhong, X. Zhang, A. Gupta, and P. LeClair, Journal of Applied Physics **110**, 084516 (2011).

[235] M. Schubert, T. Tiwald, and C. Herzinger, Physical Review B **61**, 8187 (2000).

[236] S. Babar and J. Weaver, Applied Optics **54**, 477 (2015).

[237] S. Franzen, The Journal of Physical Chemistry C **112**, 6027 (2008).

[238] N. Engheta, Science **340**, 286 (2013).

[239] G. Kenanakis, C. P. Mavidis, E. Vasilaki, N. Katsarakis, M. Kafesaki, E. Economou, and C. Soukoulis, Applied Physics A **123**, 77 (2017).

[240] G. Kajtár, M. Kafesaki, E. Economou, and C. Soukoulis, Journal of Physics D: Applied Physics **49**, 055104 (2016).

[241] M. Yan, Journal of Optics **15**, 025006 (2013).

[242] T. Paik, S.-H. Hong, E. A. Gaulding, H. Caglayan, T. R. Gordon, N. Engheta, C. R. Kagan, and C. B. Murray, ACS Nano **8**, 797 (2014).

[243] Y. Cui, X. Wang, Y. Zhou, R. Gordon, and S. Ramanathan, Journal of Crystal Growth **338**, 96 (2012).

[244] J. F. Ziegler, *Ion implantation science and technology* (Elsevier, 2012).

[245] G. Götz and K. Gaertner, (1988).

[246] J. W. Mayer and E. Rimini, *Ion beam handbook for material analysis* (Elsevier, 2012).

[247] G. Schatz and A. Weidinger, Nukleare Festkörperphysik. Series: Teubner Studienbücher Physik, ISBN: 978-3-519-23079-3. Vieweg+ Teubner Verlag (Wiesbaden), Edited by Günter Schatz and Alois Weidinger (1997).

[248] W.-K. Chu, *Backscattering spectrometry* (Elsevier, 2012).

[249] A. Kelly and K. M. Knowles, *Crystallography and crystal defects* (John Wiley & Sons, 2012).

[250] C. Hammond and C. Hammond, *Basics of crystallography and diffraction*, Vol. 214 (Oxford, 2001).

[251] Y. Waseda, E. Matsubara, and K. Shinoda, *X-ray diffraction crystallography: introduction, examples and solved problems* (Springer Science & Business Media, 2011).

[252] N. Colthup, *Introduction to infrared and Raman spectroscopy* (Elsevier, 2012).

[253] S.-J. Chang, W.-K. Hong, H. J. Kim, J. B. Lee, J. Yoon, H. C. Ko, and Y. S. Huh, Nanotechnology **24**, 345701 (2013).

[254] R. Reichelt, in *Science of Microscopy* (Springer, 2007) pp. 133–272.

[255] B. Fultz and J. M. Howe, *Transmission electron microscopy and diffractometry of materials* (Springer Science & Business Media, 2012).

[256] H. Fujiwara, *Spectroscopic ellipsometry: principles and applications* (John Wiley & Sons, 2007).

[257] L. Novotny and S. J. Stranick, Annual Review Physical Chemistry **57**, 303 (2006).

[258] L. Wang and X. G. Xu, Nature Communications **6**, 8973 (2015).

[259] G. Wollny, E. Bründermann, Z. Arsov, L. Quaroni, and M. Havenith, Optics Express **16**, 7453 (2008).

[260] A. S. McLeod, *Quantitative Near-field Microscopy of Heterogeneous and Correlated Electron Oxides*, Ph.D. thesis, University of California, San Diego (2017).

[261] L. Fan, Y. Wu, C. Si, G. Pan, C. Zou, and Z. Wu, Applied Physics Letters **102**, 011604 (2013).

[262] H.-T. Zhang, L. Zhang, D. Mukherjee, Y.-X. Zheng, R. C. Haislmaier, N. Alem, and R. Engel-Herbert, Nature Communications **6** (2015).

[263] D. Zhang, T. Wen, Y. Xiong, D. Qiu, and Q. Wen, Nano-Micro Letters **9**, 29 (2017).

[264] G. J. Kovács, D. Bürger, I. Skorupa, H. Reuther, R. Heller, and H. Schmidt, Journal of Applied Physics **109**, 063708 (2011).

[265] T.-H. Yang, C. Jin, R. Aggarwal, R. Narayan, and J. Narayan, Journal of Materials Research **25**, 422 (2010).

[266] M. Yang, Y. Yang, B. Hong, L. Wang, Z. Luo, X. Li, C. Kang, M. Li, H. Zong, and C. Gao, RSC Advances **5**, 80122 (2015).

[267] P. Barna and M. Adamik, Thin Solid Films **317**, 27 (1998).

[268] X. Li, A. Gloter, H. Gu, X. Cao, P. Jin, and C. Colliex, Acta Materialia **61**, 6443 (2013).

[269] V. Théry, A. Boulle, A. Crunteanu, J.-C. Orlianges, A. Beaumont, R. Mayet, A. Mennai, F. Cosset, A. Bessaudou, and M. Fabert, Journal of Applied Physics **121**, 055303 (2017).

[270] H. Zhou, M. F. Chisholm, T.-H. Yang, S. J. Pennycook, and J. Narayan, Journal of Applied Physics **110**, 073515 (2011).

[271] S. Kittiwatanakul, S. A. Wolf, and J. Lu, Applied Physics Letters **105**, 073112 (2014).

[272] V. Théry, A. Boulle, A. Crunteanu, J.-C. Orlianges, A. Beaumont, R. Mayet, A. Mennai, F. Cosset, A. Bessaudou, and M. Fabert, Physical Review B **93**, 184106 (2016).

[273] C. Chen, Y. Zhu, Y. Zhao, J. H. Lee, H. Wang, A. Bernussi, M. Holtz, and Z. Fan, Applied Physics Letters **97**, 211905 (2010).

[274] D. Fu, K. Liu, T. Tao, K. Lo, C. Cheng, B. Liu, R. Zhang, H. A. Bechtel, and J. Wu, Journal of Applied Physics **113**, 043707 (2013).

[275] F. Guinneton, L. Sauques, J. Valmalette, F. Cros, and J. Gavarri, Journal of Physics and Chemistry of Solids **62**, 1229 (2001).

[276] T. Peterseim, M. Dressel, M. Dietrich, and A. Polity, Journal of Applied Physics **120**, 075102 (2016).

[277] X. Zhong, P. LeClair, S. K. Sarker, and A. Gupta, Physical Review B **86**, 094114 (2012).

[278] X. Zhong, X. Zhang, A. Gupta, and P. LeClair, Journal of Applied Physics **110**, 084516 (2011).

[279] D. Ruzmetov, D. Heiman, B. B. Claflin, V. Narayanamurti, and S. Ramanathan, Physical Review B **79**, 153107 (2009).

[280] W. Yin, S. Wolf, C. Ko, S. Ramanathan, and P. Reinke, Journal of Applied Physics **109**, 024311 (2011).

[281] J. Dai, X. Wang, S. He, H. Ma, J. Lai, and X. Yi, in *Nanotechnology, 2007. IEEE-NANO 2007. 7th IEEE Conference on* (IEEE, 2007) pp. 1265–1268.

[282] V. Shorin and A. Sosnin, Nuclear Instruments and Methods in Physics Research Section B **72**, 452 (1992).

[283] M. de Keijser, G. Dormans, J. Cillessen, D. De Leeuw, and H. Zandbergen, Applied Physics Letters **58**, 2636 (1991).

[284] J. Wallace, L. B. Aji, A. Martin, S. Shin, L. Shao, and S. Kucheyev, Scientific Reports **7** (2017).

[285] P. C. Snijders, C. Şen, M. P. McConnell, Y.-Z. Ma, A. F. May, A. Herklotz, A. T. Wong, and T. Z. Ward, Scientific Reports **6** (2016).

[286] S. Fan, L. Fan, Q. Li, J. Liu, and B. Ye, Applied Surface Science **321**, 464 (2014).

[287] A. Frenzel, M. M. Qazilbash, M. Brehm, B.-G. Chae, B.-J. Kim, H.-T. Kim, A. Balatsky, F. Keilmann, and D. Basov, Physical Review B **80**, 115115 (2009).

[288] S. Kucheyev, J. Williams, A. Titov, G. Li, and C. Jagadish, Applied Physics Letters **78**, 2694 (2001).

[289] L. B. Aji, J. Wallace, and S. Kucheyev, Scientific Reports **7** (2017).

[290] H. Heinisch and B. Singh, Philosophical Magazine A **67**, 407 (1993).

[291] R. S. Crandall, MRS Online Proceedings Library Archive **149** (1989).

[292] G. Zatryb, A. Podhorodecki, J. Misiewicz, J. Cardin, and F. Gourbilleau, Nanoscale Research Letters **6**, 106 (2011).

[293] Y. Li, S. Ji, Y. Gao, H. Luo, and M. Kanehira, Scientific Reports **3** (2013).

[294] G. Rampelberg, D. Deduytsche, B. De Schutter, P. A. Premkumar, M. Toeller, M. Schaekers, K. Martens, I. Radu, and C. Detavernier, Thin Solid Films **550**, 59 (2014).

[295] G. Rampelberg, B. De Schutter, W. Devulder, K. Martens, I. Radu, and C. Detavernier, Journal of Materials Chemistry C **3**, 11357 (2015).

[296] K. Okimura, N. Hanis Azhan, T. Hajiri, S.-i. Kimura, M. Zaghrioui, and J. Sakai, Journal of Applied Physics **115**, 153501 (2014).

[297] M. Yang, Y. Yang, B. Hong, Y. Zhao, X. Li, Y. Lu, Z. Luo, and C. Gao, Progress in Natural Science: Materials International **97**, 386 (2015).

[298] E. Radue, E. Crisman, L. Wang, S. Kittiwatanakul, J. Lu, S. Wolf, R. Wincheski, R. Lukaszew, and I. Novikova, Journal of Applied Physics **113**, 233104 (2013).

[299] P. Schilbe, Physica B: Condensed Matter **316**, 600 (2002).

[300] H.-T. Kim, B.-G. Chae, D.-H. Youn, G. Kim, K.-Y. Kang, S.-J. Lee, K. Kim, and Y.-S. Lim, Applied Physics Letters **86**, 242101 (2005).

[301] G. Petrov, V. Yakovlev, and J. Squier, Applied Physics Letters **81**, 1023 (2002).

[302] M. Pan, J. Liu, H. Zhong, S. Wang, Z.-f. Li, X. Chen, and W. Lu, Journal of Crystal Growth **268**, 178 (2004).

[303] Y. Ji, Y. Zhang, M. Gao, Z. Yuan, Y. Xia, C. Jin, B. Tao, C. Chen, Q. Jia, and Y. Lin, Scientific Reports **4** (2014).

[304] K. Shibuya, J. Tsutsumi, T. Hasegawa, and A. Sawa, Applied Physics Letters **103**, 021604 (2013).

[305] J. Sakai, M. Zaghrioui, V. Ta Phuoc, S. Roger, C. Autret-Lambert, and K. Okimura, Journal of Applied Physics **113**, 123503 (2013).

[306] J. Sakai, M. Zaghrioui, M. Matsushima, H. Funakubo, and K. Okimura, Journal of Applied Physics **116**, 123510 (2014).

[307] S.-J. Chang, J. B. Park, G. Lee, H. J. Kim, J.-B. Lee, T.-S. Bae, Y.-K. Han, T. J. Park, Y. S. Huh, and W.-K. Hong, Nanoscale **6**, 8068 (2014).

[308] S. Zhang, J. Y. Chou, and L. J. Lauhon, Nano Letters **9**, 4527 (2009).

[309] J. M. Atkin, S. Berweger, E. K. Chavez, M. B. Raschke, J. Cao, W. Fan, and J. Wu, Physical Review B **85**, 020101 (2012).

[310] J. I. Sohn, H. J. Joo, K. S. Kim, H. W. Yang, A.-R. Jang, D. Ahn, H. H. Lee, S. Cha, D. J. Kang, J. M. Kim, *et al.*, Nanotechnology **23**, 205707 (2012).

[311] E. U. Donev, R. Lopez, L. C. Feldman, and R. F. Haglund Jr, Nano Letters **9**, 702 (2009).

[312] C. Marini, E. Arcangeletti, D. Di Castro, L. Baldassare, A. Perucchi, S. Lupi, L. Malavasi, L. Boeri, E. Pomjakushina, K. Conder, *et al.*, Physical Review B **77**, 235111 (2008).

[313] H. Terauchi and J. Cohen, Physical Review B **17**, 2494 (1978).

[314] M. A. Soler and F. Qu, in *Raman Spectroscopy for Nanomaterials Characterization* (Springer, 2012) pp. 379–416.

[315] A. Perucchi, L. Baldassarre, P. Postorino, and S. Lupi, Journal of Physics: Condensed Matter **21**, 323202 (2009).

[316] M. Escote, V. Barbeta, R. Jardim, and J. Campo, Journal of Physics: Condensed Matter **18**, 6117 (2006).

[317] J. Varignon, M. N. Grisolia, J. Íñiguez, A. Barthélémy, and M. Bibes, npj Quantum Materials **2**, 21 (2017).

[318] S. D. Ha, M. Otaki, R. Jaramillo, A. Podpirka, and S. Ramanathan, Journal of Solid State Chemistry **190**, 233 (2012).

[319] B. Torriss, J. Margot, and M. Chaker, Scientific Reports **7**, 40915 (2017).

[320] J.-J. Wang, Y.-Z. Xu, R. Mazzarello, M. Wuttig, and W. Zhang, Materials **10**, 862 (2017).

[321] J.-W. Park, S. H. Eom, H. Lee, J. L. Da Silva, Y.-S. Kang, T.-Y. Lee, and Y. H. Khang, Physical Review B **80**, 115209 (2009).

[322] G. Sun, X. Cao, S. Long, R. Li, and P. Jin, Applied Physics Letters **111**, 053901 (2017).

[323] J. Shi, Y. Zhou, and S. Ramanathan, Nature Communications **5**, 4860 (2014).

[324] A. Kolobov, M. Krbal, P. Fons, J. Tominaga, and T. Uruga, Nature Chemistry **3**, 311 (2011).

[325] P. W. Anderson, Physical Review **109**, 1492 (1958).

[326] L. Fan, S. Chen, G. Liao, Y. Chen, H. Ren, and C. Zou, Journal of Physics: Condensed Matter **28**, 255002 (2016).

[327] J. Salman, M. Haferman, J. Rensber, C. Wan, R. Wambold, B. S. Grundlach, R. Carsten, and M. A. Kats, Advanced Optical Materials , under revision (2017).

[328] W. Zhang, K. Wang, L. Fan, L. Liu, P. Guo, C. Zou, J. Wang, H. Qian, K. Ibrahim, W. Yan, *et al.*, The Journal of Physical Chemistry C **118**, 12837 (2014).

[329] H. Choi, J. Ahn, J. Jung, T. Noh, and D. Kim, Physical Review B **54**, 4621 (1996).

[330] P. U. Jepsen, B. M. Fischer, A. Thoman, H. Helm, J. Suh, R. Lopez, and R. Haglund Jr, Physical Review B **74**, 205103 (2006).

[331] D. Hensler, Journal of Applied Physics **39**, 2354 (1968).

[332] K. Hu, Y. Yang, B. Hong, J. Zhao, Z. Luo, X. Li, X. Zhang, Y. Gu, X. Gao, and C. Gao, Journal of Alloys and Compounds **699**, 575 (2017).

[333] G. Können, *Polarized light in nature* (CUP Archive, 1985).

[334] R. Soref and B. Bennett, IEEE journal of Quantum Electronics **23**, 123 (1987).

[335] P. Hosseini, C. D. Wright, and H. Bhaskaran, Nature **511**, 206 (2014).

[336] S. Sun, K.-Y. Yang, C.-M. Wang, T.-K. Juan, W. T. Chen, C. Y. Liao, Q. He, S. Xiao, W.-T. Kung, G.-Y. Guo, *et al.*, Nano Letters **12**, 6223 (2012).

[337] G. Kaplan, K. Aydin, and J. Scheuer, Optical Materials Express **5**, 2513 (2015).

[338] H. Liu, V. Avrutin, N. Izyumskaya, Ü. Özgür, and H. Morkoç, Superlattices and Microstructures **48**, 458 (2010).

[339] Y. Wang, A. C. Overvig, S. Shrestha, R. Zhang, R. Wang, N. Yu, and L. Dal Negro, Optical Materials Express **7**, 2727 (2017).

[340] A. Pradhan, R. Mundle, K. Santiago, J. Skuza, B. Xiao, K. Song, M. Bahoura, R. Cheaito, and P. E. Hopkins, Scientific Reports **4** (2014).

[341] J. D. Caldwell, L. Lindsay, V. Giannini, I. Vurgaftman, T. L. Reinecke, S. A. Maier, and O. J. Glembocki, Nanophotonics **4**, 44 (2015).

[342] Y. Zhong, S. D. Malagari, T. Hamilton, and D. Wasserman, Journal of Nanophotonics **9**, 093791 (2015).

[343] S. Law, V. Podolskiy, and D. Wasserman, Nanophotonics **2**, 103 (2013).

[344] A. D. Rakić, A. B. Djurišić, J. M. Elazar, and M. L. Majewski, Applied Optics **37**, 5271 (1998).

[345] J. D. Caldwell, A. Kretinin, Y. Chen, V. Giannini, M. M. Fogler, Y. Francescato, C. T. Ellis, J. G. Tischler, C. R. Woods, A. J. Giles, *et al.*, arXiv:1404.0494 (2014).

[346] D. Li and C. Ning, Optics Express **19**, 14594 (2011).

[347] T. Fukumura, Z. Jin, A. Ohtomo, H. Koinuma, and M. Kawasaki, Applied Physics Letters **75**, 3366 (1999).

[348] J. Kim, A. Dutta, G. V. Naik, A. J. Giles, F. J. Bezares, C. T. Ellis, J. G. Tischler, A. M. Mahmoud, H. Caglayan, O. J. Glembocki, *et al.*, Optica **3**, 339 (2016).

[349] S. Charnvanichborikarn, M. Myers, L. Shao, and S. Kucheyev, Journal of Physics: Condensed Matter **25**, 162203 (2013).

[350] J. Wallace, L. Bayu Aji, L. Shao, and S. Kucheyev, Applied Physics Letters **106**, 202102 (2015).

[351] J. Wallace, L. B. Aji, L. Shao, and S. Kucheyev, Scientific Reports **7**, 13182 (2017).

[352] G. Silversmit, D. Depla, H. Poelman, G. B. Marin, and R. De Gryse, Journal of Electron Spectroscopy and Related Phenomena **135**, 167 (2004).

[353] J. Meyer, K. Zilberberg, T. Riedl, and A. Kahn, Journal of Applied Physics **110**, 033710 (2011).

A | Appendix

The appendix contains some additional information, which is not absolutely necessary for the understanding of the main part of this thesis. However, the figures, tables and computer codes described below provide a valuable contribution for a comprehensive presentation of the results.

A.1. Light absorption in ultra-thin films

In a cavity comprising an ultra-thin coating on a substrate, perfect total absorption is the complete absorption of light within both the film and the substrate. Maximizing the absorptance A within a single-layer absorbing coating is not the same like minimizing the reflectance R. However, near-perfect absorption within an ultra-thin film can be achieved on substrates where both the real and imaginary parts of the refractive index of the substrate are as small as possible (low-index, low-loss materials).

Figure A.1 compares the attainable absorptance A within an arbitrary coating on silver and sapphire as a function of the reduced film thickness δ and the extinction coefficient κ_f of the film at a given wavelength and for a given real part of the refractive index n_f. For metals like silver, the point of maximum absorption is found in the ultra-thin limit ($\delta < 0.1$) only for UV and VIS wavelengths (close to the plasma wavelength were the losses of the substrate are still small). As an example, at a wavelength of 355 nm 92.1% of the incident light is absorbed within a 6 nm film on a silver substrate, provided the refractive index of the film is $\tilde{n}_f = 4 + 1.4\mathrm{i}$. However, almost no light is absorbed within an ultra-thin coating on a metal substrate at wavelengths above the near-infrared (see 1550 nm and higher wavelengths). Conversely, on polar dielectric substrates like sapphire, more than 90% of the incident light can be absorbed within an ultra-thin coating at a wavelength within the Reststrahlen band, which extends from 10.9 to 15.8 μm in Al_2O_3. As an example, at a wavelength of 11.3 μm 92.3% of the incident light can be absorbed within a 100 nm thin film ($\delta = 0.03$), provided the refractive index of the film is $\tilde{n}_f = 4 + 2.5\mathrm{i}$.

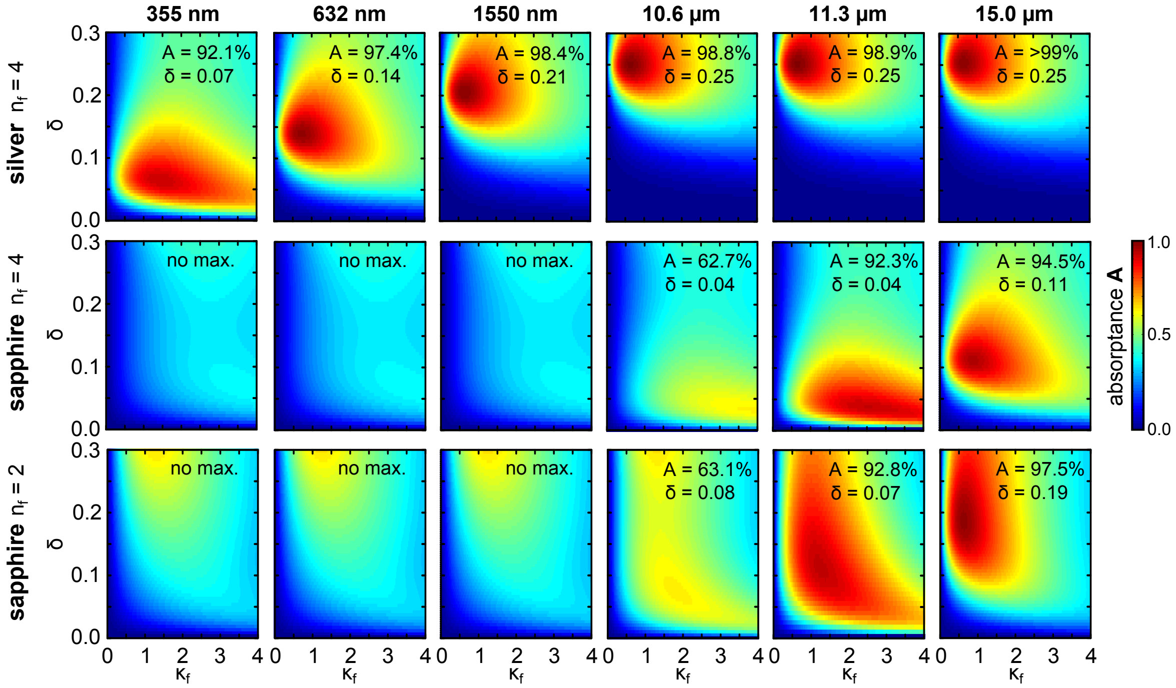

Figure A.1.: Calculated maps of the absorptance A within the coating as a function of reduced film thickness δ and κ_f at a given wavelength, for a given film index n_f, and for a given substrate, as indicated. Silver was chosen as an example for a plasmonic substrate, and Al_2O_3 as an example for a polar dielectric material with a dominant restrahlen band between 10.9 and 15.8 μm.

A.2. Aluminum-doped zinc oxide substrates

Aluminum-doped ZnO substrates were prepared by Al^+ ion implantation of (001) ZnO substrates at an elevated temperature of 400 °C. Multiple ion implantation steps with different ion energies and suitable ion fluences were used in order to achieve a homogeneous box-like doping profile. Figure A.2b shows the individual and sum concentration depth profiles calculated for various ion energies using the SRIM code[204]. The ion fluences, which are indicated in the figure, are calculated to reach a doping concentration of $c_{\mathrm{Al}} \sim 1 \times 10^{20}\,\mathrm{cm}^{-3}$. The resulting sum doping profile consists of a 400 nm near-surface layer of constant aluminum concentration and a gaussian tail extending an additional 200 nm into the ZnO substrate. All samples were annealed at 700 °C for one hour in air.

The crystal quality after ion implantation and thermal annealing was determined via 1.4 MeV He^+ Rutherford backscattering spectrometry in channeling geometry (RBS/C, compare figure A.2c). A drastically increased backscattering yield in the channeling direction (aligned spectrum), indicating a large amount of structural defects, is observed directly after ion irradiation at a nominal dopant concentration of $c_{\mathrm{Al}} \sim 10^{10}\,\mathrm{cm}^{-3}$. However, a high crystalline quality (low backscattering yield in the channeling direction) was recovered for this dopant concentration by the consequent thermal annealing step (compare figure A.2c, green curves). The morphology of a thin VO_2 film grown on the AZO sample doped with $c_{\mathrm{Al}} \sim 10^{10}\,\mathrm{cm}^{-3}$ was investigated using SEM of the sample surface and STEM of a cross section of the film (compare figure A.2a). Although ~ 20 nm elevated islands (determined by AFM) of VO_2 can be seen at the surface, the film is closed with a thickness of approximately 100 nm (compare figure

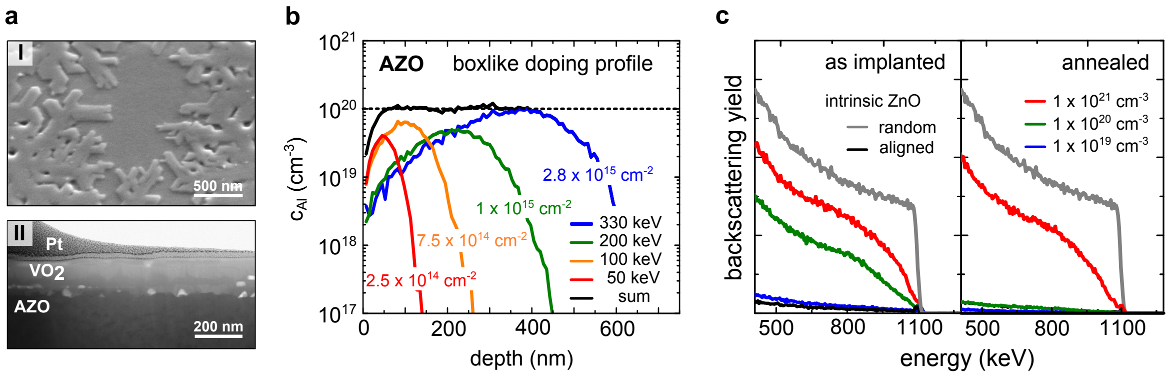

Figure A.2.: **(a)** SEM image taken of the surface of a thin VO_2 film grown on AZO (I) and a cross-sectional STEM image of the same sample (II). **(b)** Individual and sum doping profile of aluminum dopants in ZnO calculated for ion implantation with multiple ion energies and suitable ion fluences as indicated. **(c)** RBS/C using 1.4 MeV He^+ ions of as implanted and annealed AZO samples for various aluminum-dopant concentrations. Aligned and random spectra of intrinsic ZnO are given for comparison.

A.2a I). At the interface between VO_2 and AZO plenty of voids can be seen. Furthermore the AZO surface appears rather rough, which affects the optical properties of the VO_2/AZO layer system.

A.3. Successive ion irradiation

In-situ measurements of the electrical resistance of thin VO_2 films were performed after each of successive ion irradiation steps. The experiment was conducted several times with different ion species to correlate the effect of ion irradiation with the ion mass. A prerequisite for the comparability of the experimental results is a similar defect formation rate and a comparable defect distribution. Table A.1 summarizes the ion energies, ion fluences and ion fluxes that were calculated to match the irradiation condition of the Ar^+ ion irradiation.

Table A.1.: Experimental details of the successive ion irradiation with different ion species. Ion mass m_I, ion energy E_0, ion fluence N_I, ion flux Φ_I, and the corresponding beam current I.

element	m_I (amu)	E_0 (keV)	N_I (cm^{-2})	Φ_I (cm^{-2}s^{-1})	I (nA)
N	14	30	3.1×10^{13}	1.7×10^{11}	31
Al	26	50	1.5×10^{13}	8.3×10^{10}	15
P	31	60	1.2×10^{13}	6.7×10^{10}	12
Ar	40	75	1.0×10^{13}	5.6×10^{10}	10
Fe	56	100	6.7×10^{12}	3.7×10^{10}	6.7
Ga	69	120	5.6×10^{12}	3.1×10^{10}	5.6
As	75	130	5.2×10^{12}	2.9×10^{10}	5.2
In	115	160	3.4×10^{12}	1.9×10^{10}	3.4
Sb	121	180	3.2×10^{12}	1.8×10^{10}	3.2
Cs	133	200	2.8×10^{12}	1.6×10^{10}	2.8
Er	166	245	2.3×10^{12}	1.3×10^{10}	2.3
Bi	209	275	1.8×10^{12}	1.0×10^{10}	1.8

A.4. UPS and XPS

X-ray and ultraviolet photoelectron spectroscopy were employed to obtain core-level and valance-band spectra of an ion irradiated thin VO_2 film deposited on an Al_2O_3 substrate in the near surface layer of the film (compare figure A.3). The XPS and UPS measurements were performed on the as-grown VO_2 film, after a thermal annealing step, and after various 2 keV Ar^+ ion irradiation steps in the same ultrahigh-vacuum chamber (base pressure $\sim 10^{-10}$ mbar). An annealing step of 24 h at 150 °C in this chamber was necessary to prepare a surface layer that clearly corresponds to VO_2. The ion irradiation was performed in the XPS/UPS chamber and the ion energy was chosen to match the probe depth of UPS measurements of only a few nm. XPS and UPS spectra were recorded using Mg K_α (1253.6 eV) and He I radiation (21.2 eV), respectively.

Figure A.3a shows the obtained XPS spectra. The binding energy of the O1s signal (530.0 eV) was used as energy calibration.[352] Binding energies of the $V2p_{3/2}$ level in different oxidization states are indicated in the figure according to the values obtained by Silversmit *et al.*[352]. The $V2p_{3/2}$ signal of the as grown sample shows a sharp peak at a binding energy of approximately 517.3 eV, indicating that the oxidization state of vanadium is V^{5+}. The presence of V_2O_5 in the near-surface layer of the as grown VO_2 film is also evident from the UPS measurements (compare figure A.3a). The highest occupied electronic states for the as grown sample are found at roughly 2.5 eV below the Fermi energy (0 eV, calibrated on a pure Au sample), which is in good agreement with values obtained by Meyer *et al.*[353] for V_2O_5 films. The formation of a roughly 5 nm V_2O_5 surface layer was also observed in STEM images presented in figure 5.1b. Thermal annealing results in a decrease of the binding energy of the $V2p_{3/2}$ level indicating a successful reduction of the V_2O_5 surface layer towards VO_2 (V^{4+}, compare figure A.3a, blue curve). In perfect agreement, a small peak that can be attributed to V3d states of VO_2 appears shortly below the Fermi energy in the UPS spectrum (compare figure A.3b, blue curve). Ion irradiation with an increasing ion fluence shifts the $V2p_{3/2}$ signal to lower binding energies and broadens the signal. The peak position for ion irradiation with an ion fluence of $N_I = 0.4\,\mu\text{Ccm}^{-2}$ is in perfect agreement with the oxidization state V^{3+}, but also contains contributions from higher oxidization states. Lower oxidization states and even metallic vanadium appear for ion irradiation with ion fluences above $N_I = 0.4\,\mu\text{Ccm}^{-2}$, which might be caused by preferential sputtering of oxygen. Ion irradiation with increasing ion fluence shifts the onset of occupied states (V3d states) with respect to the Fermi energy in the UPS spectra. The gap between V3d and the Fermi level is closed at an ion fluence of $N_I = 0.4\,\mu\text{Ccm}^{-2}$, which is in agreement with V_2O_3 in the metal phase. For higher ion fluences the onset of O2p states shift to higher binding energies, which is in agreement with a further reduction of the V_2O_3 surface layer.

The results demonstrate that ion irradiation with increasing ion fluences reduces the oxidization state of the vanadium atoms in the VO_2 lattice, most likely caused by irradiation defects and charge transfer between those defects and lattice atoms. However, XPS is a surface sensitive method and ion irradiation with small energies results in preferential sputtering of oxygen atoms from the near surface layer, which might not be comparable to the irradiation experiments presented in this thesis.

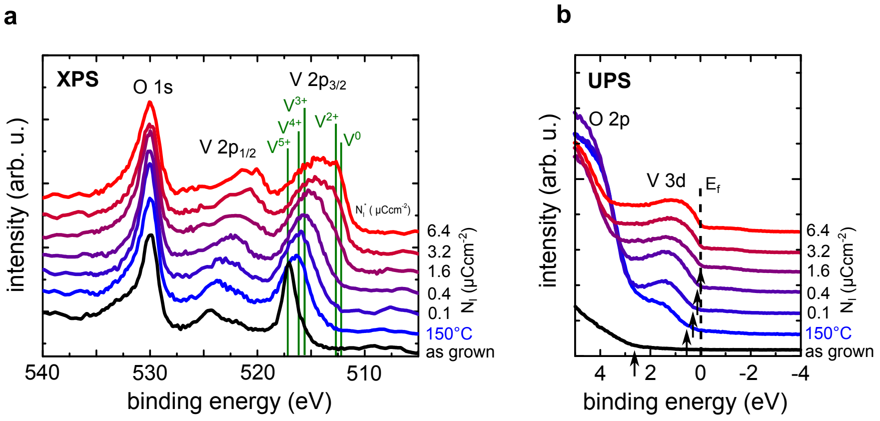

Figure A.3.: (a,b) XPS and UPS spectra of an as grown, annealed and ion irradiated VO_2 thin film grown on Al_2O_3. Ion irradiation was performed in the XPS/UPS chamber with 2 keV Ar^+ ions and with various ion fluences. The binding energies of the $V2p_{3/2}$ level of different vanadium oxidization states are indicated.[352]

A.5. Metallization of vanadium dioxide

The presence of a huge number of V^{3+} states in a thin VO_2 film can efficiently suppress the IMT and metallize the entire film.[119,159] V^{3+} states can be introduced by oxygen deficiency, because oxygen vacancies reduce the neighboring V^{4+} lattice atoms (compare figure A.4c). Here, oxygen deficiency is introduced by annealing VO_2 thin films for one hour in a reducing atmosphere (ultra-high vacuum, 10^{-8} mbar) at various annealing temperatures or by enhanced oxygen out-diffusion caused by ion irradiation at elevated temperatures.

Figure A.4a shows the temperature-dependent resistance of annealed VO_2 thin film samples. Starting at approximately 250 °C, the critical temperature of the phase transition from insulating to metallic behavior is strongly reduced with increasing annealing temperature and reaches values below room temperature for annealing at 500 °C. It can be expected that thermal annealing at an even higher temperature leads to a complete metallization.

Figure A.4b shows the temperature-dependent resistance of thin VO_2 films irradiated with 75 keV Ar^+ ions at room temperature (RT), 300 and 400 °C. At room temperature, the ion fluence of $N_I = 5 \times 10^{15}\,\mathrm{cm}^{-2}$ exceeds the amorphization threshold and the temperature-dependent resistance is typical for amorphous VO_2.[207] Note, amorphous VO_2 does not feature an IMT. Ion irradiation with this ion fluence at elevated irradiation temperatures as low as 300 °C results in metallic resistance of the VO_2 film. Obviously, the formation of irradiation defects and preferential out-diffusion of displaced oxygen atoms leads to the formation of a huge amount of V^{3+} states at lower temperatures compared to thermal annealing. Thus, ion irradiation at elevated temperatures can be used to metallize VO_2.

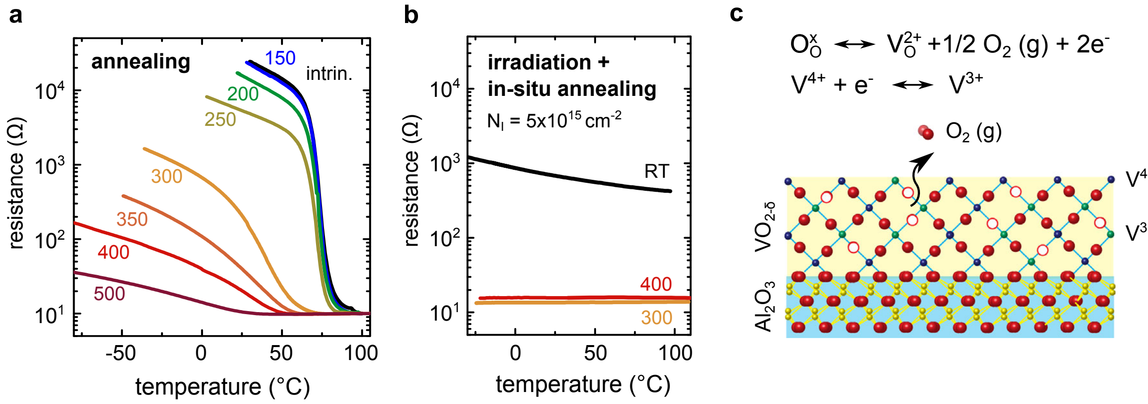

Figure A.4.: (a) Resistance of VO_2 thin films annealed for 30 min at different annealing temperatures in ultra-high vacuum (10^{-8} mbar) as a function of temperature. Annealing temperatures are indicated in °C. For clarity, only the heating cycles are shown. **(b)** Temperature dependent resistance of VO_2 thin films after irradiation with 75 keV Ar^+ at room temperature (RT) and elevated temperatures of 300 and 400 °C. The ion fluence was $N_I = 5 \times 10^{15}\,\mathrm{cm}^{-2}$ and the pressure was on the order of 10^{-8} mbar. **(c)** At low oxygen partial pressure and moderate irradiation temperatures, enhanced out-diffusion of displaced oxygen creates a large number of stable oxygen vacancies, which reduces the valance state of V^{4+} to V^{3+} in the $VO_{2-\delta}$ film (taken from [159]). By introducing a high concentration of oxygen vacancies, the metal-insulator transition is suppressed and a metallic nonvolatile $VO_{2-\delta}$ state is observed.[159].

A.6. Thin film interference

The reflectance and transmittance of light incident onto a N-layer system can be analytically calculated using the transfer matrix method and Fresnel equations (see section 2.2). These calculations were implemented within this thesis in a "MatLab"-based function, which can handle an arbitrary number of layers, and works for all wavelengths, all incident angles, and both light polarizations.

```
function [R,T] = fresnel_TFO(lambda,theta,polarization,input,substrate)

%fresnel_1(wavelength,angle of incidence,’s’(’p’),...
%[eff_i,n_i,k_i,d_i,eff_i+1,...],[n_sub,k_sub])

%’fresnel_TFO’ calculates the transmittance and reflectance of an arbitrary
% layer stack with known ni,ki,di as a function of lambda.

%embedded in this function are the fresnel coefficients giving the
%relative amplitudes of the reflected and transmitted waves at an
%interface between two media.

%input parameter:
%    - lambda (nm):      wavelength
%    - theta (deg):      angle of incidence
%    - polarization:     ’s’ or ’p’ polarized light
%    - eff_i:            fraction of backreflection [0..1]
%    - n_i:              n of i-th layer at lambda
%    - k_i:              k of i-th layer at lambda
%    - d_i               thickness of i-th layer
%    - n_sub:            n of semi-infinite rearside medium
%    - k_sub:            k of semi-infinite rearside medium
```

```
%output values
%   - R:                relflectance at wavelength lambda
%   - T:                transmittance at wavelength lambda

theta=theta/360*2*pi;   %conversion degree to rad
Matrix=[1 0;0 1];       %initilizing transfer matrix

%initilizing air frontside
N(1)=1;
d(1)=0;

%initilizing input layers
for a=1:(length(input)-1)/4
   eff(a)=(input(4*a-3));
   N(a+1)=(input(4*a-2))+1i*(input(4*a-1));
   d(a+1)=(input(4*a));
   theta(a+1)= asin(N(a)/N(a+1)*sin(theta(a)));
end
eff(end+1)=(input(end));

%initilizing substrate
N(end+1)=substrate(1)+1i*substrate(2);
theta(end+1)= asin(N(end-1)/N(end)*sin(theta(end)));

%calculation of transfer matrix
for a=1:length(N)-1

    delta = [exp(-1*1i*opticalthick(lambda,N(a),theta(a),d(a))),...
        0; 0, exp(1*1i*opticalthick(lambda,N(a),theta(a),d(a)))];

    if polarization=='s'
        M_R = [1,  rij_s(N(a),N(a+1),theta(a),theta(a+1));
        rij_s(N(a),N(a+1),theta(a),theta(a+1)), 1];
        M_T = 1/tij_s(N(a),N(a+1),theta(a),theta(a+1));
    elseif polarization=='p'
        M_R = [1,  rij_p(N(a),N(a+1),theta(a),theta(a+1));
        rij_p(N(a),N(a+1),theta(a),theta(a+1)), 1];
        M_T = 1/tij_p(N(a),N(a+1),theta(a),theta(a+1));
    end

    Matrix=(Matrix.*M_T)*delta*(eff(a)*M_R+(1-eff(a))*[1 0;0 1]);
end

%calculation of reflectance and transmittance
r=Matrix(2,1)/Matrix(1,1);
R=r*r';
t=1./Matrix(1,1);
T=abs(real(N(end)*cos(theta(end))/(N(1)*cos(theta(1))))*t*t');

%definition of Fresnel coefficients and optical thickness
    function [transmission] = tij_s(n_i,n_j,theta_i,theta_j)
```

```
        transmission = 2*n_i*cos(theta_i)/(n_i*cos(theta_i)...
            +n_j*cos(theta_j));
    end

    function [transmission] = tij_p(n_i,n_j,theta_i,theta_j)
        transmission = 2*n_i*cos(theta_i)/(n_j*cos(theta_i)...
            +n_i*cos(theta_j));
    end

    function [reflection] = rij_s(n_i,n_j,theta_i,theta_j)
        reflection = (n_i*cos(theta_i)-n_j*cos(theta_j))/(n_i*cos(theta_i)...
            +n_j*cos(theta_j));
    end

    function [reflection] = rij_p(n_i,n_j,theta_i,theta_j)
        reflection = (n_j*cos(theta_i)-n_i*cos(theta_j))/(n_j*cos(theta_i)...
            +n_i*cos(theta_j));
    end

    function [value] = opticalthick(Lambda,n_i,theta_i,d_i)
        value=2*pi*d_i*n_i*cos(theta_i)/Lambda;
    end

end
```

A.7. Random Resistor network

The resistance of polycrystalline thin films can be modeled using a random resistor network approach. In a first step, the polycrystalline film is modeled as a $m \times n$ matrix of domains each having a resistance R_{ij}. Figure A.5a exemplary shows a film composed of two different domains (red and blue). Electrical contacts are depicted as grey domains and always cover the left and right edges of the film. In a second step, a resistor network model is assigned (compare figure A.5b). Each connection of neighboring domains is represented by a resistor with the average resistance of both domains. Thus, each domain connects four different resistors and a regular mesh is formed. Each essential mesh, which is a loop in the circuit that does not contain any other loop, is composed of four resistors. Note, the electrical contacts are connected by a voltage source forming an additional essential mesh. The resistance of the resistor network can be determined using the mesh current method.[281]

As an example, a circuit with mesh currents for a 3×3 domain model is schematically depicted in figure A.5c. For simplicity, all resistances in the example are equal (R). A mesh current is a current that runs through the essential mesh in clockwise direction. Five different mesh currents can be assigned in the example given in figure A.5c (I_1 to I_5). Kirchhoff's voltage law, which states that the sum of directed voltages in a closed network is zero, is applied to express the mesh voltages in terms of the branch currents. A branch current is the same as a mesh current as long as the branch is not shared by two meshes. If the branch is shared by two meshes, the branch current is the difference of the two mesh currents. As an example,

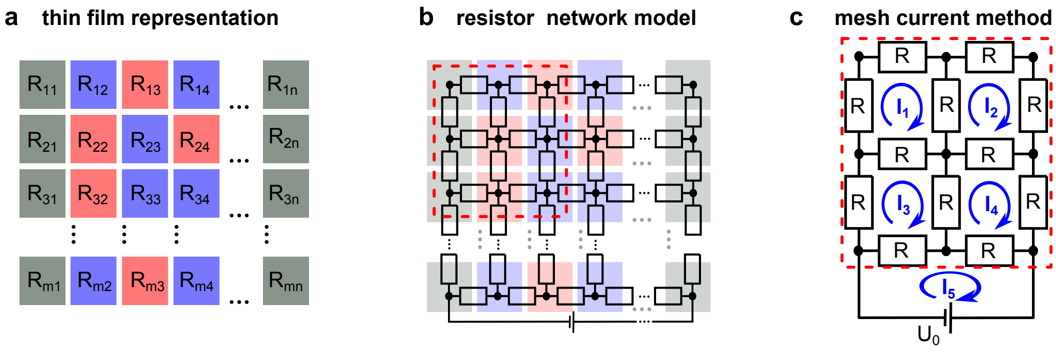

Figure A.5.: Random resistor network model of polycrystalline thin films. **(a)** The polycrystalline film is divided in $m \times n$ domains with resistance R_{ij}. The first and last column of domains represents the electrical contacts (grey domains). **(b)** A resistor network model is attributed. Each resistor represents the resistance of neighboring domains connected in series and is interconnected trough adjoining domains to the surrounding resistors forming a mesh with four resistors in each loop. **(c)** Example of a film with 3×3 domains with resistance R [compare dashed red area in (b)]. A mesh current is assigned to each essential mesh of the resistor network model (I_1 to I_5). The last essential mesh interconnects both electrical contacts. The mesh current method is used to determine the total resistance of the resistor network.

the sum of voltages across all resistors in mesh one is: $2 \times RI_1 + R(I_1 - I_2) + R(I_1 - I_3) = 0$. Similarly, the other mesh equations can be found, which can be summarized in matrix form:

$$\widehat{\mathbf{M}}\vec{I} = \begin{pmatrix} 4R & -1R & -1R & 0 & 0 \\ -1R & 4R & 0 & -1 & 0 \\ -1R & 0 & 4R & -1R & -1R \\ 0 & -1R & -1R & 4R & -1R \\ 0 & 0 & -1R & -1R & 4R \end{pmatrix} \begin{pmatrix} I_1 \\ I_2 \\ I_3 \\ I_4 \\ I_5 \end{pmatrix} = \begin{pmatrix} 0 \\ 0 \\ 0 \\ 0 \\ U_0 \end{pmatrix}. \tag{A.1}$$

To find the resistance of the resistor network, equation A.1 has to be solved for the mesh current I_5. The network resistance is than $R = U_0/I_5$.
Within this thesis, a "MatLab"-based function was developed, which sets up the matrix $\widehat{\mathbf{M}}$ for a given $m \times n$ matrix of domains with resistance R_{ij} and solves the matrix equation to determine the total resistance of the corresponding resistor network.

```
function [R_total] = RandomResistorNetwork(R_Matrix)
%RandomResistorNetwork(R_Matrix)

%’RandomResistorNetwork’ calculates the total resistance R_total for a
%given m times n resistor matrix R_Matrix using the mesh current method.
%The function sets up a linear equation system that correlates the mesh
%voltages and mesh currents according to M I = U, where M is a matrix, I a
%vector containing the mesh currents, and U a vector of the mesh voltages.

%Determination of the size of R_Matrix
dim=size(R_Matrix);
m=dim(1);
n=dim(2);


%Initializing the number of meshes and the matrix M
```

```
%The network consists of (m-1)*(n-1)+1 meshes
mesh_Nr=0;
M=zeros((m-1)*(n-1)+1);

%Setting up M
for a=1:(m-1)
    for b=1:(n-1)
        mesh_Nr=(a-1)*(n-1)+b;
        M(mesh_Nr,mesh_Nr)=(R_Matrix(a,b)+R_Matrix(a,b+1)+,...
        R_Matrix(a+1,b)+R_Matrix(a+1,b+1));
        if a-1>0
            M(mesh_Nr,(a-2)*(n-1)+b)=-0.5*(R_Matrix(a,b)+R_Matrix(a,b+1));
        end
        if b-1>0
            M(mesh_Nr,(a-1)*(n-1)+b-1)=-0.5*(R_Matrix(a,b)+R_Matrix(a+1,b));
        end
        if b+1<n
            M(mesh_Nr,(a-1)*(n-1)+b+1)=-0.5*(R_Matrix(a,b+1)+R_Matrix(a+1,b+1));
        end
        if a+1<m
            M(mesh_Nr,(a)*(n-1)+b)=-0.5*(R_Matrix(a+1,b)+R_Matrix(a+1,b+1));
        end
        if a+1==m
            M(mesh_Nr,(m-1)*(n-1)+1)=-0.5*(R_Matrix(a+1,b)+R_Matrix(a+1,b+1));
        end
    end
end

%Special case: A network of 2 resistors:
if n==2
    M(mesh_Nr+1,mesh_Nr+1)=(R_Matrix(m,1)+R_Matrix(m,end))*0.5;
end

%Adding the voltage source mesh
if n>2
    M(mesh_Nr+1,mesh_Nr+1)=(R_Matrix(m,1)+R_Matrix(m,end))*0.5+,...
    sum(R_Matrix(m,2:(end-1)));
end
for b=1:(n-1)
    M(mesh_Nr+1,(m-2)*(n-1)+b)=-0.5*(R_Matrix(m,b)+R_Matrix(m,b+1));
end

%Defining the vecor U:
U=zeros((m-1)*(n-1)+1,1);
U(end)=1;

%Solving the linear equation system:
lsg=M\U;

%Calculating the total resistance R_total = U_0/I(last entry)
R_total=1/lsg(end);
end
```

B | List of publications

Publications related to the content of this thesis:

1. **J. Rensberg**, Y. Zhou, S. Richter, C. Wan, S. Zhang, P. Schöppe, R. Schmidt-Grund, S. Ramanathan, F. Capasso, M. A. Kats, C. Ronning, Epsilon-Near-Zero Substrate Engineering for Ultrathin-Film Perfect Absorbers. *Phys. Rev. Applied* **8**, 014009 (2017).
2. Z. Zhang, F. Zuo, C. Wan, A. Dutta, J. Kim, **J. Rensberg**, R. Nawrodt, H. H. Park, T. J. Larrabee, X. Guan, Y. Zhou, S. M. Prokes, C. Ronning, V. M. Shalaev, A. Boltasseva, M. A. Kats, and S. Ramanathan, Evolution of Metallicity in Vanadium Dioxide by Creation of Oxygen Vacancies. *Phys. Rev. Applied* **7**, 034008 (2017).
3. **J. Rensberg**, S. Zhang, A. S. McLeod, C. Schwarz, M. Goldflam, M. Liu, J. Kerbusch, R. Nawrodt, S. Ramanathan, D. N. Basov, F. Capasso, C. Ronning, and M. A. Kats, Active optical metasurfaces based on defect-engineered phase-transition materials. *Nano Letters* **16**, 1050-1055 (2016).

Further publications:

1. J. Salmen, M. Hafermann, **J. Rensberg**, C. Wan, R. Wambold, B. S. Grundlach, C. Ronning, and M. A. Kats, Flat Optical and Plasmonic Devices Using Area Selective Ion-Beam Doping. *Adv. Opt. Mater.* under revision (2017).
2. S. Eckner, K. Ritter, P. Schöppe, E. Haubold, E. Eckner, **J. Rensberg**, R. Röder, M. C. Ridgeway, and C. S. Schnohr, Bond strength inversion in semiconductor alloys. *Phys. Rev. Lett.* under revision (2017).
3. L. L. Wang, X. J. Cui, **J. Rensberg**, K. Wu, W. Wesch, and E. Wendler, Growth and optical waveguide fabrication in spinel $MgGa_2O_4$ crystal. *Nucl. Instr. & Meth. B* in press (2017).
4. L. L. Wang, X. J. Cui, **J. Rensberg**, J. J. Yin, S. Creutzburg, K. Ritter, W. Wesch, and E. Wendler, The lattice expansion, damage effect and propagation loss of $KTiOPO_4$ waveguides formed by ion implantation. *Opt. Mater.* **66**, 374-380 (2017).
5. E. Wendler, G. Becker, **J. Rensberg**, E. Schmidt, S. Wolf, and W. Wesch, Direction-dependent RBS channeling studies in ion implanted $LiNbO_3$. *Nucl. Instr. & Meth. B* **379**, 195-199 (2016).
6. S. Wolf, **J. Rensberg**, A. Johannes, R. Thomae, F. Smit, R. Neveling, M. Moodley, T. Bierschenk, M. Rodriguez, B. Afra, S. B. Hasan, C. Rockstuhl, M. Ridgway, K. Bharuth-Ram, and C. Ronning, Shape manipulation of ion irradiated Ag nanoparticles emedded in lithium niobate. *Nanotechnology* **27**, 145202 (2016).
7. S. Rentrop, B. Abendroth, J. Walter, **J. Rensberg**, W. Münchgesang, R. Strohmeyer, H. Stöcker, C. Ronning, S. Gemming, and D. C. Meyer. Stoichiometry variation for the atomic layer deposition of $Sr_xTi_yO_z$ from $Sr(i\ Pr_3Cp)_2$,$Ti[N(CH_3)_2]_4$ and H_2O. *Thin Sol. Films* **577**, 134-142 (2015).
8. C. Walder, M. Kellerman, E. Wendler, **J. Rensberg**, K. von Maydell, and C. Agert, Comparison of silicon oxide and silicon carbide absorber materials in silicon thin-film solar cells. *EPJ Photovoltaics* **6**, 65302 (2015).

9. H. Wylezich, H. Mähne, A. Heinrich, S. Slesazeck, **J. Rensberg**, C. Ronning, P. Zahn, and T. Mikolajick, Adjusting the forming step for resistive switching in Nb_2O_5 by ion irradiation. *J. Vac. Sci. & Tech.* **33**, 01A105 (2015)

10. B. Abendroth, S. Rentrop, W. Münchgesang, H. Stöcker, **J. Rensberg**, C. Ronning, S. Gemming, and D. C. Meyer, ’Atomic layer deposition of dielectric thin film in the ternary system TiO_2-$SrTiO_3$’ in Functional structure design of new high performance materials via atomic design and defect engineering (ADDE), editor D. Rafaja, 118-133 (2015).

11. H. Wylezich, H. Mähne, **J. Rensberg**, C. Ronning, P. Zahn, S. Slesazeck, and T. Mikolajick, Local Ion irradiation-Induced Resistive Threshold and Memory Switching in Nb_2O_5/NbO_X Films. ACS Appl. Mat. & Interf. 6, 17474-17480 (2014).

12. S. Wolf, **J. Rensberg**, H. Stöcker, B. Abendroth, W. Wesch, and C. Ronning, Utilizing dynamic annealing during ion implantation: synthesis of silver nanoparticles in crystalline lithium niobate. *Nanotechnology* **25**, 135611 (2014).

13. R. Röder, M. Wille, S. Geburt, **J. Rensberg**, M. Zhang, J. G. Lu, F. Capasso, R. Buschlinger, U. Peschel, and Carsten Ronning, Continous wave nanowire lasing, *Nano letters* **13**, 3602-3606 (2013).

14. C. S. Schnohr, H. Kämmer, C. Stephan, S. Schorr, T. Steinbach, and **J. Rensberg**, Atomic-scale structure and band-gap bowing in Cu(In,Ga)Se_2. *Phys. Rev. B* **85**, 245204 (2012).

15. S. Milz, **J. Rensberg**, C. Ronning, and W. Wesch, Correlation between damage evolution, cluster formation and optical properties of silver implanted lithium niobate. *Nucl. Instr. & Meth. B* **286**, 67-71 (2012).

Invited talks:

1. Ion beam modification of phase transition materials - A method to turn VO_2 films into optical metasurfaces
   Seminar Talk at the Helmholtz-Zentrum Dresden-Rossendorf (October 2017).
2. Ion irradiation - A versatile tool to transform thin films into optical metasurfaces
   Seminar Talk at the department of Physics, University of KwaZulu-Natal, Durban (August 2016).
3. Ion beam modification of vanadium dioxide
   Seminar Talk at the department of Physics, University of California - San Diego (August 2014).
4. Ion beam modification of memristive oxides
   Seminar Talk at the department of Physics, University of Pretoria (March 2014).

Oral contributions at conferences:

1. Deep Sub-Wavelength Phase Coexistence Patterning of Phase Change Materials by Means of Ion irradiation
   M. Hafermann, **J. Rensberg**, C. Ronning
   Talk at the MRS Fall Meeting, Session EM 03.08.03, Boston (November 2017).
2. Optical power diodes based on phase-transition materials
   C. Wan, E. H. Horak, Y. Zhou, Z. Zhang, J. Salmen, P. Roney, J. Rensberg, B. Grundlach, S. Ramanathan, R. H. Goldsmith, C. Ronning, M. A. Kats
   Talk at the SPIE OPTO, San Francisco (April 2017).
3. Submicron scanning X-Ray diffraction imaging of strain in VO_2 microwires
   A. Johannes, M. Burghammer, **J. Rensberg**, C. Ronning
   Talk at the DPG spring Meeting, Berlin (March 2017).

4. Wavelength- and Temperature-Tunable Ultra-Thin Perfect Absorbers Using Ion Beam Irradiation
   J. Rensberg, C. Wan, S. Richter, Y. Zhou, S. Zhang, R. Schmidt-Grund, S. Ramanathan, F. Capasso, M. A. Kats, C. Ronning
   Talk at the MRS Fall Meeting, Session EM 7.2.10, Boston (November 2016).
5. Metasurfaces based on artificially induced phase coexistence in phase-change materials
   J. Rensberg, S. Zhang, A. McLeod, C. Schwarz, M. Goldflam, R. Nawrodt, M. Liu, J. Kerbusch, Y. Zhou, S. Ramanathan, D. N. Basov, F. Capasso, C. Ronning, M. A. Kats *Talk at the OSA Novel Optical Materials and Applications conference, Boston* (June 2015).
6. Lateral patterned ion beam modification of VO_2 for optical applications
   J. Rensberg, S. Vatterodt, C. Schwarz, S. Zhang, Y. Zhou, M. Kats, M. Hopfe, T. Barth, R. Nawrodt, S. Ramanathan, F. Capasso, C. Ronning
   Talk at the SPIE Photonics, San Diego (August 2014)
7. Towards selective ion beam modification of vanadium dioxide
   J. Rensberg, C. Schwarz, S. Vatterodt, M. Hopfe, P. Schöppe, A. v. Müller, J. Sommerfeld, Y. Zhou, H. Schmidt, R. Nawrodt, C. Ronning
   Talk at the DPG spring meeting, Dresden (April 2014).
8. Track Morphology and Amorphization Kinetics Induced by 185 MeV Au-Ion Irradiation in $LiNbO_3$
   J. Rensberg, S. Milz, T. Bierschenk, B. Afra, M. D. Rodriguez, P. Kluth, M. C. Ridgeway, W. Wesch
   Talk at the REI-17, Helsinki (July 2013).
9. Resistive switching properties in ion beam modified $SrTiO_3$
   J. Rensberg, T. Bierschenk, B. Afra, M. D. Rodriguez, M. C. Ridgeway, A. Johannes, A. Jungkind, B. Roessler, C. Katzer, F. Schmidl, C. Ronning
   Talk at the DPG spring meeting, Regensburg (March 2013).
10. Surface plasmon resonance of Ag nanoclusters and refractive index changes in ion irradiated lithium niobate
    J. Rensberg, S. Milz, C. Ronning, W. Wesch
    Talk at the DPG spring Meeting, Berlin (March 2012).
11. Ion beam synthesis of silver nanoclusters in lithium niobate
    S. Milz, **J. Rensberg**, E.-B. Kley, F. Schrempel, C. Ronning, W. Wesch
    Talk at the REI-16, Beijing (August 2011).

C | Ehrenwörtliche Erklärung

Ich erkläre hiermit ehrenwörtlich, dass ich die vorliegende Arbeit selbständig, ohne unzulässige Hilfe Dritter und ohne Benutzung anderer als der angegebenen Hilfsmittel und Literatur angefertigt habe. Die aus anderen Quellen direkt oder indirekt übernommenen Daten und Konzepte sind unter Angabe der Quelle gekennzeichnet. Bei der Auswahl und Auswertung folgenden Materials haben mir die nachstehend aufge- führten Personen in der jeweils beschriebenen Weise geholfen:

- Das Wachstum der VO_2-Schichten auf Al_2O_3, SiO_2, ZnO, und AZO wurde von Dr. You Zhou (Universität Harvard) durchgeführt.
- Der Aufbau der insitu elektrischen Messapparatur erfolgte in Zusammenarbeit mit Alexander Tille.
- Die Ionenimplantationen wurden zum Teil mit Hilfe von Patrick Hoffmann, Ulrich Barth, Alexander Tille und Clements Anschütz durchgeführt.
- Die insitu elektrischen Messungen wurden zum Teil mit Hilfe von Alexander Tille, Clements Anschütz und Martin Hafermann durchgeführt.
- Die TEM Bilder wurden am Otto Schott Instit für Materialforschung der FSU Jena mit Hilfe von Philipp Schöppe aufgenommen.
- Die SEM und STEM Bilder wurden mit Hilfe von Carmen Vogt und Philipp Schöppe aufgenommen.
- Die XRD Untersuchungen wurden selbstständing in der Gruppe von Prof. Meyer (Bergakademie Freiberg) durchgeführt. Dr. Barbarara Abendroth, Dr. Hartmud Stöcker und Dr. Erik Mehner halfen bei der Einarbeitung in die Röntgendiffraktometrie.
- Die Ramanmessungen wurden selbstständig am Institut für Angewandte Physik der FSU Jena durchgeführt.
- Die Elektronenstrahllithographie wurde von Shuyang Zhang (Universität Harvard) und Jochen Kerbusch (Helmholtz-Zentrum Dresden-Rossendorf) durchgeführt.
- Die s-SNOM Messungen wurden mit Hilfe von Dr. Alexander Swinton McLeod, Prof. Mengkun Liu, und Michael Goldflam bei einem Aufenthalt in der Gruppe von Prof. Basov (Universität Kalifornien - San Diego) durchgeführt.
- Die temperaturabhängige Reflektionsmessungen wurden zum Teil mit Hilfe von Shuyan Zhang bei mehreren Aufenthalten in der Gruppe von Prof. Capasso (Universität Harvard) durchgeführt. Temperaturabhängige Reflektionsmessungen zur Bestimmungen der thermischen Stabilität von ionenstrahlinduzierten Defekten wurden mit Hilfe von Dr. Ronny Nawrodt und Rene Glaser durchgeführt. Weitere Reflektionsmessungen wurden zum Teil von Martin Hafermann und Chenghao Wan (Universität Wisconsin - Madison) durchgeführt.
- Die Ellipsometriemessungen und Auswertung der Ellipsometriedaten wurden von Steffen Richter (Universität Leipzig) durchgeführt.

Weitere Personen waren an der inhaltlich-materiellen Erstellung der vorliegenden Arbeit nicht beteiligt. Insbesondere habe ich hierfür nicht die entgeltliche Hilfe von Vermittlungs- bzw. Beratungsdiensten (Promotionsberater oder andere Personen) in Anspruch genom- men. Niemand hat von mir unmittelbar oder mittelbar geldwerte Leistungen für die Arbeiten erhalten, die im Zusammenhang mit dem Inhalt der vorgelegten Dissertation stehen.

Die Arbeit wurde bisher weder im In- noch im Ausland in gleicher oder ähnlicher Form einer anderen Prüfungsbehörde vorgelegt. Die geltende Prüfungsordnung der Physikalisch-Astronomischen Fakultät ist mir bekannt.

Ich versichere ehrenwörtlich, dass ich nach bestem Wissen die reine Wahrheit gesagt und nichts verschwiegen habe.

Jena, den 01.11.2017

(Jura Rensberg)